EXPERIMENTAL AND NUMERICAL ANALYSIS OF THERMOELECTRIC MAGNETOHYDRODYNAMIC DRIVEN LIQUID LITHIUM FLOW IN OPEN CHANNELS FOR FUSION APPLICATIONS

BY

WENYU XU

DISSERTATION

Submitted in partial fulfillment of the requirements
for the degree of Doctor of Philosophy in Nuclear Engineering
in the Graduate College of the
University of Illinois at Urbana-Champaign, 2015

Urbana, Illinois

Doctoral Committee:

Professor David N. Ruzic, Chair
Adjunct Professor Thomas J. Dolan
Professor Brian G. Thomas
Professor Rizwan Uddin
Assistant Professor Yang Zhang

Abstract

The concept of using molten metal as a plasma facing material (PFM) has been widely considered, and liquid lithium, among many choices, has attracted a lot of research interests in recent years. Compared to the traditional solid plasma facing component (PFC) a liquid lithium PFC may effectively lower the erosion and thermal stress while transferring heat and prolonging the lifetime limit of the PFCs. The liquid lithium surface can also suppress the hydrogen isotopes recycling and absorb the impurities in fusion reactors.

The Lithium/Metal Infused Trench (LiMIT) concept successfully demonstrated that the thermoelectric effect can drive liquid lithium flow within horizontally placed metallic open trenches when an external magnetic field is transverse to the trench walls. Experiments at the University of Illinois have yielded experimental lithium velocities of 0.22 ± 0.03 m/s under a magnetic field of 0.059T, and a similar experiment on HT-7 tokamak measured 0.037 ± 0.005 m/s lithium flow velocity. Experiments and simulations have been performed to investigate this type of thermoelectric driven lithium flow in open trenches and the relation between different parameters such as external heat flux, magnetic field, cooling rate, trench geometry, etc.

The application of this concept for fusion reactors has been twofold. One application is to use this concept for a flowing liquid lithium divertor. The trenches can be placed at the bottom of the tokamak along the poloidal direction so that lithium can be driven by the toroidal field to flow across the strike point. Experiments have been done on Magnum-PSI and DeVEX to investigate the plasma-lithium surface interactions for this thermoelectric driven trench flow. Lithium flows at the velocity that is calculated from the theory while some phenomena, such as lithium dry-out and lithium ejection, will need further investigation. Another application is to build these trenches on the inner wall to use flowing lithium as a plasma facing surface, which requires the lithium to flow along an arbitrary angle. Capillary force within the narrow width trenches is utilized to achieve this goal. The pumping effect from the thermoelectric force is expected to overcome the gravity and drive the lithium flow. A new LiMIT design with narrow vertical trenches was manufactured, and this type of flow was proven in experiments.

Acknowledgement

First, I would like to express my deepest gratitude to my advisor Professor David N. Ruzic for his tremendous support and unlimited guidance. Professor Ruzic is not only the best scientist who has in-depth understanding of plasma science, broad knowledge of the development of controlled fusion and keen intuition of research, but also a true leader who owns a long-term vision and ability to encourage students to explore the unknown. I would also like to thank Professor Dolan, Professor Thomas, Professor Uddin and Professor Zhang from my preliminary exam and final defense committee for their time and effort to contribute thoughts and instructions from different perspectives. I wish to deeply thank Michael Jaworski who initiated the thermoelectric driven liquid lithium research in our lab and gave me a lot of valuable assistance and suggestions. Vijay Surla, Mike Williams, Daniel Andruczyk, Davide Curreli, Peter Fiflis, Matthew Szott, Mike Christenson and Kishor Kalathiparambil have significant amount of contributions to this research. We have spent many days and nights together rushing towards those deadlines for so many different conferences! At the same time I will never forget the indispensable help from undergraduates including Michael Antonelli, Matt Lee, Jason Kim, Travis Mui, Ryan Switts, Alex Press, David Lee, Jack Meister, Ian Haehnlein, Aveek Kapat, Senad Melkic and Dren Qerimi. I have to admit that pursuing a PhD degree is not easy and I have met countless problems. Fortunately, I have gained the support from my dear colleagues including Hyungjoo Shin, Wayne Lytle, Bob Lofgren, Eithan Ritz, JR Sporre, Liang Meng, Zihao Ouyang, Tae Cho, Jungmi Hong, Dan Elg, Jason Peck and Kyle Lindquist. It is especially grateful and fruitful to have Soonwook Jung, Priya Raman and Roland Wu working and learning together through most of the time during my PhD. Last but not least, I would like to thank my parents and my wife Na Li for their unconditional love.

This work is supported under DOE contract DE-FG02-99ER54515

Table of Contents

List of Figures

Chapter 1 Introduction

One of the major topics in current fusion research is plasma facing components (PFCs) and plasma facing materials (PFMs) which requires substantial development from the fusion community [1]. Although the extremely hot plasma is confined by magnetic field in the tokamak the plasma is not really isolated from the vacuum chamber, which brings in a lot of issues to the PFCs such as erosion and damage, plasma contamination, trillium retention and helium removal. To satisfy the limit coming from these issues solid plasma facing component made out of carbon, beryllium or refractory metal have been studied, designed and tested in the past. However with the increasing fusion power which usually accompanied by higher and higher particle and energy flux on the PFCs the traditional solid PFCs start to suffer from a series of problems such as permanent damage from the plasma or high-energy neutrons, erosion and redeposition, failure due to thermal stress or fatigue, etc. On the other hand the concept of utilizing liquid metal, especially liquid lithium as the PFCs has been raised and drawn a lot of interest from the fusion community. Since then extensive research works have been done to investigate this concept and gained a lot of encouraging results. In this dissertation a method of using thermoelectric (TE) effect to drive liquid lithium flow in open channel in fusion relevant environment is investigated to provide an alternative way to drive the liquid lithium flow other than the magneto-hydrodynamics (MHD) pump or the gravity driven method. In addition, designs for different PFCs purpose are raised and analyzed experimentally and numerically.

This chapter will introduce the plasma-material interactions (PMI) in tokamak and traditional PFCs which have taken these PMIs into the design criteria. Then it will introduce and review recent liquid metal PFC research. The next section will introduce the TE effect and thermoelectric magneto-hydrodynamics (TEMHD) driven flow and discuss the previous research work. The last section will briefly talk about the Liquid Metal Infused Trenches (LiMIT) concept which utilizes the TE effect to drive liquid metal flow in open channels and the motivation of this work.

1.1 Background

1.1.1 Plasma-wall interactions and plasma facing materials

Since the plasma is not fully isolated from the PFCs there are a lot of plasma-wall interactions induced by the particle bombardment, radiation and heat flux, which lead to backscattering, outgassing, sputtering and evaporation of the wall material and influences both plasma and the PFC itself. Backscattering is when particles diffuse from the core region to the PFC surface some of them may become neutral and be scattered back to reenter the core plasma. Outgassing happens when the PFC temperature increases due to the accompanied energy deposition from the plasma flux some particles with comparably lower binding energy such as water molecules may detach from the PFC surface and diffuse into the plasma. Sputtering means some particles with high kinetic energy will transfer the energy to the PFC atoms and as a result the PFC atoms may get enough energy through the collision with incident particles or the cascade collision with nearby atoms to overcome the binding energy and enter the plasma. Evaporation happens when the energy deposition is so high that some part of the PFC evaporates and emits particles into the plasma.

Obviously all of these interactions may release unwanted impurities into the plasma. Some of the impurity particles may not get ionized in the edge plasma and successfully enter the core plasma. As a result the high temperature core plasma will lose a lot of energy through the impurity's Bremsstrahlung radiation, excitation and ionization [2]. In addition the existence of the impurity substitutes the fuel ions which will dilute the fuel density and make the confinement worse. Even the recycling of the fuel particle such as deuterium may also cause problems because it provides extra deuterium to the edge plasma close to the wall. The plasma density will be out of control and the plasma temperature will be lowered through inelastic collision.

On the other hand the PWI also affect the PFC through sputtering and chemical erosion, redepositition, particle retention and sometimes even arcing, which leads to the erosion, evaporation, material failure caused by the thermal cycling and thermal fatigue and some surface damage such as blistering, flaking and even form micro structure such as fuzz on the tungsten surface.

Consequently it is very important to control the edge plasma in the tokamak and reduce the particle flux to the PFCs. One way is to attach a limiter to the inner surface of vacuum vessel. The limiter is usually a solid block that extrudes into the magnetic field lines which is plotted in Figure 1.1. Because in the tokamak charged particles mainly travel along the magnetic field lines and magnetic field lines are parallel to the wall the limiter can block the field lines close to the wall surface and create a so-called scrap-off layer (SOL) between the major plasma and the wall surface. In this way, the size of the core plasma is confined and the diffusion length from the wall to the core plasma is greatly increased. In addition, when energetic particles from disruptions or other instability effects come out the limiter will be the first part to suffer the bombardment which protects the inner wall from being damaged.

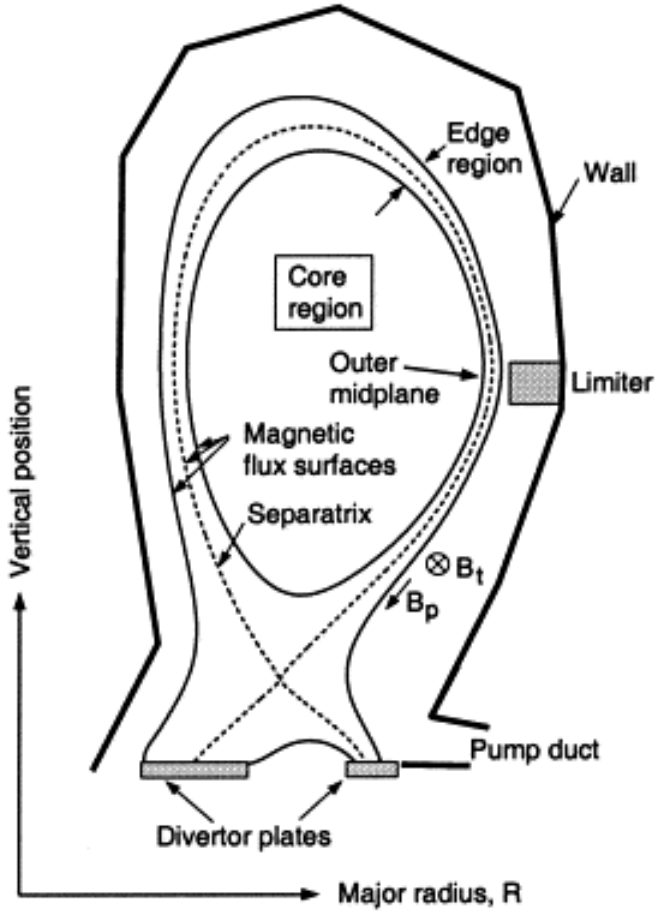

Figure 1.1 Cross section of a tokamak chamber. The first wall, the limiter and the divertor are all placed at different locations. [3]

These days, many tokamaks actually use divertor to control the edge plasma because the heat flux onto a limiter would be too high eventually. Unlike the limiter's magnetic field configuration, the idea of the divertor is to form open magnetic field lines close to the wall and conduct all these lines to enter the divertor target plate. When charged particles enter the open field lines they will travel along these lines and hit the target plate surface before diffusing back to the core plasma. With the divertor, the shape of the magnetic field lines can be actively controlled so that the plasma edge is well determined. Usually the divertor target plates are installed on top or bottom of the chamber and they are far away from the core plasma, which can be seen in Figure 1.1. Local pumping systems are sometimes installed near the target plate to pump the neutral particles formed on the target surface out of the chamber. This cannot be achieved by limiter and has become the main method to remove the He ash (one type of fusion products) from tokamak chamber.

With the application of limiter or divertor the PFCs in tokamak are actually divided into two categories: chamber wall which covers most area and bears a low particle flux and limiter/divertor which has a much higher particle flux on surface. No matter whether a limiter or a divertor is used, a big problem is how to deal with the incoming heat flux and energetic particles flux. Strong plasma material interactions always happen on the surface of the limiter or the divertor target plate. Generally speaking it is convenient to choose tungsten (W) or molybdenum (Mo) as the limiter or divertor material due to their low sputtering yield, resistance to erosion, high heat conductivity and high melting point [4]. However these types of materials are high-Z materials (high nuclear charge number) and because the Bremsstrahlung radiation is proportional to Z^2 a small amount of high-Z material existing inside core plasma will cause a huge amount of energy loss. Needless to say the strong line radiation and high energy cost of ionization. On the other hand some low-Z material such as graphite, ATJ graphite, Carbon-Fiber-Composite (CFC) [5] and beryllium (Be) [6] are also good choices. However the erosion problem on graphite is severe and its tritium retention also prevents the graphite's utilization in future tokamaks. Actually choosing the right type of material for the International Thermonuclear Experimental Reactor (ITER) divertor was still recently discussed in spite of the previous plan to use W and ATJ graphite it will now just use W. Beryllium has low sputtering yield and low hydrogen isotopes retention which makes it the wall material for ITER but it is very poisonous and expensive for large scale application [7].

Some important technologies are envisioned to improve the divertor. One is to increase the gas density close to the divertor target plate which is called gas-puff [8]. In this way the radiation is increased before the divertor target so that the directly deposited energy is lowered. Another method is called a snowflake divertor [9]. The snowflake divertor utilizes the second-order null of the poloidal field to create snowflake shape field lines before the divertor target plate. In this way the flux-expansion near the X-point is enlarged and the connection length to the target becomes much longer.

However there is no doubt that the high heat and particle flux becomes harder and harder to handle when the fusion plasma parameters keep progressing. Although ITER is planning to use solid material as its divertor surface the expected heat flux (~10MW/m^2) [10] is already very high for solid material. Once the divertor surface is permanently damaged it may need a lot of time and money to repair with remotely controlled robot, especially after tritium is used in ITER. In the meanwhile the divertor design is always complex and formed by different layers of materials. Once the high temperature gradient appears and disappears for many times the thermal stress due to different expansion rate may cause potential failure of the divertor surface, which will leave the inner structure exposed to the high temperature plasma.

1.1.2 Liquid metal plasma facing component

An alternative way is using liquid material as PFC surface. Since no matter what the PFC surface tends to be damaged what if the surface is in liquid state. Obviously the answer is the surface will not be damaged because of the self-healing from the liquid state itself. The PFC surface is no longer susceptible to damage or transient events inside fusion reactors. Even if some part of the surface is evaporated it will recover in short time. The erosion of the material is not a big problem as far as the liquid can be replenished. Even the transient events may have a lower possibility to permanently damage the PFC. Potentially the liquid surface can bear a higher heat flux compared to the traditional solid PFC. The liquid surface is free of material failure due to the thermal stress or thermal cycling.

However the utilization of liquid material, mostly liquid metal in tokamaks is not easy due to the strong magnetic field environment, vacuum limit, high heat and particle flux and material

compatibility. Trying to drive any liquid metal flow in tokamaks has to consider the MHD effects and the complex current distributions since it is in contact with plasma. The vapor pressure from the liquid surface is limited by the vacuum condition of the whole reactor. The high heat and particle flux may vaporize and sputter the material surface to pollute the plasma or redeposit to other part of the inner wall. And the structure material compatibility is an important issue for most of the liquid metal application.

The liquid metal PFC includes liquid metal inner wall and liquid metal divertor/limiter. For liquid metal wall one of the major topic is the direct deposition of liquid metal especially liquid lithium by evaporation which is investigated mostly on Lithium Tokamak Experiment (LTX) tokamak [11]. Using inertia or gravity to drive thin [12] or thick film flow [13] on the inner wall is another major concept. To utilize the liquid metal for divertor/limiter there are a lot of designs including static thick or thin film, flowing thick or thin film, waterfall, droplet and impinging jet.

Choosing the right material for the liquid metal PFC is very important. Candidates include lithium (Li), Sn-Li eutectic, molten salt (Flibe), gallium (Ga) and etc. [14], among which Li has drawn most of the interest from the fusion community. As a choice for PFC components, liquid lithium has a lot of advantages. Firstly as the liquid metal with low density, large heat capacity, high redeposition rate the erosion lifetime is not quite limited and the self-healing is good from the large heat flux and the neutron flux. Besides, flowing liquid lithium wall has the self-cooling potential and minimize the impurity accumulation. In addition to the above advantages the biggest advantage of liquid lithium is it can absorb impurity particles and pump hydrogen isotopes which can greatly lower the recycling. The low-recycling lithium PFC has the ability to improve the core plasma confinement and the overall plasma performance [15], increase the edge temperature and suppress edge localized modes (ELMs) [16]. This ability may also be utilized to pump the tritium or helium out of the reactor [17]. Another big advantage is lithium has the lowest Z among all PFC materials which makes it much more comparable and bearable for the plasma.

1.1.3 Previous research of the liquid metal application in fusion reactors

The liquid metal PFC research was firstly raised in the 1980s at University of Wisconsin, Madison, which proposed of using waterfall type annular lithium jet to protect the first wall [18]. In 1990s

Abdou and other researchers at University of California, Los Angeles designed flowing liquid metal film concept as inner wall and divertor [15]. In the meanwhile the great success of lithium pellet injection experiment on Tokamak Fusion Test Reactor (TFTR), which deposited thin lithium film on the limiter by the ablation of injected lithium pellets, has demonstrated the potential of lithium coated limiter and drawn a lot of interest on lithium [19]. Later the US Advanced Limiter-divertor Plasma-facing Systems (ALPS) program [20] has started to develop the innovative liquid metal surface divertor and demonstrate its advantage compared to the traditional divertor in terms of high power density capability, particle removal and lifetime erosion. Since then the liquid lithium and other liquid metal PFC research has become one of the most important topics in fusion PFC research.

A series of experiments on Current Drive eXperiment – Upgrade (CDX-U) used different sizes of free surface liquid lithium trays as the limiter and showed significant improvements of the plasma performance, which include the electron temperature increase, the greatly suppressed recycling and the impurity reduction. A main discovery is that the plasma loop voltage is lowered by a factor of 4 which means the plasma resistance is much smaller [21]. Similar experiments were done on Hefei Tokamak-7 (HT-7) with a movable free surface liquid lithium tray as a limiter and reveal a similar result [22]. The hydrogen recycling decreased by a factor of 4 based on the H-alpha line intensity and the particle confinement time increased by a factor of 2. In addition the lithium tray was moved inside the tokamak and the H-alpha measurement array only showed a strong intensity decrease where the tray was placed.

A crucial disadvantage of using this kind of free surface liquid lithium tray directly as the PFC is that the free surface liquid lithium under the strong heat flux and magnetic field may cause unexpected MHD effects. The Divertor Material Evaluation Studies (DiMES) project reported that large portion of liquid lithium on a test probe was ejected into the plasma during the normal discharge which led to plasma disruptions [23]. The ejection of small liquid lithium droplets was also observed on CDX-U [22] and HT-7 [23]. Some simulations of the ejection on DiMES suggested shorting out the current moving perpendicular to the field to avoid the ejection [24]. On CDX-U no significant ejection was discovered after the tray was carefully grounded which forced the current entering the tray to flow along the toloidal field [25]. But since the magnetic field strength on CDX-U is not as big as large tokamak it is hard to say if this works for all tokamaks.

Another way to minimize the ejection problem is changing the liquid lithium limiter to capillary porous system (CPS) configuration [26]. In CPS configuration the liquid lithium surface is covered by a layer of porous stainless steel mesh and because of the capillary pumping the liquid lithium will eventually form a thin layer above the stainless steel mesh appearing like a free surface. T-11M developed CPS as a liquid lithium limiter and realized a 0.3s quasi steady state tokamak regime and clean deuterium plasma with its Z_{eff} being almost 1. No lithium ejection was detected even during some transient events such as disruptions, ELMs and runaways [27]. Similar results were also achieved on Frascati Tokamak Upgrade (FTU) with a similar CPS configuration [28].

An important liquid lithium PFC was the new liquid lithium divertor (LLD) installed in National Spherical Torus Experiment (NSTX) [29]. This LLD consists of a thin porous Mo layer sprayed by plasma on top of a thin stainless steel layer with a copper heat sink attached to the back side. Liquid lithium was deposited onto the LLD surface until the target thickness was reached. ELM was strongly suppressed after a large amount of liquid lithium was coated on LLD and nearby ATJ graphite tiles [30]. Detailed analysis proves that the density profile control of the plasma is the key to the ELM suppression [31].

1.2 Thermoelectricity and TEMHD driven flow

The motionless liquid lithium PFC is not the ultimate solution for fusion since the impurity and hydrogen isotopes will eventually saturate and by then the lithium has to be replaced. Furthermore, the liquid lithium PFC is slowly eroded by the incoming energetic particle flux and the erosion speed has a positive correlation with the lithium surface temperature [32]. What is more, liquid lithium is vaporized when heated by the plasma and since its saturated vapor pressure rises exponentially with the surface temperature, which is plotted in Figure 1.2, it becomes crucial to control the surface temperature in case that the pressure is too high for the tokamak. However the surface temperature of liquid lithium is hard to control due to the intensive heat flux on the PFC surface.

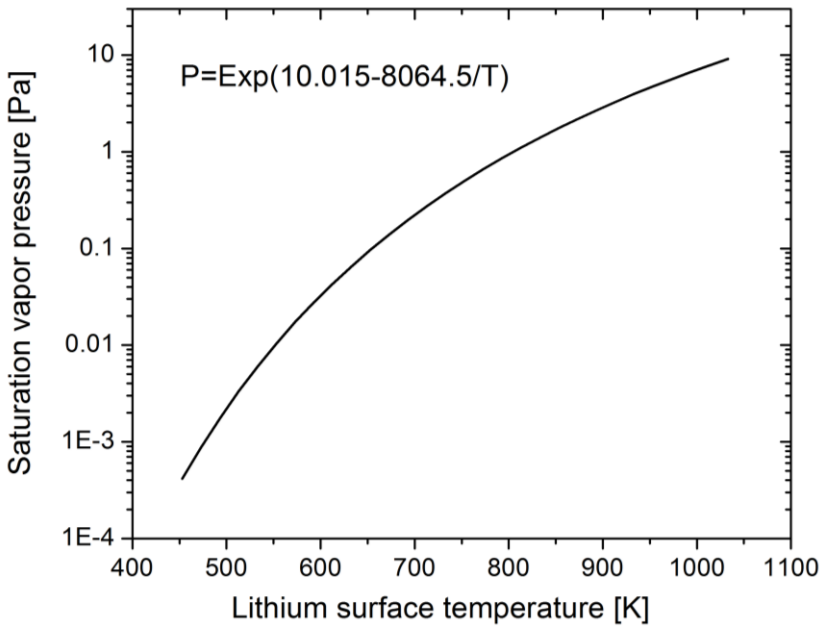

Figure 1.2 relation between Lithium saturation vapor pressure and liquid lithium surface temperature [33]

As a result flowing liquid lithium surface seems to be a better choice for the plasma facing surface. Many ideas have been proposed such as fast flowing lithium film over the divertor surface and free surface lithium jet [34] while most of them met with MHD problems due to the enormous magnetic field strength in the tokamak.

In 1979 Shercliff raised the concept of using thermoelectric effect to drive liquid lithium flow for the fusion reactors. The thermoelectric effect, also known as Seebeck effect, means that an electromotive force (e.m.f.) generates within a piece of material when a temperature gradient exists inside the material. Seebeck effect links the thermal effect with the electric effect, which makes itself a very useful phenomenon. One of the most important application of Seebeck effect is thermocouple. When two dissimilar wires are connected at two different spots to form a closed loop and if there is a temperature difference between these two spots there will be a thermoelectric current inside the wire, which can be calibrated to measure the temperature difference. Other applications include radioisotope thermoelectric power generator which is commonly used in deep

space to generate electricity from the radioactive decay heat and automotive thermoelectric power generator that can utilize the waste heat from the internal combustion engine.

However Shercliff stated that if one material is actually liquid metal the liquid metal can be driven by Lorentz force if a strong magnetic field is placed perpendicular to the thermoelectric current, which is called thermoelectric magnetohydrodynamic (TEMHD) driven flow [35], which is a potential method for the fusion reactor application. Since then many experiments have revealed the existence of the TEMHD effect and this becomes an important topic for crystal growth [36] and alloy solidification z[37] where the magnetic field is used to mitigate the convection.

1.3 Past research on the TEMHD driven flow

Using the thermoelectric effect to pump liquid metal was firstly proposed back to the 1960s. It was suggested to use the thermoelectric pump to drive liquid metal such as liquid Na to cool the fission reactor [38] [39]. The TEMHD pumping is generally analyzed and it is discovered that at under the high magnetic field limit the pumping force is proportional to the magnetic field while the flow velocity is inversely proportional to the magnetic field. The thermoelectric coefficient is pointed out as one of the essential parameters to increase the pumping ability [42]. The thermoelectric coefficient of the wall material is as important as that of the fluid material. It is also suggested that some semiconductors may generate much higher thermoelectric driven force since they have much higher thermoelectric coefficient. However not much detail of the flow was investigated in these works and the fluid structure is undiscovered.

Shercliff firstly suggested that the TEMHD driven flow can also be used for fusion application such as the blanket design to cool the fusion reactor [35]. The classic uncompressible MHD fluid equations were revised and solved by assuming a known temperature gradient at the fluid-solid interface which firstly provided a detailed description of the TEMHD driven flow. Specific cases including the Hartmann flow between two parallel plates and the two-dimensional flow of the circular pipe were analyzed. The detailed velocity distribution was solved for both cases. In addition, the TEMHD driven flow in closed containers which do not have walls parallel to the magnetic field [40] and circular pipe flow of finite length closed by plane ends parallel with the magnetic field [41] were analyzed. The TEMHD driven flow with walls parallel to the magnetic

field [42] was also investigated to reveal the existence of the fast boundary layers which exchanges the fluid with the central region.

In all the above cases Shercliff did not explore the strong effects of the heat convection. Later the effect of the heat transfer on the TEMHD driven flow was initially analyzed in 1981 [43] to find that the flow can affect the relation between the temperature and the heating/cooling which may generate unsteadiness that can cause thermal cycling. In the following paper Shercliff solved the coupled equations of the TEMHD and thermal convection under the high Hartmann number approximation with the interfacial temperature and the heat flux are both quadratic functions [44]. In this case the motion was pure rotation while non-uniqueness behavior of the flow was reported.

Since then most of the thermoelectric related research has been limited to the crystal growth and alloy solidification. Following the previous work Jaworski directly achieved the TEMHD driven swirling flow in experiment with liquid lithium and a stainless steel container. A model was developed to estimate the swirling velocity based on the interface temperature distribution measured between the liquid lithium and the container [40]. The estimated velocity actually matches the swirling velocity measured by tracking the movement of small impurity particles on the liquid top surface. Both the magnetic field and the surface heating were able to influence the flow velocity. The following work [45] on the same device investigated the heat transfer ability of this swirling flow and found that this swirling flow has a strong ability to mitigate the peak heat flux, which actually agrees with the discovery on CDX-U.

1.4 Lithium/metal infused trench (LiMIT) concept and motivation of this thesis

Although the suggestion of using TEMHD driven liquid lithium flow in fusion reactor was originally made for the lithium flow in the blanket it may also work for liquid lithium PFCs. The above CDX-U results and SLiDE results initiated the research to utilize the TEMHD driven liquid lithium flow as the PFC surface. The LiMIT concept based on the TEMHD driven flow was raised and it was proved to have a great potential for the liquid lithium PFC application [46]. The concept is described in Figure 1.3. In this concept, shallow trenches are cut on the plain metal surface and liquid lithium is melted inside these trenches. TEMHD can drive liquid lithium to flow along these trenches which keeps refreshing the surface for the plasma facing purpose.

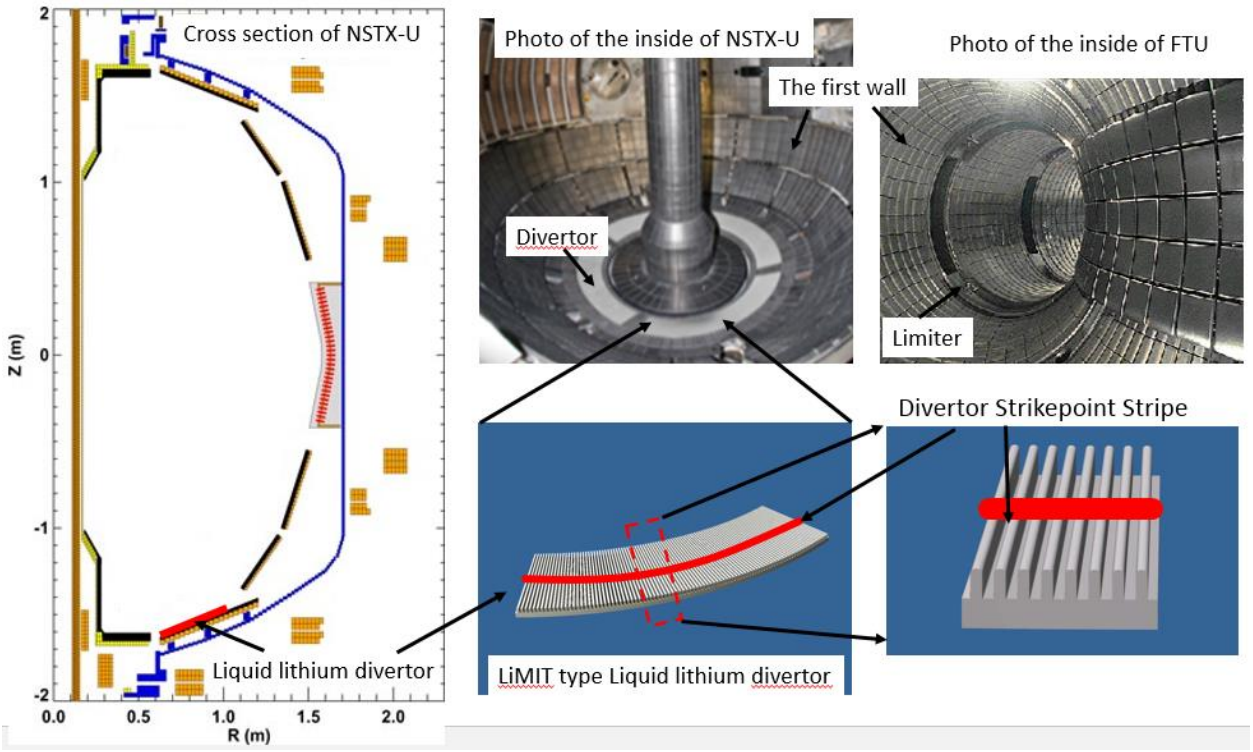

Figure 1.3 LiMIT type PFCs for tokamak application. The PFC can be used for divertor, limiter or the first wall. The cross section of NSTX-U schematic plot [47], the photo of the inner view of NSTX-U [48] and the inner view of FTU [49] are used to illustrate.

Specifically, the LiMIT type PFC can be utilized as divertor, limiter or first wall tile. When it is placed at the divertor region along the poloidal direction the toroidal magnetic field of the fusion reactor is perpendicular to the trench wall, where the thermoelectric current will generate due to the heating by the plasma. This leads to the TEMHD driven flow inside these open surface channels and this flow passing the peak heating area, which is called the strike point in tokamak, has the potential to withstand a strong heat flux without significant temperature increase and maintain the plasma facing surface fresh.

Similar design can also be used as limiter. Because both divertor and limiter receive a high heat flux in fusion reactors they are considered similar from the plasma surface interaction point of view and the same LiMIT design can be used for both of them. To use this concept for limiter the LiMIT type tray needs to be installed at the limiter's location, which can be seen in the FTU inner photo in Figure 1.3.

On the other hand if the LiMIT type PFC with active heating and cooling established can also be installed on the first wall along the poloidal direction to serve as the first wall tile. It can be designed into tile type PFC to replace those rectangular tiles attached to the inner wall in Figure 1.3. When this is applied the circulating lithium flow will act as low-recycling plasma facing surface.

To use the LiMIT concept as the PFC its performance in the fusion relevant environment needs to be investigated. It is important to note that the temperature, especially the surface temperature, of liquid lithium PFC is crucial to the hydrogen isotopes retention, erosion, lithium evaporation, edge plasma density control and heat removal. Obviously a well-designed structure based on this concept is essential to the success of this type of liquid lithium PFC, which requires a fully understand of the TEMHD driven flow and related heat transfer.

The purpose of this thesis is to demonstrate, investigate and evaluate the LiMIT concept for fusion PFC applications. In order to achieve this experiments and simulations have been done to understand the TEMHD driven flow in rectangular trenches, to test the performance of LiMIT concept under laboratorial and fusion relevant conditions, to investigate the influence of different parameters including trench geometry, surface heating flux, cooling and external magnetic field and to examine the LiMIT trenches placed at an arbitrary inclined angle. In general the study in this thesis will demonstrate the ability of using LiMIT concept for general PFC application purpose in tokamaks.

Chapter 2 Theory

2.1 Thermoelectric effect and TEMHD

2.1.1 Thermoelectric effect

The key phenomenon of the TEMHD driven flow is the thermoelectric effect. Because the diffusion speed of the charge carriers in the material is normally a function of temperature, when the temperature gradient exists the charge carriers tend to build up a concentration gradient, which leads to an inner electric field inside the material itself and this field can be represented as $-S\nabla T$. To incorporate this effect the Ohm's law is revised to:

$$\frac{\vec{\mathrm{j}}}{\sigma} = \vec{\mathrm{E}} + \vec{\mathrm{u}} \times \vec{\mathrm{B}} - \mathrm{S}\nabla\mathrm{T} \tag{2.1}$$

In the above equation $\vec{j}$ is the current density. σ is the electric conductivity. $\vec{E}$ is the electric field. $\vec{u} \times \vec{B}$ gives the e.m.f. due to motion, in which $\vec{v}$ is the velocity and $\vec{B}$ is the magnetic field. S is called the absolute thermoelectric coefficient (Seebeck coefficient) which has the unit Volt per Kelvin. ∇T is the temperature gradient.

Usually different materials have different Seebeck coefficients. The Seebeck coefficient could be either positive or negative, which depends on the type of the dominant charge carriers inside the material. The Seebeck coefficient is also a function of temperature. However the thermoelectric coefficient of liquid lithium does not change too much during the temperature range for fusion application [50] and it will be first assumed constant for all the temperature in this thesis.

When a temperature gradient is built within a certain type of material which has a constant Seebeck coefficient, the thermoelectric electromotive force (e.m.f.) will build up. However this thermoelectric e.m.f. does not generate thermoelectric current within the material because

$$\nabla \cdot \vec{\mathrm{j}} = 0 \tag{2.2}$$

$$\nabla \times \vec{\mathrm{j}} = \nabla \times \left(\vec{\mathrm{E}} - \mathrm{S}\nabla\mathrm{T}\right) = -\nabla\mathrm{S} \times \nabla\mathrm{T} - \mathrm{S}\nabla \times \nabla\mathrm{T} = 0 \tag{2.3}$$

Note that even when S is a function of T, $\nabla S \times \nabla T = 0$ is still valid.

However when two types of materials are brought together and when the interface is not perpendicular to the temperature gradient everywhere, the thermoelectric current starts to generate because at the interface the gradient of the thermoelectric coefficient is not zero. Figure 2.1 plots that the thermoelectric current flows between two different types of materials when the temperature gradient exists at the interface. This is similar to a thermocouple. When the temperature difference exists between the two junctions of the thermocouple it generates thermoelectric current. In Figure 2.1 if the thermoelectric electric field is integrated along a closed loop that passes the left and right junction we can get the thermoelectric e.m.f. ε that is

$$\varepsilon = \oint -S\nabla T \cdot d\vec{r} = -\int_{T_1}^{T_2} S_A \nabla T \cdot d\vec{r} + \int_{T_1}^{T_2} S_B \nabla T \cdot d\vec{r} = -\int_{T_1}^{T_2} S_A dT + \int_{T_1}^{T_2} S_B dT \quad (2.4)$$

In the above equation the loop integral gives a non-zero thermoelectric e.m.f. due to the difference of the thermoelectric coefficient in different materials. What is more the thermoelectric e.m.f. only depends on the temperature difference at the junctions. The temperature distribution within the material will not affect the thermoelectric e.m.f. But this only happens when there is no closed current loop other than the interface between these two types of materials.

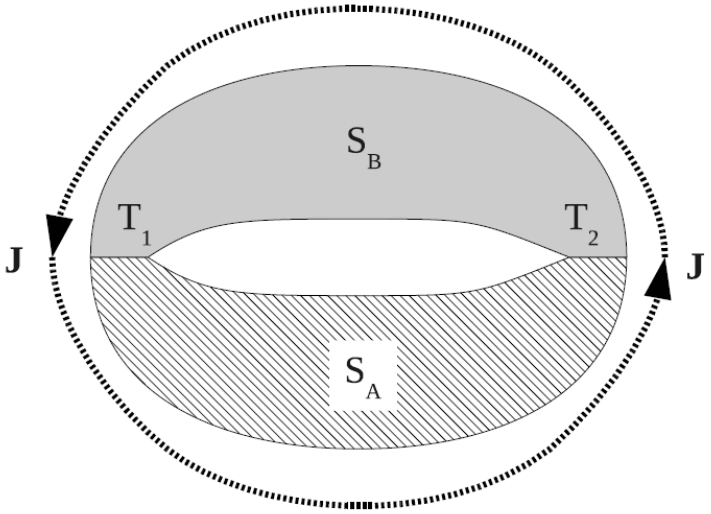

Figure 2.1 Thermoelectric current generated when the temperature difference exists at the different material interface [40].

Besides the above thermoelectric effect, which is also called Seebeck effect, there are two other thermoelectric effects. One is called Peltier effect and the other one is Thomson effect. Peltier

effect means when current is flowing through a junction of different thermoelectric materials energy is actually pumped by the current from one side to the other. The heat flux caused by this effect within one material is

$$\vec{q} = ST\vec{j} \tag{2.5}$$

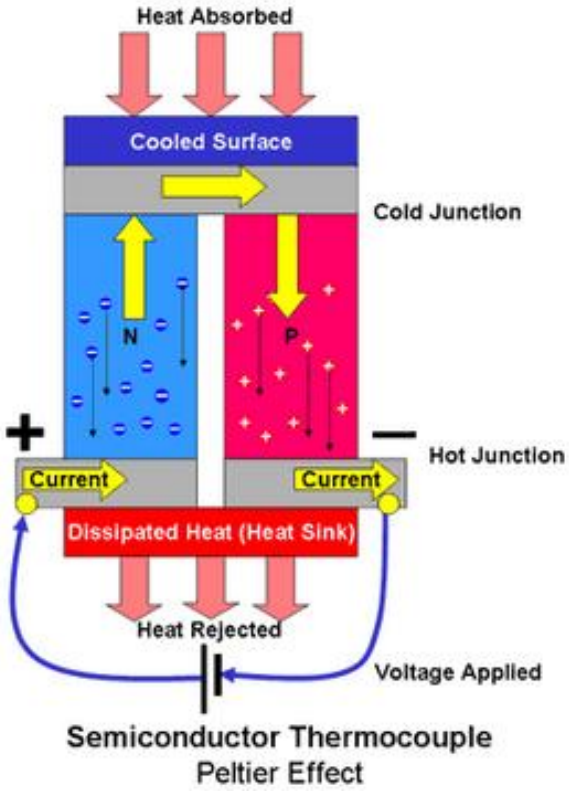

Figure 2.2 Peltier effect transfer heat from one junction to the other [51]

Thomson effect means when the current is flowing through a medium that has a temperature gradient along the current flow direction extra heat generation or absorption will happen. This is because when the current flows through the electric field built by the Seebeck effect its work will generate electrical energy or consume electrical energy. And this heat generation can be represented as

$$Q = S\vec{j} \cdot \nabla T \tag{2.6}$$

In all the heat transfer equation can be revised to

$$\rho C_P \left(\frac{\partial T}{\partial t} + \vec{u} \cdot \nabla T\right) = \nabla \cdot (k\nabla T) - \nabla \cdot (ST\vec{j}) + \frac{\vec{j} \cdot \vec{j}}{\sigma} + S\vec{j} \cdot \nabla T \tag{2.7}$$

If we assume no free charge

$$\nabla \cdot \vec{j} = 0 \tag{2.8}$$

Then equation 2.7 can be revised to

$$\rho C_P \left(\frac{\partial T}{\partial t} + \vec{u} \cdot \nabla T\right) = \nabla \cdot (k\nabla T) + \frac{\vec{j} \cdot \vec{j}}{\sigma} - T\vec{j} \cdot \nabla S \tag{2.9}$$

When S is constant the last term obviously is zero. When S is a function of temperature then the above equation can further be revised to

$$\rho C_P \left(\frac{\partial T}{\partial t} + \vec{u} \cdot \nabla T\right) = \nabla \cdot (k\nabla T) + \frac{\vec{j} \cdot \vec{j}}{\sigma} - T(dS/dT)\vec{j} \cdot \nabla T \tag{2.10}$$

2.1.2 General description of TEMHD driven flow

In the thermoelectric effect when the pair of materials becomes solid metal and liquid metal it will become complex. Because of the temperature gradient at the liquid-solid interface thermoelectric current generates from the interface. This current flows between the solid material and the liquid material to form a closed current loop. If an external magnetic field exists a Lorentz force may generate within the liquid metal when the curl between the magnetic field and the current is not zero, which can drive the liquid metal to flow.

Normally for liquid metal the magnetic Reynolds number (R_m) is much smaller than 1, which means the induced magnetic field generated by the motion of liquid metal is much smaller than the external magnetic field so it can be neglected [52].

$$R_m = \mu\sigma u l \tag{2.11}$$

In the above equation μ is the dynamic viscosity. u is the velocity and l is the characteristic length of the fluid. With this assumption the MHD equations for incompressible flow can be written as:

$$\nabla \cdot \vec{u} = 0 \tag{2.12}$$

$$\rho \left(\frac{\partial \vec{u}}{\partial t} + \vec{u} \cdot \nabla \vec{u}\right) = -\nabla p + \mu \nabla^2 \vec{u} + \vec{j} \times \vec{B} \tag{2.13}$$

$$\rho C_P \left(\frac{\partial T}{\partial t} + \vec{u} \cdot \nabla T\right) = \nabla \cdot (k\nabla T) + \frac{\vec{j} \cdot \vec{j}}{\sigma} - T(dS/dT)\vec{j} \cdot \nabla T \tag{2.14}$$

$$\vec{\mathrm{j}} = \sigma\left(\vec{\mathrm{E}} + \vec{\mathrm{u}} \times \vec{\mathrm{B}} - \mathrm{S}\nabla\mathrm{T}\right) \,\&\, \nabla \cdot \vec{\mathrm{j}} = 0 \tag{2.15}$$

In the above equations ρ is the density and C_P is the heat capacity of the liquid metal. p is the pressure and k is the thermal conductivity. The heat transfer equation is also included because the heat transfer affects the momentum transfer equation after the thermoelectric effect is added. Since the thermoelectric e.m.f. only depends on the temperature distribution at the interface in some special cases the heat transfer equation can be excluded if the temperature distribution is known.

Since the Seebeck current generates the only driven force in the Navier-Stokes equation, the induced current should always be smaller than the Seebeck current and the total current density should always be the same level as the Seebeck current density. As a result, it is convenient to assume that the total current density is $\vec{J} = C_0 \sigma S \nabla T$. Here C_0 is an arbitrary constant which is not far from one. For the sake of simplicity, some dimensionless assumptions are postulated here. The velocity is taken to be $\vec{u} = u_0 \vec{u}^*$ in which u_0 is a characteris``tic velocity. Similarly the temperature is assumed to be $T^* = \frac{T - T_0}{T_{max} - T_0}$ in which T_0 is the melting temperature (180.5C or 453.6K) of lithium and T_{max} is the maximum temperature of liquid lithium during experiment. The operator ∇ becomes $\nabla = \frac{1}{l}\nabla^*$ in which l is the characteristic length. With these dimensionless numbers, the heat transfer equation at steady state can be revised as

$$\vec{\mathrm{u}}^* \cdot \nabla^* \mathrm{T}^* = \frac{\mathrm{k}}{\rho \mathrm{C_P} l \mathrm{u_0}} \nabla^{*2} \mathrm{T}^* + \mathrm{C_0}^2 \frac{\sigma \mathrm{S}^2 \left(\frac{(\mathrm{T_{max}} - \mathrm{T_0})}{l}\right)^2}{\frac{\rho \mathrm{C_P u_0 (T_{max} - T_0)}}{l}} (\nabla^* \mathrm{T}^*)^2 - \mathrm{C_0} \frac{\sigma \mathrm{S} \frac{(\mathrm{T_{max}} - \mathrm{T_0})^3}{l^2} \frac{\mathrm{dS}}{\mathrm{dT}}}{\frac{\rho \mathrm{C_P u_0 (T_{max} - T_0)}}{l}} \mathrm{T}^* (\nabla^* \mathrm{T}^*)^2 \tag{2.16}$$

To estimate the importance of each term in the heat transfer equation, values are assigned to the characteristic paramaters. $u_0 = 0.1 m/s$. $l = 0.01 m$. $(T_{max} - T_0) = 300 K$. With these values, the coefficient of the first term is 0.02 which means in the flow direction the convection is much more important than heat conduction. The coefficient in front of the second term is $3.05 * 10^{-4}$, which means the Ohm heating is negligible. To evaluate the coefficient of the third term $\frac{dS}{dT}$ can be estimate from the experiment measurement which is $5 * 10^{-8}$ V/K^2. The coefficient of the third term equal to $1.83 * 10^{-4}$ so that the Thomson effect is also dropped in the calculation. However on the other two directions the characteristic velocity is almost zero which means the heat conduction is dominant on these two directions. The above equations 2.12 to 2.15 can be changed to

$$\nabla \cdot \vec{\mathrm{u}} = 0 \tag{2.17}$$

$$\rho\left(\frac{\partial \vec{u}}{\partial t}+\vec{u}\cdot\nabla\vec{u}\right)=-\nabla p+\mu\nabla^2\vec{u}+\vec{j}\times\vec{B} \tag{2.18}$$

$$\rho C_P\left(\frac{\partial T}{\partial t}+\vec{u}\cdot\nabla T\right)=\nabla\cdot(k\nabla T) \tag{2.19}$$

$$\vec{j}=\sigma\left(\vec{E}+\vec{u}\times\vec{B}-S\nabla T\right)\ \&\ \nabla\cdot\vec{j}=0 \tag{2.20}$$

2.1.3 1D model of the TEMHD driven duct flow

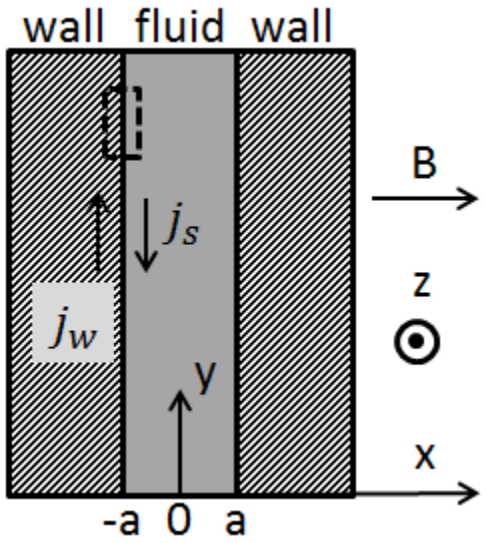

Figure 2.3 1D model of the TEMHD driven flow in narrow duct

A 1D model of the rectangular duct flow driven by thermoelectric effect is shown in Figure 2.3. In this model liquid metal flows between two parallel plates placed at x=+/-a. The magnetic field is perpendicular to the interface. The heat flux only exists along the y direction and the resulted temperature distribution is known and stable. The temperature gradient is dT/dy at the interface. The thickness of the wall is assumed to be t. The dimensions of this flow in y and z direction are assumed to be much larger than 2a. So the fluid flows along z direction with the value u while x and y components of the velocity are neglected. In this case, the heat transfer equation is excluded. The Ohm's law in the fluid becomes [35]

$$j=\sigma Bu+j_s \tag{2.21}$$

Here j_s represents the rest of the current in the fluid due the thermoelectric effect, which does not equals to the thermoelectric current, and j represents the total current in the fluid. The Navier-Stokes equation becomes

$$-\frac{\mathrm{dP}}{\mathrm{dz}}+\mu\frac{\mathrm{d^2u}}{\mathrm{dx^2}}-\mathrm{jB}=0 \tag{2.22}$$

Here $\frac{dP}{dz}$ is a constant pressure gradient within the fluid. Use the Ohm's law to cancel the total current j we can get

$$\mu\frac{\mathrm{d^2u}}{\mathrm{dx^2}}-\sigma\mathrm{B^2u}=\frac{\mathrm{dP}}{\mathrm{dz}}+\mathrm{j_sB} \tag{2.23}$$

Solving this equation with no-slip boundary condition $u(x=\pm a)=0$ while assuming j_s not varying with the velocity gives the velocity profile as

$$\mathrm{u}=-\frac{1}{\sigma\mathrm{B^2}}\left(\frac{\mathrm{dP}}{\mathrm{dz}}+\mathrm{j_sB}\right)\left[1-\frac{\cosh(\mathrm{Ha}*\mathrm{x/a})}{\cosh(\mathrm{Ha})}\right] \tag{2.24}$$

In the above equation Ha is called Hartmann number which is defined as $Ha=Bl\sqrt{\sigma/\mu}$ and l is the characteristic length of the fluid. This number describes the ratio of the electromagnetic force to the viscous force. The integral average of the velocity over the [-a, a] gives the average flow velocity u_m

$$\mathrm{u_m}=-\frac{1}{\sigma\mathrm{B^2}}\left(\frac{\mathrm{dP}}{\mathrm{dz}}+\mathrm{j_sB}\right)\left[1-\frac{\tanh(\mathrm{Ha})}{\mathrm{Ha}}\right] \tag{2.25}$$

To solve the thermoelectric part in the above equation we need to solve for the current. First the Kirchhoff's current law requires that the total current flows in the liquid should equal to the total current flows in the wall plates. Assuming the total current density inside the wall is j_w we can get

$$(\sigma\mathrm{Bu_m}+\mathrm{j_s})\mathrm{a}=-\mathrm{tj_w} \tag{2.26}$$

Here the minus sign means the direction of j_w should be opposite to the direction of the current flows inside the fluid.

Second, the Kirchhoff's voltage law requires that the loop integral of the electric field over the loop that encircles a certain part of the boundary as is shown by the dash line rectangle in Figure 2.2 should be zero. This gives another equation

$$\frac{j_w}{\sigma_w} - \frac{\sigma B u_m + j_s}{\sigma} = (S - S_w)\frac{dT}{dy} - u_m B \tag{2.27}$$

In the above equation σ_w is the electric conductivity of the wall and S_w is the thermoelectric coefficient of the wall material. Use these equations to cancel j_w and j_s we can get the mean velocity to be

$$u_m = \frac{Ha - \tanh(Ha)}{Ha + C\tanh(Ha)}\left(\frac{S - S_w}{B}\frac{dT}{dy} - \frac{1+C}{\sigma B^2}\frac{dP}{dz}\right) \tag{2.28}$$

This result is similar to what Shercliff got in 1978 which uses a different boundary condition [35]. In the above equation, $C = {a\sigma}/{t\sigma_w}$.

From this result we can see that when the Hartmann number is much larger than one we have $\frac{Ha - \tanh(Ha)}{Ha + C\tanh(Ha)} = \frac{Ha}{Ha + C}$, which is a constant. In this case the speed of the thermoelectric driven duct flow is proportional to the temperature gradient at the interface and the difference of the thermoelectric coefficients of the fluid and wall materials. However since the velocity is also inversely proportional to the magnetic field the flow speed will decrease if the magnetic becomes high.

2.2 LiMIT concept

2.2.1 LiMIT concept for fusion applications

The concept is illustrated in Figure 2.4. Shallow trenches are cut on the metal plate (such as stainless steel) surface and are placed at the divertor region. Liquid lithium will be melted inside these trenches. The right figure in Figure 2.4 is the cross section view of the trench. When the top surface is heated a vertical temperature gradient is established which generates the thermoelectric current from the lithium and stainless steel (SS) interface. Inside the liquid lithium this current flows downwards and since the toroidal magnetic field is perpendicular to the side wall the resulted Lorentz force will drive the liquid lithium flow into the plane. In the left figure of Figure 2.4 when the center of the LiMIT structure is heated by the plasma the liquid lithium is expected to flow across the heat strip which will bring the heat away from the direct heating area. Note that this has a self-limited effect which means when the heating is higher the flow velocity will be higher. When

other parameters being fixed, this flow only depends on the heating while no extra pumping is needed. It is believed that this design can bear a much higher peak heat flux compared to a pure solid metal plate serving as the divertor surface.

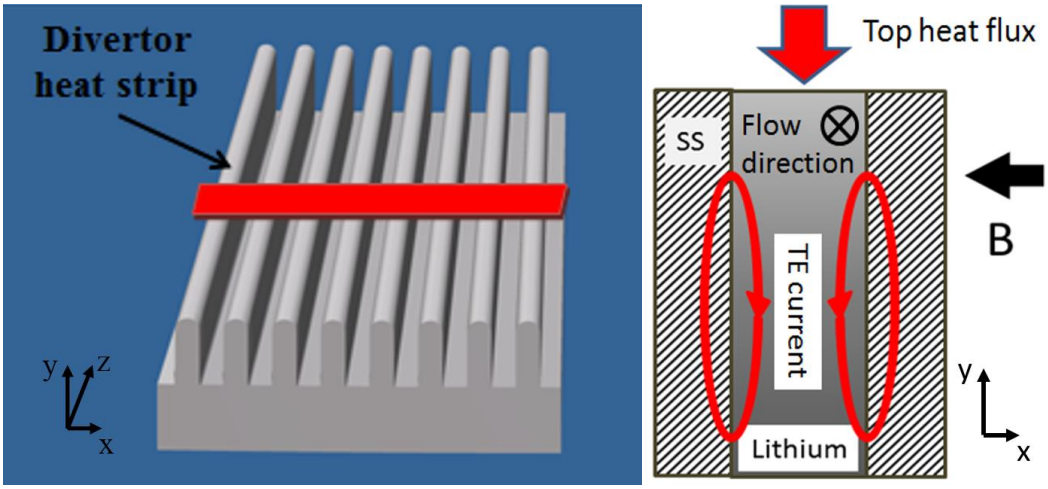

Figure 2.4 (a) LiMIT concept for divertor application (left figure) (b) cross section view of the open surface lithium channel (right figure)

2.2.2 TEMHD driven duct flow with non-uniform heating

When the heating is not uniform the temperature distribution becomes complicated in the TEMHD driven duct flow. In this case the flow is determined by the balance between the MHD damping force and the TEMHD driven force. If the mean flow velocity does not change through the whole trench the pressure will increase at the place where the TEMHD driven force is higher than the MHD damping and decrease at the place where the MHD damping is higher. In general the momentum transfer and the heat transfer equations need to be solved simultaneously to analyze the balance between these two forces. However if we assume that the length of the trench is much longer than the height of the trench and for most region the temperature gradient along y direction is much higher than the temperature gradient along z direction we can get [50]

$$u_m = \frac{Ha - \tanh(Ha)}{Ha + C\tanh(Ha)}\left(\frac{S - S_w}{B}\frac{\partial T}{\partial y} - \frac{1+C}{\sigma B^2}\frac{\partial P}{\partial z}\right) \tag{2.29}$$

$$\rho C_p u_m \frac{\partial T}{\partial z} = k\frac{\partial^2 T}{\partial y^2} \tag{2.30}$$

Here the coordinate uses the same definition in last section. The continuity equation requires the mean velocity u_m to be constant. These equations can be solved directly. First the temperature can be solved by the variable separation. And bring the temperature solution into the first equation the pressure can be solved. With the boundary conditions all the coefficient can be determined to get the exact solution.

Furthermore, if the surface heat flux is limited to a very narrow region on the trench top surface, which is the case in our test experiments for the LiMIT concept, we can assume that the temperature of the flow changes little along z direction. After the flow meets the narrow peak heat flux the temperature jumps up to a higher temperature value and stays unchanged until it flows out of the channel. This leads to the incontinuity of the temperature and the pressure gradient at the peak heat flux position but for most part of the fluid it works. With this assumption we can simply solve the above equations and estimate the temperature and the mean velocity.

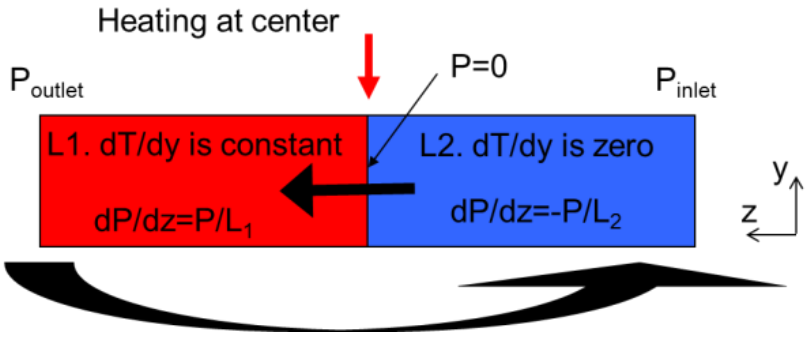

Figure 2.5 A 1D model to estimate the velocity and temperature distribution within the open surface lithium channel when the heat flux is not uniform.

Figure 2.5 describes the detail of the above assumption. The fluid enters the channel from the right side and leaves the channel from the left side. The pressure of the inlet and the outlet are assumed to be the same. The length of the right side which is considered as non-heated region is L_2 and the length of the left side which is the heated region is L_1. Then we have the equations

$$u_m = \frac{Ha-\tanh(Ha)}{Ha+C\tanh(Ha)}\left(\frac{S-S_w}{B}\frac{dT}{dy} - \frac{1+C}{\sigma B^2}\frac{P}{L_1}\right) = \frac{Ha-\tanh(Ha)}{Ha+C\tanh(Ha)}\left(\frac{1+C}{\sigma B^2}\frac{P}{L_2}\right) \quad (2.31)$$

And the power balance requires

$$k\frac{dT}{dy}L_1 a + k_w\frac{dT}{dy}L_1 t + \rho C_P\left(\frac{1}{2}\frac{dT}{dy}h\right)u_m ha = Q \tag{2.32}$$

Here k is the thermal conductivity of the fluid and k_w is the thermal conductivity of the wall material. h is the height of the trench and Q is the total power that is deposited onto the top surface. Cancel P and u_m we can get the ODE of $\frac{dT}{dy}$

$$\frac{1}{2}\rho C_P h^2 a\frac{L_1}{L_1+L_2}\frac{Ha-\tanh(Ha)}{Ha+C\tanh(Ha)}\frac{S-S_w}{B}\left(\frac{dT}{dy}\right)^2 + (kL_1 a + k_w L_1 t)\frac{dT}{dy} = Q \tag{2.33}$$

Based on the above equations the velocity and the temperature gradient can be calculated. If we assume the width of the trench is 2mm, the width of the wall is also 2mm, the height of the trench is 1cm, the total length is 10cm and the heated length is 1cm which is at the center, the bottom surface temperature is 200C, the wall material is stainless steel, whose electrical conductivity is $1.6*10^6$S/m and the thermal conductivity is 16W/(m*K), then the surface temperature and the average flow velocity can be calculated as a function of magnetic field or surface heat flux.

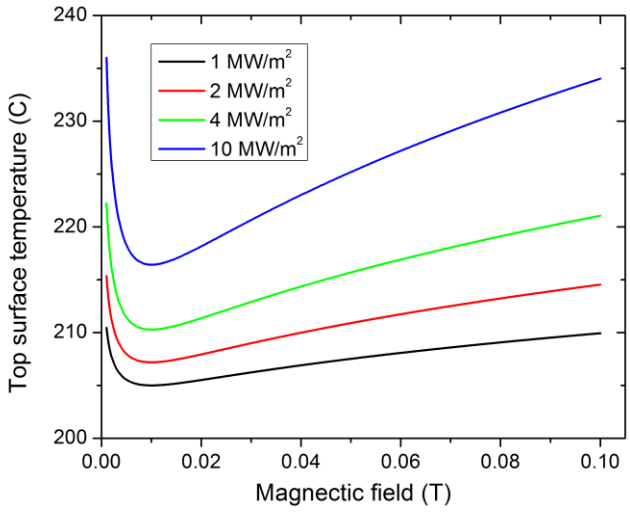

Figure 2.6 Surface temperature vs. magnetic field when the magnetic field is low (0~0.1T)

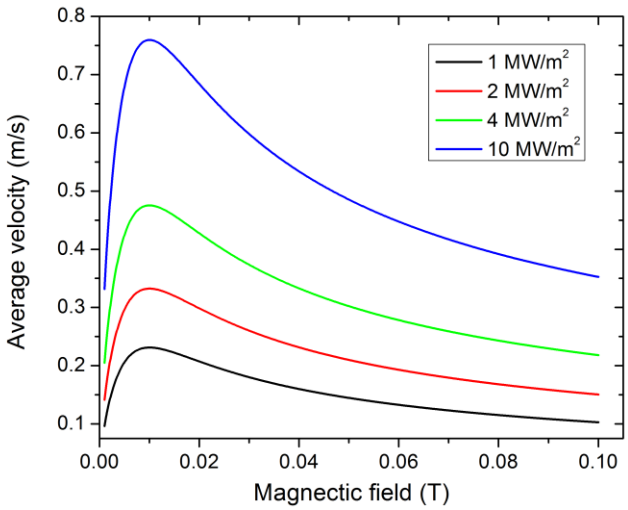

Figure 2.7 Average flow velocity vs. magnetic field when the magnetic field is low (0~0.1T)

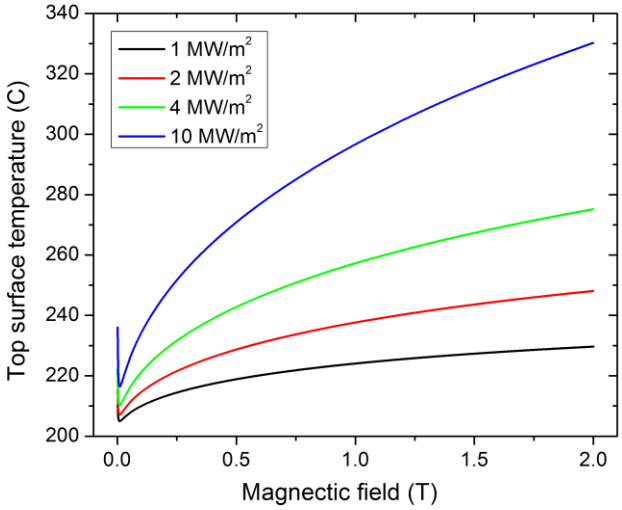

Figure 2.8 Surface temperature vs. magnetic field when the magnetic field is high (0~2T)

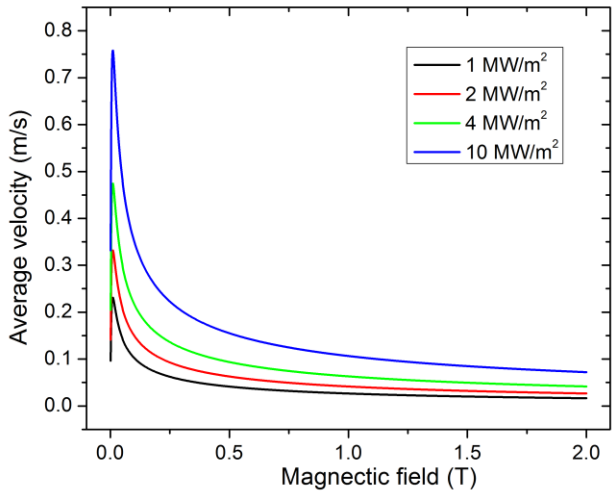

Figure 2.9 Average flow velocity vs. magnetic field when the magnetic field is high (0~2T)

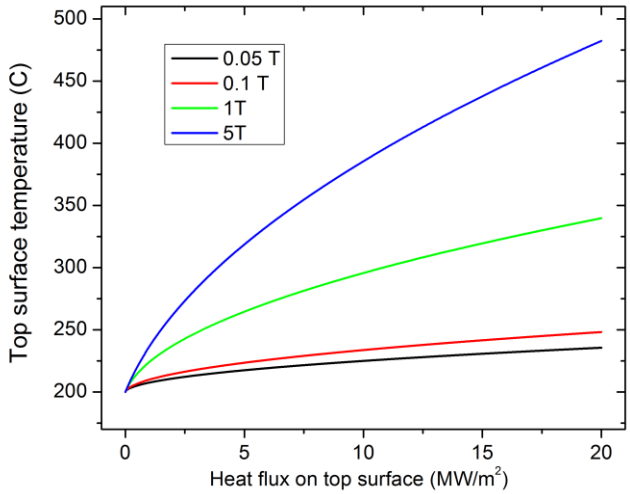

Figure 2.10 Surface temperature vs. top heat flux under different magnetic fields

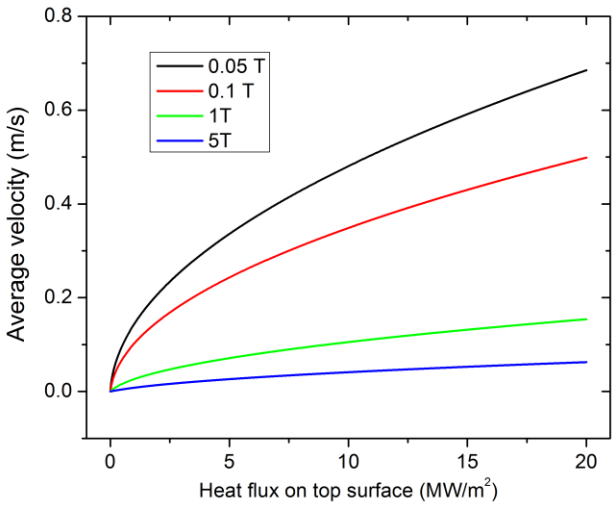

Figure 2.11 Average flow velocity vs. top heat flux under different magnetic fields

From Figure 2.6 and Figure 2.7 we can see that for different surface heat flux the surface temperature has a minimum and the average flow velocity has a maximum at a certain magnetic field. This is because the TEMHD driven force is a linear function of magnetic field while the MHD damping force is proportional to the square of magnetic field. When the magnetic field is low the TEMHD driven force overcomes the MHD damping force while after a certain point the MHD damping starts to be higher. Figure 2.8 and Figure 2.9 reveal the change at high magnetic fields. Under the high magnetic field limit, the velocity drops at the rate of 1/B while the surface temperature increases at the rate of $B^{1/2}$. As a result the velocity will not drop to zero and the increase of the surface temperature is far less than linear. Figure 2.10 and Figure 2.11 plots the surface temperature and average flow velocity increase with the surface heat flux at the rate less than linear. When the magnetic field is high the flow velocity drops to a few centimeters and is not enough to keep the surface temperature low. Note that in the calculation the bottom temperature is assumed to be a constant and this may not be valid in the real situation since the cooling rate at the bottom surface may not be able to keep the temperature.

2.2.3 Heat transfer of LiMIT

Two types of heat transfer are included. When the temperature gradient exists heat conduction happens. When lithium flows across the heating area, heat is brought to the downstream side by convection. Obviously if the heat is even over the whole surface the temperature is the same along the flow direction and there is no convection. But when the heat is not uniform there is always convection part in the heat transfer.

To evaluate the ratio of each part the first two terms of equation 2.32 are evaluated. In this equation the first term is the heat transferred by conduction while the second term is the heat transferred by convection. The ratio of the convection heat transfer over the conduction heat transfer is

$$\frac{\text{Convection}}{\text{Conduction}} = \frac{\rho C_P \left(\frac{1}{2}\frac{dT}{dy} h\right) u_m h a}{k \frac{dT}{dy} L_1 a + k_w \frac{dT}{dy} L_1 t} \tag{2.34}$$

If $ka + k_w t = k_{eff} a$ and $L = 2L_1$ then the above equation can be revised to

$$\frac{\text{Convection}}{\text{Conduction}} = \frac{\rho C_P u_m h^2}{k_{eff} L} = \text{Pe} \left(\frac{h}{L}\right)^2 \tag{2.35}$$

Here Pe is Peclet number which describes the ratio of advective transport rate over diffusive transport rate and $Pe = (\rho C\_P\ u\_m\ L)/k\_eff$. If h/L is assumed to be 0.1, trench thickness is the same as the wall thickness and L is 0.1m the Peclet number and the convection over conduction ratio can be plotted for different wall materials. For stainless steel convection is more important for a large range of velocity while for molybdenum and tungsten the conduction is stronger. However this ratio is sensitive to h/L and when h/L drops from 0.1 to 0.01 the convection/conduction will drop by 100 times, at which time the conduction becomes much more important compared to the convection.

To maintain the temperature gradient the cooling at the boundary is as important as the heat transfer through the trench. In the previous calculation the boundary is simply set at a constant temperature. In reality this condition may not be valid. The boundary is actually cooled by the flowing coolant.

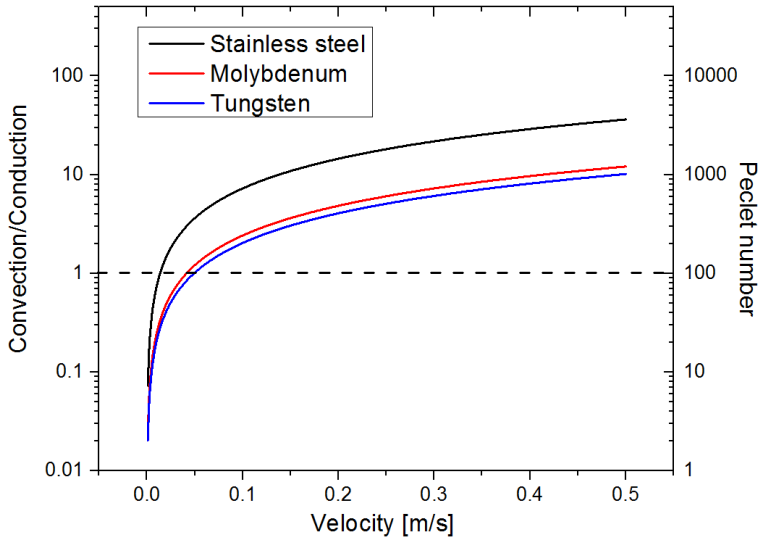

Figure 2.12 Convection over conduction ratio and Peclet number as a function of the average flow velocity for different materials

If the forced turbulent internal flow is assumed within the cooling channels then the Nusselt number can be estimated by the Dittus-Böelter correlation [53]

$$Nu = 0.023Re^{0.8}Pr^{0.4} \tag{2.36}$$

In this equation the Nusselt number $Nu = \frac{h_{coolant} * L_{coolant}}{k_{coolant}}$, Reynolds number $Re = \frac{\rho_{coolant} u_{coolant} L_{coolant}}{\mu_{coolant}}$ and Prandtl number $Pr = \frac{C_{p_{coolant}} \mu_{coolant}}{k_{coolant}}$.

If compressed air is used as the coolant we can estimate the Nusselt number and the heat transfer coefficient to find out the maximum heat transfer rate it can handle. If the wall temperature T_W is assumed to be 200C and the fluid temperature is assumed to be 20C the film temperature T_f at which the property of air will be evaluated is taken as arithmetic mean of the wall temperature and the fluid temperature at the entrance is 110C. If the pressure is assumed to be 50Psi (1 psi=6894.8 Pa) then the density is 3.14kg/m^3. The heat capacity is 1015J/kg*C. The dynamic viscosity is 2.24*10^{-5}Pa*s. The heat conductivity is 3.2*10^{-2}W/m*K. As a result the Prandtl number is 0.71. If the flow rate is 1cfm, which is 1 cubic foot per minute equaling to 4.72*10^{-4} m^3/s, and the inner diameter of the cooling tube is 1/4 inch (1 inch = 0.0254 m) which is 0.635cm then the velocity is

14.9m/s. The Reynolds number can be calculated to be 13263. So the Nusselt number is 39.8 and the heat transfer coefficient is 201W/m^2*K.

The heat flux at the cooling surface is $q_w = h_{coolant}(T_W - T_{coolant}) = 3.62 * 10^4 \mathrm{W/m^2}$. If the heated length over the total length along the flow direction is 1/10 then the surface heat flux this cooling can handle is 3.62*10^{5}W/m^2. In order to efficiently cool the trench that has up to 10MW/m^2 heat flux on the surface a much better cooling rate seems crucial to maintain the surface temperature.

If water is used as the coolant similar calculation can be done. When water is used and if it is not pressurized the wall temperature T_W is assumed to be 100C and the fluid temperature is assumed to be 20C the film temperature T_f is 60C. At this temperature the density is 983kg/m^3. The heat capacity is 4185J/kg*C. The dynamic viscosity is 4.67*10^{-4}Pa*s. The heat conductivity is 0.65W/m*K. The Prandtl number is 3. If the flow rate is 1gpm, which is 1 gallon per minute equaling to 0.00378 m^3/min or 6.3*10^{-5} m^3/s, and the inner diameter of the cooling tube is still 1/4 inch then the velocity is 2m/s. The Reynolds number can be calculated to be 26732. So the Nusselt number is 124.2 and the heat transfer coefficient is 12715W/m^2*K. The heat flux at the cooling surface is $q_w = h_{coolant}(T_W - T_{coolant}) = 1.02 * 10^6 \mathrm{W/m^2}$. If the heated length over the total length along the flow direction is 1/10 then the surface heat flux this cooling can handle is 1.02*10^{7}W/m^2. It can be seen that when water is used the cooling rate is efficient for 10MW/m^2 surface heating.

In many cases water cannot be used as coolant in experiments for safety issue since water can react with liquid lithium severely. On the other hand the high heat transfer coefficient of liquid is preferred for high power application in fusion reactors. Coolant such as mineral oil may be potential choices. If mineral oil is taken here for the same calculation above. The wall temperature T_W is assumed to be 150C and the fluid temperature is assumed to be 20C the film temperature T_f is 85C. At this temperature the density is 0.8*10^{3}kg/m^3. The heat capacity is 1.67*10^{3}J/kg*C. The kinetic viscosity is 1.17*10^{-6}m^2/s. The heat conductivity is 0.16W/m*K. The Prandtl number is 9.6. If the flow rate is 1gpm, which is 1 gallon per minute equaling to 0.00378 m^3/min or 6.3*10^{-5} m^3/s, and the inner diameter of the cooling tube is still 1/4 inch then the velocity is 2m/s. The Reynolds number can be calculated to be 10854. So the Nusselt number is 96.4 and the heat

transfer coefficient is 2459W/m^2*K. The heat flux at the cooling surface is $q_w = h_{coolant}(T_W - T_{coolant}) = 3.2 * 10^5 \mathrm{W/m^2}$. If the heated length over the total length along the flow direction is 1/10 then the surface heat flux this cooling can handle is 3.2*10^{6}W/m^2. This value is lower than water cooling. However the flow rate is only assumed to be 1gpm. If the flow rate is higher the cooling capability will also increase.

Now the average surface temperature can be estimated again based on the method in section 2.2.2. Instead of setting an arbitrary trench bottom temperature in section 2.2.2 the bottom temperature can be calculated in a different. Now assume that there is a layer of heat exchange interface between the lithium trench and the coolant which locates at the bottom of the trench in Figure 2.5. The heat exchange surface is cooled by water. In addition assume that all of the heat received from the top surface is transferred through the heat exchange surface and brought away by the coolant. The wall temperature T_W can be estimated as $T_W = T_{coolant} + \frac{q_w}{h_{coolant}} = T_{coolant} + \frac{q_{surface}/10}{h_{coolant}}$. Similarly the temperature at the trench bottom T_b can be calculated as $T_b = T_W + \frac{q_{surface}/10}{k_W} * d_{ex}$. Here d_{ex} is the heat exchange layer thickness. Substituting the bottom temperature in section 2.2.2 by the new T_b the average surface temperature can be calculated.

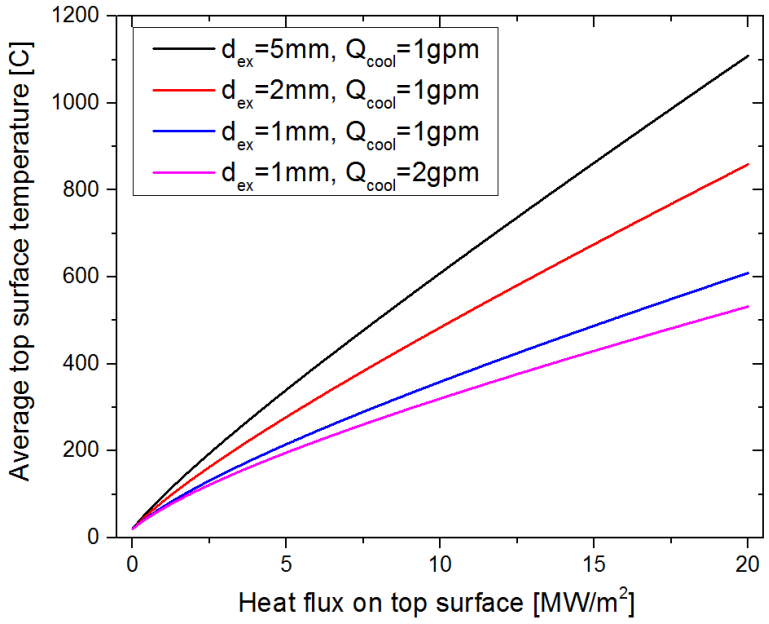

Figure 2.13 Average top surface temperature as a function of top surface heat flux. Heat exchange layer thickness and coolant flow rate are changed.

In Figure 2.13 the average surface temperature of the trench when magnetic field is 5T is plotted as a function of surface heat flux. Note that when the temperature is changed the thermal property of water is also changed. However when the volume flow rate is 1gpm and the water temperature is 20C the Nusselt number is 96 and the heat transfer coefficient is 9082W/m^2*K. So an average heat transfer coefficient 1.1*10^4W/m^2*K is used for simplicity.

From Figure 2.13 we can see that the average surface temperature increases almost linearly with surface heat flux. Decreasing the heat exchange layer thickness can greatly lower the surface temperature. Increasing the coolant flow rate also helps to lower the average surface temperature. In general water cooling is able to maintain the surface temperature low enough to avoid massive evaporation into the vacuum chamber.

Chapter 3 TEMHD driven open surface flow in horizontal trenches

In order to demonstrate the LiMIT concept and test its performance in different magnetic fields two experiments have been done. The first one was achieved on the Solid/liquid Lithium Divertor Experiment (SLiDE) chamber, during which we demonstrated the feasibility of LiMIT concept and investigate the TEMHD driven open surface flow in relatively weak magnetic field (0.01T~0.2T) and in addition another experiment was done on a middle size tokamak, Hefei Tokamak-7 (HT-7), as a limiter placed at the bottom of the chamber, in which the magnetic field can reach about 2T [13], to test this concept in the real tokamak level magnetic field. Both experiments will be discussed in this chapter to reveal the TEMHD driven open surface flow in horizontal trenches.

The first experiment, the SLiDE experiment is to demonstrate the LiMIT concept and to test its performance in lab-scale magnetic fields. In our experiment, a linear electron beam with Gaussian distribution which provides the heat flux up to 10 MW/m^2 is used to mimic the intensive heat flux in the fusion reactor. A Helmholtz coil is used to generate a magnetic field parallel with the electron beam which ranges from zero to about 800 Gauss (1 Gauss=$1*10^{-4}$ T) when a group of high current power supplies serve as the power source. Later eight car batteries are connected to this coil to generate about 0.23T magnetic field. The chamber is pumped to around 10^{-6} Torr (1 Torr=133.3 Pa) during the experiments. The whole system is tilted by about 55 degree, which means the e-beam and the magnetic field have a 35 degree angle with respect to the horizontal plane. A LiMIT type lithium tray is designed and installed horizontally in the vacuum chamber with additional heating and cooling system attached. A few K-type thermocouples are attached to the tray to measure the temperature change. Both IR camera and high speed camera are used to observe the surface of the liquid lithium through a 1.5” diameter view port on the side wall or through the view port above the electron gun. The whole setup is shown in Figure 3.1 and the design of the trench will be discussed first.

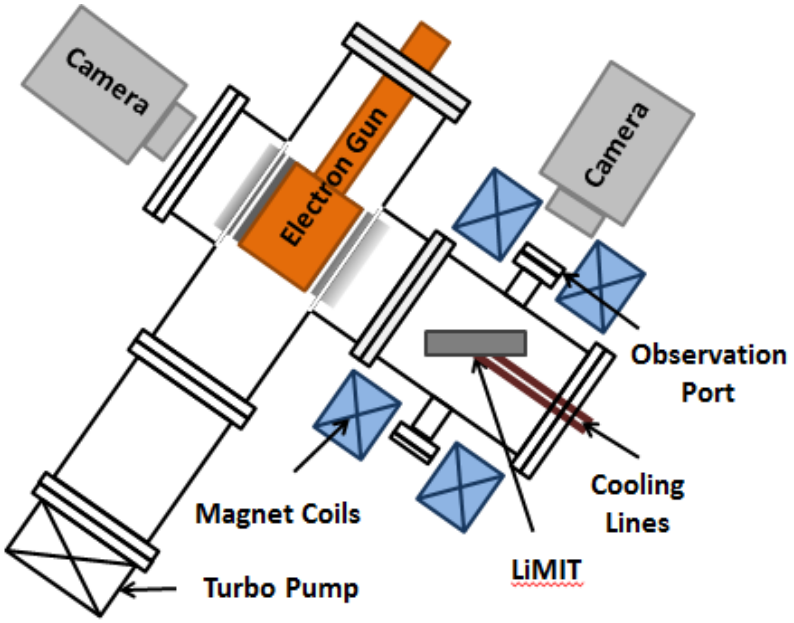

Figure 3.1 SLiDE experiment setup to test the LiMIT concept

3.1 Design LiMIT trenches

3.1.1 Overview of the design

LiMIT concept provides a method to drive lithium flow in open surface ducts. Generally speaking parallel open surface trenches need to be cut on the metal surface and lithium needs to be melted inside. However a few questions need to be considered to achieve a realistic design that can realize this concept and eventually utilize it for fusion application. These include the dimension of the trenches, the design of return flow path and the end of the trench, cooling channels and what solid structural material to choose. The goal for the design is to generate a stable liquid lithium flow under the experiment conditions.

The dimension of the trenches directly determine a few aspects of the trench such as surface temperature and flow velocity. Firstly the trench cross section is a narrow rectangular shape so that the flow is more determined by the side wall compared to the top surface. At the same time the length of the trench needs to be much larger than the width and the height in order to avoid the influence of the edge to the center part.

To choose the right dimension for the trench let us first consider the velocity. From the 1D model discussed in chapter two we know that the flow velocity is a function of Hartmann number, the C parameter, Seebeck coefficient, magnetic field and the temperature gradient if the pressure gradient does not exist. If the Seebeck coefficient, magnetic field and temperature gradient all fixed then the velocity is only the function of Hartmann number and C parameter.

$$u_m = \frac{Ha - \tanh(Ha)}{Ha + C\tanh(Ha)} \left(\frac{S - S_w}{B} \frac{dT}{dy} \right) \tag{3.1}$$

$$C = {}^{a\sigma}/_{t\sigma_w} \tag{3.2}$$

For example if the magnetic field is 1T, the temperature gradient is 10^4 K/m and the Seebeck coefficient difference between the lithium and the wall material is $2.5*10^{-5}$V/K, the velocity can be calculated as a function of Hartmann number at different C values, which is plotted in figure 3.2.

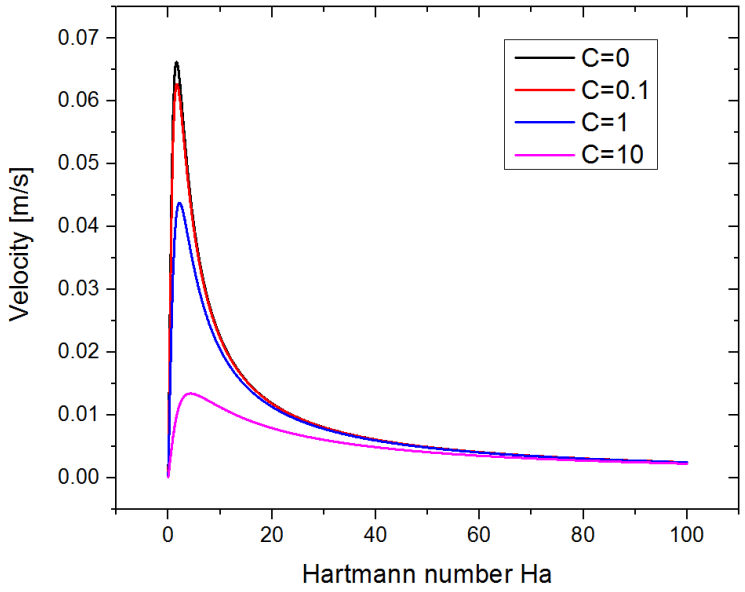

Figure 3.2 Flow velocity vs. Hartmann number at different C values, B=1T, Temperature gradient=10^4K/m and S=$2.5*10^{-5}$V/K

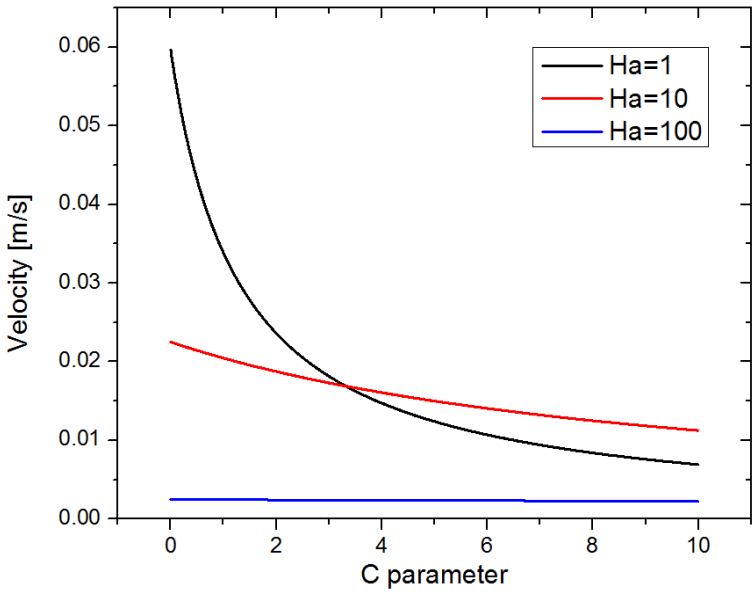

Figure 3.3 Flow velocity vs. C parameter at different Hartmann number, B=1T, Temperature gradient =10^4K/m and S=2.5*10^{-5}V/K

We can see that the velocity reaches a peak value at a certain Hartmann number, which does not depend on the magnetic field, temperature gradient or Seebeck coefficient. If we need to get the maximum velocity at a certain magnetic field, the width of the trench needs to be adjusted to gain the right Hartmann number. This needs to be considered when determine the trench width. On the other hand from Figure 3.3 it is easy to discover that the velocity drops when the C value increases because from equation 3.1 we can see that velocity is inversely proportional to C. When C equals zero it means the wall is superconducting. When the Hartmann number equals 1 after C is larger than 1 the velocity drops a lot. However when the Hartmann number is very high the influence from C becomes much smaller. If the trench width is already fixed C value can only be changed by adjust the wall material or the thickness of the wall.

From the discussion in chapter two we know that the surface temperature is strongly affected by the height of the trench. For a given surface heat flux, in other words a given temperature gradient, if the bottom of the trench has a fixed temperature then the top surface temperature can be determined. Since the surface temperature of lithium is very important in vacuum system the height of the trench needs to be well designed so that the surface temperature and the vapor pressure do not exceed the limit.

The design of return flow path and the end of the trench is another problem to solve. In some cases such as long-term fusion reactor application lithium may need to be collected at the outlet of the trenches, pumped out to desorb the trapped fuel, impurity, helium or other species and then injected back to the trench. At this time the pump speed, the pump pressure and the collector at the outlet need to be designed so that the vacuum system will not be affected. In our experiment the return flow is just set at the bottom of the open trench so that the lithium can easily circulate from the outlet of the open surface trench back to the inlet of the open surface trench. At the end of the trench there is a collection area without any trenches and lithium from all trenches join together and redistribute into bottom channels, which balances the amount of lithium in each trench to minimize the dry-out during the lithium filling and flow test.

Cooling of the trench is another complex topic. Obviously the temperature gradient and the bottom temperature requires the cooling at the bottom to maintain. However designing the cooling channels to be compatible with the experiment condition is complex. First the safety of the system is the most important to consider. If the cooling channels are close to liquid lithium the coolant should not react with liquid lithium when it leaks out. As a result water is not a good choice as the coolant. Potential choices include dry air, helium or some liquid such as mineral oil. In experiments the heat flux on the surface varies. In some cases the cooling rate needs to be able to maintain the temperature so that the lithium can stay liquid. In some fusion divertor applications the heat flux onto the divertor surface may be as high as 10 MW/m^2 and this is also what the cooling channels need to handle [54]. A few concepts such as T-tube [55] and porous cooling channels [56] have been raised to dramatically increase the heat transfer coefficient in cooling channels.

In the LiMIT design the structural material is another important problem. The wall material determines a lot of parameters such as Seebeck coefficient, electric conductivity, and thermal conductivity. In general the material needs to have a large enough Seebeck coefficient difference compared to lithium, a good electric conductivity and thermal conductivity. In addition since lithium is a very corrosive material to many types of metal the material needs to be resistant to the lithium erosion for a long time. In many cases the trench surface will suffer from a high heat flux and the temperature of the top of the solid wall may be much higher than lithium trench. As a result the melting point of the wall material should be high enough to bear this situation. Another problem is how well lithium can wet the wall material. Our experiments found that lithium's wetting on the

solid material is very important when filling the trench and to achieve a stable flow. Since the wetting can also be affected by the temperature a good wetting should be achievable within the temperature limit for the lithium in vacuum system [57]. The last question to consider is how much it will cost to machine the trench, which varies depending on the structural material and sometimes it can be very expensive. End mill, wire-EDM, laser machining, chemical or plasma etching can be used to cut these trenches.

In a word a lot of requirements need be satisfied when choosing the structural material and so far potential candidates include stainless steel, molybdenum, titanium-zirconium-molybdenum (TZM) alloy, tungsten, ect. However each type of material has its own advantage and disadvantage. Stainless steel is cheap, easy to machine and its Seebeck coefficient is much lower than lithium compared to other candidates. However it has a relatively low melting point and thermal conductivity. Molybdenum and TZM have better wetting property, high thermal conductivity and melting point but the Seebeck coefficient difference against lithium is much smaller compared to stainless steel. Tungsten has higher thermal conductivity, melting point and Seebeck coefficient difference but its wetting seems poor. Currently no material can satisfy all the aspects for the LiMIT design. Some solid material with special coating layer may ultimately solve this question and the detail will be discussed later.

Above are the general criterial to design the LiMIT trenches. As we can see from the discussion in most cases the design needs to be compatible with the experiment condition and to comply with different requirements. In next part the detail of the trench for the LiMIT test on SLiDE will be discussed.

3.1.2 LiMIT trenches for the experiment on SLiDE

The TEMHD driven flow in horizontal placed open surface trench was firstly proved on SLiDE experiment. The general experiment conditions have been introduced at the beginning of this chapter. The goal of this experiment is to examine the LiMIT concept and investigate how the lithium flow looks like at this horizontal orientation. Two versions of LiMIT trenches was used in this experiment and the diagrams are compared in Figure 3.4 and Figure 3.5. When testing both versions, e-beam is heating the center part of the trenches and magnetic fields are applied in the

same direction. Lithium is driven to flow along the top trenches and into the return flow channels. The difference is mainly the size of the trench and the position of the cooling channels. In the first version the cooling is far away from the trench. It more relies on the transient temperature increase to establish the temperature gradient. As a result keeping a steady state temperature gradient in top trenches to maintain a steady state flow is very hard. In the second version the cooling is embedded directly under the top trenches, which makes keeping the temperature gradient much easier.

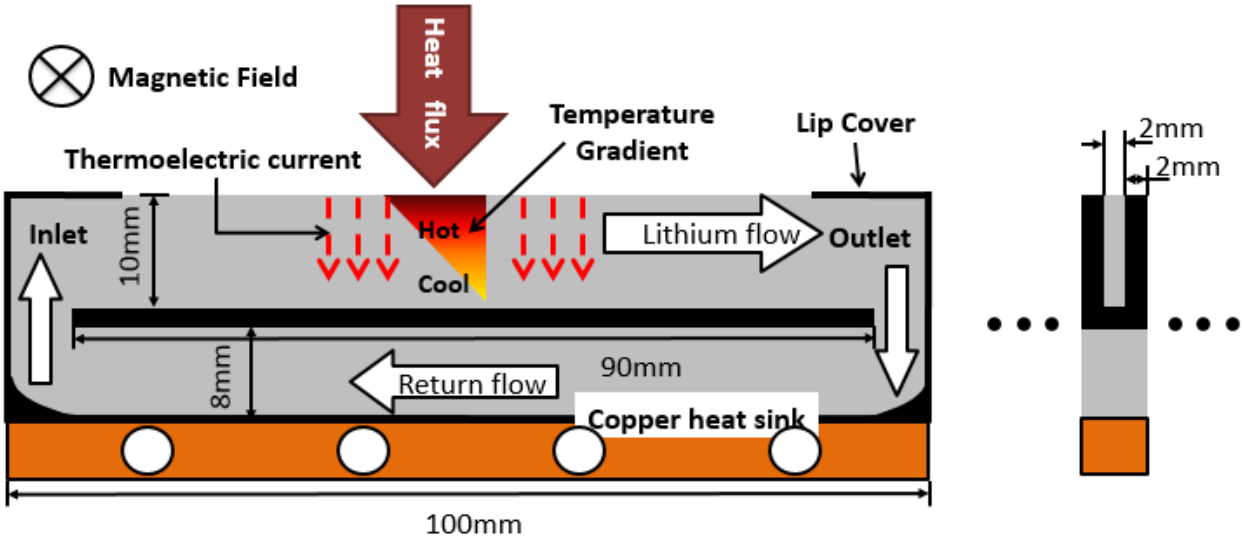

Figure 3.4 Diagram of the TEMHD driven lithium flow in the first version LiMIT trenches

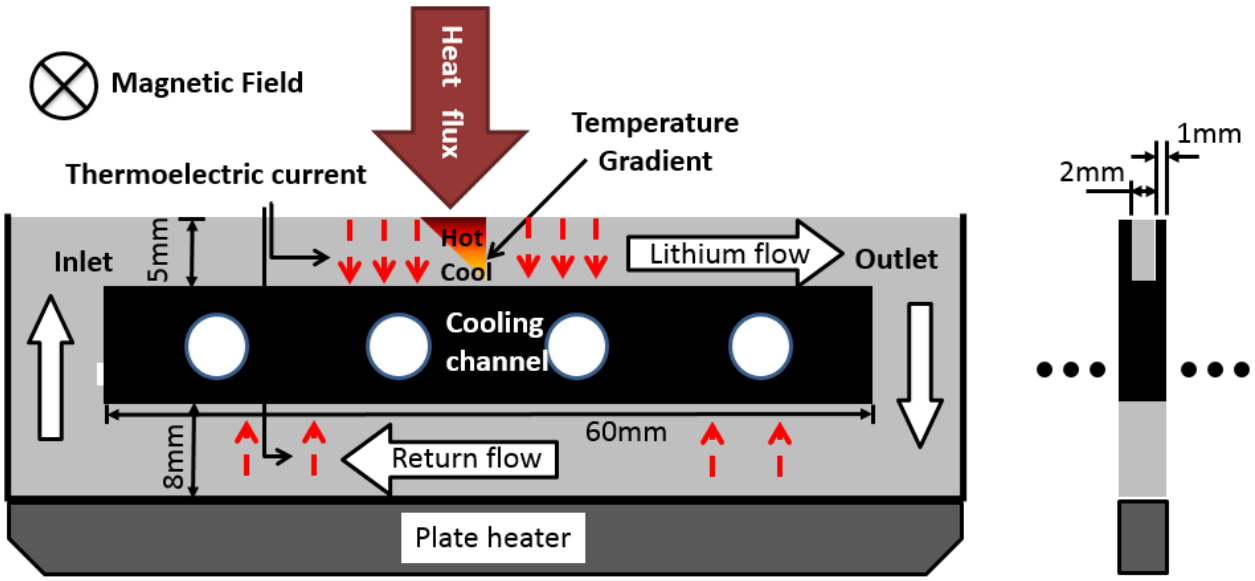

Figure 3.5 Diagram of the TEMHD driven lithium flow in the second version LiMIT trenches

The first version of LiMIT trenches is shown in Figure 3.6. Stainless steel 316 (SS 316) was chosen to manufacture the whole tray since the heat flux in this experiment is not very high and the flow velocity is more emphasized in this test. In this design the lithium trench is 2mm wide, 10mm deep and 90mm long. The stainless steel wall is also 2mm wide. In this case when the magnetic field changes from 0.01T to about 0.2T the Hartmann number ranges from 1.7 to 33.8 which is the range to get a clear change of the flow velocity. It is not great that the C parameter is 2.3 in this case since the electric conductivity of stainless steel is not high compared to lithium but it is still acceptable.

These parallel trenches are cut on top of a 1/2 inch thick stainless steel plate and the whole plate is suspended in a rectangular tray. In this case the gap between the bottom of the trench and the bottom of the tray serves as the return flow channel. Gaps at both ends allow the lithium from each trench to join other trenches and enter the return channel freely. A copper heat sink is attached to the bottom of the round shape stainless steel plate and two stainless steel bellows are attached to this copper heat sink to supply the coolant. Since the cooling line is away from the lithium both water and compressed air have been used in the experiment. The whole tray is suspended by two threaded rod attached to two sides and the tray is adjusted to horizontal when it is installed.

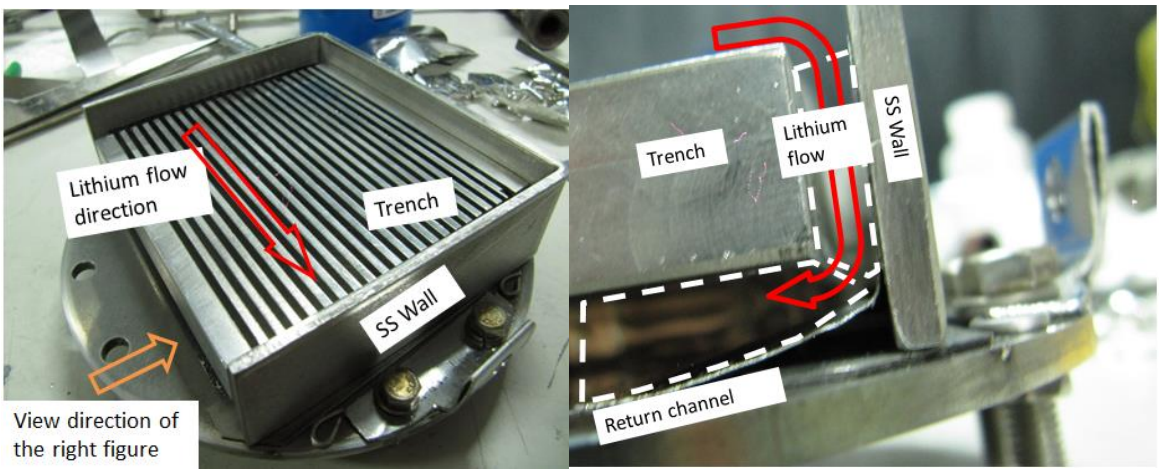

Figure 3.6 First version LiMIT trenches for SLiDE experiment

The CAD drawing of the tray is presented in Figure 3.7 and the detail of the CAD drawings can been found in the appendix Figure A.1 to Figure A.3.

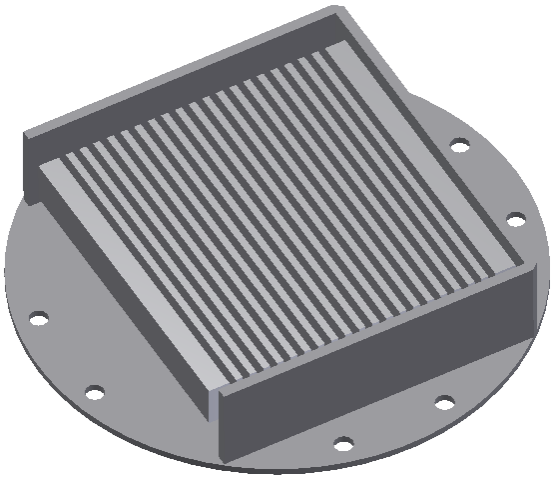

Figure 3.7 CAD drawing of the first version LiMIT trenches for SLiDE experiment

After lithium is melted into the trench the whole tray looks like Figure 3.8. Relatively uniform filling can be achieved through the whole area. Occasionally a small gap may appear and this is normally because some part of the trench cannot meet high enough temperature to get a good wetting. The detail of filling the trench will be discussed later. Note that the trenches would be slightly overfilled in a real application in tokamaks.

Figure 3.8 LiMIT trenches filled with lithium

A second version of LiMIT trenches was later designed as an improvement to the previous design. A CAD drawing and an assembled picture are presented in Figure 3.9. In this new version SS 316 is still used as the structural material. The dimension of the lithium trench is 2mm wide, 5mm deep and 60mm long so Hartmann number is still the same. The thickness of the wall is changed to 1mm so the C parameter is about 4.5 at this time. The change in the dimensions is to comply with the space inside the chamber and to mitigate the e-beam burning on top of the wall material. A tungsten strip is attached to the end where the e-beam comes from to shield the e-beam from hitting the stainless steel edge directly.

In this design the cooling channels are drilled through the center part of the trench to directly cool the bottom of the top trench and to separate the top trench from the return channel. In this way the temperature gradient through the trench is expected to be larger compared to the previous version and additional temperature gradient exists in the return channels to generate additional TEMHD driven force inside the return flow. Obviously water cooling is not applicable in this case and up to 50 psi compressed air is used as the coolant.

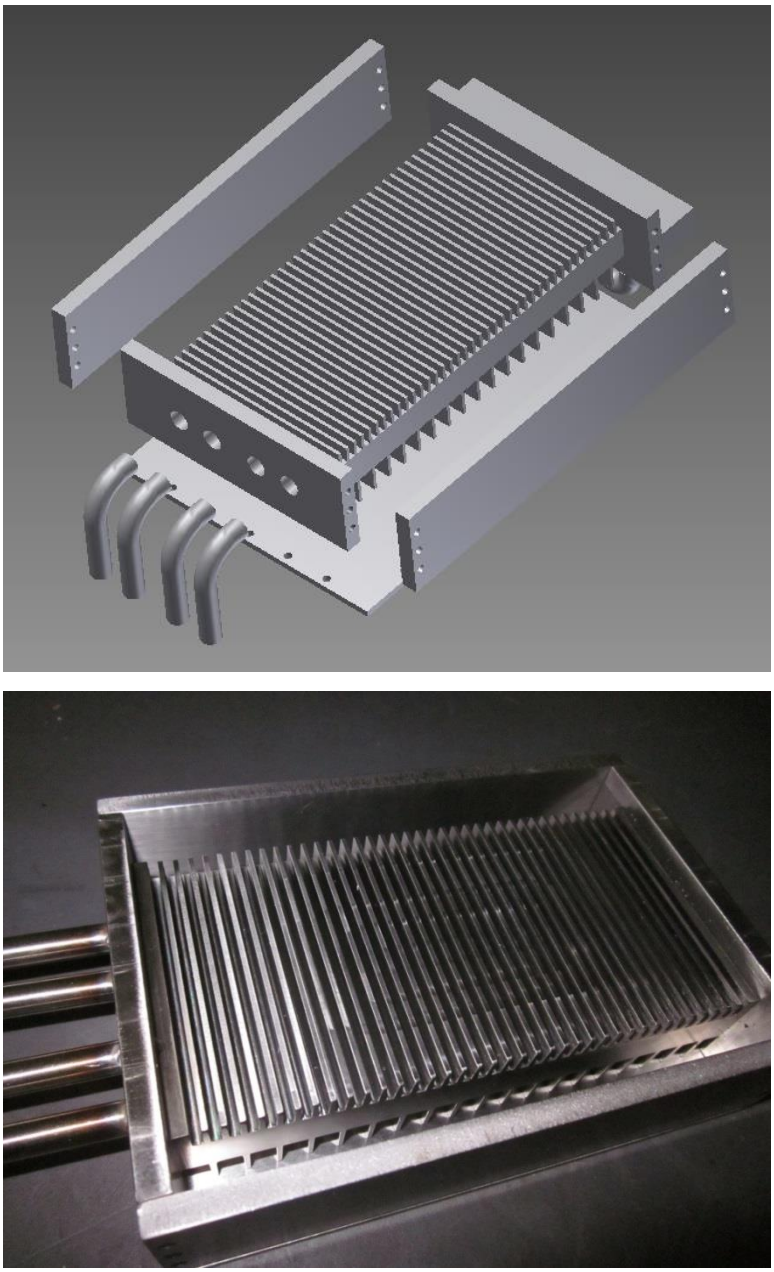

Figure 3.9 CAD drawing and assembled picture of the second version LiMIT trenches for SLiDE experiment. Detail of CAD drawings can be find in the appendix (Figure A.4 to Figure A.9)

3.2 SLiDE apparatus

3.2.1 Vacuum system

Lithium related experiments are always challenging because lithium reacts with many types of gases such as nitrogen, oxygen, carbon dioxide and water vapor quickly and easily. If a lithium chunk is exposed to air directly its silver surface becomes dark in a few seconds and this process can be accelerated if the air is humid. If fresh lithium is left inside the vacuum only maintained by a rough pump it will become dark in days. Worse still, when lithium is heated to a high temperature or melted the reaction rate becomes faster.

The vacuum system of SLiDE consists a turbo pump (Pfeiffer 1080), a dry pump and a few gauges. The base pressure is usually kept at around $5*10^{-7}$ Torr and the lithium surface is able to stay fresh. Occasionally the chamber may need to be opened when the lithium is still in side. In this case the chamber needs to be filled with Ar first to a slightly higher pressure than outside to avoid the pollution from the air.

During experiments lithium surface keeps vaporizing and depositing onto other surfaces and sometimes small lithium droplet may even eject out of the tray. Because of this, the vacuum gauges are usually installed in the way that the opening is not facing the main chamber and the ion gauge may be shut off before the experiment in case it is damaged by the lithium vapor. The turbo is also intentionally installed far away from the main chamber but still we can find some oxidized lithium powder or droplet on the protection stainless steel mesh in front of the turbo pump. If the turbo blades are polluted by lithium droplets the turbo can be cleaned immediately by soaking the blades with fresh water.

3.2.2 Magnet

The magnetic field is indispensable to this experiment and it functions for two purposes. One is to provide the magnetic field to drive the liquid lithium and another is to focus the e-beam onto the tray surface. The magnetic field is generated by a pair of Helmholtz coils and it can be powered by four high current DC power supplies or eight standard car batteries. The magnetic field was

measured by a Gauss meter and scaled to the current inside the coil which can be displayed instantaneously by the high current DC power supply. Because that the uniformity of the standard Helmholtz coil is beyond the second order of the field gradient the field around the liquid lithium can be assumed uniform in the experiment. The magnetic field is linear with the current inside the coil and the relation between the field and the coil current is

$$B\ [Gauss] = -2.2 + 6.8 * I_{coil}\ [A] \qquad (3.3)$$

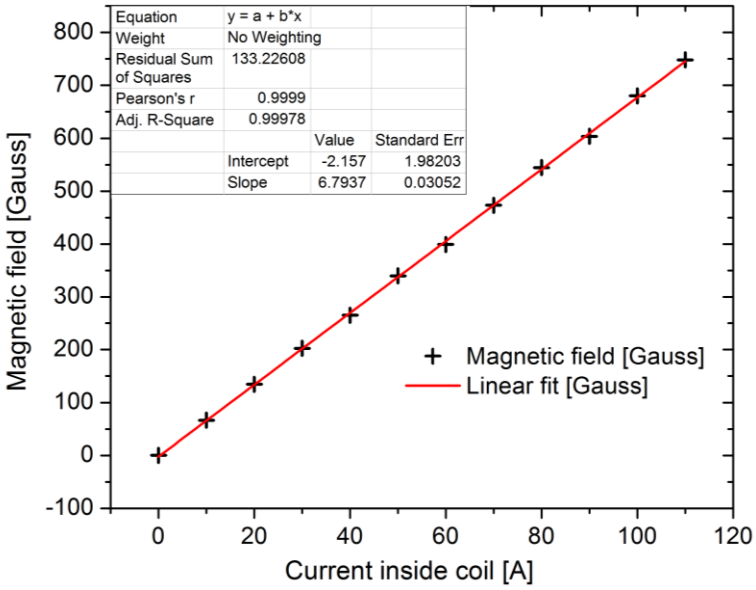

Figure 3.10 Magnetic field calibrations to the current inside Helmholtz coil, measured at the center of the tray surface by gaussmeter

When coil is powered by the high current DC power supply the maximum current can go up to 130A which means the maximum magnetic field can reach 881.8G. However when the coil is powered by the batteries the current can be much higher. These batteries are standard deep cycle batteries and the voltage is around 12.6V when the batteries are full. Each group of the coil normally has three or four batteries connected in series. A giant double-pole double-throw (DPDT) switch is used to switch the power source between the high current DC power supplies and the batteries. These are shown in Figure 3.11.

When four batteries are used to power the coil the current can be as high as 344A and since the inductance values of both coils are 1.38mH and 1.34mH, which are relatively high, the current will

not drop to zero instantly when the switch is opened. Instead a huge voltage will arise between the switch blades to generate huge arc plasma. To quench this spark a snubber needs to be added into the circuit. Snubber is a device that can provide a second path for the induced current around the current switching device and normally it is made of RC circuit or power diode. In our circuit two diodes (the silver rod connected to the middle poles in Figure 3.11) are used to minimize the induced current from generating sparks when the switch is opened. In the circuit diagram Figure 3.12 these diodes are connected in parallel with the coil and in reverse direction to the voltage so that it is not conducting at normal state. When the switch is opened the induced voltage starts to climb to open the diode so that the residual energy inside the coil can gradually dissipate through the diode resistance. Obviously the diode should be able to handle the current and have fast enough open time so that the induced voltage can open the diode gate as soon as it rises. The diode in this experiment is normally used for rectifier in power system and has 1200V maximum reverse voltage, 320A average forward current and 1us open time, which is enough for the mechanical knife switch whose open time is normally in milliseconds. Also if the switching time is 1ms and pick 1.35mH as the inductance for the coil, the induced voltage will be 464.4V for 344A maximum current. And 1200V voltage limit should be enough in this case.

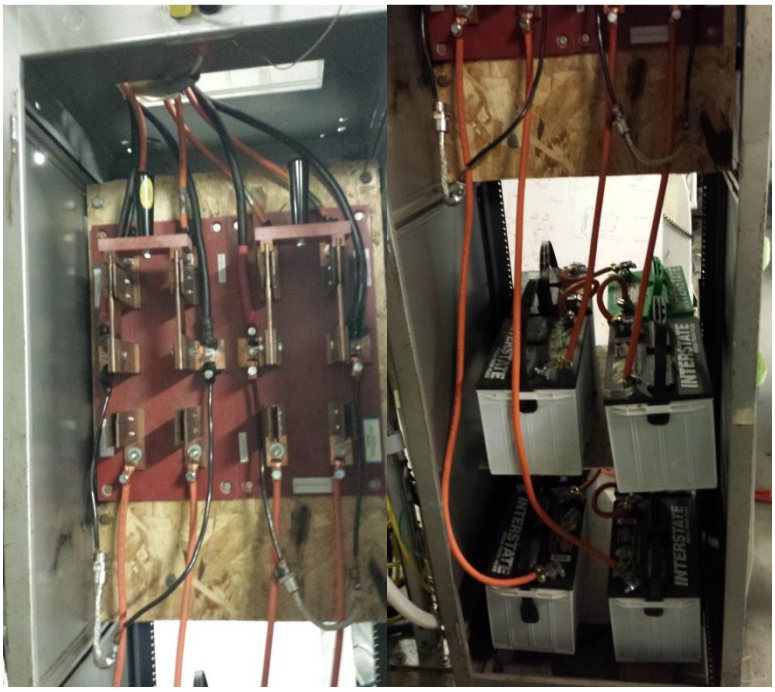

Figure 3.11 DPDT knife switches, batteries and power diodes for the high current generation

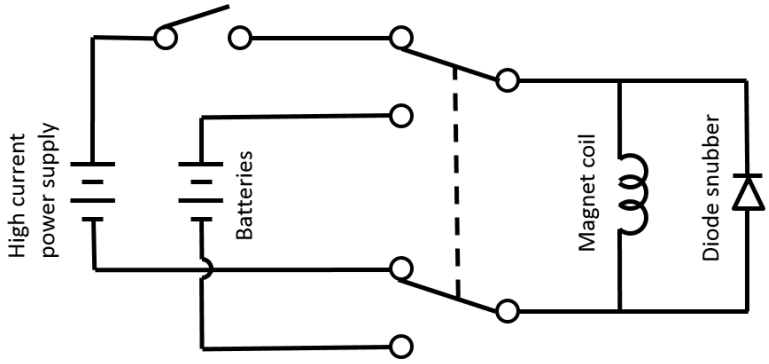

Figure 3.12 Circuit diagram to generate the magnetic field

The current in the coil and the generated magnetic field at the center of the chamber are measured by high current resistor and gaussmeter and listed in table 3.1 for different number of batteries in use. Note that when the current is high the current actually drops slowly during the discharge since the inner resistance slowly climbs because of the heat. But the rate is about 1A/s for three batteries and 2A/s for four batteries. In our experiments the discharge time is usually less than 5 seconds and this dropping current is ignored in the analysis.

Table 3.1 Magnet current and field for different batteries

Number of Batteries	Current [A]	Magnetic field [G]
1	97.7	661
2	186.2	1263
3	269	1825
4	344	2335

3.2.3 Electron beam

A linear e-beam is utilized to mimic the heat flux from the plasma up to 10MW/m^2. From Figure 3.1 we can see that the e-beam is installed right above the tray. The electrons are accelerated by a high voltage power supply and its voltage is normally set to 10 kV and the current is up to 1 A. The e-beam generates a Gaussian shape profile with the profile on the other direction being linear.

The e-beam can be focused by the magnetic field from the magnet coil. The length of the beam is L_{beam} on y direction and the distribution on x direction is a Gaussian profile with the standard deviation a_0**.** The current density of the electron beam is

$$J = \begin{cases} J_0 * Exp\left(-\frac{x^2}{a_0^2}\right) \ when \ \ |y| \le L_{\boldsymbol{beam}}/2 \\ 0 \qquad\quad when \ |y| > L_{\boldsymbol{beam}}/2 \end{cases} \tag{3.4}$$

Here the values of $L_{\boldsymbol{beam}}$ and a_0 are determined by the magnetic field and they are in table 3.2.

Table 3.2 Electron beam profile summary [40]

Magnet current [A]	a_0 [mm]	Beam length L_{beam}[mm]
2	44.2	82
5	29.2	87
10	12.5	77
20	6.7	70
40	4.6	65
60	4.7	69
80	3.8	70
100	3.6	69

In equation (3.4) J_0 is the solution of the equation

$$J_0 = I_{beam} / \left(L_{beam} * \int_{-L_{tray}/2}^{L_{tray}/2} Exp\left(-\frac{x^2}{a_0^2}\right) dx\right) \tag{3.5}$$

In above equations L_{tray} is the length of the lithium tray which is 10 cm. x is the position on the lithium surface. I_{beam} is the total current emitted by the e-beam and it can be read directly from the high voltage power supply.

Since the energy of the electrons from the electron beam is 10keV the stop range of the electrons in the lithium can be found on National Institute of Standards and Technology (NIST) website. The average stop range of 10keV electrons in the lithium is 1.4 μm. So during the experiment when the electrons hit the lithium surface all of the kinetic energy is assumed to deposit onto the surface of the liquid lithium. The Bremsstrahlung radiation at the surface is neglected here because the fraction of kinetic energy that is converted to Bremsstrahlung is small which is plotted in Figure 3.13.

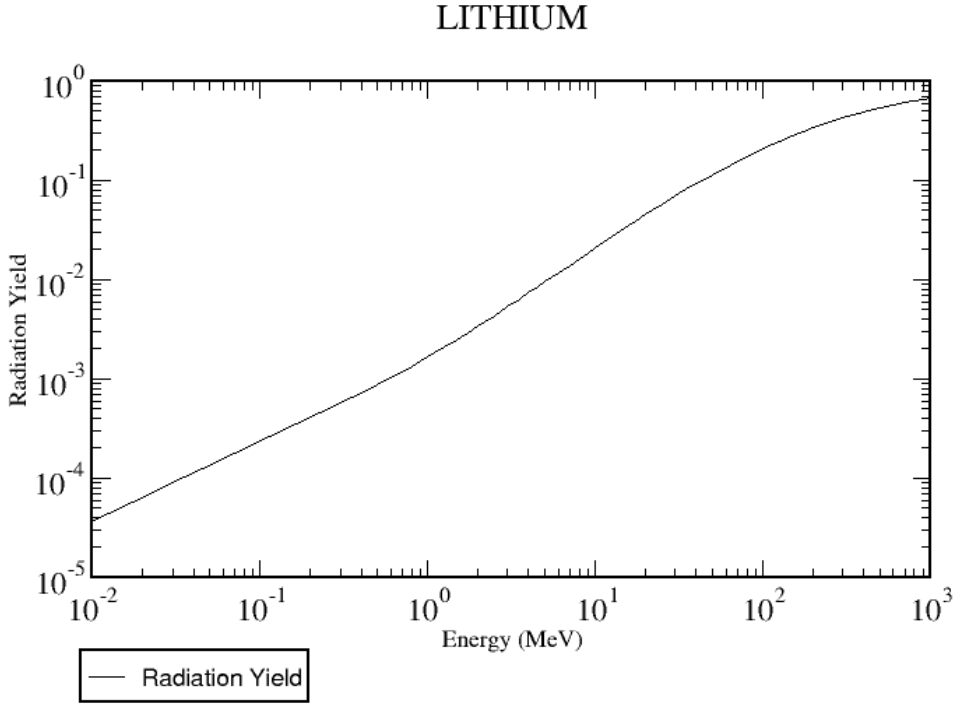

Figure 3.13 Fraction of kinetic energy of primary electron converted into Bremsstrahlung, data from NIST database

Under the above assumptions the heat flux profile q is

$$q = V * J = \begin{cases} q_0 * Exp\left(-\frac{x^2}{a_0^2}\right) \ when \ \ |y| \le L_{\boldsymbol{beam}}/2 \\ 0 \qquad\quad when \ |y| > L_{\boldsymbol{beam}}/2 \end{cases} \tag{3.6}$$

Here V is the voltage of the acceleration power supply and $q_0 = V * I_{beam}/\left(L_{beam} * a_0 * \sqrt{\boldsymbol{\pi}}\right)$ is the peak heat flux at the center. If we use the parameters when the current of magnet is 100A and assume the voltage is 10kV and current is 0.5A the peak heat flux will be about 11.4 MW/m^2. This

is the maximum we normally use in experiments. However the maximum power of the power supply is 20kW which means the maximum peak heat flux of this e-beam can reach as high as 45 MW/m^2.

3.2.4 Lithium loading and lithium surface cleaning

Handling lithium is not easy especially when it is in liquid state. Loading lithium is the first problem to solve in this experiment. First argon plastic bag is used to transfer the lithium chunk from the argon glove box to the chamber. In this process, lithium is cut to the right amount, punched into a flat shape and stored in a sealed plastic bag in the argon glove box. At the same time the chamber is filled with argon and ready to open. Then the plastic bag filled with lithium and argon is transferred to the chamber and lithium can be loaded on top of the tray.

However lithium usually gets polluted to some extent in this process because of the air diffusion. Normally the more humid the room is, the worse it is polluted. In order to solve this problem, a lithium injector was developed to directly inject liquid lithium into the tray. The design is plotted in Figure 3.14. Lithium is firstly cut, shaped and stored in a lithium reservoir in the argon glove box and then the reservoir is attached to the chamber. Both the reservoir and the injection tube can be heated above the melting point and then argon gas is injected into the reservoir to pressurize the backside to inject lithium out of the nozzle inside vacuum chamber to fill the tray. In this way lithium is always surrounded by argon.

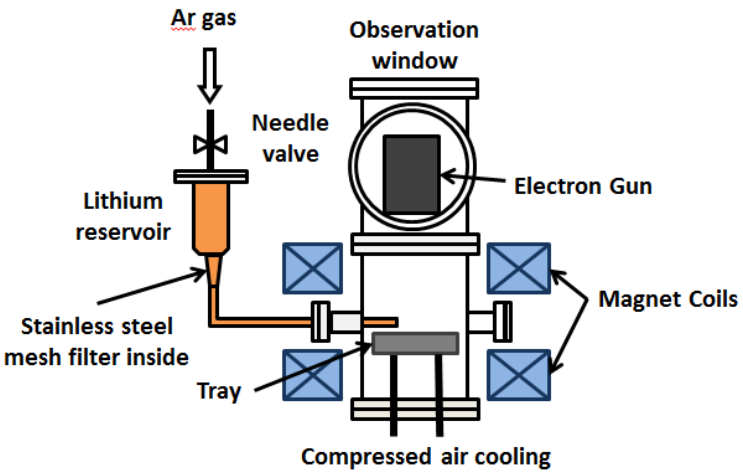

Figure 3.14 Setup of the lithium injector loading lithium into the tray

In this design everything is made out of SS 316. 1/4 inch tubing is used to make the delivery tube. A three-axis nozzle is developed to be able to aim the lithium jet to any direction, which is plotted in Figure 3.15. The inner diameter of the nozzle outlet is 0.027inch.

Figure 3.15 Three-axis lithium nozzle

The lithium inject speed v_{inject} or the inject volume flow rate q_{inject} can be calculated through these equations. Here p is the pressure used to pressurize the reservoir. Note that the absolute pressure in the reservoir is not the gauge pressure read directly from the gas tank. The absolute pressure is the gauge pressure adding the atmospheric pressure since the chamber is under vacuum. ρ is liquid lithium density. A_{in} is the cross section area of the delivery tube inlet and A_{out} is the cross section area of the nozzle outlet. All parameters use standard units in these equations.

$$v_{inject} = \left[2p/\left(\rho * (1 - (A_{out}/A_{in})^2)\right)\right]^{1/2} \tag{3.7}$$

$$q_{inject} = A_{out} * \left[2p/\left(\rho * (1 - (A_{out}/A_{in})^2)\right)\right]^{1/2} \tag{3.8}$$

Note that when the outlet diameter is much smaller than the inlet, the ratio of A_{out}/A_{in} becomes very small and it can be neglected. As a result these equations are reduced to the equations below and we can see that the velocity only depends on the pressure and the volume flow rate is proportional to the outlet cross section area.

$$v_{inject} = [2p/\rho]^{1/2} \tag{3.9}$$

$$q_{inject} = A_{out} * [2p/\rho]^{1/2} \tag{3.10}$$

Now we can estimate the flow speed, flow rate and how long it takes to inject the lithium (discharge time). The mass of lithium we normally use is around 70g. Assume the gauge pressure of the argon gas tank changes from 0 psi to 20 psi. The inner diameter of the nozzle outlet is 0.027inch and the inner diameter of the inlet is 1/4 inch. In this case the ratio of A_{out}/A_{in} is safe to drop out. The inject speed, the volume flow rate and the discharge time as functions of the gauge pressure of argon gas tank can now be plotted in Figure 3.16.

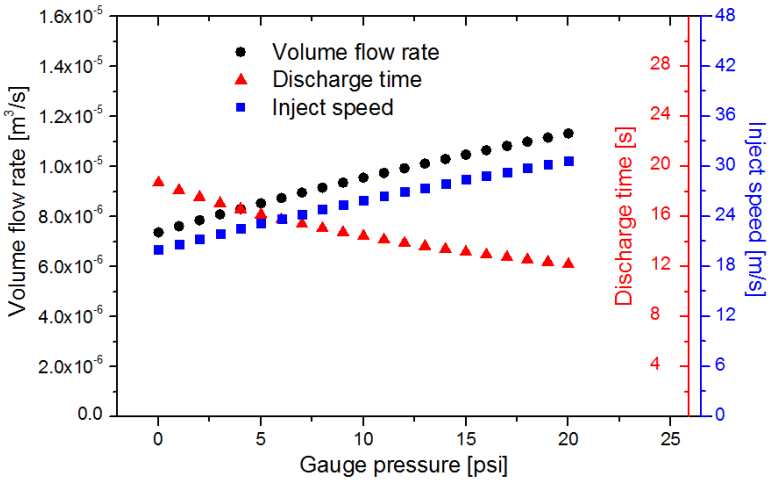

Figure 3.16 Inject speed, volume flow rate and discharge time of lithium injection as functions of the gauge pressure of argon gas tank

For 10psi gauge pressure, which is normally used in our loading process, it takes about 14.4 seconds to inject all the lithium. The real injection time at this pressure is about 50~60s. The reason is probably that when the nozzle was cut off by a tube cutter the end got squeezed and the real inner diameter is smaller than the norminal diameter. Also the residual lithium salt after the cleaning may also reduce the inner diameter to some extent.

When we were trying to load lithium into the trenches first we simply put the lithium chunk on top of the trench and melt it. It was discovered that after lithium was melted lithium did not sink into the trench at all. Liquid lithium just floated on top of the trench and formed a pool. After the temperature of the lithium was heated to about 480C all trenches were filled in one or two seconds. This is shown in Figure 3.17.

Figure 3.17 Melting lithium into trenches by loading lithium chunk on top of trenches and heat it to about 480C

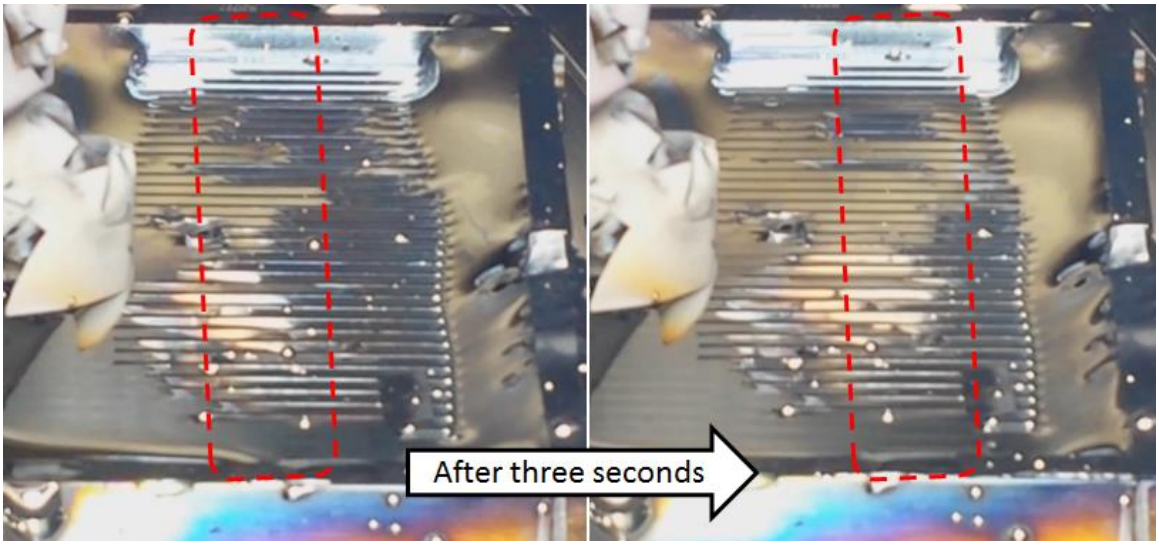

Figure 3.18 Lithium slowly wicking along trenches

After we changed to lithium dropper we also found that only when the tray was heated above 480C lithium could enter the trenches. Instead of entering all trenches at the same time in the first method, lithium slowly wicked along trenches and eventually all trenches can be filled. This was presented in Figure 3.18. This is because when lithium was injected its temperature was still lower than 480C although the tray was hot enough. When lithium was heated up by the tray its temperature slowly rose above 480C and was able to wick into all trenches.

When the lithium is in the vacuum impurity scale may still appear on the surface because of impurity from the argon glove box or possible outgassing from other components. When this happens an elastic impurity layer floats on lithium surface and it is extremely hard for the lithium flow itself to break it. When this layer exists the surface does not move at all although lithium may flow underneath it. In this case an active way to clean the surface or at least break the impurity scale is necessary. Multiple methods have been tried to clean the lithium surface such as plasma sputtering, e-beam burning, overheating and mechanically brushing the surface. It seems that using the brush to simply push the impurity away works well. In experiment a stainless steel brush is installed through the side window to clean the liquid lithium surface from time to time.

3.2.5 Heating, cooling and temperature measurement

In this experiment different heating and cooling methods have been used such as e-beam heating and heating plate. Temperature is measured by thermocouples and IR camera. E-beam heating has been discussed above. In general most of the energy from the e-beam deposits with a few micrometers surface layer of the tray. On the other hand auxiliary heating is also attached to preheat the tray for lithium loading and to enhance the flow inside the return flow channels. This is done by the heating plate.

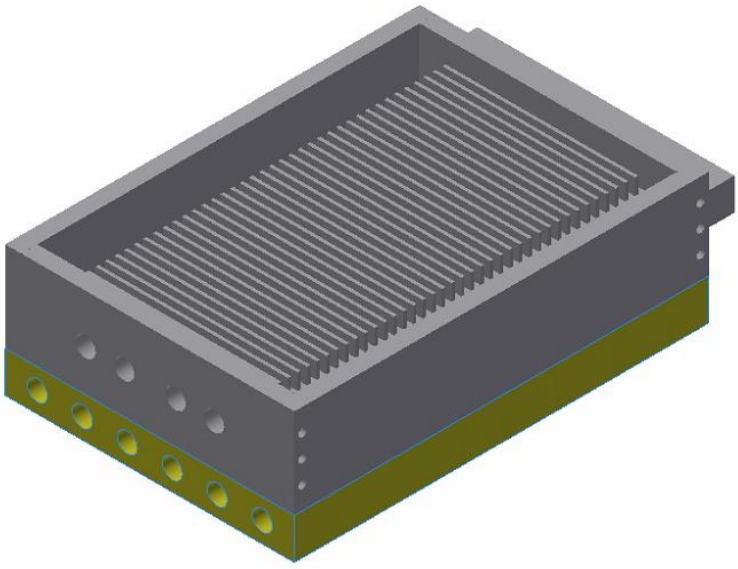

Figure 3.19 CAD drawing of the heating plate attached to the bottom of the tray

Figure 3.19 is the CAD drawing of the heating plate (in green color) attached to the bottom of the tray. It is the same size as the tray and its thickness is 0.5 inch. Six 0.25 inch diameter holes are drilled through the center of the heating plate and six 200W cartridge heaters are inserted in these holes. The heating plate is firmly attached to the tray by a few screws at the edge but in order to enhance the thermal contact and to prevent the heating plate surface from being thermally fused to the bottom surface of the tray, a thin layer of graphite thermal paint is applied between the heating plate and the bottom surface of the tray. A few thermocouples are attached to measure the temperature change. The temperature change during the heat-up is plotted in Figure 3.20. During the heating the heater is set to different powers labelled by the rectangles. The heating plate is capable to heat the tray higher than 480C, which takes hours to reach.

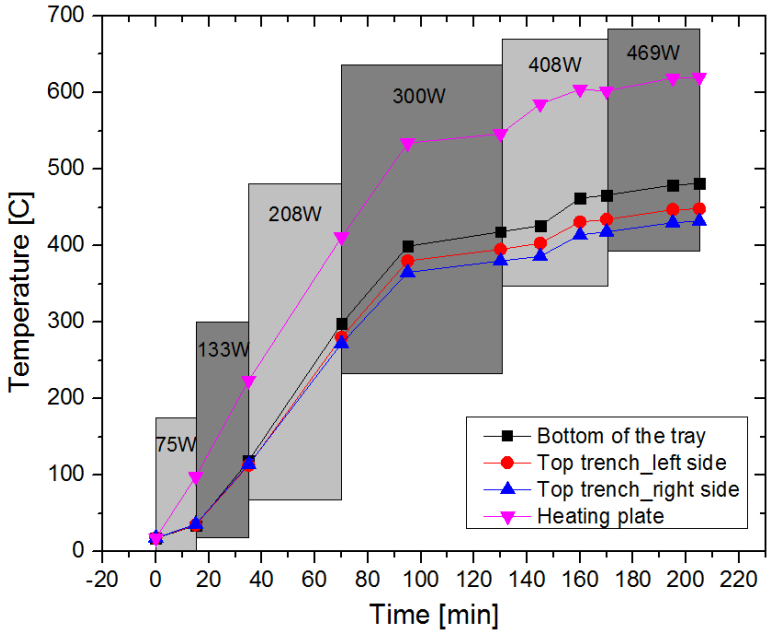

Figure 3.20 Temperature rise of the tray when it is heated by the heating plate

Other than the tray, the lithium reservoir and the delivery tube also need to be heated. The reservoir and the delivery tube outside the vacuum is heated by the fiber glass belt heater and it should be noted that the welding point where the delivery tube joins the vacuum feed-thru is usually the coldest point. The heating of the delivery tube inside uses nichrome ribbon and kapton tape is used as electric insulation material. The heat-up of the whole lithium loading tool has been carefully measured to ensure the temperature is above the melting point everywhere.

From the discussion we know that the tray is normally cooled by compressed air. In the experiment the flow rate is usually up to 2scfm and the inlet pressure is usually up to 50psi. The magnet coils and the chamber wall around the tray area are water-cooled.

In the experiments temperature is usually measured by thermocouples and the surface temperature can be measured by IR camera. The IR camera will be discussed in next section. Usually a few thermocouples are embedded in the tray to measure the temperature distribution inside.

3.2.6 IR camera

Infrared radiation (IR) is the light with the wavelength between 750nm and 1mm. Any object whose temperature is higher than 0K has thermal emission. If the surface of a certain object can absorb all radiation hitting its surface it is a black body. Its thermal emission spectrum can be described by Planck's law [58].

$$B_\lambda(T,\lambda) = \frac{2hc^2}{\lambda^5}\frac{1}{e^{\frac{hc}{\lambda k_B T}}-1} \tag{3.11}$$

Here $B_\lambda(T)$ is the spectral radiance and its unit is W/m^3. h is Planck constant. c is the speed of light in vacuum. k_B is the Boltzmann constant. T is the surface temperature. The power that a black body emits through a unit area can be achieved by integration of Planck's law from zero to infinity and over the solid angle corresponding to a hemisphere with an additional cosine law associated to the light emission.

$$I_{emission} = \int_0^\infty B_\lambda(T,\lambda)\,d\lambda \int_0^{2\pi} d\varphi \int_0^{\frac{\pi}{2}} \cos\theta \sin\theta\, d\theta$$

$$= \int_0^\infty \frac{2hc^2}{\lambda^5}\frac{1}{e^{\frac{hc}{\lambda k_B T}}-1}\,d\lambda \int_0^{2\pi} d\varphi \int_0^{\frac{\pi}{2}} \cos\theta \sin\theta\, d\theta = \sigma T^4 \tag{3.12}$$

Here $\sigma = \frac{2{k_B}^4\pi^5}{15c^2h^3}$ is Stefan-Boltzmann constant which is 5.67*10^{-8} W/m^{2}K^4.

However the thermal emission in the real world is more complex and three important parameters are normally used, including emissivity, reflectivity and transparency. Firstly, the thermal emission

from all materials always has a fraction which is called emissivity ε. Theoretically the emissivity is a function of surface temperature, wavelength, emission angle and thickness. On the other hand if the surface of the object cannot absorb all the radiation, some part of the radiation will be reflected. The surface reflectivity r is the fraction of the radiation that is reflected. In addition when the object is not opaque and some of radiation can transmit with a fraction of τ. The relation between these three parameters is $\tau + \varepsilon + r = 1$. Normally if the object is opaque the reflectivity $r = 1 - \varepsilon$.

From the above analysis we know that if the emission from a certain object is measured it surface temperature can be derived and this is the mechanism of IR camera. However IR camera can only measure the thermal radiation within a certain spectrum region and this is called the filter range of the IR camera ($\lambda_1 \sim \lambda_2$).

$$I_{emission} = \int_{\lambda_1}^{\lambda_2} \varepsilon B_\lambda(T,\lambda)\, d\lambda = \int_{\lambda_1}^{\lambda_2} \varepsilon \frac{2hc^2}{\lambda^5} \frac{1}{e^{\frac{hc}{\lambda k_B T}} - 1} d\lambda \tag{3.13}$$

Usually if the object is not transparent and the emissivity does not change too much for the spectrum span of the IR camera it is safe to assume that the emissivity is only a function of temperature. This is called gray body assumption and under this assumption the equation can be changed to

$$I_{emission}(T) = \int_{\lambda_1}^{\lambda_2} \varepsilon B_\lambda(T,\lambda)\, d\lambda = \varepsilon(T) \int_{\lambda_1}^{\lambda_2} \frac{2hc^2}{\lambda^5} \frac{1}{e^{\frac{hc}{\lambda k_B T}} - 1} d\lambda \tag{3.14}$$

And this integration can be solved numerically so that the emission intensity is only a function of temperature. The intensity is measured by the detector and calibrated to the temperature with the help of a unique object having an emissivity very close to 1. This forms the calibration file for the IR camera which translates the relative measurement of the intensity to a temperature value.

However in real measurement we have to consider the infrared light from the background since the object surface reflectivity is not zero which means that there exists some infrared light that is reflected by the object surface and enters the IR camera.

$$I_{measure} = I_{emission} + I_{reflection=} \varepsilon(T) \int_{\lambda_1}^{\lambda_2} \frac{2hc^2}{\lambda^5} \frac{1}{e^{\frac{hc}{\lambda k_B T}} - 1} d\lambda +$$

$$\left(1-\varepsilon(T)\right)\int_{\lambda_1}^{\lambda_2}\frac{2hc^2}{\lambda^5}\frac{1}{e^{\frac{hc}{\lambda k_B T_{background}}}-1}d\lambda \tag{3.15}$$

For the IR camera since the relative intensity measurement corresponds to the temperature we can have

$$I_{real}=\int_{\lambda_1}^{\lambda_2}\frac{2hc^2}{\lambda^5}\frac{1}{e^{\frac{hc}{\lambda k_B T}}-1}d\lambda \tag{3.16}$$

and

$$I_{background}=\int_{\lambda_1}^{\lambda_2}\frac{2hc^2}{\lambda^5}\frac{1}{e^{\frac{hc}{\lambda k_B T_{background}}}-1}d\lambda \tag{3.17}$$

Now

$$I_{measure}=\varepsilon(T)*I_{real}+\left(1-\varepsilon(T)\right)*I_{background} \tag{3.18}$$

and the real surface temperature can be measured if the emissivity is known.

The IR system on SLiDE includes an IR camera (Inframetrics 760), a Zinc Selenide (ZnSe) window to transport IR light, the framework to hold the camera, a PCI digital card (DT3152-LS) to communicate with the IR camera and a computer to record data and install control software (SandIR from Sandia National Lab). The IR camera is pointing to the trench surface through the 2.75 inch view port from the side.

The main parameters of the IR camera Inframetrics 760 are summarized here. All related information can be found in its manual. The detector is made by Mercury/Cadmium/Telluride (HgCdTe) and runs at 77K. Each time before the camera starts it takes about half an hour to cool down the detector. The camera has three spectral band pass including 8~12μm, 3~5μm or 3~12μm. Usually only 8~12μm is used in experiments. The resolution is 1.8mRad which corresponds to distance/1000 approximately. Temperature measurement accuracy is ±2C or ±2%. Field of view (FOV) is 15 degree (vertical)*20 degree (horizontal) and it has 4 times continuously adjustable electric-optic zoom. The temperature measurement range is -20C to 400C with a normal filter when emissivity is set to 1.

3.2.7 Fast frame camera

The velocity of the flowing liquid lithium in the trench is measured by the fast frame camera. Fast frame camera can record video at much higher frames rate compared to the regular digital camera. However the trade-off for the increased frame rate is the exposure time for each frame becomes smaller. As a result the light strength from the object also limits the maximum frame rates.

In our experiment fast frame camera is looking into the chamber through the view port which faces the surface of the tray. The optical axis of the camera is actually not perpendicular to the tray surface. The angle between the optical axis and the surface normal is 55 degree. This gives us an inclined top view of the tray surface instead of a vertical top view. Since the diameter of the window is about 3.5cm which is comparably smaller than the size of the tray, only part of the tray surface is captured. The distance from the camera sensor to the lithium surface is about 50cm. Since the width of the trench is 2mm which is much smaller compared to the distance the reproduction ratio of the image on the CCD is very important.

In macro photography the reproduction ratio is the ratio of the size of the object image on sensor plane to the size of the real object. When the object is small macro lens, close-up filter or extension tube can normally be used to get a high reproduction ratio in order to capture the detail. In this experiment 100mm macro lens is used in front of the camera. The reproduction ratio can be estimated by this equation, in which d_0 is the distance from the sensor to the object and f is the focal length of the lens.

$$\text{Reproduction ratio } \beta = 0.5 * \left[(d_0/f - 2) - \sqrt{(d_0/f - 2)^2 - 4}\right] \qquad (3.19)$$

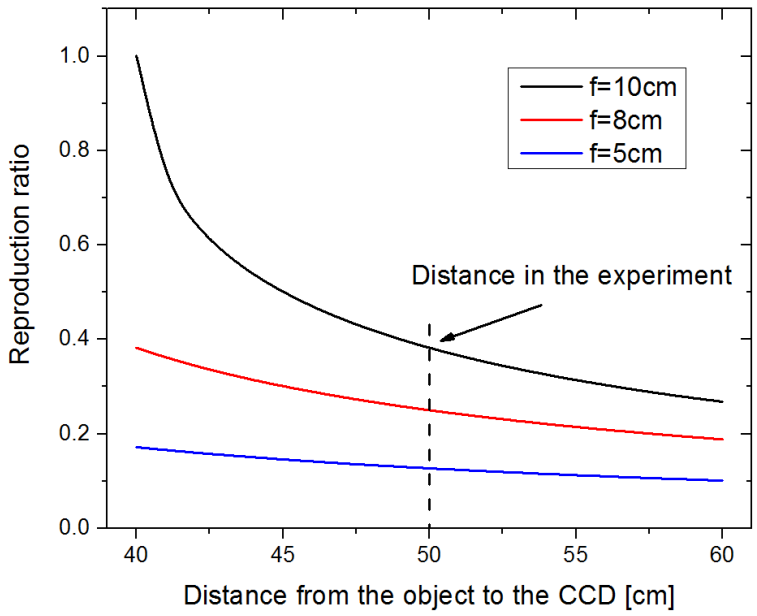

Figure 3.21 Reproduction ratio of the photograph as a function of the distance from the object to the CCD

From the above figure we can see that longer focal length can lead to larger reproduction ratio and once the distance is longer than four times of the focal length the reproduction ratio drops quickly. Because of these the 100mm macro lens is utilized and the camera needs to be installed as close as possible. The size of the CCD sensor is 17.6mm*13.2mm and the pixel array is 800*600. The reproduction ratio is about 0.38 and the width of the trench image on the CCD is 0.76mm. In this case there are about 35 pixels across the width direction of the trench, which should be enough to identify the motion inside the trench.

3.3 TEMHD driven Li flow in SLiDE experiment

3.3.1 Velocity measurement

The movement of the impurity scale can be tracked by the fast frame camera and the distance is measured by image processing software to find out the moving speed. The moving speed of the impurity scale is assumed to be the same as the local lithium surface moving speed based on the

facts that the mass of the impurity scale is much smaller compared to the surrounded lithium and the surface tension of liquid lithium can drag the impurity scale to move.

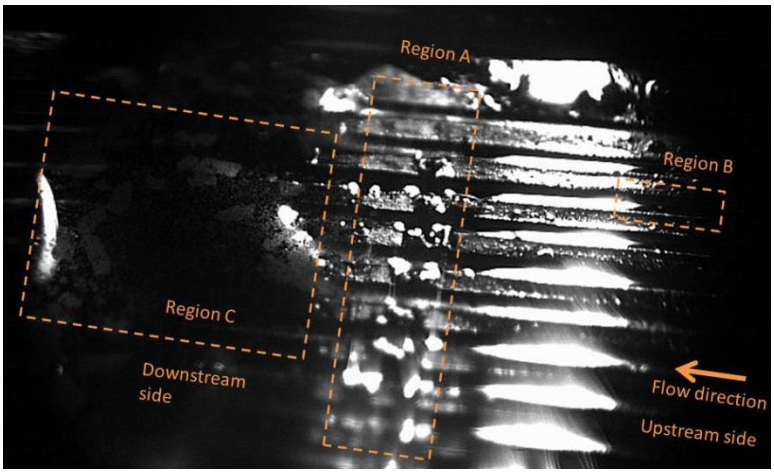

Figure 3.22 An example frame image of the lithium tray surface taken by fast frame camera

Figure 3.22 is a typical frame of the fast frame video, facing the center of the tray. Because the inclined surface causes different distances from different part of the tray to the lens and the depth of field is shallow for macro lens we can hardly reach a good focus for the whole image. Instead only the few trenches close to the center of the image can be seen clearly. Another problem is some part of the image is saturated because of the light reflection from the electron beam filament. That is the reflection from the shiny liquid lithium surface.

In this figure the liquid lithium is found to flow from right to left. The image is divided into few regions. Region A is the center of the tray directly hit by the electron beam. The width of this region is about 1 cm. Some dim straight lines can be found in region A and those are the Bremsstrahlung emission when electrons hit the lithium surface.

The right side of region A is the upstream side and the left side of region A is the downstream side of the lithium flow. Some part of the upstream side has light reflection from the electron beam filament while the rest looks dark. The shiny surface of pure lithium can hardly be seen without any light reflection from the surface of liquid lithium. However, when an impurity particle flows across the dark region it looks white because its rough surface can diffusively reflect the light. For example in region B a small particle is flowing along the trench.

The left side of region A is the downstream side. Since the thermoelectric current has a positive correlation with the temperature gradient and obviously the direct heating by the electron beam in region A generates a high temperature gradient at the center, after the liquid lithium passes region A it will get accelerated by the Lorentz force and enter the downstream region. From the picture we can see some lithium pile-up in region C and the reason will be discussed later.

In the experiment the flow on the upstream side is laminar and the flow on the downstream side is turbulent. Because of the mass flux conservation we only measure the velocity of the upstream side and use that as an estimate of the average velocity within the whole trench. It is also observed that different trenches have different velocity values due to the non-uniformity of the electron beam heat flux and impurity accumulation. As a result a 12.5 second video is taken for each experimental condition, based on which the velocity values from different trenches are measured and averaged. The standard deviation is used as the error bar.

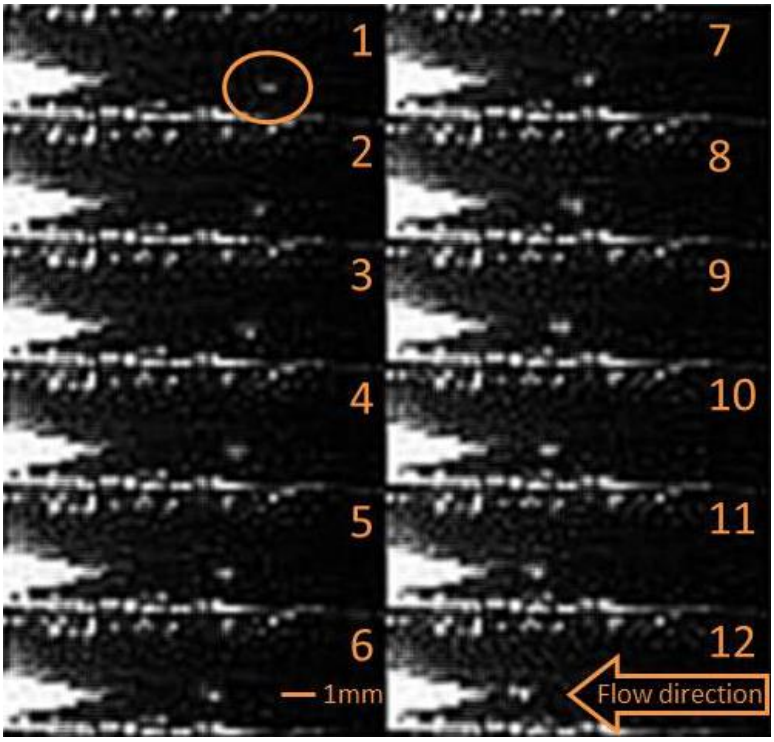

Figure 3.23 Sequence frames (totally 12 frames) of a moving impurity particle on liquid lithium surface

Figure 3.23 presents an example of measuring the moving particle through sequence frames, which actually includes the frame of figure 2. Due to the size of the image only region B in each frame is shown in Figure 3.23. The positions of the particle on each frame look like a straight line which indicates that the velocity of the particle is stable during these 12 frames. The bright horizontal lines on each frame are the light reflection from the edges of the trench, so we can tell that the particle flows almost at the center of the trench. The software ImageJ is used to measure the length of the moving path on the picture in the unit of pixels. The length of the path is then scaled to the width of the trench (2 mm) to get the real length during the 12 frames' time. In the experiment the frame rate is 400 frames per second (fps) so that the time interval through these frames is known. With these values the average velocity of the particle during the 12 frames' time can be calculated. For each experimental condition about 10 groups of frames are chosen to calculate the velocity in order to lower the random error when picking the moving particles.

The one-dimensional model in chapter two can be used to calculate the flow velocity as a function of the magnetic field or the heat flux. Similar to what has been discussed in chapter two the velocity will decrease when the magnetic field increases when the velocity value is on the right hand side of the peak velocity. With the help of the above particle tracing method flow velocities under different magnetic fields are plotted in Figure 3.24 and compared to the predicted value under the same conditions. It can be seen that both measurements match the predicted velocity which proves that the velocity decreases when the magnetic field increases.

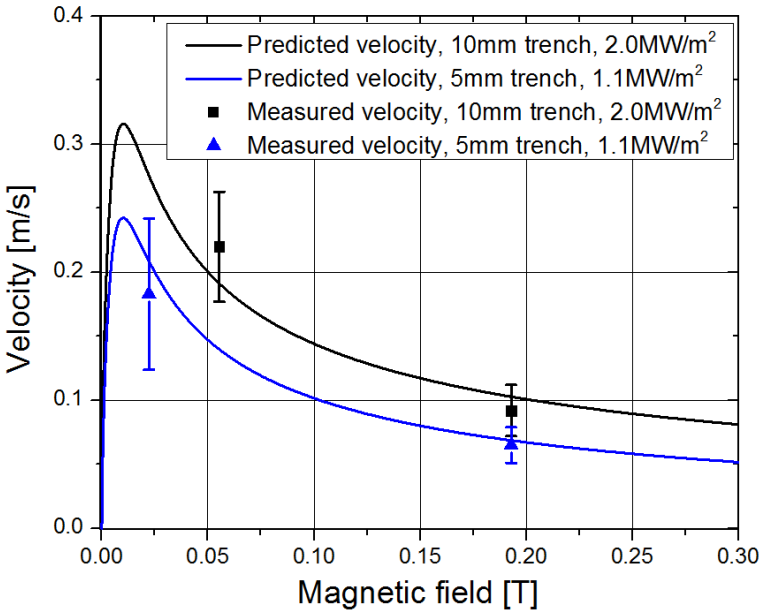

Figure 3.24 Liquid lithium flow velocity under different magnetic fields

This slowing-down is not in favor of the application in fusion reactors because a higher flow velocity means higher lithium refreshing rate and higher convection heat transfer rate. If the slowing-down is too severe then it will be not efficient to use this concept in real fusion reactor fields which is normally in the tesla range. However since the velocity drops in the speed of ~1/B when the magnetic field is increasing to tesla level the actual dropping rate is not that high. For the 10mm trench if other conditions are the same as Figure 3.24 and if we extend the prediction curve to the tesla range when the magnetic field is 1T the velocity is 0.040m/s and when the magnetic field is 2T the velocity is 0.026m/s, which still seems enough to refresh the lithium surface, although this velocity may require mostly good heat conduction underneath the trenches to keep the surface temperature below the limit.

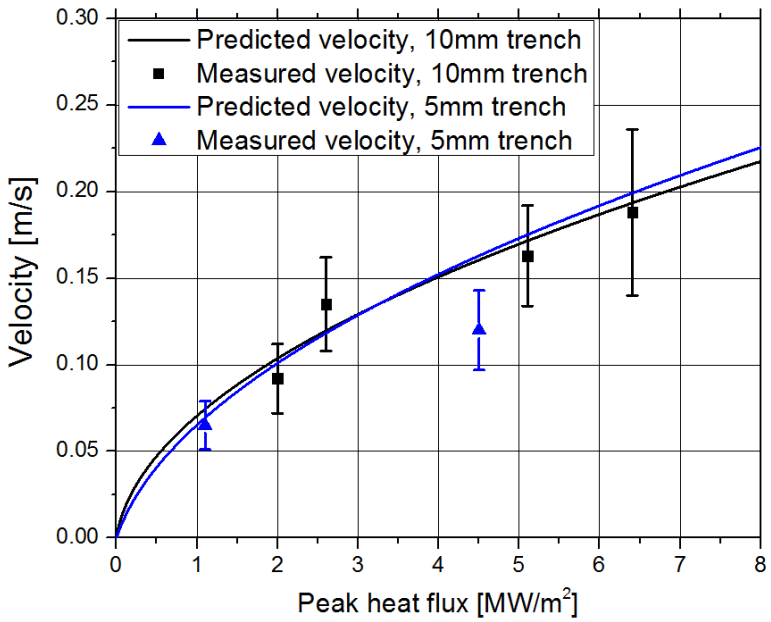

Figure 3.25 Liquid lithium flow velocity changes with the incoming e-beam heat flux

On the other hand when the surface heating increases the flow velocity will also increase. This can be seen in Figure 3.25. When the heat flux is increased the temperature gradient will also increase which leads to a higher flow velocity to draw back the influence of the heat flux increase, which leads to a higher convection heat transfer rate. Such flow effectively transfers the heat from a narrow area to the whole volume of the fluid and even when some transient event happens the explosively growing heat flux can accelerate the flow and the extra deposited heat will eventually be removed.

3.3.2 Temperature measurement

The temperature change is very important to the application of LiMIT concept because the temperature is crucial to the vacuum application and the temperature change inside channels may reveal other information of the flow itself. The temperature inside the trench is measured by embedded thermocouples and the temperature the surface of the trench is measured by IR camera.

Figure 3.26 and Figure 3.27 show that four thermocouples (TC1~TC4) are embedded inside the tray. TC1 and TC2 are place inside the return flow channel. TC1 is attached to the bottom of the

tray and TC2 is attached to the back side of the suspended trench. These two thermocouples can tell the temperature difference within the return flow channel. TC3 and TC4 are embedded inside the same lithium trench close to the top surface. These two will tell the change of the temperature after the lithium flows across the heating region. TC3 is placed at the downstream side and TC4 is placed at the upstream side. TC4 is placed closer to the direct heating area than TC3 so that if there is no flow the temperature of TC4 should be higher than TC3. But once the lithium starts to flow we can expect that the temperature of TC3 will be higher due to the convection.

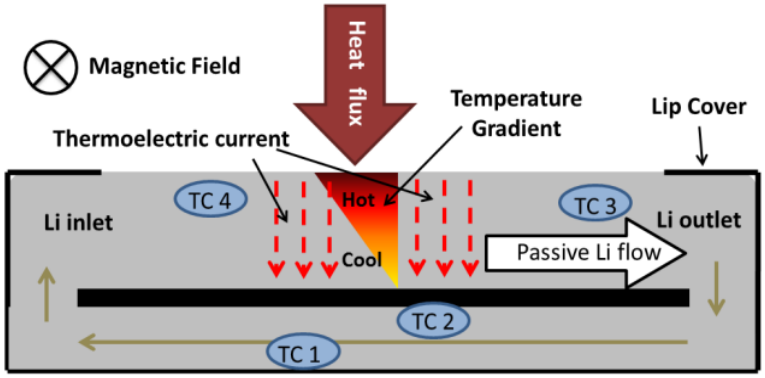

Figure 3.26 Cross section view of the tray design. Four thermocouples (TC1~TC4) are embedded. TC3 and TC4 are embedded in the trench. TC1 is attached to the bottom inner face of the tray. TC2 is attached to the back side of the trench structure

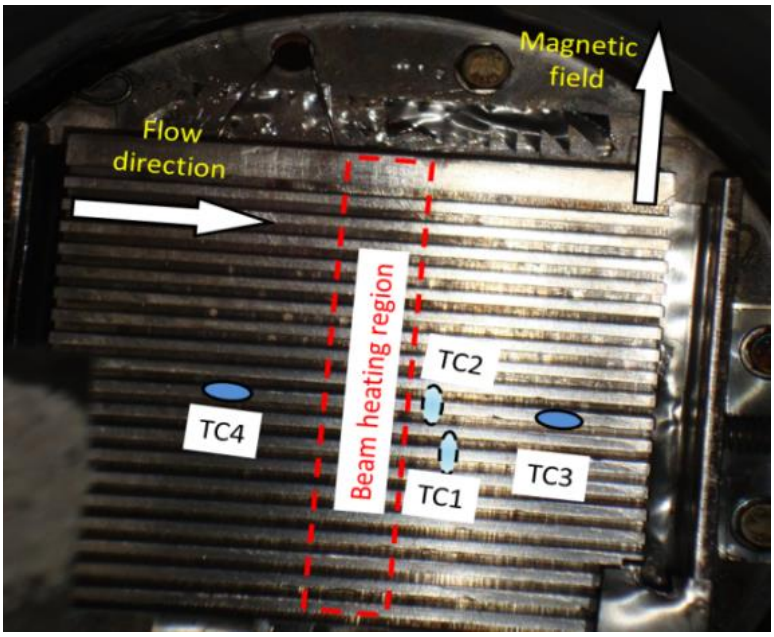

Figure 3.27 Top view of the trench with stainless steel tray

Figure 3.28 shows the temperature change of embedded thermocouples when lithium was heated from solid to liquid. Because TC4 is placed closer to the heating area, its temperature increases faster than TC3 and the temperature difference keeps increasing. After the lithium starts to melt TC4 does not increase while TC3 increases to the melting point. After the lithium is totally melted the flow starts to build up which brings cooler lithium towards the heating area and transfers heat from the heated area to the downstream side so that the subtraction of (TC3-TC4) quickly becomes a positive value, which agrees with the IR image. This flow also increases the heat transfer to the back flow channel and this explains the speedup of the TC1 temperature increase after the top trench is totally melted (at t~40s).

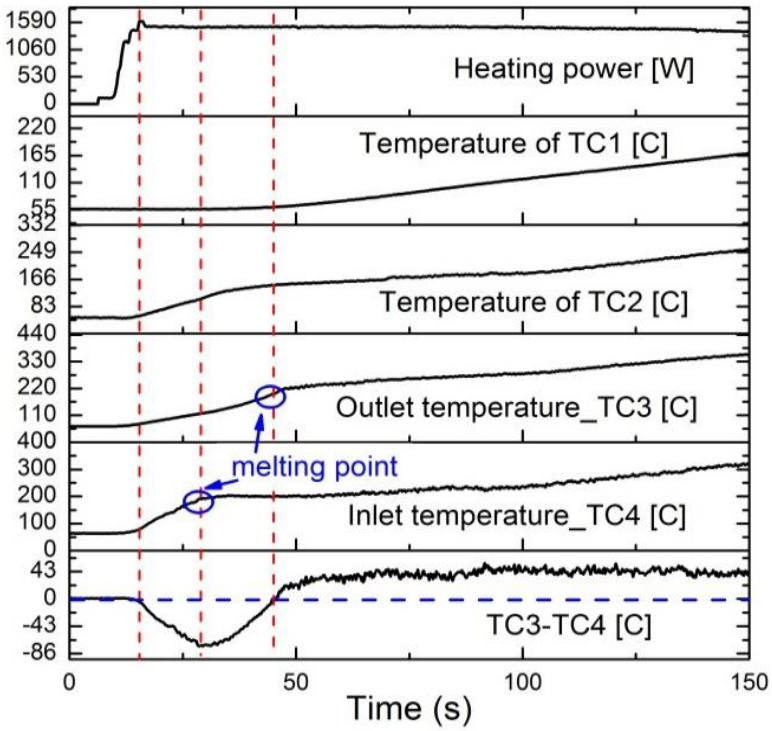

Figure 3.28 Temperature changes of embedded thermocouples when lithium is heated from solid to liquid phase

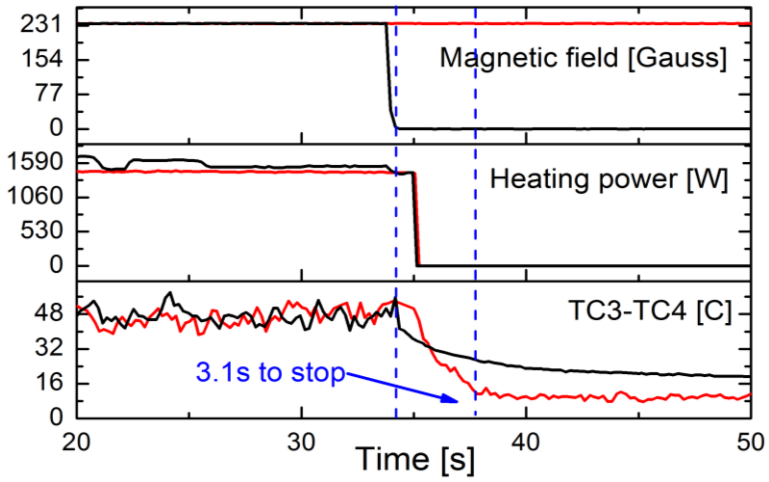

Figure 3.29 Comparison of the temperature changes of thermocouples inside the lithium trench when the magnetic field is kept on or off after the electron beam is turned off

Previous swirling flow experiment [40] found that TEMHD driven flow can exist for a long time after the direct heating is turned off while the magnetic field still exists. Such effect also appears

in the trench flow, as is shown in Figure 3.29. After the heating is turned off the inlet temperature will stay at a high value for about 3.1 second before it starts to decrease. If the magnetic field is turned off when the heating stops the temperature of the outlet will immediately decrease. In addition with the magnetic field the speed of the falling temperature difference between TC3 and TC4 quickly decreases to a low value since the continuous flow acts to even-out the temperature profile along the trench.

The 1D model reveals that a higher heating power can lead to a higher temperature gradient which will in turn accelerate the fluid and mitigate the temperature gradient. The overall effect is the relation between the temperature increase and the heating power is less than linear. This is also observed in Figure 3.30. After the beam is turned on, the temperature difference between inlet and outlet starts to ramp up, but after few seconds (<5s) it becomes stable since the fluid has already been accelerated to a stable velocity and during the 30 seconds heating period the temperature difference keeps more or less stable. From 1kW to 3kW the temperature difference only increases by a factor of two.

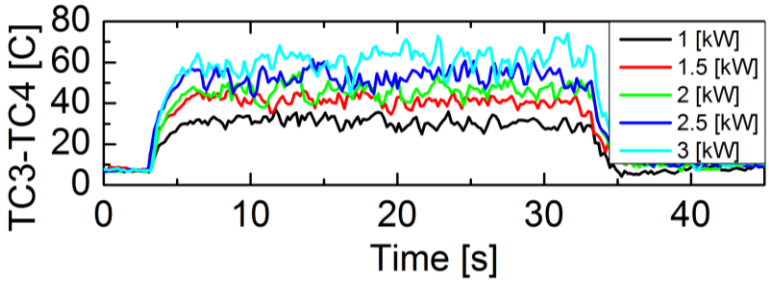

Figure 3.30 Temperature differences between inlet and outlet of a lithium trench with different power

Figure 3.31 plots the influence of the higher magnetic field. In Figure 3.31 once the heating starts the temperature of the downstream side increases immediately while the upstream side temperature remains flat. The temperature difference builds up in less than 2 seconds. This agrees with the speed-up of the fluid that is discovered by the fast frame camera video. After the flow becomes stable the temperature of the upstream and the downstream side increase at the same rate.

However after the high field is on it seems that the upstream temperature stops increasing while the downstream temperature increases faster. In the fast frame video we observed the damped

velocity at the upstream side while the downstream side becomes highly turbulent. It is believed that with the existence of the high field the downstream side starts to have eddy flow due to the TEMHD stirring, which may greatly enhance the heat transfer there, while the upstream side is more or less slowed down. This actually helps to remove the heat from the narrow direct heating region to the downstream side although the total volume flow rate may be lowered by the increased magnetic field.

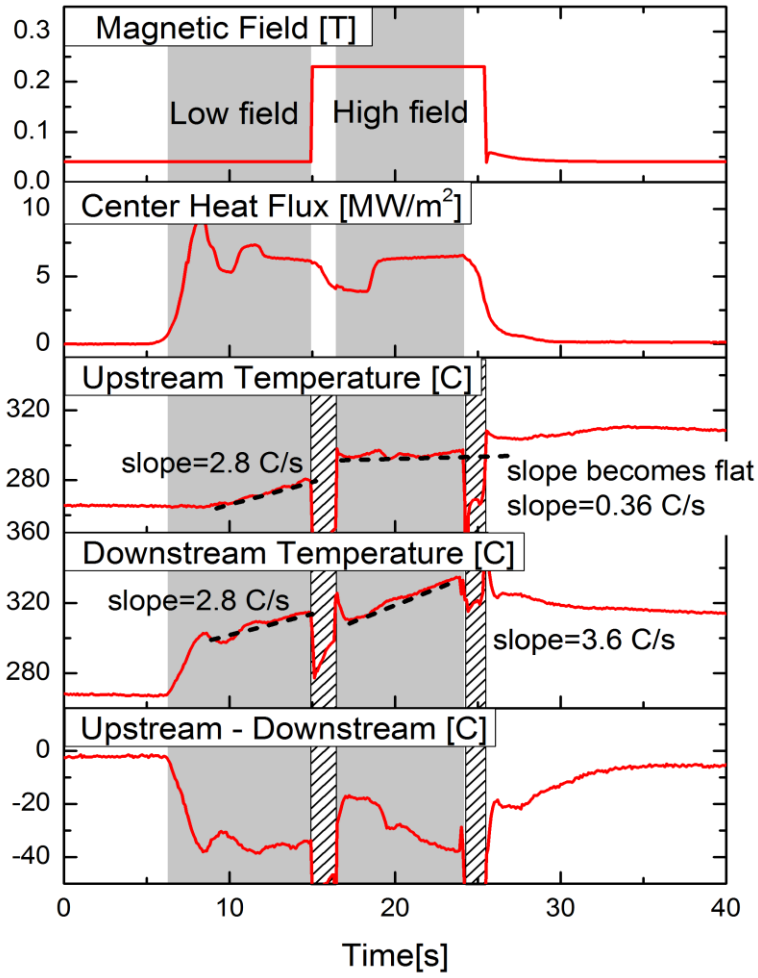

Figure 3.31 The temperature change of the flowing liquid lithium due to the change of the magnetic field

IR camera is used to monitor the surface temperature. The setup and the general concept of the IR camera have been introduced above. For the IR measurements the first important step is to find out the emissivity of the material. From the previous introduction we can see that the emissivity

of the material is normally less than one and the emissivity of shiny metal surface is usually much less than one. In fact some theoretical calculation reveals that the emissivity of pure lithium is less than 0.1 when the temperature is less than 1000K.

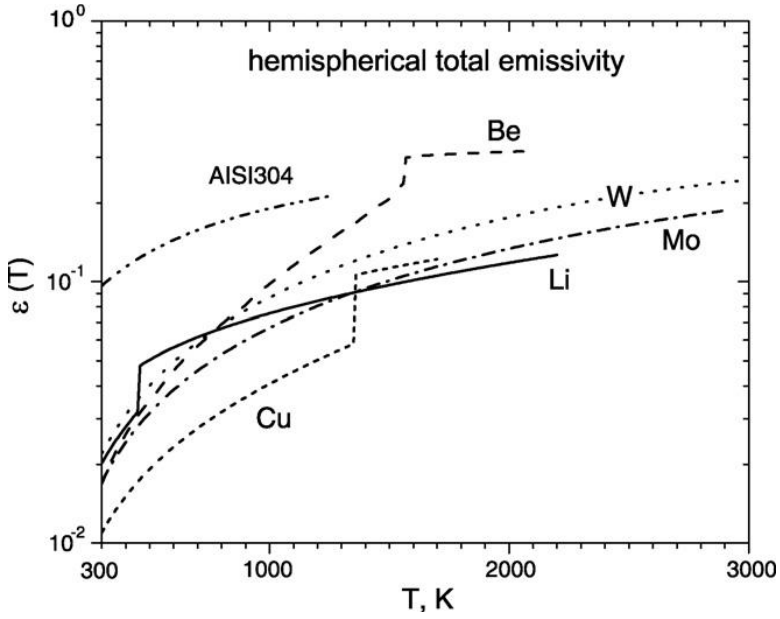

Figure 3.32 Calculated total emissivity of different material at various temperature [59]

On the other hand the ZnSe window also reflects and absorbs a small portion of IR light, which makes the emissivity looks even lower. The infrared light emission from the background will also affect the IR from the lithium surface. In all it is very hard to take everything into consideration. Instead, the effective emissivity can be used to compensate all the influence based on equation 3.20

$$\varepsilon(T^4 - T_0^4) = (T_*^4 - T_0^4) \tag{3.20}$$

Here T is the real temperature. T* is the uncorrected temperature from IR camera and T_0 is the background temperature which was set to be 298K in experiment. As far as we can measure this effective emissivity the uncorrected IR temperature measurement can be corrected to the real temperature.

An IR calibration experiment was done to extract the effective emissivity. A thermocouple was immersed in the liquid lithium to record the real temperature and IR camera record the surface temperature at the same time. The temperature was measured after lithium had been heated to a

high temperature (~350C). Then the heater was turned off and the liquid lithium started to cool down by itself. During the cooling, the convective cooling system was off so the cooling only relied on the radiation and the contact between the stainless steel tray and its holding frame. Such a cooling process requires more than two hours to cool down to the room temperature while the thermal equilibrium time of the liquid lithium can be calculated by $\rho C_p /(kl^2)$, which is about 30 seconds. Here l is the height of the trench. This means 30 seconds after the liquid lithium started to cool down the value that was measured by the immersed thermocouples can be considered as the surface temperature. The calibration is plotted in Figure 3.33 and equation 3.20 is used here to fit the data. The slope of the curve is the effective emissivity and it is 0.0473 and the error is 0.00243. This value is used to correct all IR measurements.

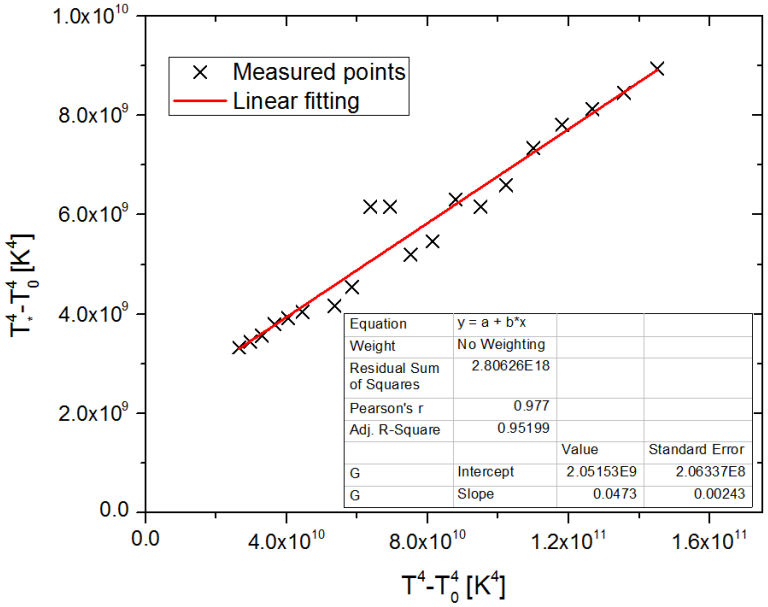

Figure 3.33 Lithium temperature measured by IR camera vs. temperature measured by thermocouple

Even with the emissivity correction the IR measurement may still be affected by the reflection light from the e-beam or the impurity scale. The e-beam filament is much hotter than the lithium, which looks like a hot spot on the image. The impurity scale which is at the same temperature as the lithium has a higher emissivity due to the material property and rough surface. In all these influences also need to be taken into consideration. In experiments without the acceleration voltage of the e-beam one IR image was taken when the filament is heated to the required temperature as

a background image. After IR measurement was taken in experiments the subtraction of both images gives the actual temperature rise caused by heating.

Figure 3.34 is the temperature increase when the tray was heated by a 3MW/m^2 beam for about 20 seconds and the transverse magnetic field is 0.055T. In the IR image on the upstream side lithium trenches look like cooler thin stripes lying horizontally and the hotter region is mostly stainless steel wall and impurity since their emissivity is higher. On the downstream side lithium trenches actually look hotter. Some cold spots in the hot region are caused by the subtraction of the saturation regions. The asymmetric temperature distribution is clearly shown in the figure. It is predicted that lithium flows from right to left and Figure 3.34 shows that such flow can bring the heat away from the center region to the left side while the right side has much smaller temperature increase. At the position where lithium meets the electron beam the steep temperature gradient can be observed.

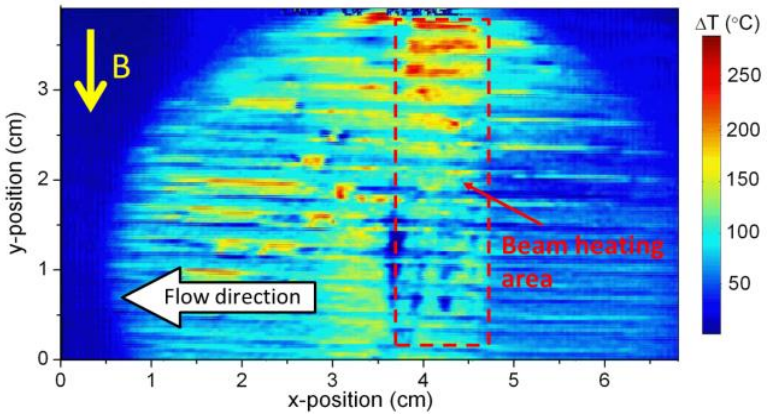

Figure 3.34 Surface IR temperature contour of liquid lithium when the center is directly heated

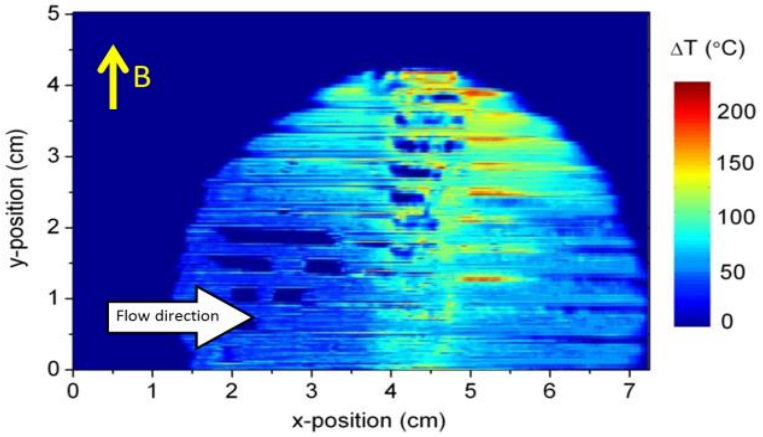

Figure 3.35 Surface temperature contour of liquid lithium after the magnetic field is changed to the opposite direction

When the magnetic field is changed to the opposite direction, the flow direction is expected to reverse. This is confirmed by our experiment, where an asymmetry of the temperature distribution is found after the reversal of the field, as reported in Figure 3.35.

The surface temperature increases of the low field and the high field situations are also compared. In both figures the heating starts when the embedded thermocouple is at 240C. Figure 3.36 reveals the temperature increase in the low field, which is 0.04T and its component vertical to the side wall is 0.033T. In the low field the flow velocity is high which brings the heat away immediately. The liquid lithium flows from left to right and the downstream side has a higher temperature than the upstream side. The temperature at the direct heating region is slightly higher than the downstream side which indicates good heat convection ability.

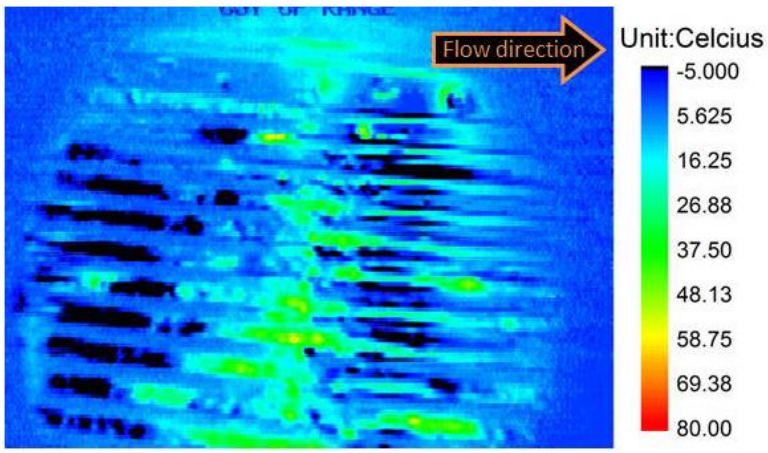

Figure 3.36 The temperature increase of the liquid lithium surface after it has been heated by the 2 MW/m^2 e-beam for 10 seconds when the transverse magnetic field is 0.033 T

In Figure 3.37 the temperature distribution in high field, which is 0.23T and its component vertical to the side wall is 0.19T, is different from that in the above figure. The uneven temperature distribution still exists which means the flowing liquid lithium can still transfer the heat to the downstream side. But the temperature increase is higher than the low field result and this is in agreement with the slowing-down in the high field. The direct heating region can be clearly identified in this figure because the damped velocity lowers the heat transfer ability.

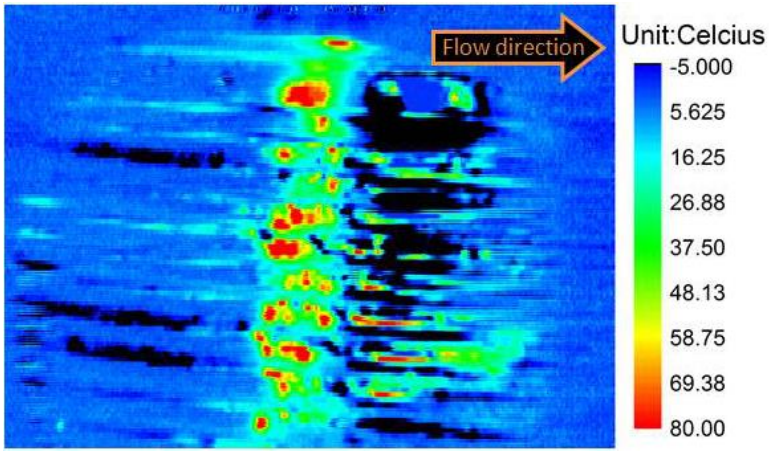

Figure 3.37 The temperature increase of the liquid lithium surface after it has been heated by the 2 MW/m^2 e-beam for 5 seconds when the transverse magnetic field is 0.19 T

3.3.3 Li acceleration, dry-out and pile-up

When the magnetic field is low the TEMHD driven flow looks stable while when the magnetic field is increased to 0.23T some effects start to appear. During the high field test, the electron beam is turned on first and then the magnetic field is turned on. When the high magnetic field starts it is discovered that lithium starts to accumulate on the downstream side and the velocity of the flow starts to increase. From the fast frame video it takes less than 0.1s for the liquid lithium to starts to response to the driven force and to pile up on the downstream side. And then it takes about 0.1~0.2s for the lithium pile-up stops growing. After that it seems the velocity keeps increasing for about 0.2s. The start-up is shown in Figure 3.38. When the lithium starts to flow the velocity is still almost zero and the center temperature gradient builds up quickly. As a result the driven force keeps rising and accelerates the flow to the balance point. The acceleration time actually reveals the response time of the flow to the variation of the heat flux.

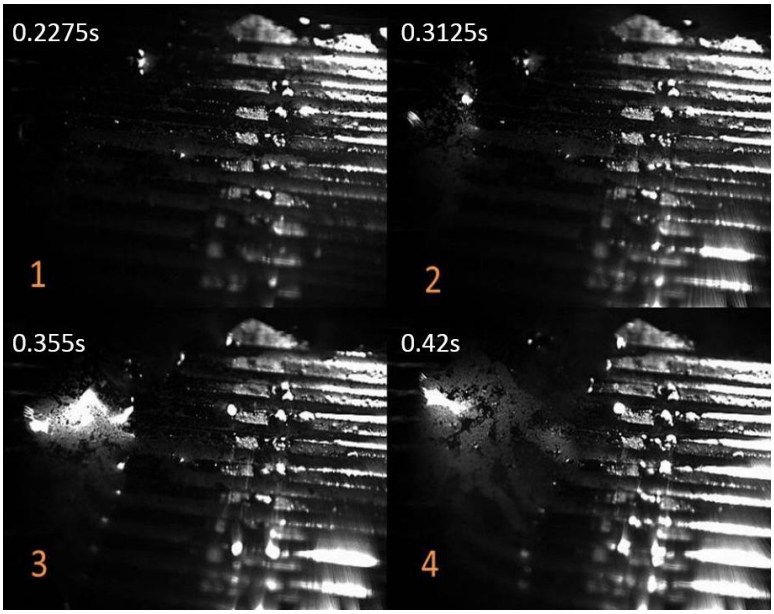

Figure 3.38 Change of the lithium surface when the flow starts. Pile-up and speed-up are observed.

Another interesting phenomenon is the dry-out of lithium at where the e-beam hits. At the direct heating area lithium was accelerated to a higher speed with a comparably short rage. The stronger the heat flux is the faster the acceleration is. Due to the mass conservation when the lithium flows faster the height of the liquid actually decreases which exposes the solid wall material in the direct

heating area. Accompanied by the dry-out the pile-up on the downstream side is expected. This is shown in Figure 3.22. The height difference creates a pressure difference between both sides of the trench and drives the back flow under the trench from left to right.

These phenomena may potentially influence the application of LiMIT concept in fusion reactors. The acceleration is not a problem for our test. However for the real application as a divertor target plate this may become a problem because at the beginning of the plasma discharge in fusion reactors the current ramp up time [60] is usually less than this acceleration time. In addition when transient events such as ELMs or disruption happen the transient heat load would be very large within milliseconds. The response of LiMIT trenches to this transient effect actually needs further investigation.

The dry-out obviously is not good for the LiMIT trenches because the exposed solid part starts to get direct bombarding from the plasma in fusion reactors. Even in our experiment the dry-out caused the top of the stainless steel wall to melt. This is presented in Figure 3.39 and Figure 3.40. The e-beam heat flux in this case is 11.4 MW/m^2 which is similar to the divertor heat flux.

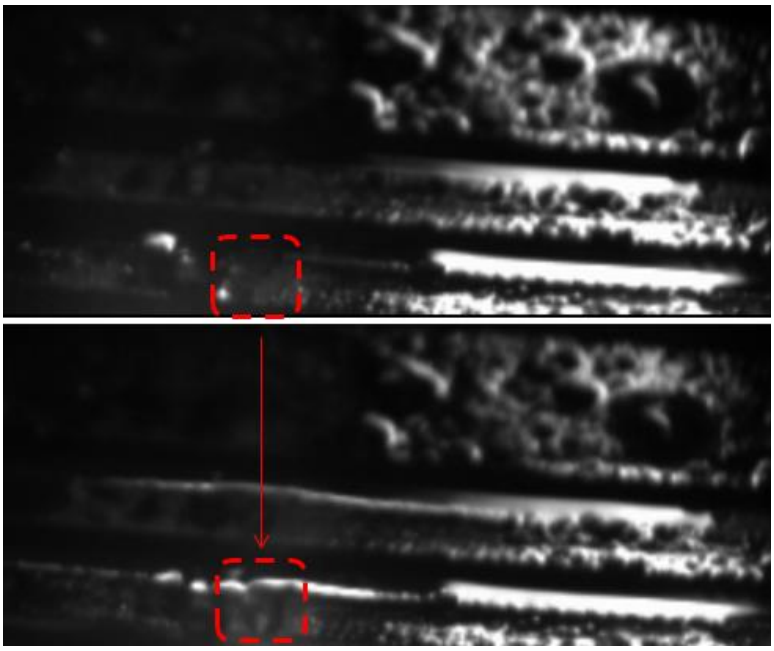

Figure 3.39 Top of wall damaged when the e-beam was at 11.4MW/m^2

Figure 3.40 Top of stainless steel wall damaged

The pile-up may become a big problem in tesla level field because the MHD damping becomes large in the backflow channel and requires a higher pile-up to provide enough pressure difference across the backflow channel. The damping in the back channels increases in the rate of B^2 while the pressure provided by the pile-up only increase linearly with the height of the pile-up. The height of the pile-up may be too high eventually. Active pumping on the return flow channels is one choice to increase the back flow rate and lower the pile-up. Sizing the channels correctly is another way.

3.4 LiMIT test in HT-7

In order to test how this concept works in the real fusion reactor environment a similar liquid lithium tray was tested as a limiter in HT-7 tokamak, which is a medium-size tokamak reactor with a major radius of 1.22m and minor radius of 0.27m. Its toroidal magnetic field is about 1.8T and the peak heat flux on the limiter is 6MW/m^2 [61]. This is also the first flowing liquid lithium limiter test in fusion reactors [13].

3.4.1 Experiment setup

In this experiment the liquid lithium tray is also made by stainless steel. The depth of the trench is 5mm and the width of the trench is 2mm. The thickness of the stainless steel wall is 1mm. The size of the whole tray is 120mm by 100mm. The CAD drawing of the trench is presented in Figure 3.41. From the figure we can see that the cooling channels are between the top trenches and the return flow path to provide a larger temperature gradient within the top trenches. Up to 60psi compressed air was used in the experiment to provide the cooling.

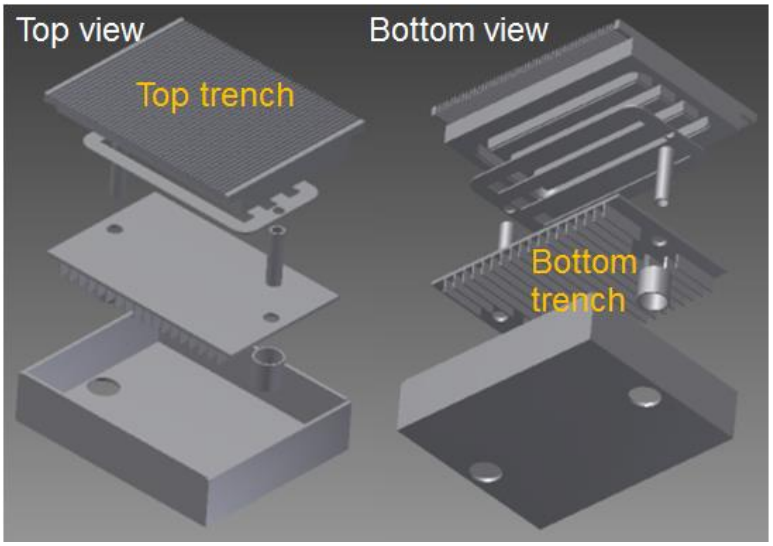

Figure 3.41 The explosive view of the CAD drawing for the LiMIT design tested in HT-7 tokamak

The whole tray is attached to a vacuum feed-thru at the bottom of the tokamak as a movable limiter which is shown in Figure 3.42. Figure 3.43 is the installed tray inside the HT-7 chamber. The trenches are along the poloidal direction so that the toroidal field is transverse to the trench wall, by which way the toroidal field can drive the liquid lithium to flow across the heating area. On one side of the trench an inclined stainless steel plate is attached to serve as a lithium loading plane.

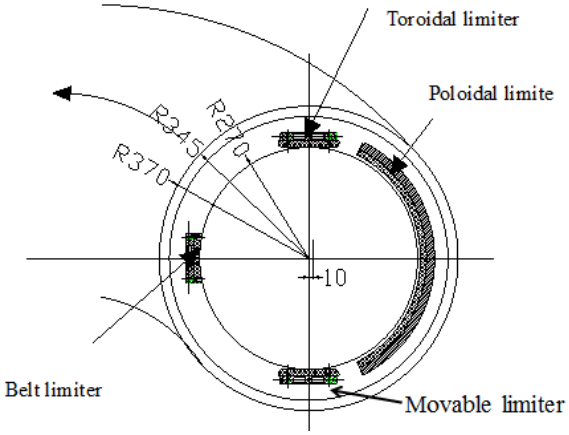

Figure 3.42 The cross section of the HT-7 tokamak with the location of all the limiters

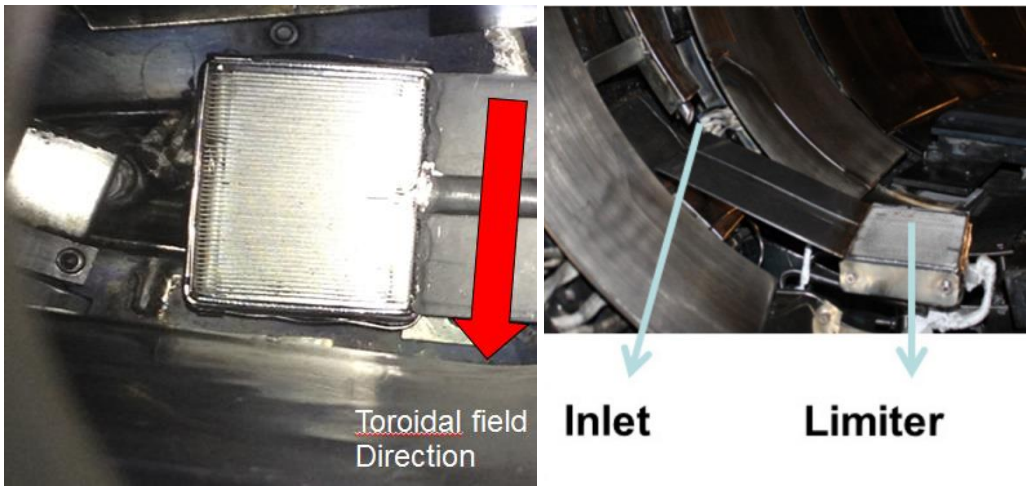

Figure 3.43 The top view and side view of the installed lithium tray inside HT-7 with lithium loading tool attached to the side

3.4.2 Li loading, movement and velocity measurement

During the experiment lithium was loaded through the inlet in Figure 3.43 onto the inclined surface and then to the tray. Before loading the lithium the trench was heated and unfortunately the heater on the back of the tray was broken. In order to compensate the broken heater the cooling line was used to inject hot compressed air and eventually it was able to heat the tray to 390C. Although the

tray was still not at the perfect temperature for loading the lithium the bottom of the tray was still filled and some trenches on the top were also filled. The filling process is presented in Figure 3.44.

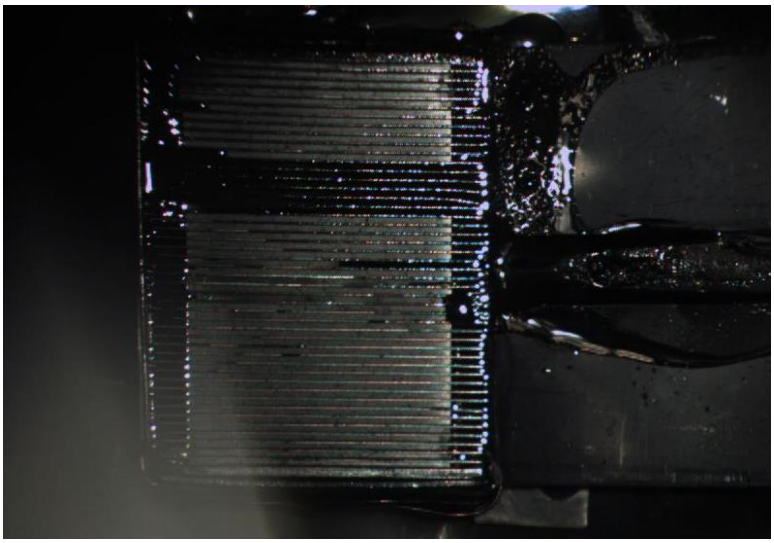

Figure 3.44 Filling LiMIT limiter in HT-7 tokamak

In the experiment the movement of the liquid lithium was observed and taped by a fast frame camera. Figure 3.45 showed two frames of moving lithium inside trenches during the plasma discharge. Lithium was observed to flow from right to left and no ejection of lithium out of the tray was found during the discharge.. Based on the method in chapter two the velocity is estimated to be 0.042m/s. The measured velocity from these frames is 0.037 ± 0.005m/s. We can see that the moving velocity is a bit slower that the estimate value which may be caused by the inaccurate estimate of the surface heat flux because the tray was still in the SOL layer. However the liquid lithium is proved to be able to move in such a strong magnetic field environment with the aid of TEMHD driven force.

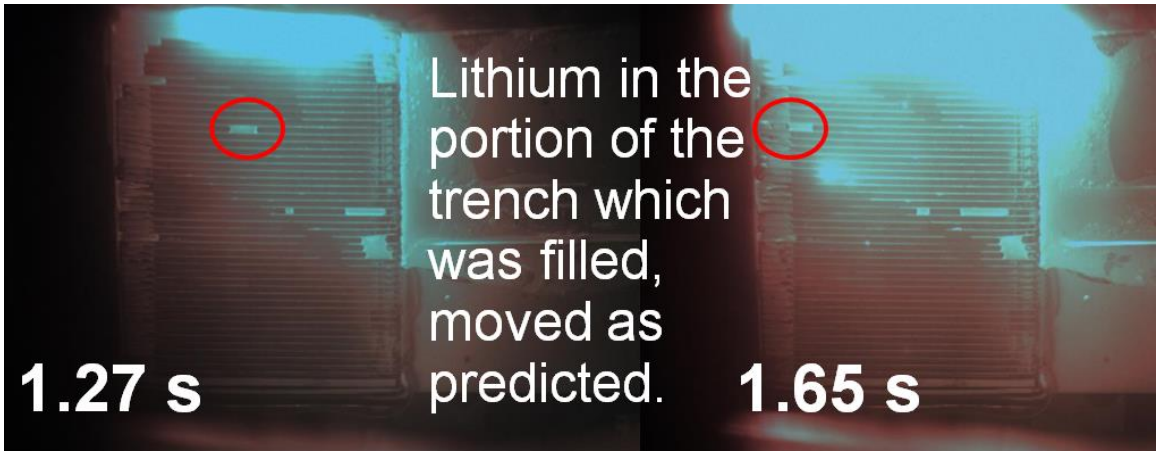

Figure 3.45 Moving lithium in trenches during HT-7 plasma discharge

3.4.3 Influence on the plasma performance

The plasma performance in shot 117617 was monitored and compared to shot 117570 without the lithium limiter in Figure 3.46. Both shots have similar plasma current but the loop voltage drops by about 10% when the lithium is applied which indicates the resistivity drops. Since the resistivity is proportional to the effective Z this indicates lower impurity pollution to the plasma which leads to this improved confinement time [62].

This is also demonstrated by the reduction of soft x-ray radiation which indicates the reduced impurity particle concentration. Because of lithium's outstanding ability to absorb hydrogen isotopes and impurity particles the recycling and the emission of impurity particles from the edge are greatly suppressed. Less particles from the wall entering the plasma leads to a lower emission which is given the radiation measurement. In this way the edge temperature is raised and the radial temperature gradient of the plasma is lowed. The turbulence driven by the temperature gradient, which is the main part of anomalous transport, is suppressed and the particle and energy confinement become better [63]. On the other hand some Li atoms are sputtered into the plasma during the discharged which can been seem from the light emission in Figure 3.45. But since the atomic number of lithium is small the influence is not as big the other impurity particles.

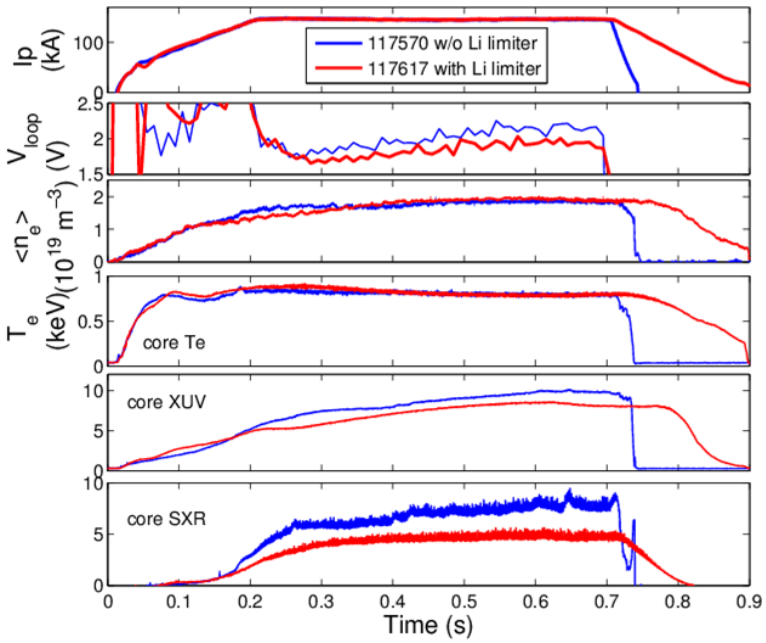

Figure 3.46 Comparison of the plasma discharge with and without the LiMIT limiter

Chapter 4 Numerical analysis of the TEMHD driven flow in open channels

A few experiments have been done to investigate the TEMHD driven lithium flow in open channels and we have gained some knowledge. But it is hard for the experiment to examine extensive conditions for different parameters and to get in-depth knowledge of how the flow looks like in detail. On the other hand numerical analysis provides a feasible way to solve these questions. With the knowledge gained from experiments a numerical model can potentially describe the TEMHD driven flow and make it easier to examine different parameters and incorporate more physics into the study.

In this chapter numerical analysis of TEMHD flow and LiMIT trenches are presented. A multi-physics finite element software COMSOL is used to do the analysis. The first section discusses the general consideration of the analysis and how to incorporate the thermoelectric effect. The second section presents a 2D model that can simulate the TEMHD driven flow in infinite long trenches. The third section presents a 3D model to simulate the lithium flow and heat transfer in LiMIT trenches. The last section compares the 3D model results with the experiment results to suggest some improvements to the LiMIT design.

4.1 COMSOL modelling TEMHD driven flow

4.1.1 Modelling the thermoelectric effect

The first step is to model the thermoelectric effect in COMSOL to make sure that this feature can be added into COMSOL. A very simple example is modeled to test this and also to find out the thermoelectric current pattern itself when there is no influence from the magnetic field. This example contains two rectangular blocks in contact with each other. One is defined as stainless steel and the other one is lithium.

In order to incorporate the thermoelectric effect a thermoelectric term $-S\nabla T$ is added into the Ohm's equation by adding an extra source term in the electrostatic module in COMSOL

$$\frac{\vec{J}}{\sigma} = -\nabla\varphi - S\nabla T \tag{4.1}$$

In the above equation φ is the electric potential. The potential from the $\vec{u} \times \vec{B}$ term is neglected since the goal is to find out the current distribution just with pure thermoelectric effect.

$$\nabla \cdot \vec{j} = -\sigma\nabla^2\varphi - \sigma S\nabla^2 T = 0 \tag{4.2}$$

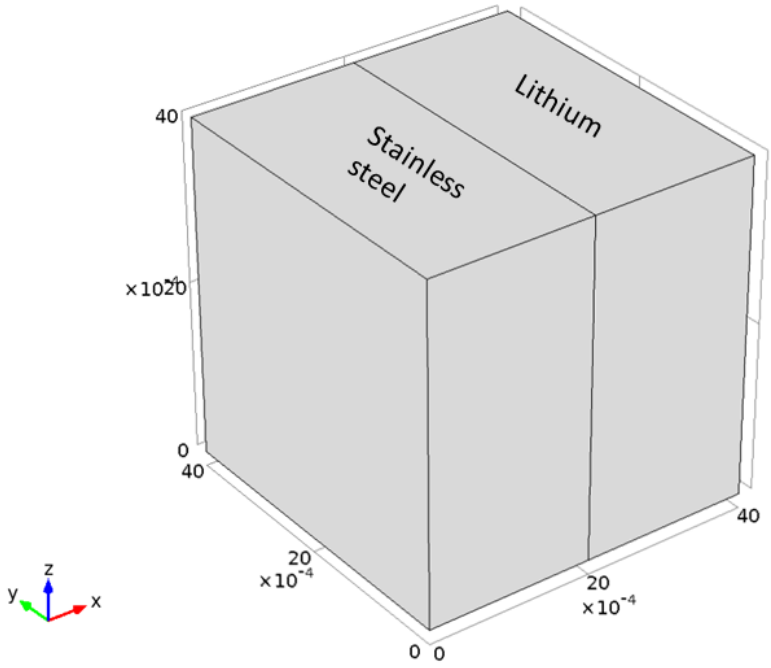

Figure 4.1 Simulation domain

In the electrostatic module of COMSOL the Poisson equation is solved in the domain that is plotted in figure 4.1. Two blocks of material are attached to each other. The size of the stainless steel is 4mm by 4mm by 2mm and the size of the lithium is same as the stainless steel block. The thermoelectric coefficient of the lithium is $25\mu V/K$ and the thermoelectric coefficient of the stainless steel is zero.

To calculate the Poisson equation we need the boundary conditions and also the temperature distribution. Two cases are investigated and compared in this study. In the first case the bottom surface is also set to be insulated the edge of the bottom surface at x=0 & z=0 is set to zero potential as a reference potential edge. In another case the bottom is set to be grounded and both cases will be discussed. All other boundaries are set to electric insulated surfaces.

The temperature of the top surface (the z=4mm surface) is set to 573K and the bottom surface (the z=0 surface) is set to 473K. Other surfaces are set to be thermally insulated. The heat transfer equation is run once at the beginning to get a temperature distribution through the entire simulation domain, which is shown in figure 4.2. After this the Poisson equation is solved with this temperature distribution for insulated bottom and grounded bottom cases.

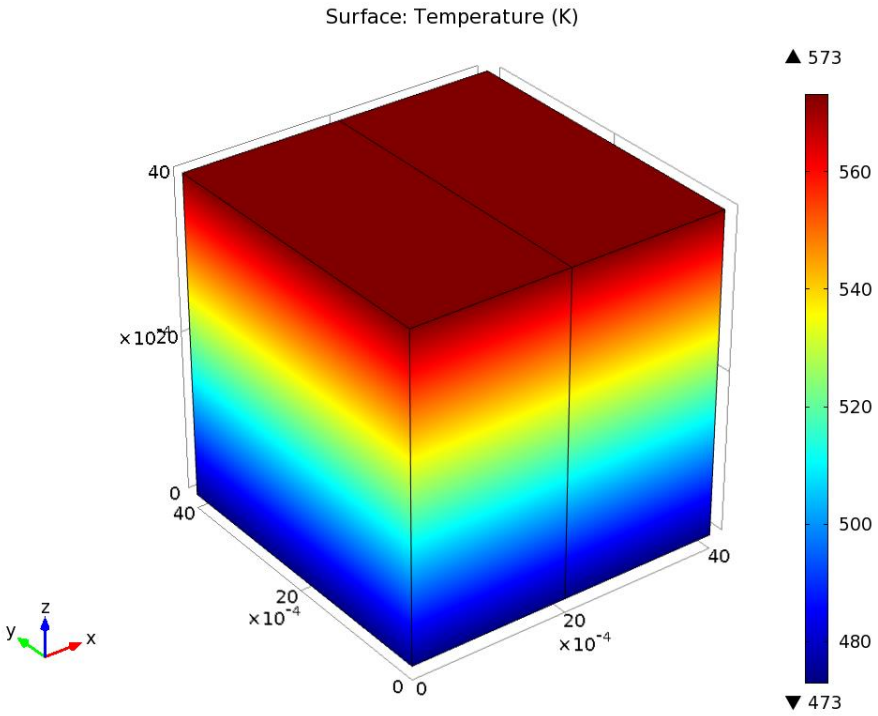

Figure 4.2 Temperature result for the thermoelectric current calculation

The current density result of the insulated bottom case is plotted in Figure 4.3 and Figure 4.4 and that of the grounded bottom case is plotted in Figure 4.5 and Figure 4.6. Generally the current flows downwards in the lithium and flows upwards in the stainless steel part. Figure 4.4 is the 2D plot of the x-z plane at y=2mm with those small arrows indicating the direction of the current.

As what we expected in chapter 2 all the current is generated at the interface and spreads through the entire domain. In Figure 4.3 the current density is higher close to the interface and the highest point is at the interface close to the top and bottom. When the bottom is insulated in Figure 4.4 the current density profile is symmetric about the x-y plane at z=2mm. However when the bottom is grounded in Figure 4.6 the current does not need to go through the interface to form a closed loop.

In this case the current density profile is not symmetric about the x-y plane at z=2mm and we can see a more uniform current density distribution close to the grounded bottom surface.

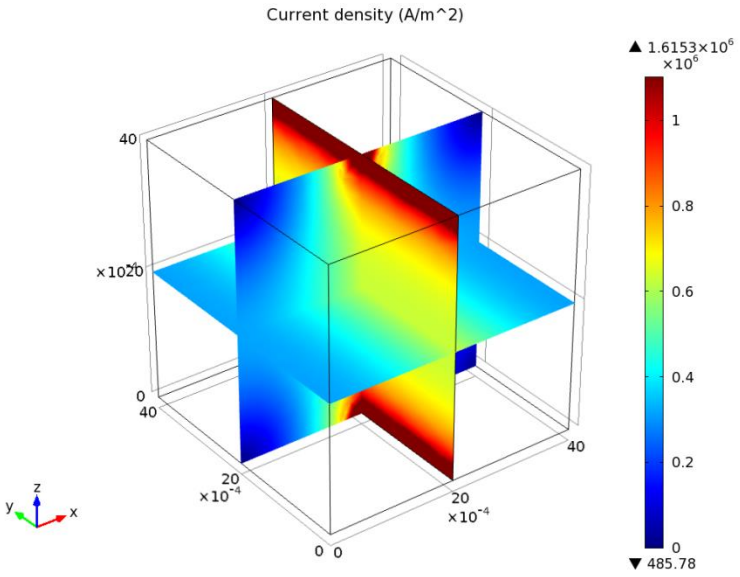

Figure 4.3 3D Current density distribution (insulated bottom)

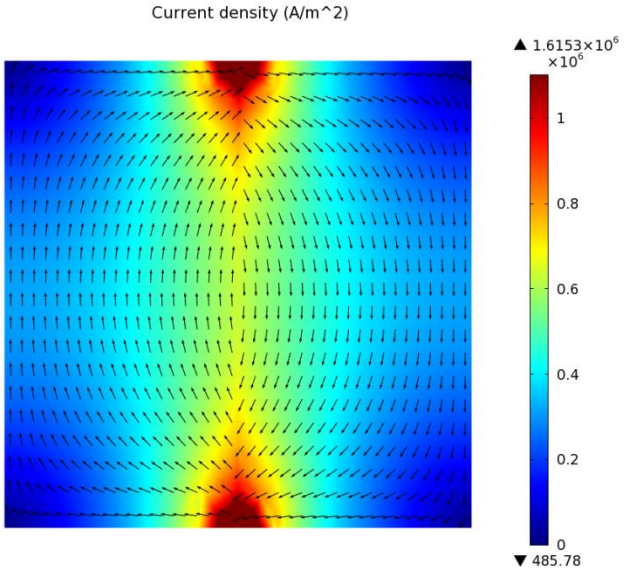

Figure 4.4 2D Current density distribution (insulated bottom)

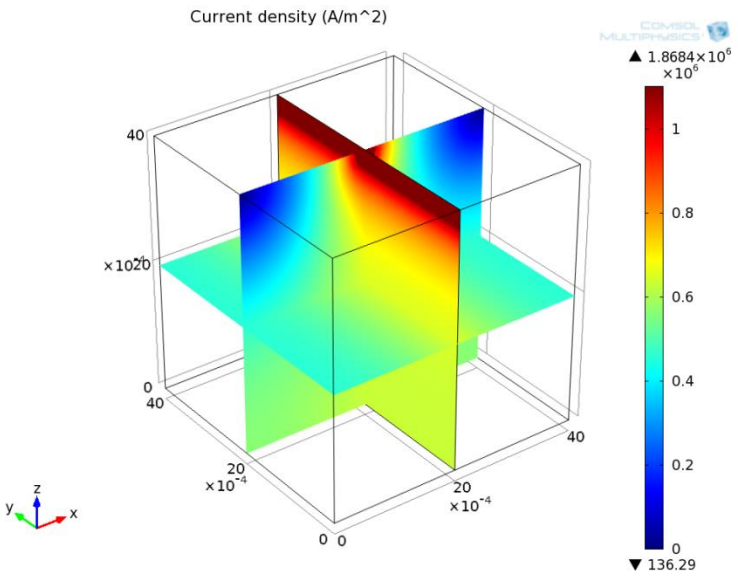

Figure 4.5 3D Current density distribution (grounded bottom)

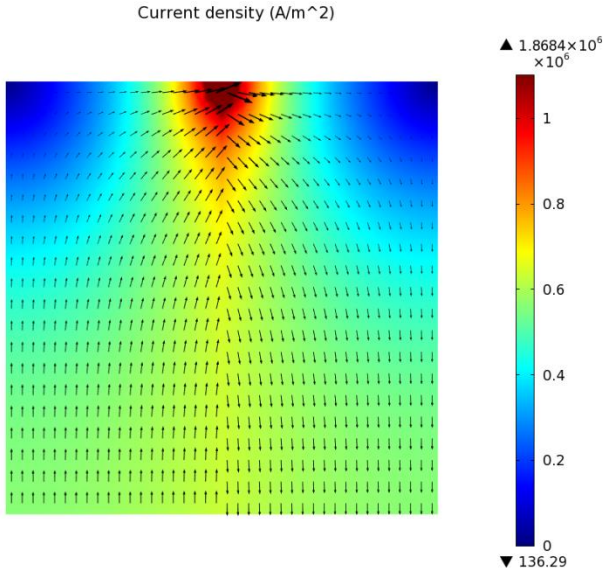

Figure 4.6 2D Current density distribution (grounded bottom)

From the above result we can see that the electrostatic module in COMSOL has no problem to solve the extra source term in Ohm's equation. And due to the way COMSOL works the temperature in the source term will automatically update after every iteration. On the other hand the results from this study reveal that the current is parallel with the stainless steel interface and the grounding affects the distribution of the thermoelectric current flow path close to the boundary.

4.1.2 General equations and boundary conditions

The general equations to describe the TEMHD driven flow have been presented in chapter 2 and they are listed here again.

$$\nabla \cdot \vec{u} = 0 \tag{4.3}$$

$$\rho\left(\frac{\partial \vec{u}}{\partial t} + \vec{u} \cdot \nabla \vec{u}\right) = -\nabla P + \mu \nabla^2 \vec{u} + \vec{j} \times \vec{B} \tag{4.4}$$

$$\rho C_P\left(\frac{\partial T}{\partial t} + \vec{u} \cdot \nabla T\right) = \nabla \cdot (k \nabla T) \tag{4.5}$$

$$\vec{j} = \sigma\left(-\nabla \varphi + \vec{u} \times \vec{B} - S\nabla T\right) \;\&\; \nabla \cdot \vec{j} = 0 \tag{4.6}$$

Generally speaking the added thermoelectric term in the Ohm's equation couples the heat transfer equation to the rest of equations so that the heat transfer equation has to been solved together with others, which means fluid flow module, electrostatic module and heat transfer module are used in COMSOL. However in some cases the temperature gradient does not change with the flow and then the heat transfer equation is decoupled.

The periodicity of the design suggests us to focus on one trench in the analysis. And this requires the simulation to use periodic or symmetric boundary conditions on some boundaries. The surface of the lithium channel needs free surface boundary condition, which requires the material derivative of the pressure equal zero, and for simplicity the zero shear stress boundary condition is actually used to represent the lithium surface. Surface tension, changing density and viscosity are not included in the model.

4.2 Two-dimensional model of the TEMHD driven flow in infinite long trench

4.2.1 Reduced equations

In the last section the thermoelectric effect is successfully incorporated into the Ohm's equation and the current distribution can be solved with a given temperature distribution. In this section a 2D model will be simulated to solve the Li flow in an infinite long narrow trench with steady state uniform heat flux from the top surface. In this model lithium flows between two stainless steel

plates. The top surface of the lithium has rigid-lid assumption which assumes that the shear stress is zero and the bottom contacts the wall. A 1T magnetic field exists along the x direction. On the top surface there is an incoming heat flux along the y direction. The pressure gradient is neglected. The simulation domain is presented in Figure 4.7. The lithium is expected to flow along the z direction which is flowing out of the page in Figure 4.7.

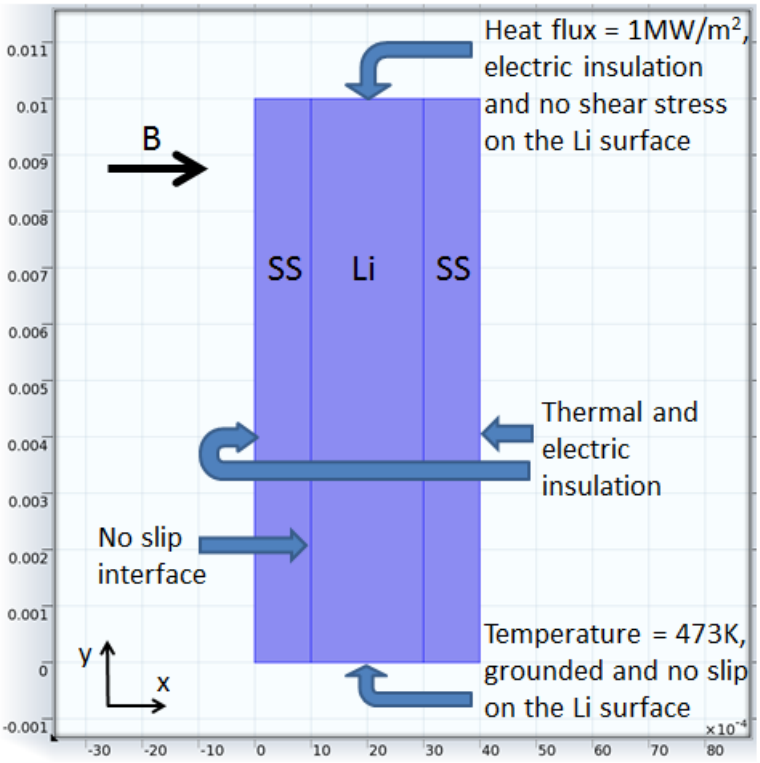

Figure 4.7 Simulation domain of the 2D trench flow modeling and corresponding boundary conditions

Under these given conditions the equations can be simplified to 2D. Because the heat flux is uniform and the trench is infinite long the gradient of velocity and temperature along z direction becomes zero. As a result the thermoelectric current along z direction is zero. In addition the magnetic field is along the x direction which leads to the driven force along the x and y direction to be zero. In this case the velocity only has the z component left. To conclude the velocity only has the z component while the temperature and electric potential distribution are on x-y plane. Previous equations can be reduced to

$$\mu\left(\frac{\partial^2 u_z}{\partial x^2}+\frac{\partial^2 u_z}{\partial y^2}\right)-BJ_y=0 \tag{4.7}$$

$$\frac{\partial^2 T}{\partial x^2}+\frac{\partial^2 T}{\partial y^2}=0 \tag{4.8}$$

$$J_x=\sigma\left(-\frac{\partial \varphi}{\partial x}-S\frac{\partial T}{\partial x}\right) \tag{4.9}$$

$$J_y=\sigma\left(-\frac{\partial \varphi}{\partial y}+u_z B-S\frac{\partial T}{\partial y}\right) \tag{4.10}$$

$$\frac{\partial J_x}{\partial x}+\frac{\partial J_y}{\partial y}=0 \tag{4.11}$$

Now these equations can be solved in the domain in Figure 4.7. All the boundary conditions are also stated in Figure 4.7. The height of stainless steel wall and lithium channel is 1cm. The width of the lithium part is 2mm and the width of each stainless steel wall is 1mm. In Figure 4.7the unit of the coordinate is meter, which is defined by the software. The top surface of the lithium and stainless steel is electric insulated. A uniform heat flux of 1MW/m^2 is deposited on the top surface. No shear stress boundary condition is applied to the liquid lithium surface. Since the lithium is assumed to touch a wall at the bottom no-slip boundary condition is used here. At the interface between the lithium and the stainless steel no-slip boundary condition is used. At the outer surfaces of the stainless steel wall both thermal and electric insulation boundary conditions are used. The bottom surface is set to 473K and grounded.

Because of the free surface one concern is if the surface tension needs to be taken into consideration. Generally speak the free surface affects the top surface boundary condition in two ways. The surface may curve towards one direction so that the surface tension can provide a normal stress which balances with the normal stress at the top surface. On the other hand the tangential stress has to balance the gradient of the surface tension, which comes from the Marangoni effect [64]. For the normal stress term the ratio between the surface tension force and the TEMHD force can be calculated by $\frac{\Sigma}{\sigma SB\nabla Tah}=0.017$, which uses the parameters given in the above problem. So the normal stress provided by the surface tension is very small compared to the TEMHD force and the surface tension may not be able to maintain the surface stable. If the experiment conditions in Figure 3.31 is plug into the above calculation it will give 1.35, which means the surface will not bend too much because of the TEMHD. However the free surface also means that the height of the lithium inside the channels will change to maintain the normal stress to be zero and this effect

needs to be taken into consideration in the future. On the other hand Jaworski has proved that when the Hartmann number is larger than 1, the TEMHD is dominant compared to the Marangoni effect [65]. In conclusion the tangential stress can be assumed to be zero and the velocity normal on the top surface also needs to be zero.

4.2.2 Simulation results

It can be seen that the heat transfer equation is decoupled with the change of the flow. First the heat transfer equation is solved within the entire domain to get the temperature distribution which is plotted in Figure 4.8(a). After the temperature distribution is calculated the Navier-Stokes equation and the Poisson equation will be solved simultaneously to get the velocity distribution which is plotted in Figure 4.8(b). In the software the thermoelectric effect is incorporated into the Poisson equation in the same way as the previous section.

In Figure 4.8(b) we can see that most part of the liquid lithium has a uniform velocity distribution, which agrees with the classic pressure driven MHD duct flow as Hunt has demonstrated [45]. Velocity drops to zero in a very short distance close to the side wall. The velocity varies close to the top and bottom surface.

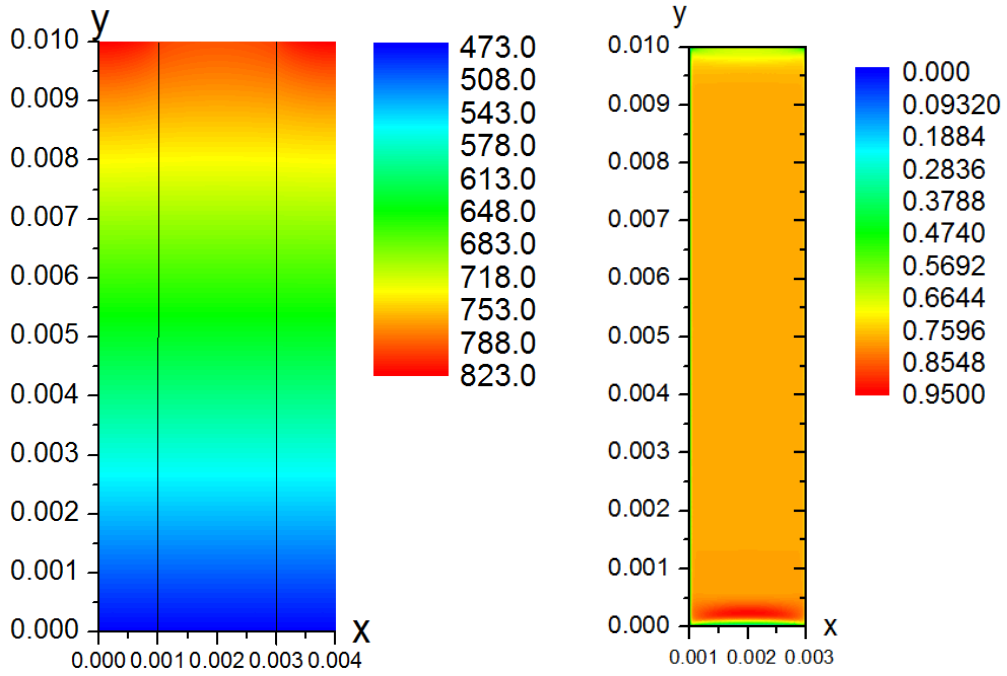

Figure 4.8 (a) Temperature distribution (unit:K) from the heat conduction equation (left figure), (b) z-component of the velocity (unit: m/s) distribution from the model (right figure)

The velocity distributions along x direction at different y values (y=0.0001m, 0.0003m, 0.005m, 0.0095m, 0.01m) are plotted in Figure 4.9. The shape of the velocity profiles at these locations all look typical velocity profile for MHD flow. The velocity profile predicted by the theoretical model in chapter two is also plotted in Figure 4.9as the orange line. Recall that one assumption of the theoretical calculation is the height of the trench needs to be much larger than the width. Since the width of the lithium part is much smaller than the height this theoretical result actually gives a good approximation to this problem. The theoretically predicted result is very close to the simulated velocity distribution at y=0.005m, which is at the middle of the lithium trench.

On the other hand the velocity distribution along the center vertical line of the lithium channel which is plotted in Figure 4.10 seems interesting. In Figure 4.10 the velocity increases to a peak value close to one edge and keeps at a certain value for most of the area. Close to the free surface the velocity actually drops a bit. Close to the bottom surface which is parallel with the magnetic field and the flow direction, the MHD current start to drop because it starts to flow into the side wall to form the current loop while the thermoelectric current generated at the lithium-stainless steel interface extends further into the stainless steel part. In this case within a distance to the

bottom interface the TE driving becomes higher than the MHD damping. This is the reason that the velocity increases close to the bottom interface. However since the no slip boundary condition is applied at the boundary the velocity has to drop to zero from the peak value close to the edge. On top surface the current profile is different. Since the top surface is insulated a large portion of the current including the TE driving and MHD damping has to turn direction to become parallel with the insulated surface, which is also in parallel with the magnetic field. As a result the velocity close to the surface actually drops.

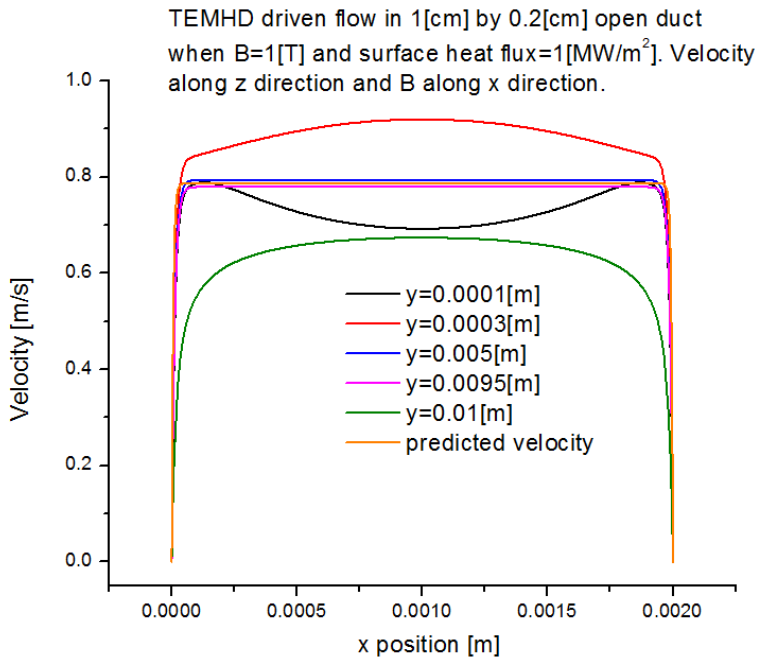

Figure 4.9 Calculated velocity distribution along the x direction at different y positions and the theoretical solution

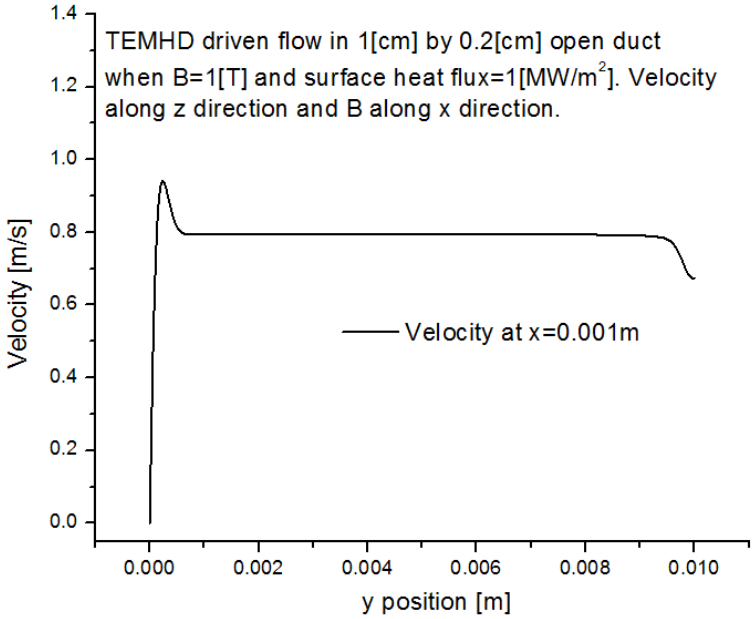

Figure 4.10 Calculated velocity distribution along the vertical central line of the lithium channel

In all this method to simulate the thermoelectric effect is validated by this 2D model with a given temperature distribution. However when the heat flux in reality is not uniform the heat transfer equation cannot be simply decoupled which requires the heat convection along the flow direction in the simulation. As a result 3D model is needed and all the equations in section 4.1.2 have to be calculated simultaneously.

4.2.3 Lithium flow in overfilled trench

When LiMIT is used as divertor target plate the liquid lithium will always need to be overfilled to protect the top of the solid structure from the direct impinging of the plasma. In this section the 2D model is utilized to analyze this situation. In order to do this the domain is revised to Figure 4.11. Lithium now is 1mm higher than the stainless steel wall. Other boundary conditions keep the same. The magnetic field is still 1T. The side of the overfilled part is set to symmetric boundary.

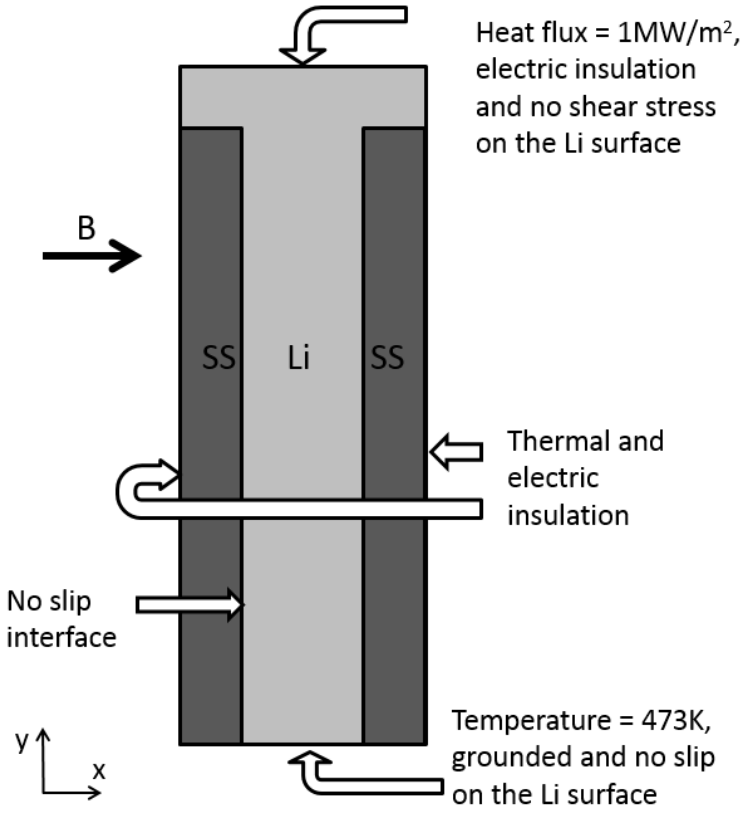

Figure 4.11 1mm overfilled lithium with stainless steel trench.

Follow the same procedure in last section the temperature profile is firstly solved in figure 4.12(a) and then the velocity profile can solved and presented in figure 4.12(b). In figure 4.12(a) we can see that the temperature profile is similar to Figure 4.8(a). After all only heat conduction is calculated through the trench. However the velocity profile looks quite different from Figure 4.8(b) especially at the overfilled region. For most area inside the trench the flow velocity stays the same. However close to the open area of the trench the velocity is higher than the bulk velocity of the trench part while on the other hand the velocity close to the open area in Figure 4.8(b) is lower than the bulk velocity. What is more the velocity profile looks quite uniform in the overfilled region and the value is not very small although it is expected that the TE current in the overfilled region diminishes and the MHD damping still exists. When lithium is overfilled the TE driving inside the trench region is able to drive the overfilled region to flow at a decent velocity.

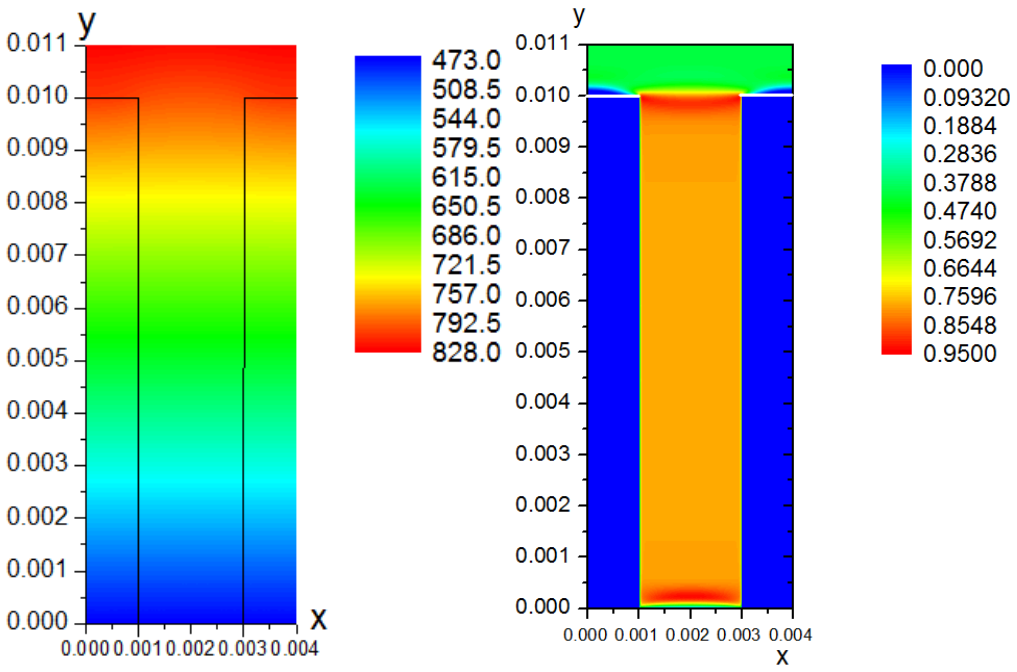

Figure 4.12 (a) Temperature distribution (unit:K) from the heat conduction equation in the overfilled situation (left figure), (b) z-component of the velocity (unit: m/s) distribution from the model in the overfilled situation(right figure)

To inspect the detail similar to the last section the velocity curves along x direction at different y values and the velocity along y direction at the center line of the trench are plotted in Figure 4.13 and Figure 4.14. In Figure 4.13 we can see that the velocity profile along x direction stays the same for most y values. The overfilled region cannot affect the flow in most area of the trench. However close to y=0.01m where the lithium in the trench region joins the overfilled region the velocity becomes higher than the value in Figure 4.9. In addition the velocity starts to have an M-shape which indicates that the high current concentration close to the top left and top right corner of the trench region becomes not aligned with the magnetic field. This is actually beneficial for the protection of the top of the solid wall because higher flow rate close to the corner of the wall may lower the local temperature. The surface velocity however is only around half of the bulk velocity but the surface velocity profile is quite flat. If this can be kept all the time the uniform velocity can keep the surface replenished at a relatively same speed.

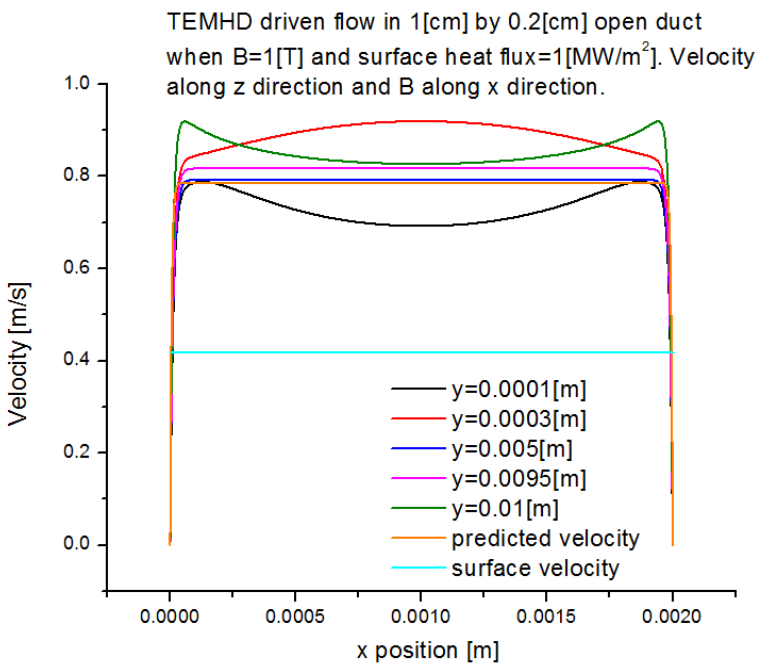

Figure 4.13 Calculated velocity distribution along the x direction at different y positions and the theoretical solution in the overfilled situation. The surface velocity profile is also included.

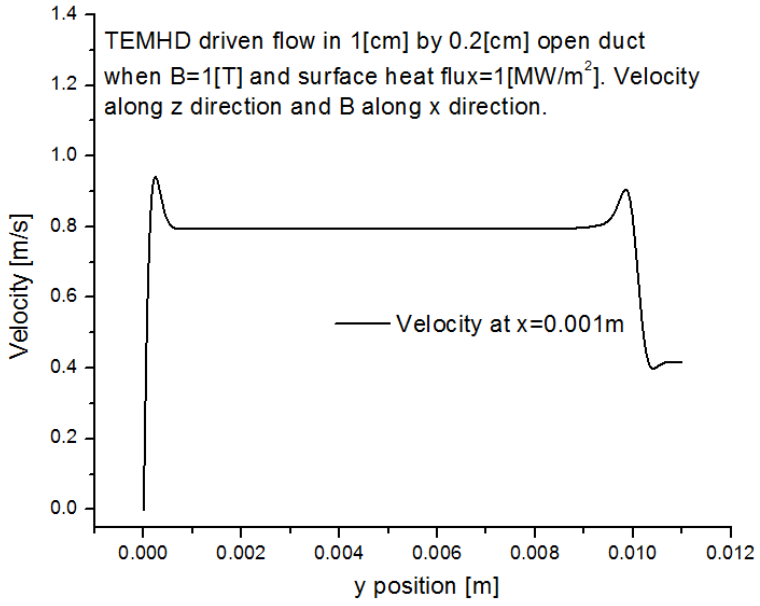

Figure 4.14 Calculated velocity distribution along the vertical central line of the lithium channel in the overfilled situation

In Figure 4.14 the velocity along y direction is different from the curve in Figure 4.10 on the right side. The velocity peaks again at where the trench region joins the overfilled region. In Figure 4.10 the current is forced to flow along x direction, which is the direction of the magnetic field, close to the top of the trench because of the boundary condition, which leads to the drop of the velocity. However in Figure 4.14 the current starts to be able to flow through the joint area between the trench region and the overfilled region and this becomes similar to a conducting boundary condition which is on the left side. This is the reason that the velocity peaks the similar way to the left side. However in the overfilled region the current is still forced by the insulated boundary condition to flow along x direction. And this leads to the drop of the velocity in the overfilled region similar to the drop on the right side in Figure 4.10.

In general the fact that the velocity of the overfilled part does not drop dramatically is very important to maintain a necessary surface velocity in fusion reactors. On the other hand the confinement from the capillary force in the overfilled region drops greatly which makes it vulnerable to the transient event in the fusion reactors. And this problem needs to be addressed in the future research work.

4.3 Three-dimensional model for LiMIT concept

4.3.1 Model establishment and validation

In order to simulate the TEMHD driven lithium flow in open surface trench when the heat flux is not uniform a three-dimensional model is built in COMSOL in the similar way as the previous section. This model is firstly verified by a uniform temperature profile as the boundary condition to compare with the theoretical calculation and it is plotted in Figure 4.15. Only half of the trench is included here to save the simulation time.

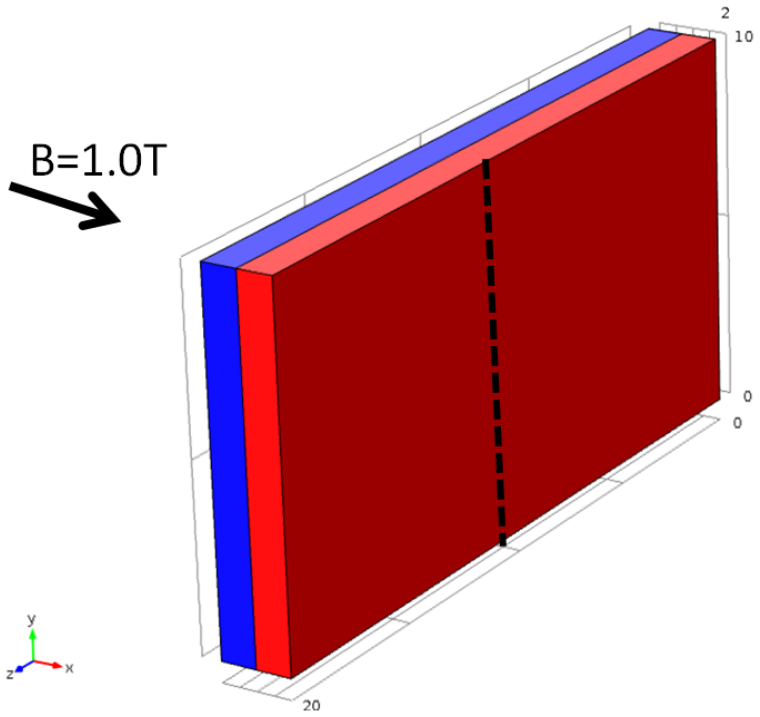

Figure 4.15 Simulation domain of the 3D trench flow modeling

The liquid lithium trench is 1 (x direction) by 10 (y direction) by 20 (z direction) mm facing a solid stainless steel wall of the same size. The red block is lithium and the blue block is stainless steel. The top surface uses a slip wall boundary condition, and constant temperature at 573K. The bottom surface is a no-slip boundary at uniform temperature of 473K. The external sides of the liquid part and of the solid part use symmetric boundary conditions. The inlet and the outlet use the periodic boundary conditions, to mimic the infinite-long trench. A transverse magnetic field of 1 T is set parallel to *x*. The density, thermal conductivity, electric conductivity, viscosity are assumed to be constants. The position of the grounded electrode is chosen to be at the edge.

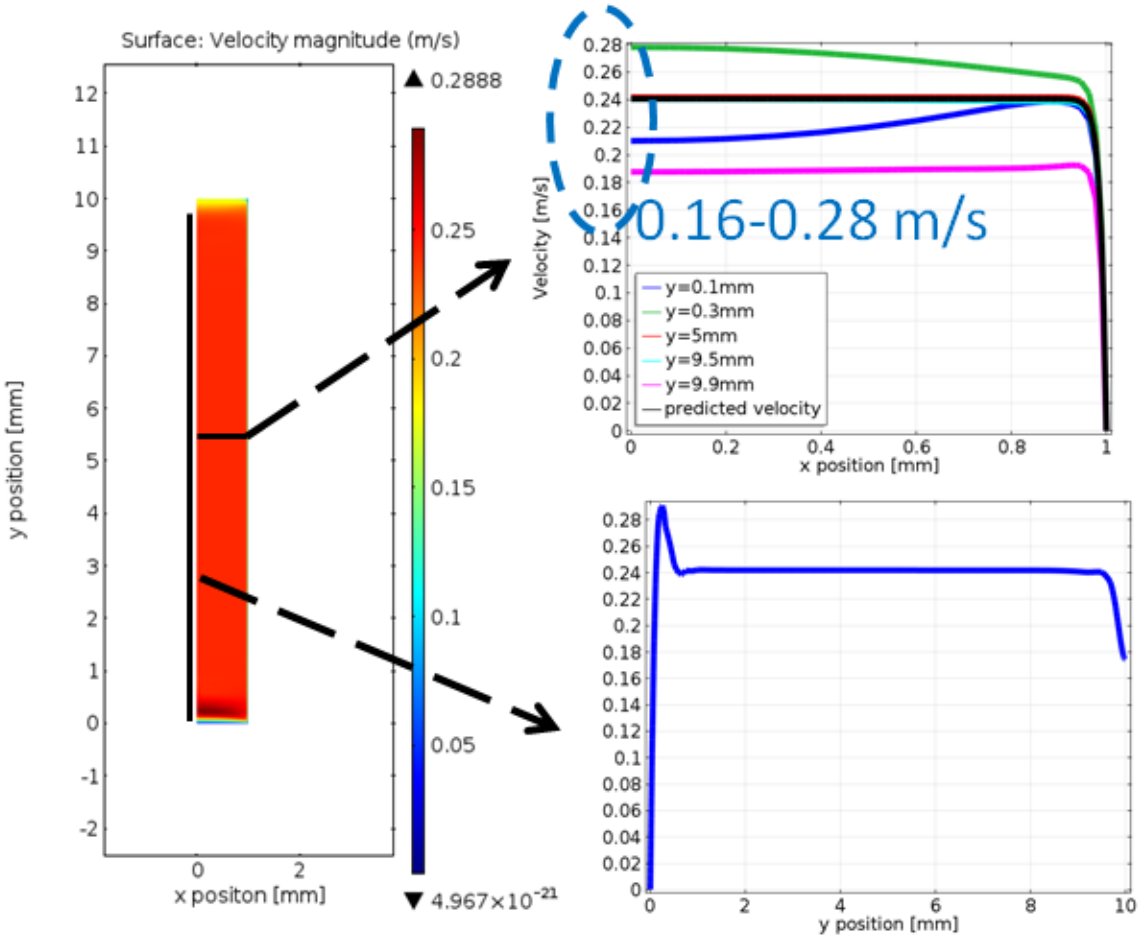

Figure 4.16 Validation tests of the TEMHD flow on an infinite rectangular trench with an open surface. Left: magnitude of the flow velocity on a section of the trench. Top Right: velocity profile along x direction at several y positions, and comparison with the theoretical result from [35]. Bottom Right: flow velocity along the y direction.

Figure 4.16 shows our simulation results. The results are compared to the analytical result from Shercliff's model. As expected, the velocity at the center of the channel are the same as results predicted by Shercliff (see the overlapping black and red lines in the top right figure). This can validate the simulation of the velocity. It also shows that the value close to the boundaries departs from Shercliff's solution. The velocity along the *y* direction has a peak value close to the bottom wall and decreases close to the top surface. This is reasonable, and is due to the three-dimensionality of the current density profile. In fact, near the top surface the current becomes parallel to the top surface and to the magnetic field, so the Lorentz force becomes weaker there.

On the other hand the heat transfer part of the model only has the conduction and the convection terms. In this case the convection part is should be zero since the temperature on the top surface and the bottom surface is uniform and the periodic boundary condition is applied on the inlet and the outlet. Ideally this will give a linear temperature profile from top to the bottom. This can be demonstrated in Figure 4.17.

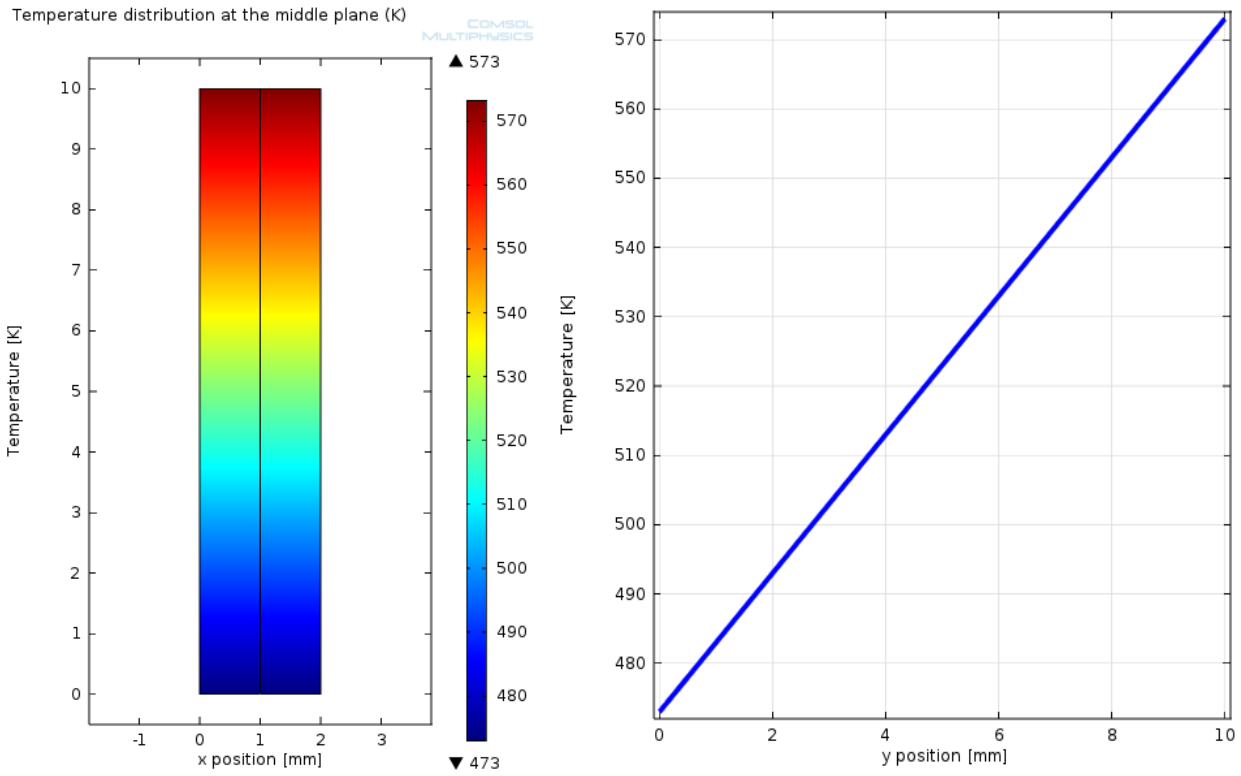

Figure 4.17 Temperature distribution in the 3D validation test. Left: the temperature distribution on the x-y plane at z=50mm location. Right: the temperature profile along the y direction at x=0mm and z=50mm.

4.3.2 3D model of the TEMHD driven flow in open surface trench

Since the 3D model works fine with a fixed temperature gradient the model is revised so that the heating on the top surface is not uniform. The lithium trench in the above section is elongated to be 1 (x direction) by 10 (y direction) by 100 (z direction) mm facing a solid stainless steel wall of the same size. The blue block is lithium and the red block is stainless steel.

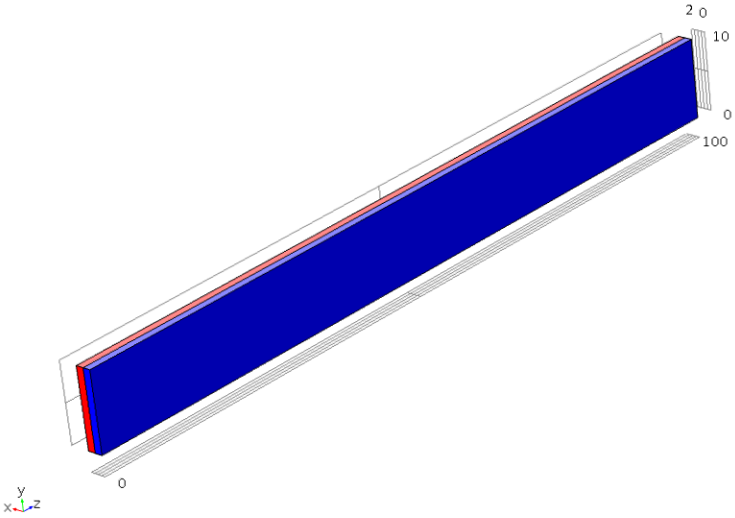

Figure 4.18 Simulation domain of TEMHD driven lithium flow in open trench when the heating is non-uniform

All the boundary conditions are the same except that the inlet and the outlet are changed to open boundary conditions and the heating on the top is changed to a non-uniform heat flux. In this equation the heat flux is a Gaussian shape and q_0 is the peak heat flux at the center. The unit of distance z along the trench direction is meter. When there is no flow and $q_0 = 1[MW/m^2]$ the temperature distribution from this heat flux is plotted in Figure 4.19. This heat flux is similar to what the e-beam generates in experiments.

$$\mathrm{q} = \mathrm{q}_0 \exp\left(-\frac{(\mathrm{z}-0.05)^2}{(0.005)^2}\right) \tag{4.12}$$

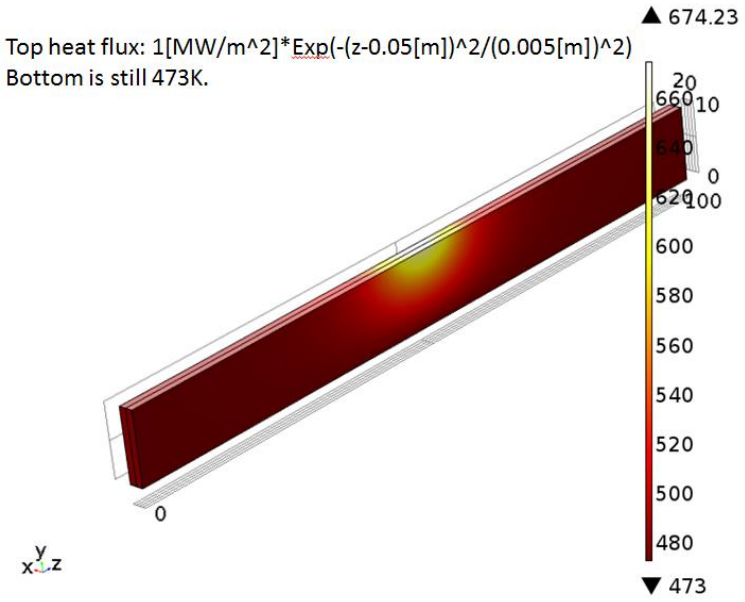

Figure 4.19 Temperature (unit: K) distribution when there is no flow

Now if the magnetic field is 0.05T the 3D model can be solved to find out the velocity and temperature distribution due the influence of the TEMHD driven flow. The velocity vector field of the x=0 plane, where the symmetric boundary condition is used for the lithium trench is plotted in Figure 4.20. From the figure we can see that lithium flows from left to right. On the upstream side the velocity field is very uniform while right after the heating area it accelerates a lot and start to change the direction, which leads to a non-uniform flow velocity distribution on the downstream side. This actually matches the acceleration of lithium flow across the direct heat area in the experiment. Figure 4.21 is the contour plot of the absolute value of flow velocity and similar to Figure 4.20 the accelerated area is clear in this figure.

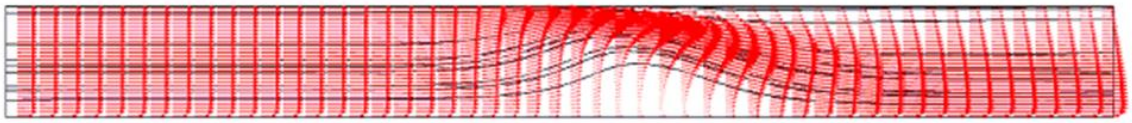

Figure 4.20 Velocity vector field in the trench of the y-z plane at x=0

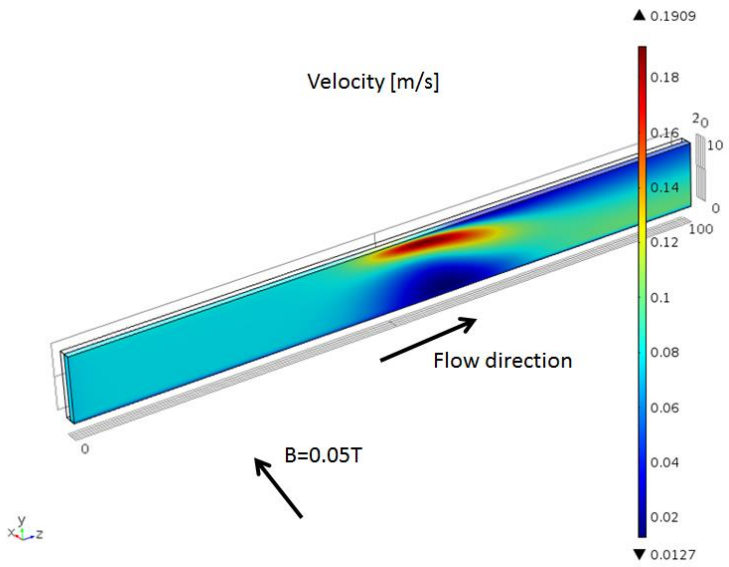

Figure 4.21 Velocity contour of the 3D model with non-uniform heating

To look at the detail of this accelerated area the velocity contour of the x-y cross section at z=50mm and the electric current stream line at z=50mm are plotted in Figure 4.22. In this figure the accelerated region is close to the top where the temperature gradient is at maximum and the highest point is close to the interface between lithium and stainless steel. This is because the thermoelectric current comes from the difference of the thermoelectric coefficient which happens at the material interface. Since the thermal conductivity of stainless steel is smaller than lithium the temperature gradient in the stainless steel wall is higher. The current stream line also matches this. On the other hand the top surface velocity of the lithium trench is lower than the accelerated region. This is because close to the top current starts to flow in parallel with the top surface which is in parallel with the magnetic field. As a result although the current there might be stronger the Lorentz force, which is the cross product between the current and the magnetic field, is smaller.

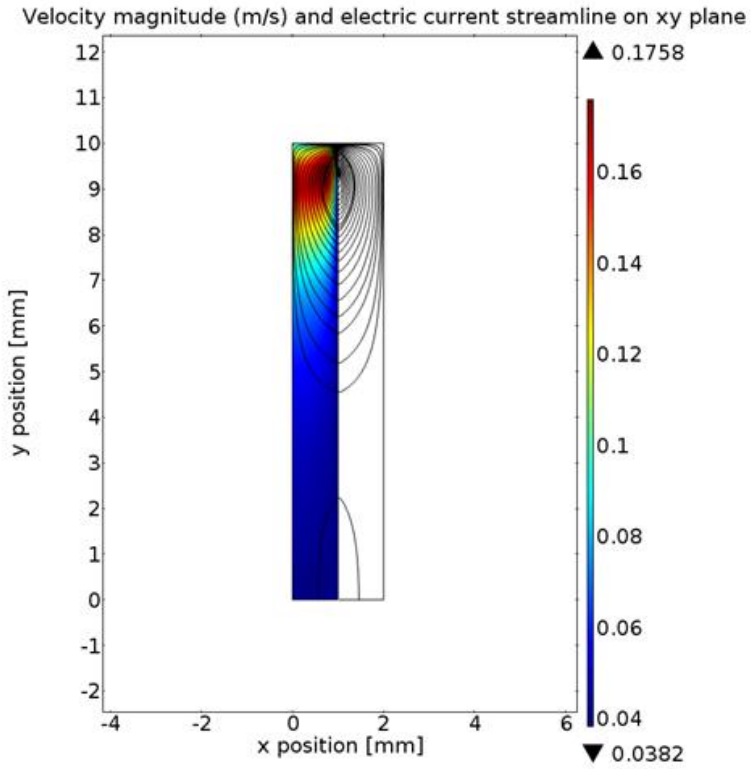

Figure 4.22 Velocity contour of the x-y cross section at z=50mm and electric current stream line at z=50mm

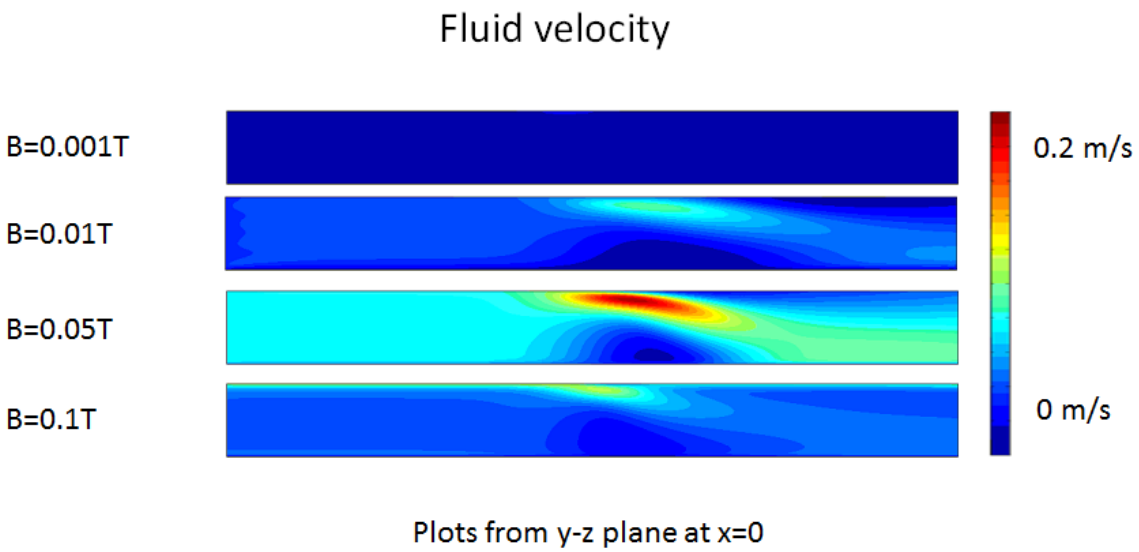

Figure 4.23 Velocity contour of y-z plane at x=0 for different magnetic fields

If other conditions are kept the same and the magnetic field is changed from 0.001T to 0.1T it is expected the average velocity increases first and then decrease according to the analysis in Figure 2.7. However when the heating is not uniform the change of the velocity needs to be investigated. This is modelled and presented in Figure 4.23. It can be seen that the velocity profile is obviously not uniform. The highest value of the velocity is close to the center on the downstream side since that is where the highest temperature gradient is. When the magnetic field increases the velocity becomes higher and higher. However after some point the velocity also drops similar to the theoretical calculation in Figure 2.7. It seems that not only the peak velocity drops, the average velocity also drops. In addition the shape and the position of the high velocity region also changes with the magnetic field. This is due to the convection of the heat that leads to the change of the temperature gradient distribution, which can be seen in the next figure.

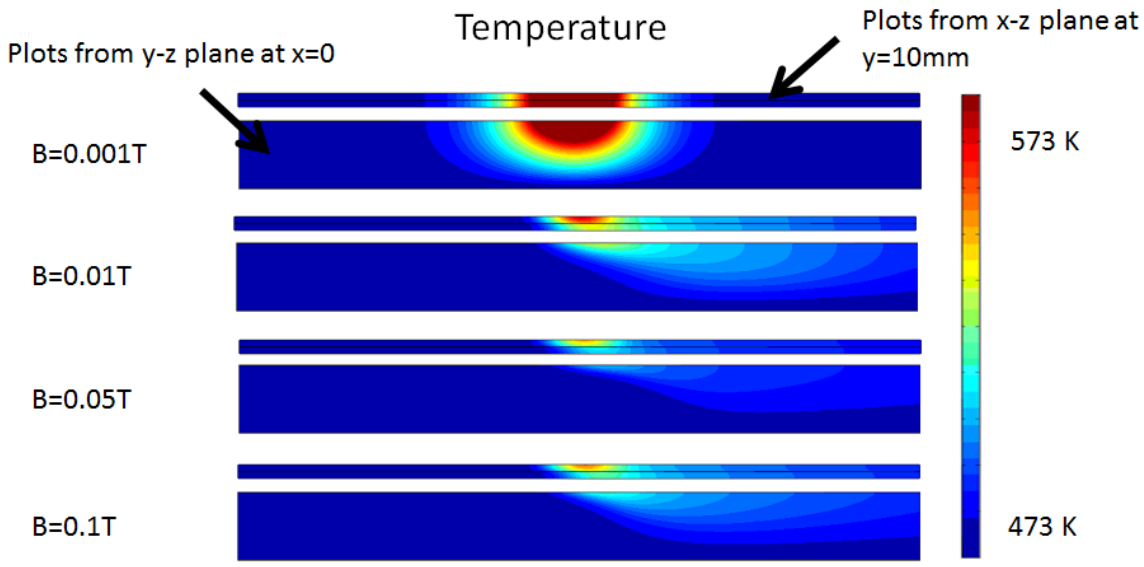

Figure 4.24 Temperature distribution of y-z plane at x=0 and x-z plane at y=10mm for different magnetic fields

The temperature distributions for each case are also compared in Figure 4.24. The temperature distribution of y-z plane at x=0 and x-z plane at y=10mm are all plotted to provide a top view and side view of the temperature distribution. When the magnetic field is very small the velocity is also very low and the temperature distribution is similar to the case without any flow in Figure 4.24. When the magnetic field starts to increase the velocity also increases to bring the heat to the

downstream side. The faster it flows the lower the temperature is. However after a certain point the flow velocity starts to drop and the temperature on the downstream side starts to rise.

4.3.3 LiMIT trenches with return flow

In reality the LiMIT concept needs the return flow for the lithium to flow back from the outlet to the inlet. In order to incorporate the return flow a three-dimensional slice of the LiMIT system has been analyzed using the 3D model described in this section. The periodicity of the system suggests the most convenient simulation domain, reported in Figure 4.25. In the figure, the liquid lithium is represented in blue, the solid metal (stainless steel) in red. The domain includes one trench, half of the stainless steel walls, the four cooling channels, and the surrounding structure. The lithium trench is 2mm by 5mm by 80mm. The total length of the lithium channel, comprising the side channels, is 90 mm. The width of the steel wall is 0.5 mm and only half of the wall is simulated on each side. The top surface of lithium is a slip-wall boundary condition and the side faces of the stainless steel use symmetric boundary conditions. The entire lithium-stainless steel interface uses no-slip boundary condition. The bottom of the whole trench is electrically grounded and other sides are electrically insulated. The top surface receives a Gaussian heat flux. The other three surfaces are thermally insulated. The heat flux is similar to equation 4.12 which heats the top surface of the lithium and the steel part,

$$q = q_0 \exp\left(-\frac{(z-0.045)^2}{(0.005)^2}\right) \tag{4.13}$$

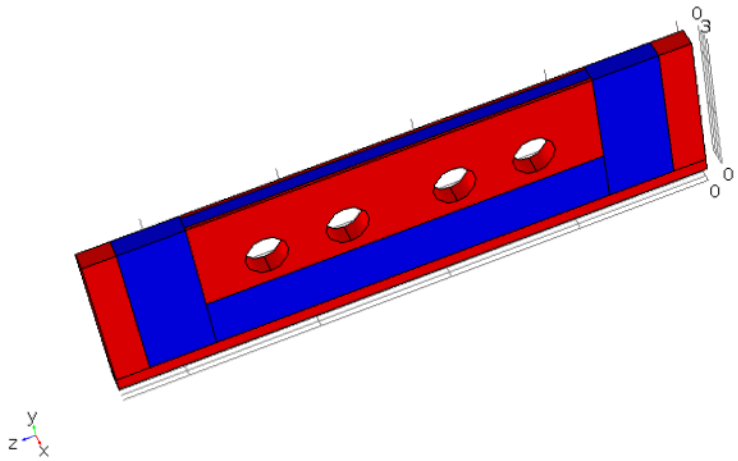

Figure 4.25 Simulation domain, comprising the liquid lithium (blue) and the solid metal (red). The domain includes one trench, half of the metal walls, the four cooling channels, and the surrounding metal structure.

The peak heat flux q0 is parametrically varied. The heat is exhausted into the four cooling channels, having a local heat transfer coefficient h which will be varied later for parametric study. In most of this study the local heat transfer coefficient is assumed equal to h=500 W/(m^2 K). This value has been estimated for gas cooling channels. This value is also parametrically from 500 to 40000 W/m2K. The coolant temperature is set to be 293 K, which will also be varied later to study the influence of the cooling efficiency.

Figure 4.26~ Figure 4.28 present an example of the calculation, obtained for a peak heat flux of q_0=1.0MW/m^2, B=0.1T, h=500 W/(m^2 K), and trenches of 5 mm height. Figure 4.26 plots the magnitude of the fluid velocity of y-z plane at the center of the trench which is x=1.5mm. The liquid lithium flows counterclockwise in this figure. The velocity peaks on the downstream side of the heated area. This high velocity region is close to the surface and extends into the bulk of the fluid. This is similar to the result from the previous section without the return flow. In the return flow channels the velocity is smaller. A higher velocity region is close to the interface since this is the side wall for the MHD damping in the return flow channel and extra TEMHD driven force is expected since a temperature gradient exists here.

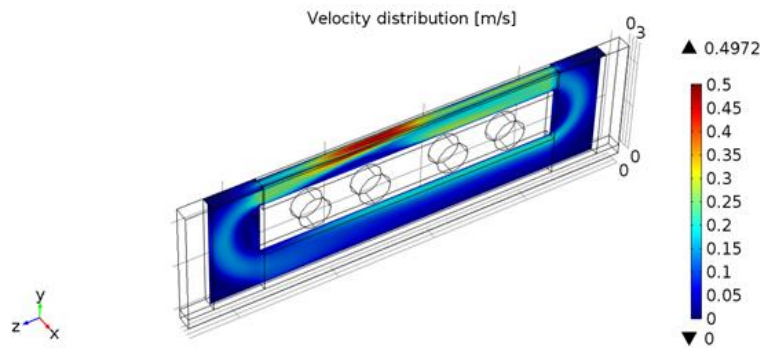

Figure 4.26 Flow velocity contour of the y-z plane at x=1.5mm

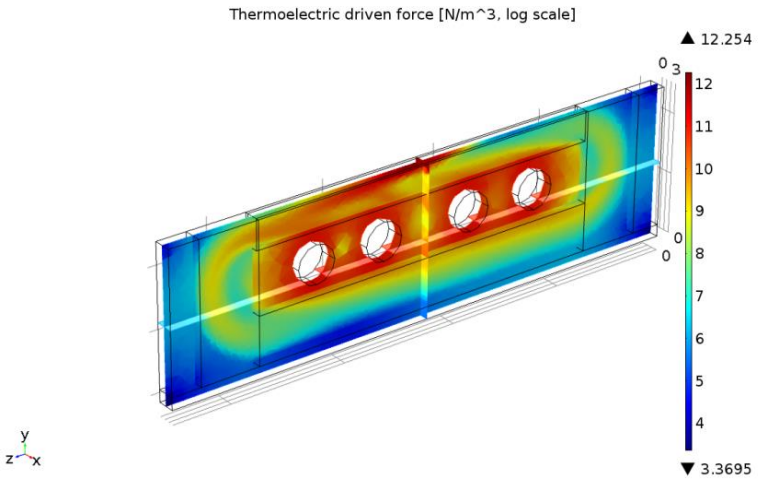

Figure 4.27 TE driven force contour of the y-z plane at x=1.5mm

Figure 4.27 is the contour of the thermoelectric force. The thermoelectric JxB force propels the liquid lithium into the channels. The highest thermoelectric force is close to the Li-SS interface, right under the direct heating region. The region of lithium acceleration extends downstream, as long as the temperature gradient is established at the interface between lithium and stainless steel. A small thermoelectric force is observed also in the return channel at the bottom which agrees with the higher velocity region in the velocity contour. Most of the force there is observed at the interface between the two metals. The cooling effect at the interface between the lithium and the wall in proximity of the cooling channels generates a high temperature gradient close to this interface, which in turn produces acceleration. However, most of the acceleration comes from the direct heating on the top surface and some acceleration exists close to the heat exchange interface between the liquid and the solid parts.

Figure 4.28 is the temperature field, showing the convective heat transport due to the lithium flow. Heat is brought to the downstream side and all the way into the return flow channel through which lithium is cooled before it enters the inlet again.

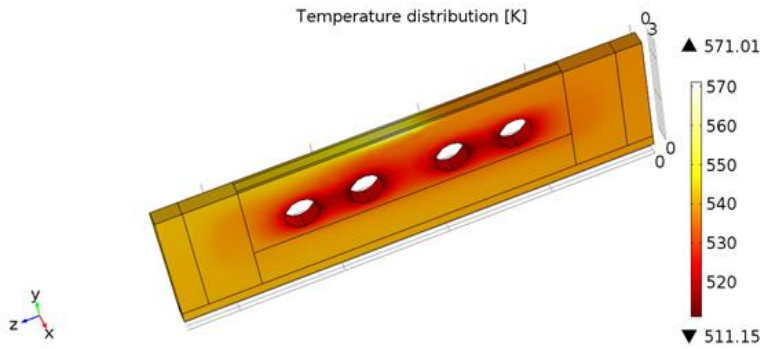

Figure 4.28 Temperature distribution of the trench

In the following sections, we perform parametric studies to investigate the influence of some parameters of interest on the performance of LiMIT at steady state. The success of this concept requires a reasonable speed of the lithium flow (at least few mm's per second) even in the fusion-relevant magnetic fields, and a maximum surface temperature of the liquid lithium below <550 ℃, or 823K, to maintain lithium vapor pressure reasonably low. Our parametric study has been done by varying those parameters that most greatly affect the lithium flow and the heat transfer: magnitude of the magnetic field, peak heat flux, trench height, and heat transfer coefficient. The influence of each parameter will be highlighted in the following sections, in order to characterize the trends and identify possible operating ranges. The heat-flux wetter length, although very important, has a similar effect as the peak heat flux: both can change the total power deposition. As a result, this additional parameter can be incorporated in the same trend as the peak heat flux, and it will not be addressed separately. Two scalar variables will be used to present the modeling results: the first is the average lithium velocity in the top trench; the second is the maximum temperature on the lithium surface. The former gives an indication on how fast the top channel can be replenished of lithium. The latter is an important factor to determine the maximum operating range.

The influence of the toroidal magnetic field and the peak heat flux q_0 at the divertor are parametrically investigated in the range B=0.0-2.0 Tesla, and q_0 = 1.0-10 MW/m^2. In these runs,

all the calculations are done for a trench height of 5 mm and heat transfer coefficient h=500 W/(m^{2}K). These parameters will be sub-optimal, but an optimization of the device is not sought at this stage. The figures from Figure 4.29 to Figure 4.35 will present the average lithium velocity in the top trench, and the maximum temperature on the lithium surface, at different magnetic fields and heat fluxes. The results from the 3D simulations (points) are compared to the predictions from the 1D model in chapter two.

Figure 4.29 shows the average lithium velocity vs. the magnetic field, for heat fluxes in the range 1.0-10 MW/m^2. The velocity increases up to a critical field B_{cr}, always below 0.5 Tesla for the heat fluxes of interest. After the critical value, the velocity starts to decrease. In this regime, the increasing MHD drag slows down the motion of the liquid metal. Before the peak, the relation is close to linear, and after the peak the velocity is roughly proportional to a 1/B.

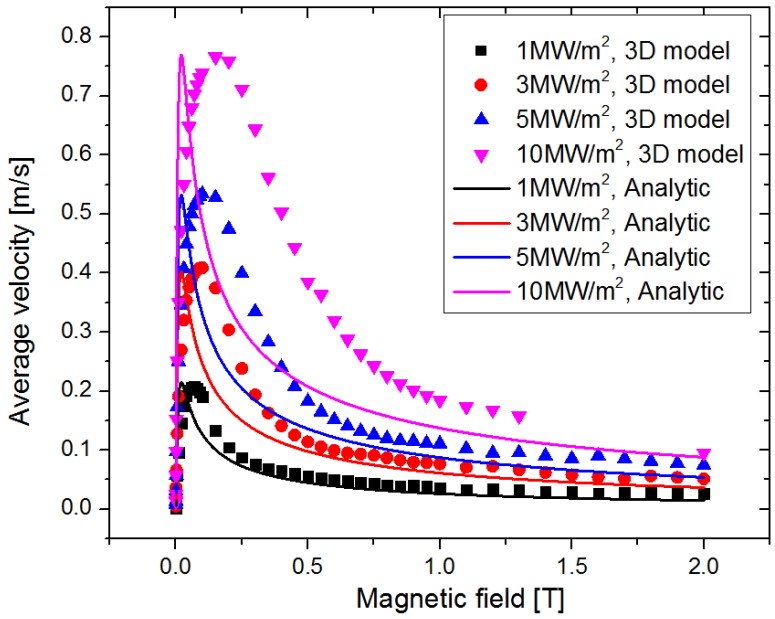

Figure 4.29 Average lithium velocity vs. magnetic field, for different peak heat fluxes in the range 1.0-10 MW/m^2. Simulations are run for heat transfer coefficient h= 500 W/(m^{2}K), and trench height = 5 mm. Each point is the result from a simulation and the curve is the analytical result

The 3D simulations and the 1D model give similar peak velocities and similar trends. However, the critical field B_{cr} is different in the two cases. The 1D model predicts that all the peaks occur at

the same magnetic field, while the 3D model exhibits a dependence of the B_{cr} on the heat flux. The discrepancies between the two models have not been further investigated, but they can be either due to the different dimensionality of the two models or to the different definition in the return flow channels.

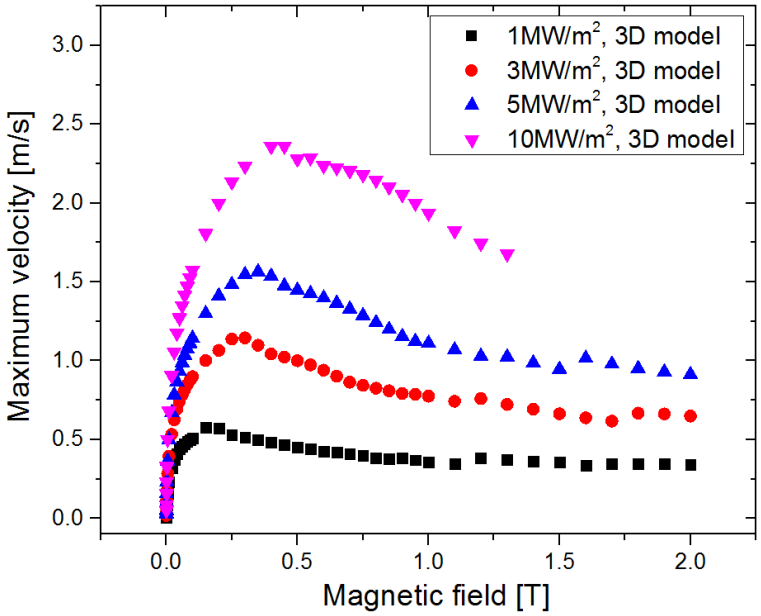

Figure 4.30 Maximum flow velocity vs. magnetic field, for different peak heat fluxes in the range 1.0-10 MW/m^2. Simulations are run for heat transfer coefficient h= 500 W/(m^{2}K), and trench height = 5 mm. Each point is the result from a simulation.

In the meanwhile the maximum value of the magnitude of the flow velocity is also plotted as a function of the magnetic field in Figure 4.30. It can be seen that the change of the maximum velocity is similar to the average velocity which increases first and then decreases after it peaks at a certain value. However the decrease of the maximum velocity is not as fast as the average velocity. Instead, it seems that the maximum velocity changes little when the magnetic field is higher than 1T. In addition the peak value of the maximum velocities at a constant heat flux is 2~3 times higher than the peak value of the average velocities at the same heat flux. The plot of the maximum velocity also peaks at different magnetic field compared to the peak location in Figure 4.29.

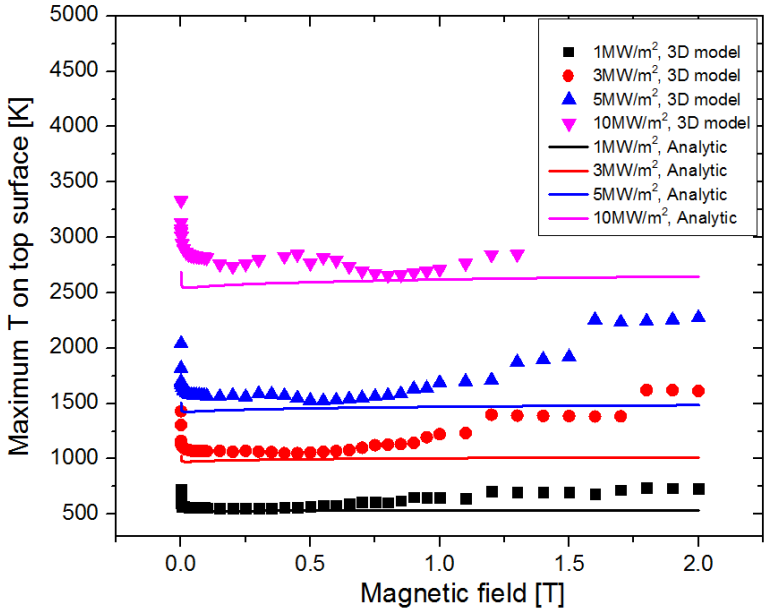

Figure 4.31 Maximum top surface temperature vs. magnetic field, for different peak heat fluxes in the range 1.0-10 MW/m^2. The results from the 3D numerical model (points) are compared to the analytical result (solid lines). Simulations are run for heat transfer coefficient h= 500 W/(m^{2}K), and trench height = 5 mm.

Figure 4.31 plots the maximum temperature on the top surface as a function of the magnetic field. The calculation shows that for this sub-optimal configuration the acceptable range T_{max}<823K is maintained only at moderate heat fluxes, below <3 MW/m^2. But the reason for such high surface temperature is the poor cooling efficiency by compressed air which is not enough to transfer the heat out at steady state and maintain the stainless steel-lithium interface temperature low enough. With a better heat transfer coefficient brought by more efficient coolant or cooling channel design the surface temperature can be greatly reduced, which will be presented in the following parameter study. The results from the 3D simulations are compared to the 1D model, showing good qualitative agreement. However, the trends from the 3D runs are richer in features, also exhibiting changes in the derivative. In the 1D model the temperature of the top surface is assumed to be a single value after the heated area while the 3D model calculates the detailed temperature distribution. It can be expected that also the trend looks similar the temperature increase with the

directly heated region should be more sensitive to the velocity change and the temperature increase of this area should be higher than the average of the whole downstream side surface.

In Figure 4.32 and Figure 4.33 average velocity and the maximum top surface temperature are plotted as the function of the peak heat flux q_0. The results from 3D simulations are similar to the 1D model prediction. Both show the same trend and similar peak values. The average lithium velocity increases with the heat flux, but the relation is less than linear, resembling a square-root law. This may lead to a lower fraction of the convection compared to the conduction when the heat flux is high. On the other hand the top surface temperature increases linearly with the incoming heat flux and the value changes little with the magnetic field. At 3 MW/m^2 the maximum temperature is already over 823K, which is unfeasible for lithium operation in a fusion device. To identify the feasible working regions of LiMIT, the heat transfer coefficient and the trench height are varied to quantify their influence on the design's performance. In the following sections we proceed with a preliminary optimization of the device, characterizing the influence of the heat transfer coefficient of the cooling channel, and of the trench size.

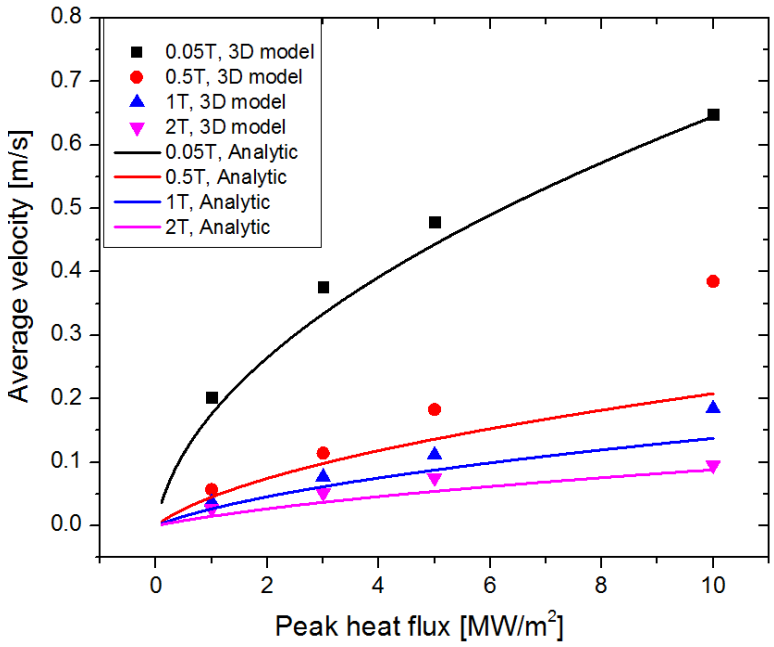

Figure 4.32 Comparison of the average lithium velocity vs. peak heat flux, for magnetic fields in the range 0.05T-2.0T. The results from the 3D numerical model (points) are compared to the analytical result (solid lines). Simulations are run for heat transfer coefficient h= 500 W/(m^{2}K), and trench height = 5 mm.

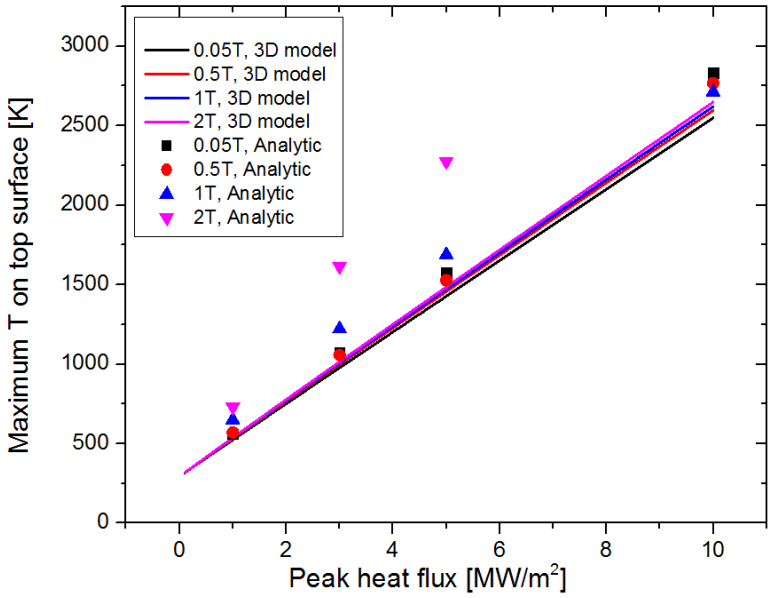

Figure 4.33 Comparison of the maximum top surface temperature vs. peak heat flux, for magnetic fields in the range 0.05T-2.0T. The results from the 3D numerical model (points) are compared to the analytical result (solid lines). Simulations are run for heat transfer coefficient h= 500 W/(m^{2}K), and trench height = 5 mm.

The heat transfer coefficient of the cooling channel is directly related to the technology used to exhaust the heat (gas cooling, Hypervapotron [66], T-tubes [56], etc.). In this study, we assume a fusion relevant condition of B_0=1.0T and peak heat flux q_0=10 MW/m^2. The height of the trench is fixed to 5 mm. Three cooling cases are discussed here. First is h=500 W/(m^{2}K) which corresponds to a normal gas cooling system. The second is h=5000 W/(m^{2}K) which corresponds to water or other liquid cooling. The third is h=40000 W/(m^{2}K) and this value comes from the T-tube cooling concept [16] which has been raised as a cooling method for the divertor target plate. In the first two cases the coolant temperature is 293 K and the coolant temperature of the third case is 453 K which is lithium's melting point to prevent the liquid lithium from solidification.

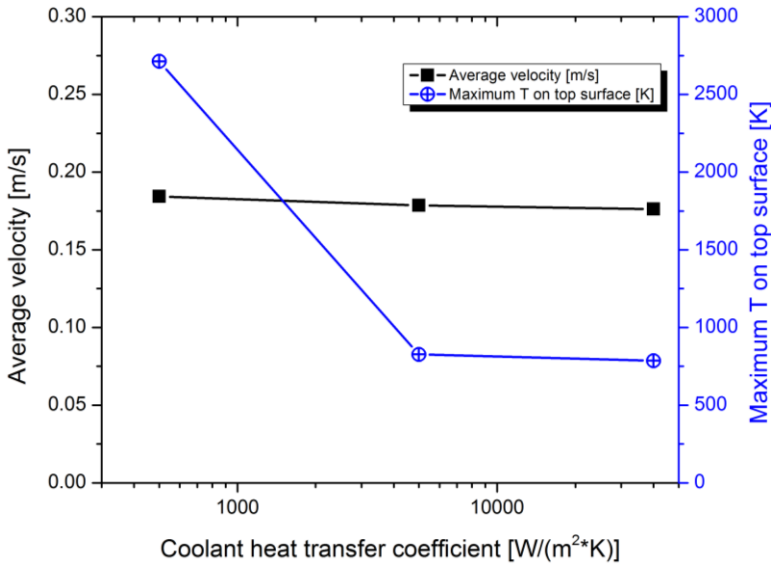

Figure 4.34 Influence of the coolant heat transfer coefficient on the average velocity and maximum surface temperature

The influence of the heat transfer coefficient *h* is reported in Figure 4.34. As expected, the top surface temperature dramatically drops by changing the cooling method. For the last two cases the top surface temperature is around 750 K, within the acceptable range for fusion reactors. This proves the LiMIT trenches are capable of bearing up to 10MW/m^2 heat flux at steady state. The average velocity is only minimally affected, which means that the ability to refresh the lithium is not lowered by increasing the cooling rate. It can be seen that the influence of the coolant heat transfer coefficient reaches plateau after some point. Since then further reducing the thickness between the coolant-stainless steel interface and the lithium-stainless steel interface can further reduce the top surface temperature.

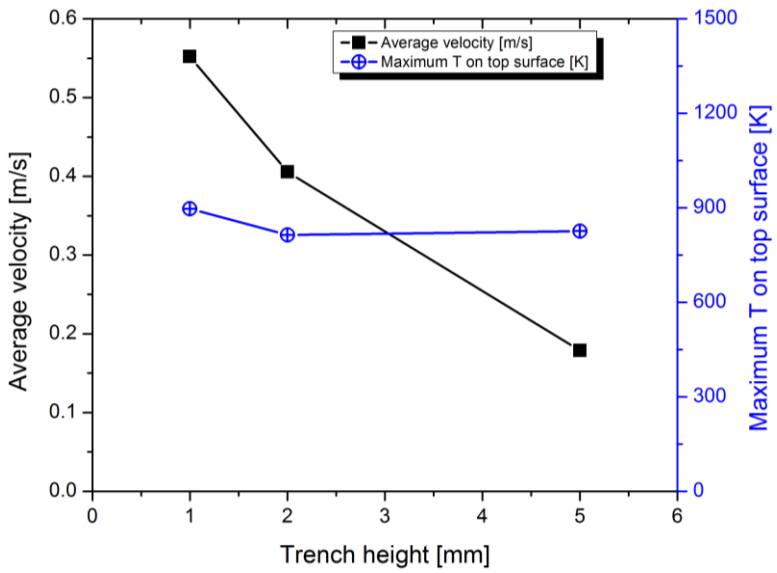

Figure 4.35 Influence of the trench height on the average velocity and maximum surface temperature

Three different trench heights have been investigated, 1 mm, 2 mm, and 5 mm. As in the previous paragraphs, we assume a magnetic field of B_0=1.0T and peak heat flux q_0=10 MW/m^2. The heat transfer coefficient is 5000 W/(m^{2}K). Figure 4.35 reports the results. Varying the trench height has minor effect on the maximum top surface temperature. However, decreasing the trench height greatly increases the lithium flow velocity, which makes the lithium surface refresh faster. Combined with the observations in the heat transfer coefficient study it appears that a higher heat transfer coefficient and a lower trench height might be beneficial to the design of an optimal LiMIT system.

4.4 Comparison with the experiment results

The simulation result is also compared to the experiment results. Note that the experiment values are actually taken in the transient situation so the measurements especially the temperature may differ a lot. Instead the 3D model from the previous section is changed to a time dependent model in COMSOL.

4.4.1 Lithium acceleration in the trench

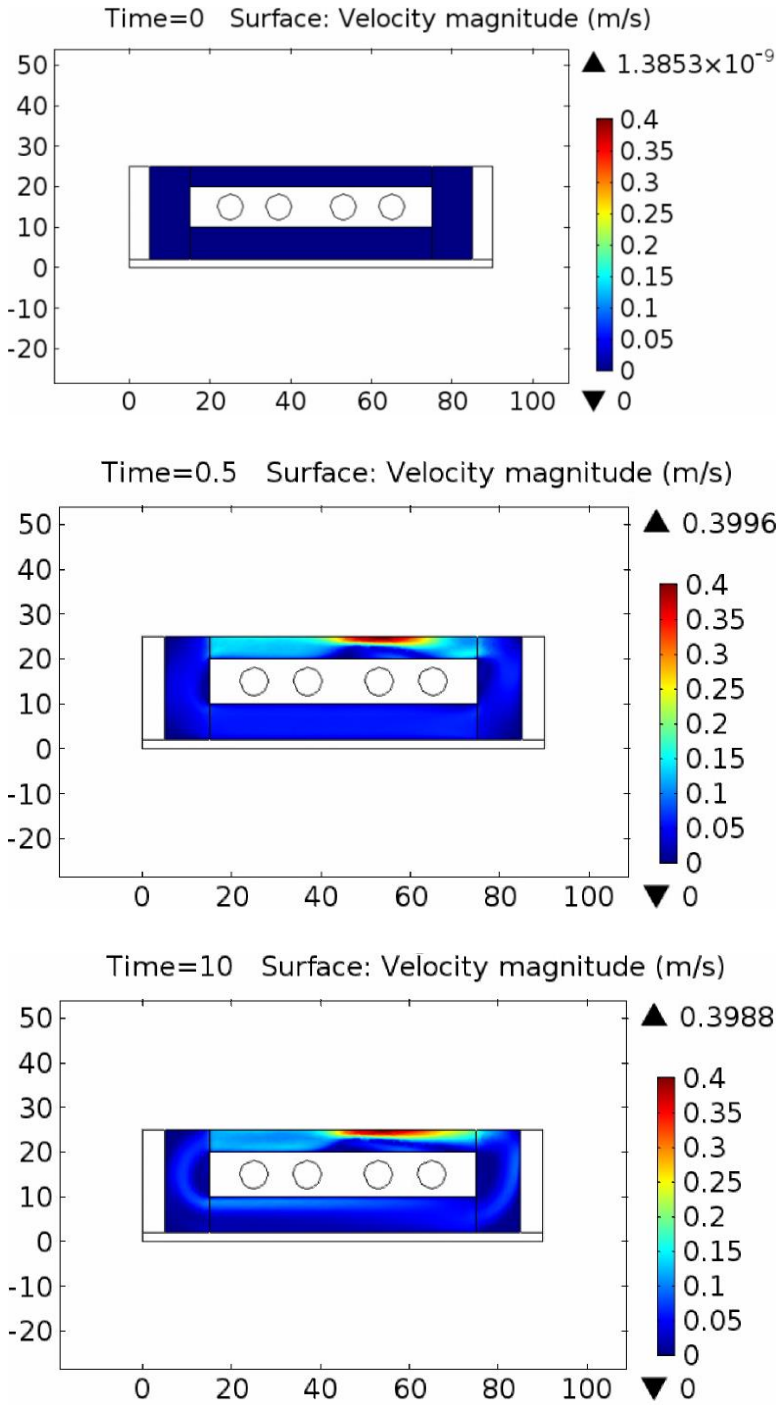

Figure 4.36 Velocity contour of y-z plane at x=1.5mm changes as function of time. Three frames are chosen here at t=0s, t=0.5s and t=10s.

Here is an example of the velocity change in a 10 seconds simulation. The magnetic field is 0.05T. The heat transfer coefficient is 500 W/(m^2K) and the coolant temperature is 293K. A series of plots here show the y-z plane velocity profile changing with time. Time is counted in seconds.

It is discovered that the velocity increases within the first 0.5s and after that the velocity profile changes little. This actually agrees with the acceleration time measured from the fast frame camera. This is the reason that the experiment measurement, which is in transient state, is similar to the steady state theoretical velocity calculation.

4.4.2 Comparison of the flow velocity

The flow velocity values from the simulation are compared to the experiment measurements and the comparison is plotted in Figure 4.37. It can be seen that the velocity measured at 0.022T is similar to the simulation result while the velocity measured at 0.19T is lower than the simulation results. Actually similar to Figure 4.29 the shape of the simulation curve matches both the theoretical calculation and experiment measurements while the location of the peak velocity seems shifting to higher magnetic field. The reason for the difference is not very clear. One possible reason is the influence of the return flow channels. In experiment the return flow channel is wider than the trench on the top. In order to simulate this symmetric boundary condition is assumed for the wall of the return flow which actually equals to insulated boundary. As a result the MHD damping inside the return flow channel is less than that in experiments. When the damping is weaker the velocity under high field limit will be higher than the experiment measurement.

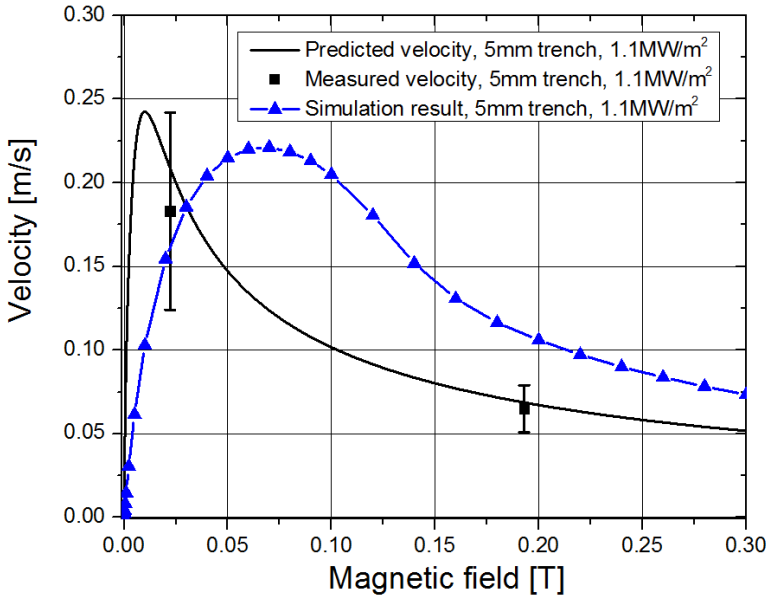

Figure 4.37 Comparison of the simulated flow velocity, the measured velocity and the theoretical calculation

4.4.3 Surface temperature change

The surface temperature values from the simulation can be extracted and compared to the IR camera measurements from Figure 3.36 and Figure 3.37. First the surface temperature value from the simulation and the IR measurement is compared for the case in Figure 3.36. In the experiment the heating starts when the thermocouple embedded in the top trench reaches 240C/513K. This value is set to be the initial temperature for the simulation. The comparison is plotted in Figure 4.38. The IR measurement before and after the heating are all plotted. The temperature is extracted along the centerline of the trench from inlet to outlet direction. From this figure we can see that the simulated temperature after the heating is quite different from the IR measurement. The reason is when the IR measurement was taken a lot of factors can strongly disturb the result especially the floating impurity and the reflection light from the e-beam. Even before the heating the IR measurement is not uniform. These effects are hard to take into the model because they may change from case to case. However in each single discharge these influences are relatively stable and the difference between the IR measurements before and after the heating, which is the temperature increase, is influenced much less compared to the absolute value measurement.

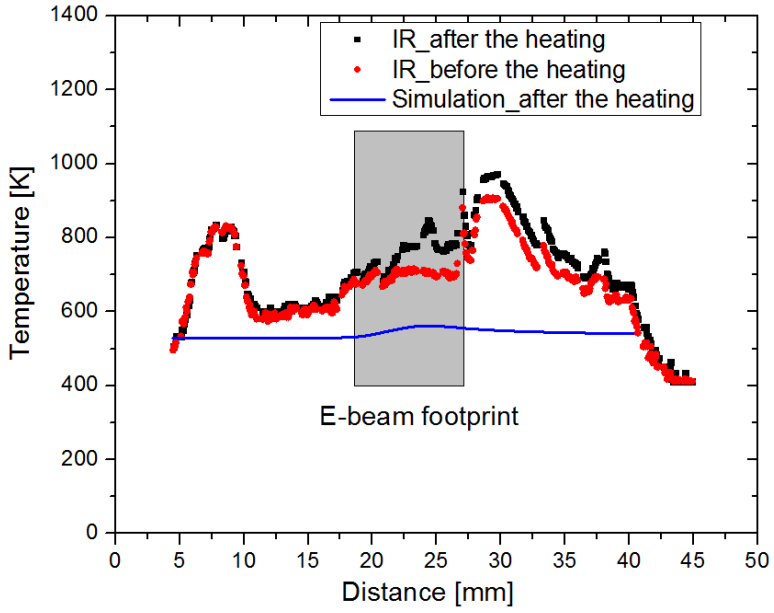

Figure 4.38 Comparison of simulated surface temperature and IR measurement at B=0.033T, q=2MW/m^2 and t=10s

The comparisons of the temperature increases in both cases are plotted in Figure 4.39 and Figure 4.40. Generally speaking the shape of the temperature profile matches in both cases. But it seems that the value matches better in Figure 4.39 while in Figure 4.40 a big difference between the IR measurement and the simulation can be seen on the downstream side. It is possible that the severe change of the IR measurement in Figure 4.40 is still caused by the disturbance of the reflected light from the e-beam filament, which may not be offset well when the IR temperature is corrected for the emissivity.

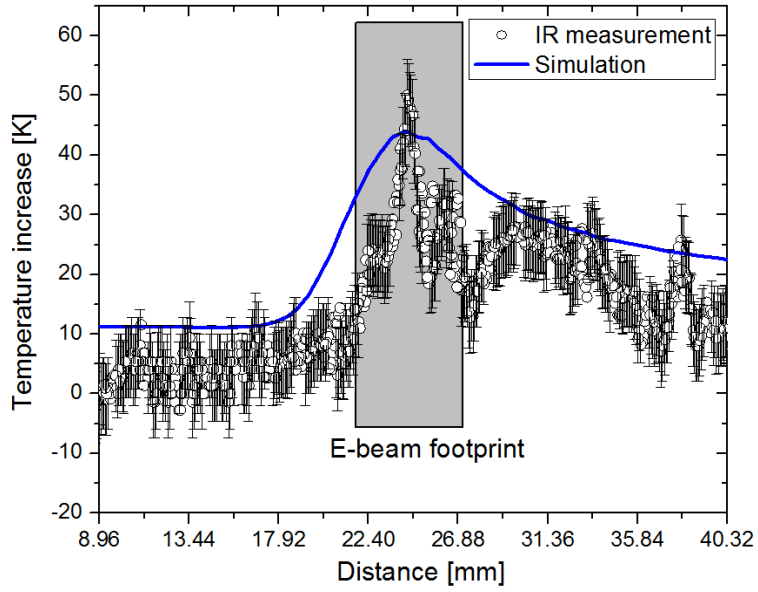

Figure 4.39 Comparison of the temperature increases from simulation and IR measurement at B=0.033T, q=2MW/m^2 and t=10s

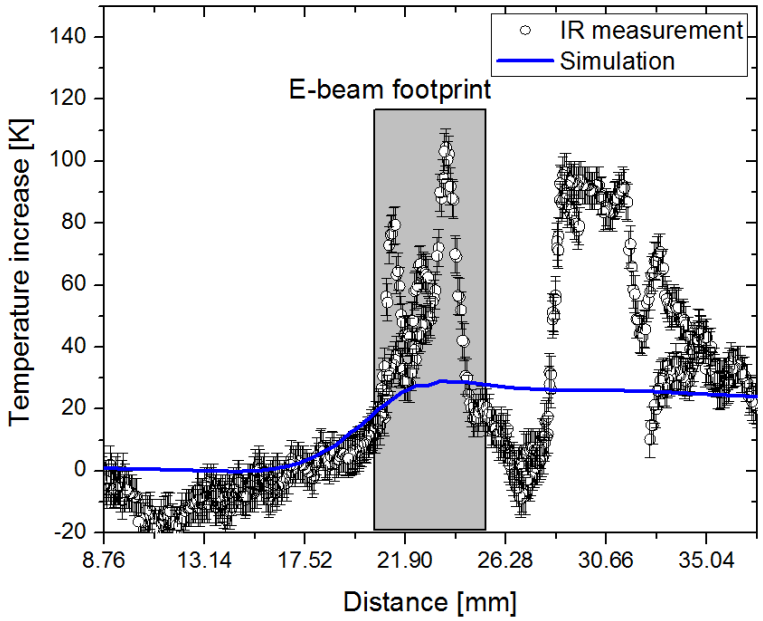

Figure 4.40 Comparison of the temperature increases from simulation and IR measurement at B=0.19T, q=2MW/m^2 and t=5s

4.4.4 Compare to the thermocouple measurement

Besides the temperature measurement from the IR the temperature measurement from the thermocouple can also be compared to the simulation results. Same experiment conditions from Figure 3.31 is input into the model. The heating from t=5.203s to t=14.493s from Figure 3.31 is imported into the model to construct the time-dependent heat flux on the top surface. Since the measurements from the thermocouples on the upstream side and the downstream side have 2K difference, the initial value of the temperature in the simulation is taken as the average of the initial values of both thermocouples. The result is plotted in Figure 4.41.

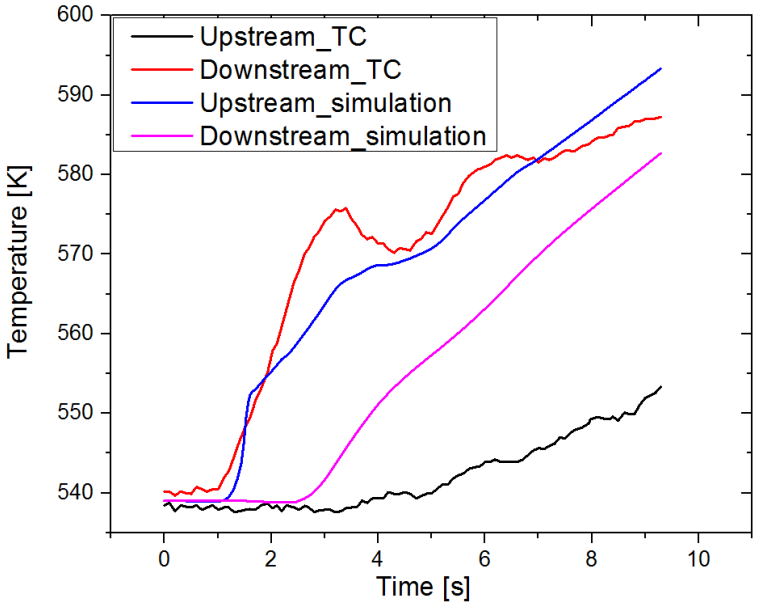

Figure 4.41 Comparison of the temperature measurements from the thermocouples embedded in upstream and downstream sides to the simulation result at the same condition. B=0.033T, the top heat flux in the simulation is constructed based on the experiment measurement.

From this figure we can see that the simulation result from the upstream side has similar values to the thermocouple measurement. Both curves increase at the same time and the shape of these curves are similar. However the simulation result from the downstream side is different from the thermocouple measurement. One possible reason is that the body of the embedded thermocouple in the trench may affect the flow which leads to the change of the heat transfer.

Chapter 5 Vertical trench experiment

In previous chapters the LiMIT concept has been discussed when the surface receives an incoming flux. In addition the influence of the gravity is not included in previous experiments and the tray is set to be horizontal. However installation of LiMIT type PFCs inside fusion reactors for general purpose such as using as wall tiles requires the PFCs installed at an inclined angle respect to the horizontal direction. If the trench is still aligned along the poloidal direction then the question is if lithium is able to flow along an inclined or even vertical trench.

5.1 TEMHD flow along arbitrary directions

5.1.1 General consideration

To find out the influence of the gravity we need to add an extra term to describe the gravity in equation 2.33 as an extra body force.

$$\rho\left(\frac{\partial\vec{u}}{\partial t}+\vec{u}\cdot\nabla\vec{u}\right)=-\nabla P+\mu\nabla^2\vec{u}+\vec{j}\times\vec{B}+\rho\vec{g} \tag{5.1}$$

Follow the similar steps in section 2.1.3, the 1D mean velocity can be revised to

$$u_m=\frac{Ha-\tanh(Ha)}{Ha+C\tanh(Ha)}\left(\frac{S-S_w}{B}\frac{dT}{dy}-\frac{1+C}{\sigma B^2}\frac{dP}{dz}+\frac{1+C}{\sigma B^2}\rho g\cos\theta\right) \tag{5.2}$$

Here θ is the angle between the gravity and the flow direction. To evaluate the influence of this term the temperature gradient is assumed to be 5000K/m, the angle θ is assumed to be 0 degree, C is assumed to be 1 and the wall material is stainless steel. The TEMHD term, the gravity term in the bracket and their ratio are plotted in Figure 5.1. Since this driven/damping from the gravity drops in the rate of B^2 it will be very small compared to the TEMHD driven term at the high magnetic field limit. When the magnetic field is 0.031T the TEMHD term equals the gravity term while when the magnetic field is larger than 0.32T the TEMHD term is much larger than the gravity term. But when the gravity is smaller than 0.32T its influence is still necessary to consider.

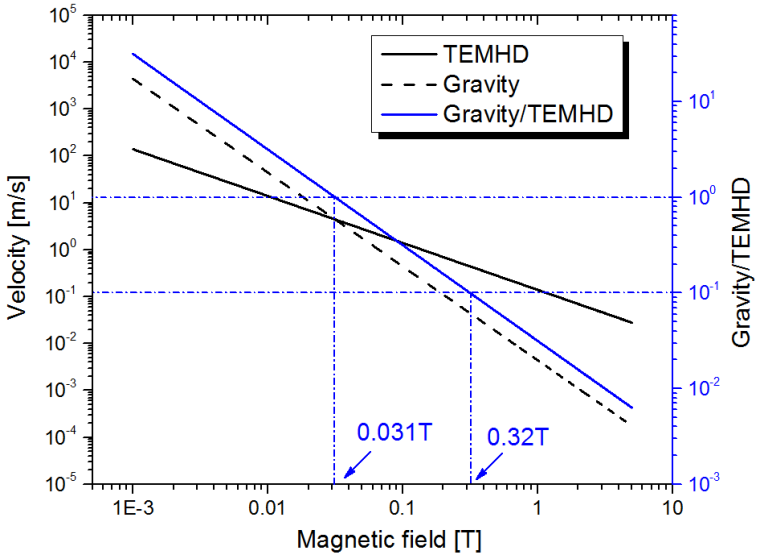

Figure 5.1 TEMHD driven, Gravity and their ratio as functions of the magnetic field

5.1.2 Flow along arbitrary directions

If the trench is tilted to an arbitrary direction it can be decomposed into two directions. One is tilted towards the flow direction while the other is tilted perpendicular to the flow direction.

If the tray is tilted while the trench is still along the horizontal direction, which is plotted in Figure 5.2, the gravity will not accelerate or decelerate the flow since the angle between the flow direction and the gravity is still 90 degree. However the gravity may still affect the flow if the trench width is large. In this case the gravity will affect the shape of the fluid within the trench and the cross section may become what is plotted in Figure 5.3. In this case the fluid may flow out of the trench edge to the lower level. Because of the loss of the pressure provided by the gravity the return flow may also be a problem. Another problem is part of the structural material is exposed and the heat flux may potentially cause permanent damage.

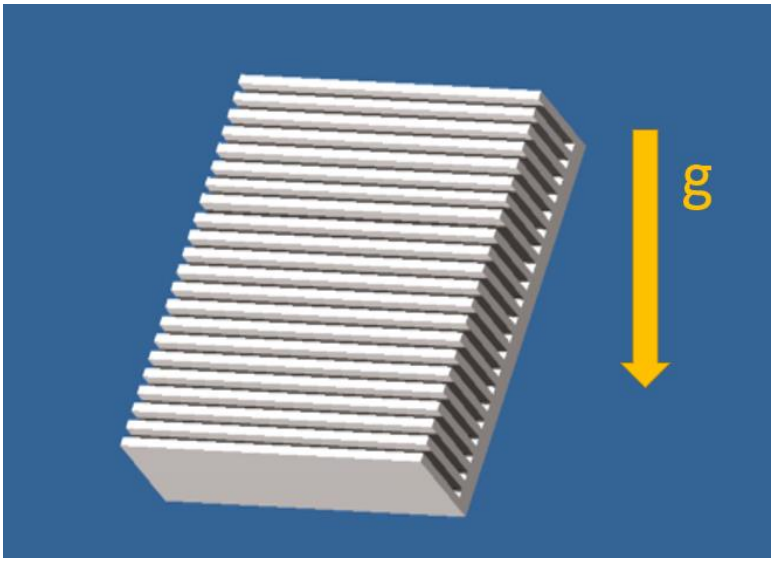

Figure 5.2 Trench tilted to the side while the flow direction is still perpendicular to the magnetic field

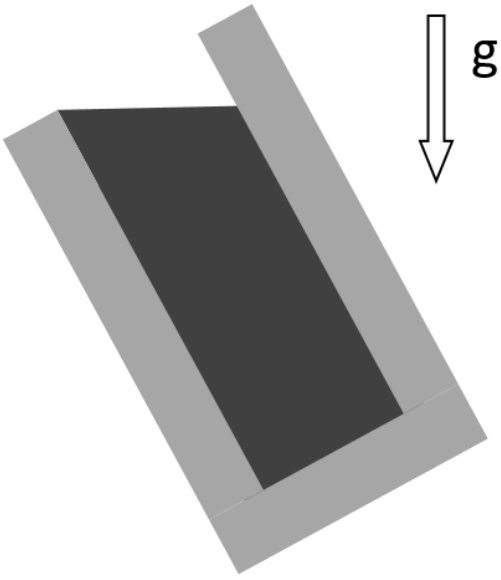

Figure 5.3 Potential change of the lithium trench cross section when the tray is tilted

If the trench is tilted in the way that the angle between the flow and the gravity is smaller than 90 degree the influence of the gravity needs to be taken into consideration in the way of adding the extra term as equation 5.2. However since the curl of the gravity is zero when the return flow is

added the loop integral of the gravity along the flow direction is zero, which means the net work it does to the kinetic energy is zero. In this case the mean velocity should be the same at any tilted angle.

5.1.3 Vertical trench concept

In order to act as the general PFCs function and generate lithium flow along the poloidal direction the lithium trench can be design as Figure 5.4, in which lithium is able to be pumped by TEMHD along arbitrary angle.

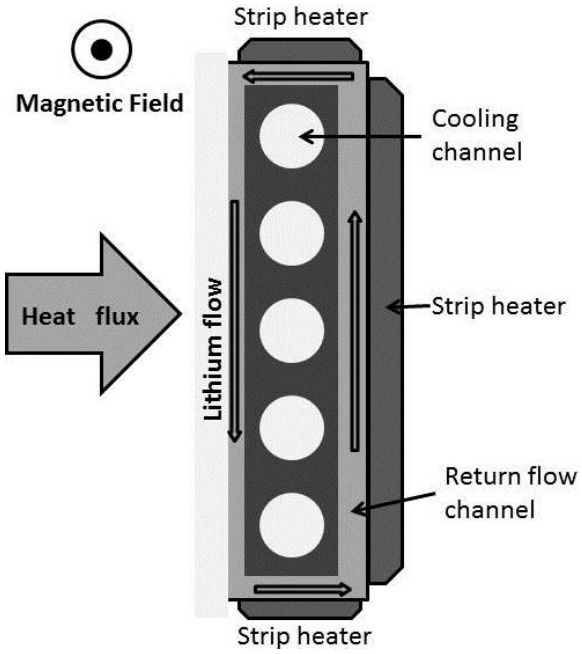

Figure 5.4 Vertical LiMIT trenches for general PFC purpose

In order to achieve this, a few questions need to be answered. First, all of the previous experiments used surface heating including electron beam heating in the experiment at UIUC and the direct plasma heating in the experiment in HT-7. But the surface heating may not be necessary if the back flow channels can be utilized. In fact when a heater is attached to the back side of the tray and if the power and the cooling efficiency at the center are high enough there will be a temperature gradient within the back flow channels, which can generate TE force inside the back flow channels. Even if the trench is inclined or even vertical the TE force within the back flow channels is still

possible to overcome the gravity to drive the lithium. In fact if the flow only relies on the plasma heating it is not very useful for some devices with short plasma duration time. In this way even if there is no heat flux on the top trenches, the back flow channels can still keep pumping lithium upwards to the top so that lithium can fall down by itself through the top trenches. The whole concept is plotted in Figure 5.4. The drawback of this method is the temperature gradient provided by the heater is not as high as the plasma heating. But even with this comparably lower velocity flow the lithium surface may still stay clean.

The second problem is if the TE driven force is large enough to overcome gravity. If the trench is placed vertically and the TEMHD pumping is at standstill the rising pressure gradient ∇p is given as

$$\nabla p = \frac{\sigma BP}{(1+C)} \nabla T \tag{5.3}$$

Thus if the thermoelectric force needs to overcome the gravity to drive the lithium this only happens when the rising pressure gradient by TEMHD is larger than the body force ρg by gravity, which equals to

$$\nabla T > \frac{\rho g(1+C)}{\sigma BP} \tag{5.4}$$

Here ∇T is the temperature gradient across the back side channel. $\rho = 508\ kg/m^3$ is Li density and σ is Li electrical conductivity. B is the transverse magnetic field and g is the gravity. P is the thermoelectric power between the pair of materials and $C = (a\sigma)/(t\sigma_W)$, which describes the wall impedance in comparison with that of Li. a is the thickness of liquid channel and t is the thickness of the wall. σ_W is the electrical conductivity of the wall.

When the thickness of the liquid channel is the same as the wall thickness the required temperature gradient as a function of magnetic field is plotted in Figure 5.5 for different material pairs. The thermoelectric power values are taken from [51]. Since this minimum temperature gradient is inversely proportional to the magnetic field higher field actually requires lower temperature gradient. For the experiments at UIUC with 0.111 T transverse magnetic field the necessary temperature gradient is around $2.66*10^3$ K/m while for the experiment in real fusion devices with much stronger magnetic fields such as EAST only about 45 K/m temperature gradient is enough

to provide large enough TEMHD driven force. Gravity seems negligible compared to TEMHD force in fusion reactors.

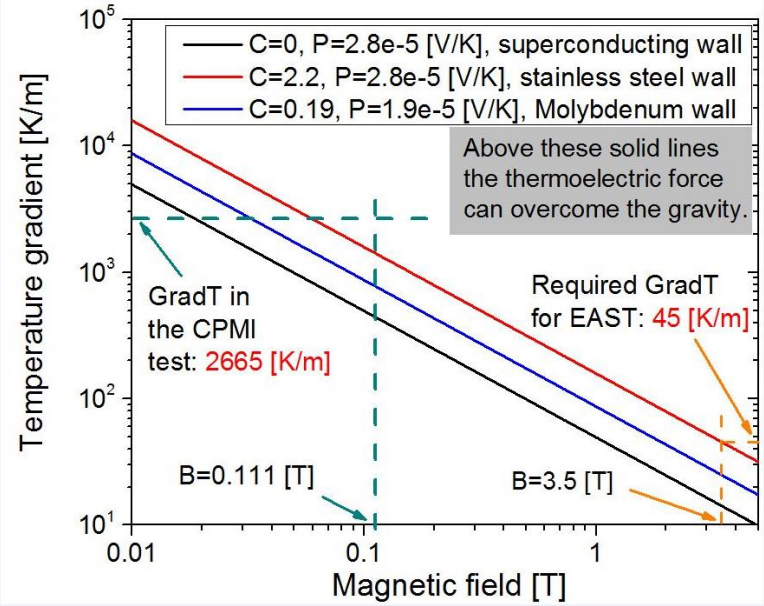

Figure 5.5 Temperature gradient required to overcome gravity under different magnetic fields

Another concern of this type of flow is if the surface of the liquid lithium in top trenches will be stable. In order to solve this problem we reduced the width of the trench to 0.5 mm so that the surface tension is strong enough to maintain the surface. In the last chapter the influence of the surface tension has been discussed. Similarly the ratio of the surface tension over TEMHD is 24.3. This is due to the reduced size of the trench. Because there is no surface heating of course the Marangoni effect does not exist. On the other hand we need to evaluate the Weber number which describes the ratio between the fluid inertia over the surface tension force. This number equals to $\mathrm{We} = \frac{\rho v^2 a}{\Sigma} = 0.008$, which means the inertia is much smaller than the capillary force. Under the same conditions the typical lithium flow velocity (~0.1 m/s) is far below the critical condition $v_{crit} = 1.34\ m/s$ that leads to the surface collapse [67]

$$v_{crit} = 0.755\sqrt{\frac{4\Sigma}{\rho\frac{4ab}{2b+a}}} \tag{5.5}$$

Here $\Sigma = 0.32$ N/m is the surface tension of liquid lithium. $a = 0.5\ mm$ is the width of lithium trench and $b = 1\ mm$ is the height of lithium trench. Physical properties of liquid lithium are taken

from Hanford report [38] assuming T= $523\ K$. In experiments it was observed that trenches are completely filled and capillary force was strong enough to maintain the surface from horizontal to vertical orientation.

5.2 Vertical trench experiment setup

To investigate the flow within the LiMIT trenches at arbitrary inclination angle, a vacuum rotatable vacuum chamber was constructed. A special lithium injector loads the liquid lithium into the tray at horizontal position. Then the chamber is rotated to an angle and both the magnetic field and cooling will start. The surface is monitored by camera during the experiment.

5.2.1 Design of the LiMIT trenches

To accommodate the requirements of this experiment special LiMIT trenches were designed and manufactured. The material is also SS 316. The CAD drawing of this trench is in Figure 5.6. Trenches are cut on the front side, the back side and the edges to form a closed loop. The width of the trench is 0.5mm and the width of the wall is also 0.5mm. The depth of the trench is 2mm on the backside and 1mm on the front side. Cooling channels are drilled at the center. The detail of the CAD drawings can be find in the appendix (Figure A.10 to Figure A.16).

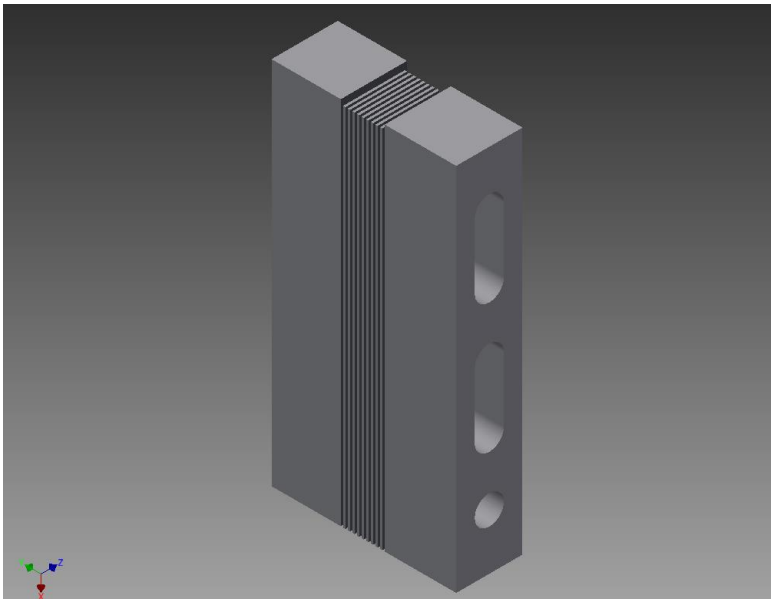

Figure 5.6 CAD drawing of LiMIT trenches for the vertical trench test

Figure 5.7 is the assembled trench. When the trench is at horizontal position it looks like the left figure in Figure 5.7 and when it is at vertical position it looks like the right one. The blue color structure is a small reservoir to contain extra lithium in case too much lithium is filled and flows out. On the other side there is a small gap between the trench part and the green color wall. This gap will be used to fill the lithium. Note that the top trench is only 1mm high and the top surface of the trench wall is actually 1mm lower than the front surface. This is to prevent the lithium from flowing out of trench area. The rotation of the trench is illustrated in Figure 5.8.

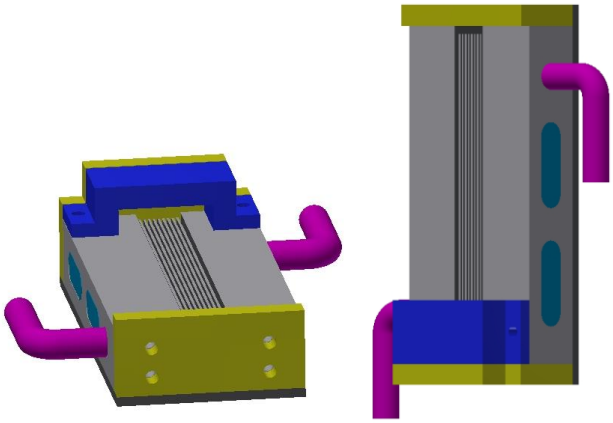

Figure 5.7 CAD drawing of assembled LiMIT trenches for the vertical trench test

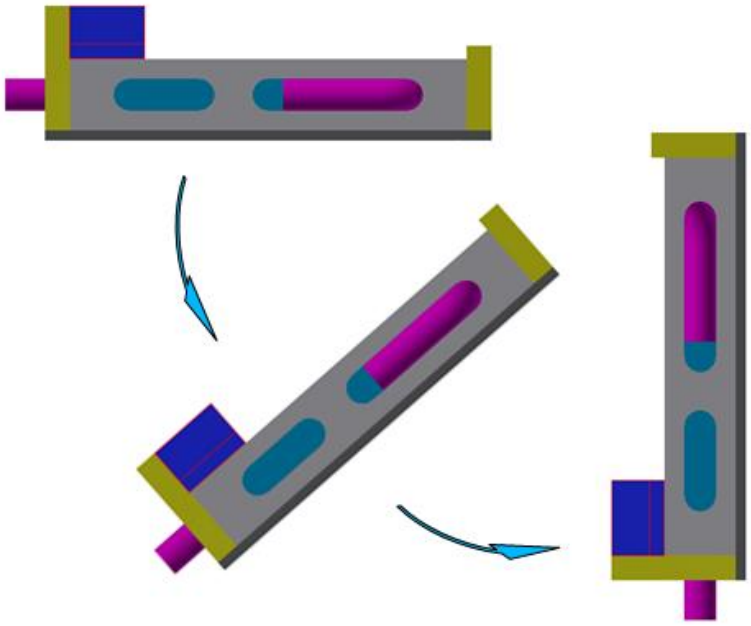

Figure 5.8 LiMIT trenches rotate from horizontal position to vertical position

5.2.2 Experiment apparatus

A rotatable vacuum chamber was constructed so that the trench inside can rotate with the chamber to an arbitrary angle. The chamber is installed on two pivots which are at the same height as the center of the LiMIT trenches. The entire chamber was rotatable about this central pivot and during the rotation the trench can be kept at relatively same height. The whole setup is in Figure 5.9. The rotation angle can be directly read out through an angle level, which is the white block attached to the green bar in this figure.

Figure 5.9 The rotatable chamber for the vertical trench test

The vacuum base pressure is kept below 10^{-3} Torr with the help of a dry pump. About 0.111 T magnetic field at the LiMIT structure position is generated by powering four magnet coils with car batteries. This is the same as the previous experiment. The whole structure is cooled by compressed air flowing through five ¼" diameter holes at center and heated on the back side with a Watlow strip heater (20 cm by 4 cm by 0.3 cm) with a maximum power of 500 W at 120V. Two thermocouples are attached to the front side close to the edge of the front trenches while one thermocouple is attached to the heater surface. The heater is attached to the backside of LiMIT by four stainless steel clamps with about 0.05 mm thick ultra-high vacuum carbon paste at the interface. The carbon paste can bear around 2000C and its thermal conductivity is about 1 W/K*m.

Filling of these narrow channels is very hard and it was accomplished with a special lithium injector with the addition of a needle type nozzle and two linear shifts. A schematic is shown in Figure 5.10. The trench is firstly heated to about 480C and the lithium is also heat to about 300C. Then the nozzle was lowered via the linear shift into the gap on the side of the trenches and lithium was slowly injected filling the trenches from the bottom up. Once the trenches are filled the nozzle will be lifted above the lithium surface and moved away.

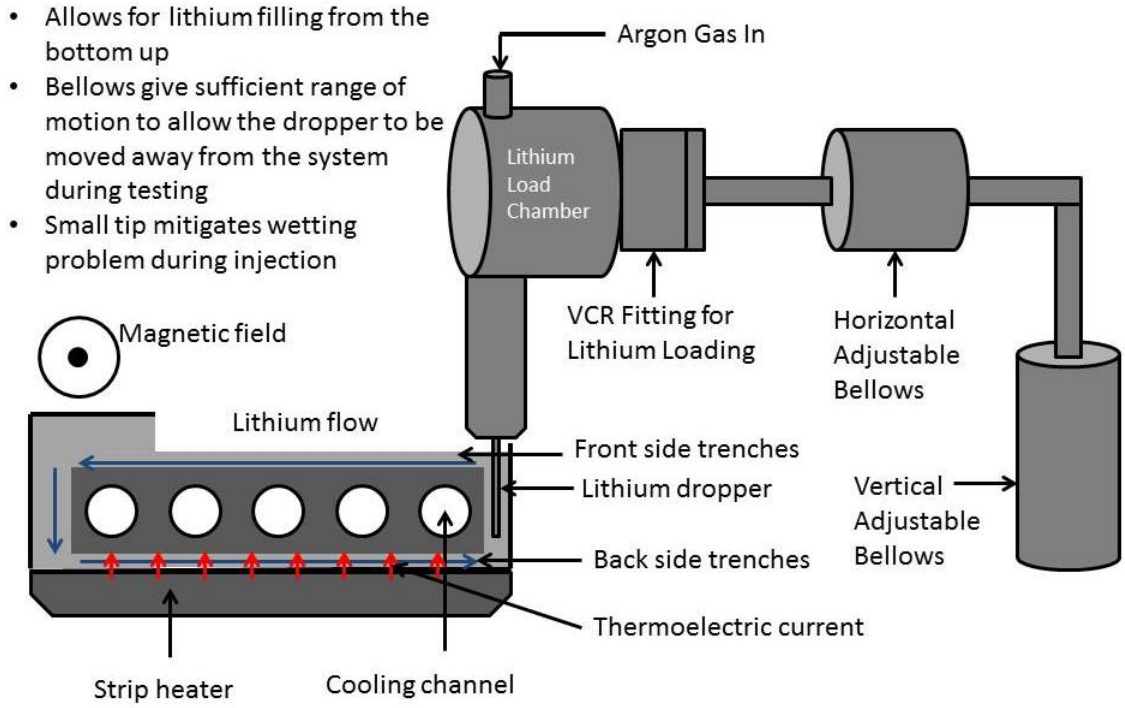

Figure 5.10 Load lithium into the trench by a movable lithium injector

5.2.3 Experiment procedure

To investigate lithium flow at arbitrary inclination, a temperature gradient is established in such way. First the LiMIT structure is kept at 400C steady state and the heater surface is kept at about 600 C while the heater is set to 100 V. Then the compressed air is turned up to 2 cfm at 30 psig. This can generate a higher transient temperature gradient than what the heater can provide at steady state. The magnetic field is then toggled on and the chamber is inclined to the desired angle while

recording with the high speed camera. Velocity of the lithium was extracted from frame to frame displacement of impurities entrained in the lithium flow similar to the previous experiment.

5.3 Vertical trench results

5.3.1 Qualitative observation

One of the concerns for this experiment is if the capillary force is enough to hold the lithium within trench. This is demonstrated in the experiment. When the trenches were overfilled at horizontal position the tray was rotated to the vertical position and the residual lithium would just fall into the reservoir at one end while all the trenches could still remain filled. This is shown in Figure 5.11. This means the capillary force is strong enough to capture all the lithium inside the trench.

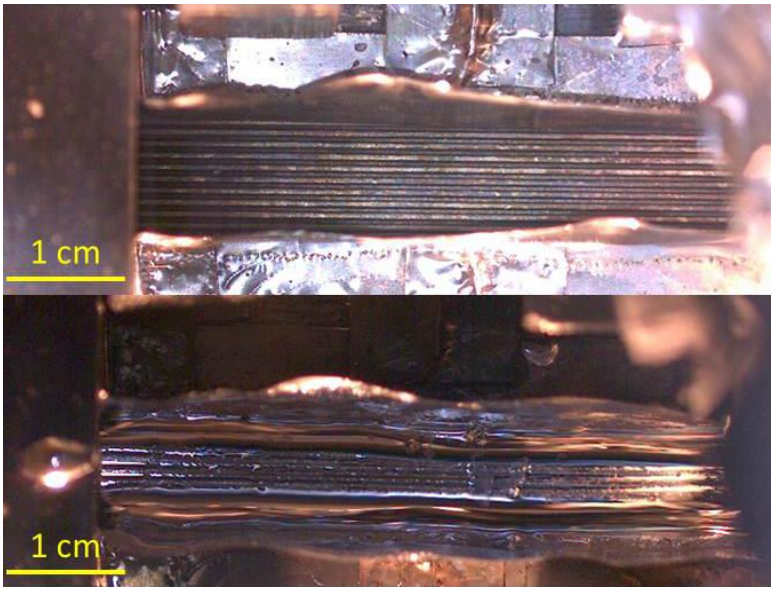

Figure 5.11 Empty trench at horizontal position and filled trench at vertical position

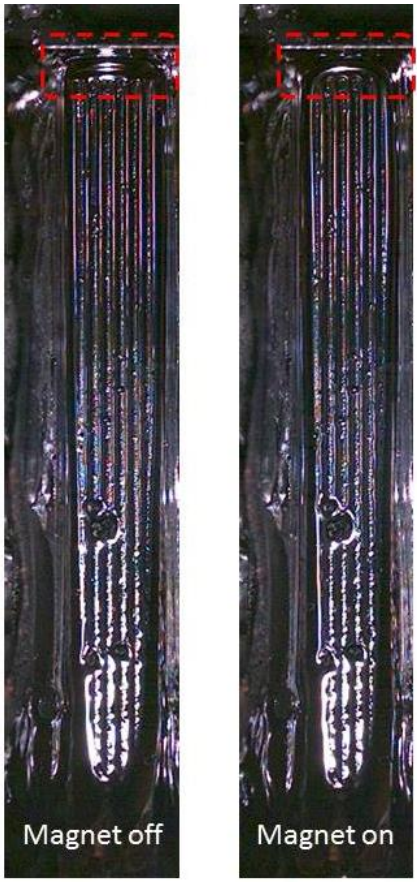

Figure 5.12 Empty top gap was filled when magnetic field was turned on

Another discovery in the experiment is when the trench was rotated to vertical position the gap on the top became empty because the gap size was too large for the capillary force to overcome the gravity. However after the magnetic field was turned on lithium was successfully pumped through trenches on the back side and filled the gap on the top. Then lithium was distributed at the edge into each trench. This is a direct proof of TE pumping force within back side channels being higher than the gravity.

5.3.2 Quantitative measurement of flow velocity

Flow velocity measurements with LiMIT aligned horizontally were taken by the fast frame camera. A series of frames processed using ImageJ are shown in Figure 5.13. In total, 12 clips of moving impurity scale are analyzed giving an average velocity of 0.095 +/- 0.041 m/s.

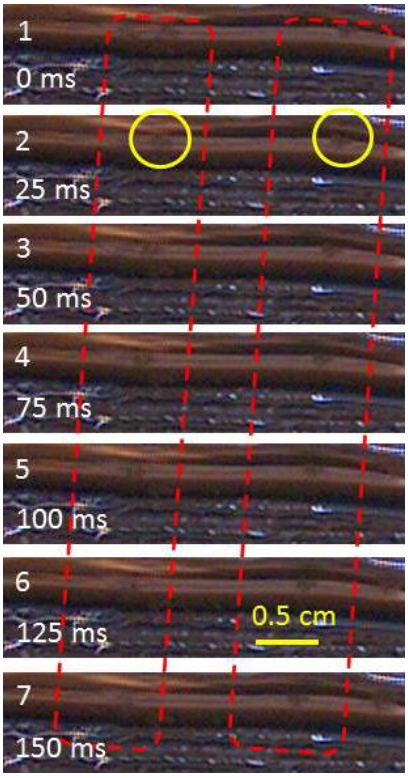

Figure 5.13 Continuous camera frames to calculate the flow velocity at horizontal position

The velocity can also be derived in an indirect way through the temperature gradient within the back side channels. In the experiments described here, direct measurement of the thermal gradient in the lithium channels is difficult, and is therefore calculated from a 3D, time dependent model implemented in COMSOL, balancing heat in from the heater with heat lost to the coolant. Temperature values are averaged across the top surface and bottom surface of the lithium channels to determine the average temperature gradient in the channels. Both average temperature values, and the temperature gradient are plotted as the function of time in Figure 5.14. From this figure we can see that after about 10 seconds the temperature gradient changes little. An averaged value 2665 ± 500 K/m is chosen for further calculation.

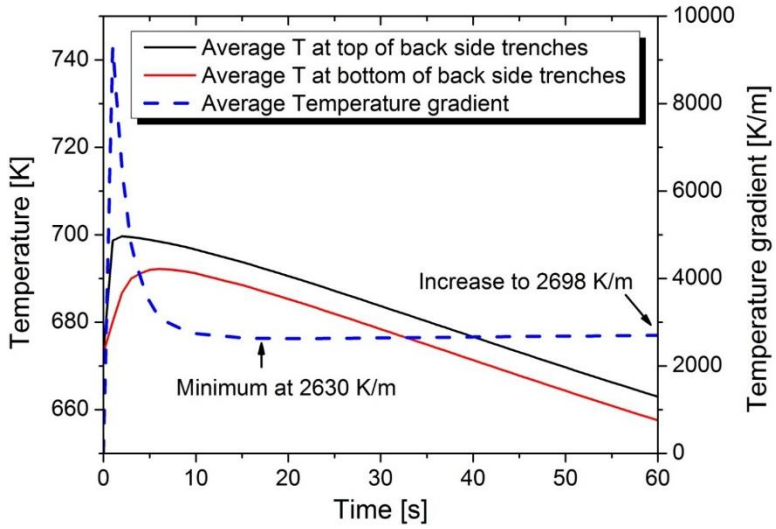

Figure 5.14 Calculated average temperatures and temperature gradient across the back side trenches as the function of time. Result of a 3D time dependent heat transfer model calculation.

The mean velocity of the front side trenches is:

$$u_{m\_front} = \frac{2}{3}\frac{Ha - tanh(Ha)}{Ha + Ctanh(Ha)}\frac{P}{B}\frac{dT}{dy} \tag{5.6}$$

which is equal to 0.114±.021 m/s for this case. Here the Hartmann number is $Ha = B\ a\ /\ 2\sqrt{(\sigma\ /\ \mu)}$ and μ is the dynamic viscosity of liquid lithium.

The lithium trenches were subsequently inclined to a series of angles between 0 and 90 degrees from the horizontal. The velocities of the lithium were similarly extracted and the results can be seen in Figure 5.15. Also plotted within Figure 5.15 is the theoretical prediction for the velocity, as well as error bars resulting from the uncertainty in the determination of the thermal gradient in the rear channels. Good agreement can be seen between the theoretical prediction and the experimental velocity at higher inclination angles. Poorer agreement is seen at lower angles, even though in most cases there is overlap of the error bars. The general trend however, appears to be increasing from low inclination to high inclination, even though the gravitational force is predicted to be small compared to TE force. This is attributed to an overfill layer seen in LiMIT structure. At low inclination angles, the overfill is spread over the entire LiMIT tray, whereas at large inclination angles, the overfill was collected by the reservoir. Since velocity measurements were taken near the center of the structure, the overfill would lead to an increased cross sectional area,

and due to conservation of flow rate, a lower velocity. A ratio of velocities implies an overfill of approximately 1mm in the cases of low inclination angle. Evidence of such an overfill can be seen in Figure 5.11.

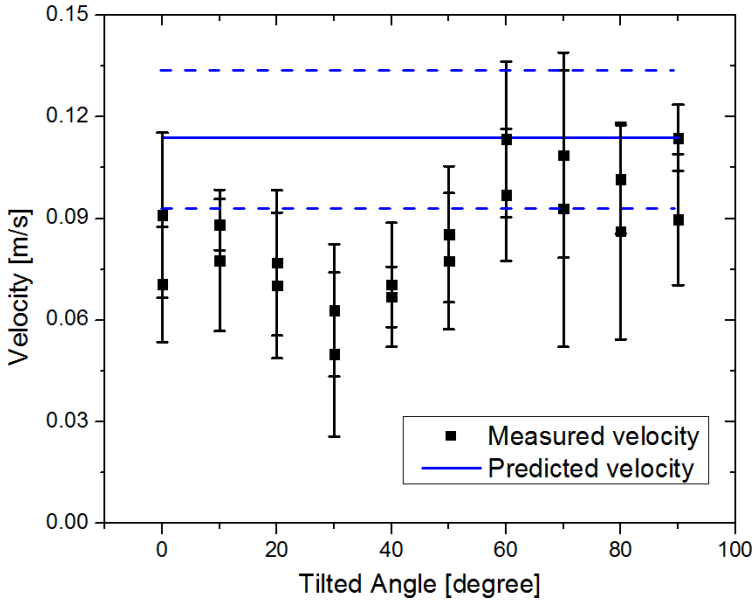

Figure 5.15 Lithium velocity as a function of inclination angle, higher inclination angles show better agreement with theoretical prediction. Lower inclination angles have a lower measured velocity than theoretically predicted, which is hypothesized to be due to overfill

5.4 Vertical trench test on EAST

5.4.1 Experiment design

In order to test the performance of this type of narrow size LiMIT trenches in fusion reactors when it is used as general PFCs a test on EAST has been planned. EAST is a mid-size fully superconducting tokamak with about 3.5T toroidal field. From the calculation in Figure 5.5 the temperature gradient to overcome the gravity in this magnetic field is easy to generate by additional heater. Assuming a same temperature gradient as what we got in the vertical trench test at CPMI the velocity can be estimated to be 0.012m/s. This velocity is not very fast but it may still be enough to refresh the surface between each shot.

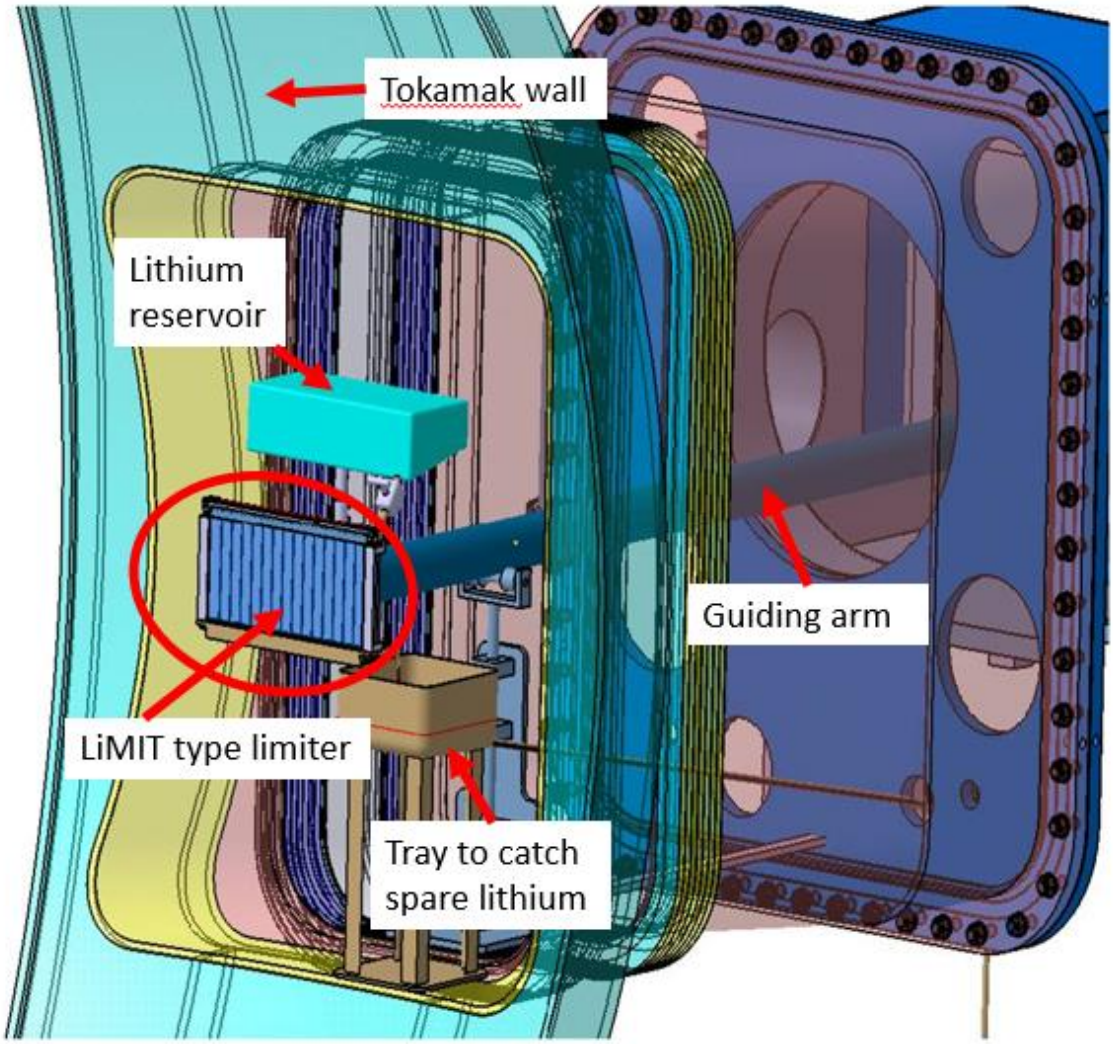

Figure 5.16 LiMIT type limiter installed on linear motion arm on EAST

On EAST LiMIT type limiter will be tested as a movable limiter installed vertically on a linear motion arm and inserted from the middle plane, which is plotted in Figure 5.16. The surface of the trench will stay in SOL region. Before the experiment lithium will be injected into the trenches in a separate vacuum chamber. Because of the trench is installed vertically the lithium has to be loaded at this orientation. A lithium injector will guide the liquid lithium through a needle type nozzle onto the top of the trench and lithium is expected to fill all the trenches with the help of capillary force. On the other hand liquid lithium needs to be captured when it flows to the bottom along the front side trench. Unlike the test at CPMI in which a small reservoir is used to catch the

lithium no extrusion is allow on the front side when it is tested in fusion plasma environment and it is necessary to shape the bottom of the trench to capture the falling liquid lithium.

5.4.2 Prototype vertical trench

To solve these questions related to the real application a new prototype vertical trench has been designed and the vertical trench chamber is also revised to test all of those features that need to be considered for the test on EAST. The CAD of the design is presented in Figure 5.17.

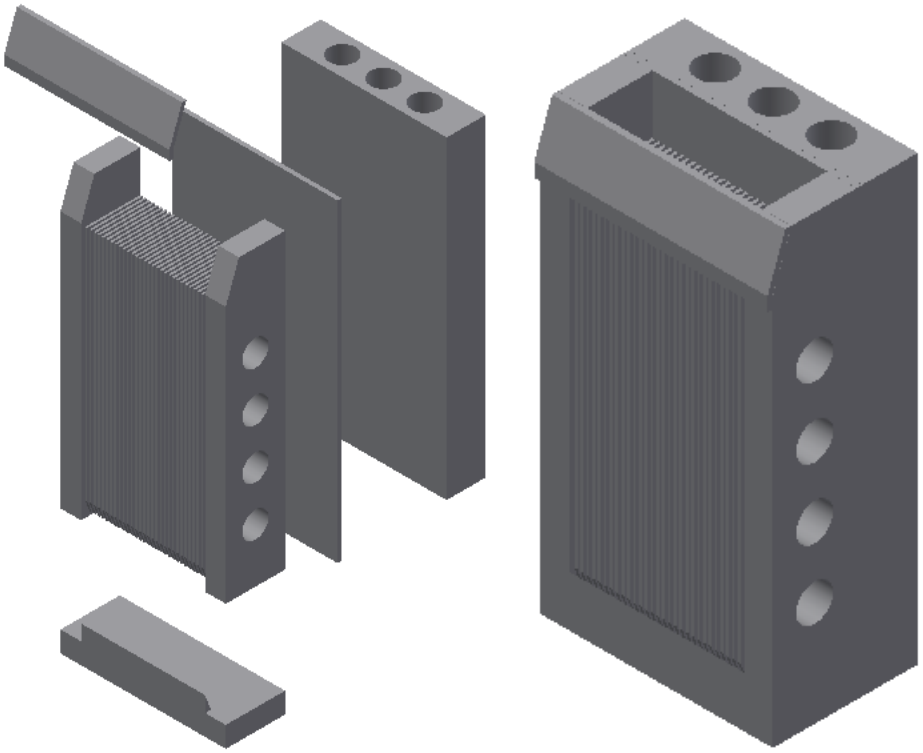

Figure 5.17 CAD drawing of the new prototype vertical trench design. The left figure is the explosive view and the right figure is the assembled trench.

In this design the size of the trench will stay the same as the previous vertical trench. A small empty volume is added to the top of the trench where lithium will be loaded into first and then the capillary force will drag lithium into the trench. The needle type movable lithium injector will be used to load lithium into this region. On the top front side a flat stainless steel plate with a small bend at one edge will be attached to guild lithium flow into the top trenches. At the bottom edge

of the front side a slope is created instead of a right angle. When lithium flows along the trench it will flow along the slope into an empty volume at the bottom where the lithium will meet the entrance of the back side trench. Heater for the back side is redesigned to accommodate the installation on the linear motion arm. Similarly a stainless steel arm will be attached to the back side in the same way when it is tested inside the vertical trench chamber.

Chapter 6 Discussion of the transient effect

6.1 Transient heat load on LiMIT during transient event

In previous chapters the LiMIT concept has been examined under a heat flux up to 10MW/m^2, which is the peak heat flux onto the divertor during normal operation. However this heat flux may increase by one or even two magnitudes during the so-called transient events. The transient event has been briefly discussed in chapter 1 and usually transient events include disruption and ELM (usually type I) which can release a large amount of confined energy and particles into the SOL within a short time and eventually place a large heat load to the PFCs especially the divertor. The energy usually is deposited from 0.1ms to 1ms and the total deposited energy ranges from 0.01MJ/m^2 to 1MJ/m^2 [68] [69] which depends on the power of the device. And for ITER the type I ELM can release 1MJ/m^2 energy within 0.5ms and the heat flux parameter $E/\sqrt{t}$ is about 45MJ/m^2*s$^{0.5}$ [68], which is higher than the recrystallization and melting heat flux threshold of tungsten and this will greatly reduce the lifetime of tungsten PFC [70].

As for liquid lithium strong evaporation is still expected. The lithium vapor shielding effect is not considered here and all the energy is assumed to deposit onto the lithium surface within the ELM duration. Since the duration of the ELM is small lithium can be assumed to be static during this time. When the surface starts to be heated the temperature increase on the lithium surface can be estimated as

$$T = T_0 + \frac{2}{\sqrt{\pi C_p \rho k}} q\sqrt{t} \tag{6.1}$$

Here T_0 is the original temperature of the surface, q is the heat flux onto the surface and t is the time. If the initial temperature is 473K the boiling threshold at which the surface will reach 1603K boiling temperature at the end of ELM can be calculated as $(T - T_0) * \sqrt{\pi C_p \rho k}/2$ which is 10MJ/m^2*s$^{0.5}$. If the energy of the ELM is higher than this the rest of the energy will be used to vaporize lithium. When the heat flux is assumed to be the ITER type I ELM heat flux which is 2GW/m^2 it costs 0.025ms for the surface temperature to reach the boiling temperature. This time is much smaller than the 0.5ms duration time and after the temperature reaches the boiling point the energy starts to be consumed mainly by the heat of vaporization. If the heat of vaporization for

lithium is 136kJ/mol the thickness of lithium that will be vaporized is about 100um. However as far as this amount of lithium can be replenished the surface will not be permanently damaged. On the other hand this can also be considered as the minimum thickness for the overfilled liquid lithium to protect the solid structure for LiMIT concept and any other liquid lithium PFCs. Obviously when the lithium starts to boil the large evaporation flux from the surface will form a very dense vapor cloud to shield the energy from the plasma and release the energy in the form of radiation and ionization. The real evaporated thickness could be much smaller.

6.2 Fluid flow and temperature evolution during transient event

From the previous calculation we can see that at the end of the transient event the peak temperature may reach 1603K if the heat flux parameter is higher than $10MJ/m^2*s^{0.5}$. For LiMIT trenches if the surface is heated to such high temperature within a short time it is expected that a steep temperature gradient will build up inside and instantaneously a large thermoelectric current will generate. Because of the elevated heat flux on the surface this thermoelectric current may increase by one or two magnitude which corresponds to a large Lorentz force inside lithium trench. Under the influence of this Lorentz force the lithium itself may be accelerated severely and cause some unexpected phenomena such as dry-out, deformed surface or event ejection.

In this section the influence of the transient heat load on the LiMIT surface will be briefly analyzed to find out the velocity and temperature evolution post the transient event. On the other hand the transient event is also accompanied by large current into the PFC, disturbed magnetic field or strong dynamic pressure on the PFC surface. The influence of these will not be analyzed here.

When the transient event happens the heat is not uniformly deposited to the divertor surface. Instead the heated area is actually quite narrow compared to the whole divertor target plate. Usually the full width at half maximum (FWHM) ranges from 1cm to 5cm in most devices [55] [71] [72]. In the later calculation the transient load will be considered as a point heat load which happens within a short time.

Now let us estimate the current and flow evolution during a relatively short time ~100ms after the transient event. In this calculation the liquid lithium is static at the very beginning. The transient

heat load is assumed to be 0.1MJ/m^2 for 0.5ms which is lower than the heat flux threshold for boiling. At the beginning this amount of heat is release to a point on the boundary and after that the heat starts to transfer radially. Since the time is very short the convection is temporarily not included in this estimate. Based on the above assumption the temperature change from the point source can be written as [73]

$$T(r,t) = \frac{2Q}{C_p\rho(4\pi\alpha t)} exp\left[-\frac{r^2}{4\alpha t}\right] \tag{6.2}$$

And in the above equation r is the radial distance and α is the thermal diffusivity. The temperature gradient can be derived from the above equation to be

$$\frac{dT(r,t)}{dr} = \frac{2Q}{C_p\rho(4\pi\alpha t)}\left(\frac{-2r}{4\alpha t}\right) exp\left[-\frac{r^2}{4\alpha t}\right] \tag{6.3}$$

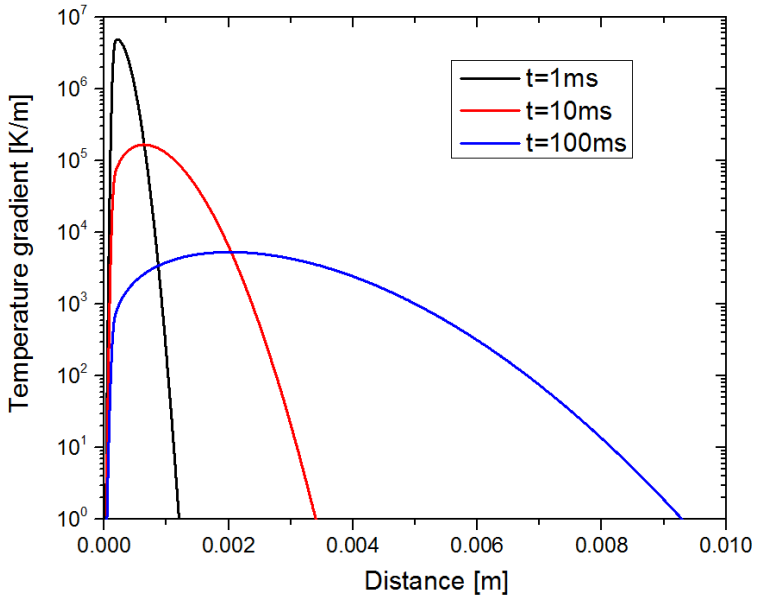

Figure 6.1 Spatial temperature gradient distributions at different time of heat conduction from an initial point heat load

The temperature profile can be plotted along the radial direction to be It can be seen that right after the transient event the temperature gradient is two orders of magnitude higher than the normal temperature gradient and after about 100ms the temperature gradient drops to the regular level. This also indicates that the driving force in the LiMIT within this 100ms is very strong and the resulted influence needs further investigation.

To find out the change of the velocity the Navier stokes equation is reduced to

$$\rho \frac{du}{dt} = -\sigma BS \frac{dT}{dr} - \sigma u B^2 \tag{6.4}$$

Solve the velocity for the time at a particular radius location the velocity evolution as time can be plotted in Figure 6.2. The magnetic field is 1T.

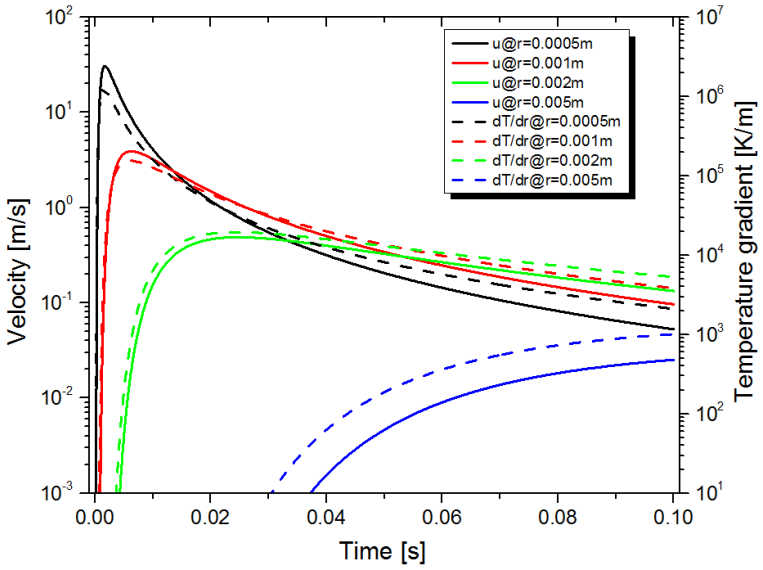

Figure 6.2 Velocity driven by transient TEMHD force changes as function of time at different radial locations

From Figure 6.2 we can see that the velocity at different radial location is quite different. Since the heat transfers along the radial direction the lithium close to the heated area of course is accelerated earlier. And since the temperature gradient drops along the radial direction the peak velocity also drops along the radial direction. Close to the heating area the peak velocity can be more than 10m/s and quickly drops below 1m/s within 30ms. On the other hand the driven force drops quickly along the radial direction and the lithium more than 5mm away from the heating area accelerates slowly to less than 0.1m/s. It can be seen that after 0.1s the velocity at different locations gradually converges to a same value.

Since the temperature gradient is along the radial direction the TE current should be in the same direction as the temperature gradient. Because the TE body force is perpendicular to the TE current

the TE force should be along the azimuthal direction around the heated area, which is plotted in Figure 6.3.

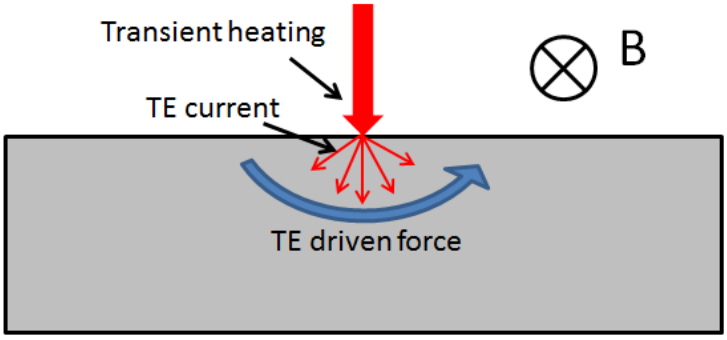

Figure 6.3 Radial TE current and azimuthal TE driven force

Because of the heated area is greatly accelerated while the rest part is at a relatively low speed in order to satisfy the mass conservation the center part is expected to shrink to a smaller cross section, which will lower the level of the liquid lithium at the heat area and potentially causes the center part to dry out. In addition this thermoelectric driven force actually generates a torque within the lithium around the heating area. This torque tends to rotate the heated area so that the downstream side next to the direct heating area tends to rise while the upstream side next to the direct heating area tends to lower. It can be seen that close to the heating area there is a small fast moving region. When current is too high and when the TE force is able to overcome the surface tension ejection of lithium may happen.

Now we can examine the assumption for the above calculation. The heating is assumed to be a point source but in fact the FWHM of the transient heat load is larger than the heating area. The heat transfer is more into the lithium than along the lithium surface. This is actually an advantage which will lower the possibility of deformation and ejection. The heating time is assumed to be small enough to neglect which seems valid. That the convection is not included in the heat transfer is however skeptical since the flow velocity in a small area is very high. If the radial direction is taken as the characteristic length the Peclet can be calculated which ranges from 761 to 6.2. So the influence of the convection will further lower the temperature and in turn lower the velocity increase.

Chapter 7 Conclusion and future work

Liquid metal, especially liquid lithium has drawn a lot of interest from the fusion community because of it great potential as the candidate for plasma facing components. A lot of advantages of liquid lithium have been confirmed on most major fusion reactors. However static liquid lithium surface may become passivated eventually inside fusion reactors since it absorb hydrogen isotopes and impurity particles. As a result it requires a method to replenish fresh lithium or at least refresh the liquid lithium surface. Driving the free surface liquid lithium to move is a potential method and different driving methods have been investigated on many experiments but they all have their own advantages and disadvantages. In most cases the tesla level strong magnetic field and resulted MHD damping is always a major problem.

In this dissertation, a new method called LiMIT concept has been discussed and investigated. This concept utilizes the thermoelectric current generated at the lithium-structural material interface and uses the Lorentz force from the product of the transverse magnetic field and the TE current to drive liquid lithium flow. Besides the damping effect the magnetic field is also a driving force in this concept, which greatly offsets the influence from the MHD damping.

The key of this concept is the TEMHD driven lithium flow in open surface trenches. In order to examine this concept the TEMHD open surface trench flow is firstly analyzed to derive a few equations to relate the flow velocity and temperature distribution to a few parameters. A few LiMIT type lithium trays with multiple trenches have been designed and tested both on a lab-scale chamber and a tokamak. The results confirm the relation between velocity and magnetic field, velocity and surface heating. The related heat transfer is also investigated by thermocouples and IR camera. Experiment results proved the ability of LiMIT concept to drive liquid lithium flow in low and high magnetic fields and to survive a high heat flux bombarding on the surface. In above experiments a lot of unique techniques to handle liquid lithium have been developed. A 3D FEM model is also built to extend the study of this concept to a much larger parameter regime. Experiments results are partially confirmed and the importance of trench geometry and cooling rate of the trench are highlighted. The transient study of the model reveals more detail of the flow as a function of time. In order to fulfill the requirements as the general PFCs narrow LiMIT trenches are built and tested at an inclined angle and it is successfully proved that TEMHD is able

to pump lithium flow along arbitrary directions and this concept can be potentially used as general PFCs besides the divertor surface. In addition, the influence of transient events in tokamaks is briefly studied. It is discovered that the transient event can cause lithium evaporation and severe acceleration. This is caused by the enormous TE current generated during the rapid temperature change right after the transient events.

Future study of the LiMIT concept has a lot of interesting and useful topics. One topic following the vertical trench test is to test the concept in real fusion reactors or similar conditions. The scheduled test on EAST is going to test lithium injection, lithium flow, lithium collection, heat transfer, the influence of the plasma on the lithium surface and the influence of the flowing lithium surface on the plasma. A prototype trench will be tested at CPMI ahead of time and eventually the LiMIT type limiter will be designed for EAST. If most features can be demonstrated in the test on EAST the steady state flow needs to be achieved by designing heaters with higher heat flux in vacuum to achieve a high enough temperature gradient. In addition our experience tells that once the impurity layer forms on lithium surface the flow itself is not capable to break it. The passivation of the lithium surface and the accumulation of impurity inside liquid lithium on a long term scale will be crucial for the wall tile application. In order to remove the impurity scale on the surface methods such as plasma sputtering, thermal desorption need further investigation. The ultimate goal is to create sustainable lithium flow that can last and keep fresh for the entire campaign without replenishing the lithium.

Another topic is to study the effect caused by the transient events. TELS has been constructed and it will be a good platform for this study. The discussion in chapter 6 shows the large TE current generated during the transient event. The disturbance to the lithium flow and potential ejection caused by the TE current may lead to problem for the divertor application. In addition transient event may evaporate and sputter lithium off the surface within shot time and possibly damage the solid structure underneath. The motion of the free surface, the temperature evolution during the transient event and methods to suppress the influence of the transient events are necessary to find out.

The third topic is related to the structural material. Although stainless steel is used in this experiment due to its wetting and thermoelectric coefficient it may not have enough life time in tokamaks. On the other hand Mo seems to be a good choice for the long term application.

Combining them by coat stainless steel trench with thick Mo layer may utilize the advantages of both. Other structure material that has high thermoelectric coefficient such as thallium-doped lead telluride alloy [74] or bismuth chalcogenides [75] can also be investigated. The magnetron sputtering or metal deposition by atmospheric microwave plasma torch can be utilized to manufacture this multilayer material. The ideal wall material would have high melting point, high heat transfer coefficient, high thermoelectric power respect to lithium and good corrosion resistance to liquid lithium.

The fourth topic is related to the dry-out effect, which becomes more and more severe when the heating power is increasing. This effect definitely needs to be avoided for divertor application. The fact of dry-out is actually the unbalanced flow velocity between the higher temperature gradient area and the low temperature gradient area. In direct heating area the elevated velocity and the conservative of mass flow rate requires the cross section of lithium to shrink. Trenches with changing shape along the flow directions may accommodate the velocity change across the heating area. Utilizing the capillary force by adding mesh to the heated area may also stabilize the lithium flow. In addition the direct heating area can also be coated by different material to balance the TE driven force along the trench.

In general LiMIT trenches have great potential to serve as general PFCs and divertor/limiter. Further study will be more related to the problems raised when it is in real fusion environment. However there are a lot of design criteria in the LiMIT concept to work on which on the other hand give a lot of freedom for the engineering of the LiMIT type PFCs to accommodate different requirements from the fusion reactors.

Reference

1. Greenwald, M., et al., *Priorities, gaps and opportunities: Towards a long-range strategic plan for magnetic fusion energy.* A Report to the Fusion Energy Sciences Advisory Committee, 2007.

2. Miley, G.H., *Fusion energy conversion*. 1976: Amer Nuclear Society.

3. *Cross section of Tokamak http://ars.els-cdn.com/content/image/1-s2.0-S0920379602000054-gr1.gif.*

4. Shimada, M., et al., *Overview of goals and performance of ITER and strategy for plasma–wall interaction investigation.* Journal of nuclear materials, 2005. **337**: p. 808-815.

5. Barabash, V., et al., *Carbon fiber composites application in ITER plasma facing components.* Journal of nuclear materials, 1998. **258**: p. 149-159.

6. Barabash, V., G. Federici, and R. Matera, *Armour materials for the ITER plasma facing components.* Physica Scripta, 1999. **1999**: p. 74.

7. Keilhacker, M., *Overview of results from the JET tokamak using a beryllium first wall.* Physics of Fluids B, 1990. **2**: p. 1291.

8. Gruber, O., A. Kallenbach, and M. Kaufmann, *Observation of continuous divertor detachment in H-mode discharges in ASDEX Upgrade.* Physical Review Letters, 1995. **74**: p. 4217.

9. Ryutov, D., *Geometrical properties of a "snowflake" divertor.* Physics of Plasmas, 2007. **14**: p. 064502.

10. Herrmann, A., T. Eich, and S. Jachmich, *Stationary and transient divertor heat flux profiles and extrapolation to ITER.* Journal of Nuclear Materials, 2003. **313-316**: p. 759-767.

11. Kaita, R., et al., *Experiments with liquid metal walls: Status of the lithium tokamak experiment.* Fusion Engineering and Design, 2010. **85**: p. 874-881.

12. Hu, J.S., et al., *An overview of lithium experiments on HT-7 and EAST during 2012.* Fusion Engineering and Design, 2014. **89**: p. 2875-2885.

13. Morley, N. and J. Burris, *The MTOR LM-MHD flow facility, and preliminary experimental investigation of thin layer, liquid metal flow in a 1/R toroidal magnetic field.* Fusion science and technology, 2003. **44**: p. 74.

14. Abdou, M., et al., *On the exploration of innovative concepts for fusion chamber technology.* Fusion Engineering and Design, 2001. **54**: p. 181-247.

15. Ruzic, D., M. Allain, and R. Budny, *The effect of lithium wall conditioning in TFTR on plasma–surface interactions.* Journal of nuclear materials, 1999. **269**: p. 1303-1308.

16. Kugel, H.W., et al., *Effect of lithium PFC coatings on NSTX density control.* Journal of Nuclear Materials, 2007. **363-365**: p. 791-796.

17. Nieto, M., et al., *Helium retention and diffusivity in flowing liquid lithium.* Journal of Nuclear Materials, 2003. **313-316**: p. 646-650.

18. Esser, P.D., *Stability of the lithium'waterfall'first wall protection concept for inertial confinement fusion reactors.* Nuclear Technology Fusion, 1981. **1**: p. 285-294.

19. Strachan, J.D., et al., *Wall conditioning experiments on TFTR using impurity pellet injection.* Journal of Nuclear Materials, 1994. **217**: p. 145-153.

20. Brooks, J.N., et al., *OVERVIEW OF THE ALPS PROGRAM.* Fusion science and technology, 2005. **47**: p. 669-677.

21. Majeski, R., et al., *Testing of liquid lithium limiters in CDX-U.* Fusion Engineering and Design, 2004. **72**: p. 121-132.

22. Zuo, G., et al., *First results of lithium experiments on EAST and HT-7.* Journal of Nuclear Materials, 2011. **415**(1): p. S1062-S1066.

23. Whyte, D., et al., *Experimental observations of lithium as a plasma-facing surface in the DIII-D tokamak divertor.* Fusion engineering and design, 2004. **72**(1): p. 133-147.

24. Morley, N., et al., *Progress on the modeling of liquid metal, free surface, MHD flows for fusion liquid walls.* Fusion Engineering and Design, 2004. **72**(1): p. 3-34.

25. Majeski, R., et al., *Recent liquid lithium limiter experiments in CDX-U.* Nuclear fusion, 2005. **45**(6): p. 519.

26. Evtikhin, V., et al., *Technological aspects of lithium capillary-pore systems application in tokamak device.* Fusion engineering and design, 2001. **56**: p. 363-367.

27. Evtikhin, V., et al., *Main directions and recent test modeling results of lithium capillary-pore systems as plasma facing components.* Plasma Science and Technology, 2004. **6**(3): p. 2291.

28. Apicella, M., et al., *Lithium capillary porous system behavior as PFM in FTU tokamak experiments.* Journal of Nuclear Materials, 2009. **386**: p. 821-823.

29. Kugel, H., et al., *Physics design requirements for the National Spherical Torus Experiment liquid lithium divertor.* Fusion Engineering and Design, 2009. **84**(7): p. 1125-1129.

30. Bell, M., et al., *Plasma response to lithium-coated plasma-facing components in the National Spherical Torus Experiment.* Plasma Physics and Controlled Fusion, 2009. **51**(12): p. 124054.

31. Canik, J., et al., *Edge transport and turbulence reduction with lithium coated plasma facing components in the National Spherical Torus Experiment a).* Physics of Plasmas (1994-present), 2011. **18**(5): p. 056118.

32. Allain, J., M. Coventry, and D. Ruzic, *Temperature dependence of liquid-lithium sputtering from oblique 700 eV He ions.* Journal of nuclear materials, 2003. **313**: p. 641-645.

33. Jeppson, D., et al., *Lithium literature review: lithium's properties and interactions*, 1978, Hanford Engineering Development Lab., Richland, Wash.(USA).

34. Ying, A., et al., *Exploratory studies of flowing liquid metal divertor options for fusion-relevant magnetic fields in the MTOR facility.* Fusion engineering and design, 2004. **72**(1): p. 35-62.

35. Shercliff, J., *Thermoelectric magnetohydrodynamics.* Journal of fluid mechanics, 1979. **91**(02): p. 231-251.

36. Khine, Y. and J. Walker, *Thermoelectric magnetohydrodynamic effects during Bridgman semiconductor crystal growth with a uniform axial magnetic field.* Journal of Crystal Growth, 1998. **183**(1): p. 150-158.

37. Moreau, R., et al., *Thermoelectric magnetohydrodynamic effects on solidification of metallic alloys in the dendritic regime.* Materials Science and Engineering: A, 1993. **173**(1): p. 93-100.

38. Osterle, J. and S. Angrist, *The Thermoelectric-Hydromagnetic Pump.* Journal of Heat Transfer, 1964. **86**(2): p. 166-168.

39. Perlow, M. and K. Davis, *THE DEVELOPMENT OF THE SNAP-10A THERMOELECTRIC PUMP.* Transactions of the American Nuclear Society (US), 1965. **8**.

40. Shercliff, J., *Thermoelectric magnetohydrodynamics in closed containers.* Physics of Fluids (1958-1988), 1979. **22**(4): p. 635-640.

41. Shercliff, J., *The pipe end problem in thermoelectric MHD.* Zeitschrift für angewandte Mathematik und Physik ZAMP, 1980. **31**(1): p. 94-112.

42. Shercliff, J., *Thermoelectric MHD with walls parallel to the magnetic field.* International Journal of Heat and Mass Transfer, 1980. **23**(9): p. 1219-1228.

43. Shercliff, J. *Thermoelectric MHD affects heat flow in liquid lithium*. in *Proceedings of the 9th Symposium on the Engineering Problems of Fusion Research, Chicago, 198l*. 1981.

44. Shercliff, J., *Non-uniqueness in thermoelectric magnetohydrodynamic heat convection.* Proceedings of the Royal Society of London. A. Mathematical and Physical Sciences, 1982. **382**(1783): p. 273-293.

45. Xu, W., et al., *Investigation of the heat transfer in TEMHD driven swirling lithium flow.* Journal of Nuclear Materials, 2011. **415**(1): p. S981-S984.

46. Ruzic, D., et al., *Lithium-metal infused trenches (LiMIT) for heat removal in fusion devices.* Nucl Fusion, 2011. **51**(102002): p. 4.

47. Gerhardt, S., et al., *Progress in understanding the enhanced pedestal H-mode in NSTX*. Nuclear Fusion, 2014. **54**(8): p. 083021.

48. Ono, M., et al., *Recent progress in the NSTX/NSTX-U lithium programme and prospects for reactor-relevant liquid-lithium based divertor development.* Nuclear Fusion, 2013. **53**(11): p. 113030.

49. *FTU Mo Limiter* *http://www.fusione.enea.it/multimedia/albums/FTU/FTURepertorio/images/FTU%20-%2007.gif*.

50. Fiflis, P., et al., *Seebeck coefficient measurements on Li, Sn, Ta, Mo, and W.* Journal of Nuclear Materials, 2013. **438**(1): p. 224-227.

51. *Peltier Effect* *http://www.mpoweruk.com/images/peltier.gif*.

52. Davidson, P.A., *An introduction to magnetohydrodynamics*. Vol. 25. 2001: Cambridge university press.

53. Incropera, F.P., *Fundamentals of heat and mass transfer*. 2011: John Wiley & Sons.

54. Maingi, R., et al., *Heat flux scaling experiments in NSTX*. Journal of nuclear materials, 2003. **313**: p. 1005-1009.

55. Ihli, T., et al., *Design and performance study of the helium-cooled T-tube divertor concept.* Fusion engineering and design, 2007. **82**(3): p. 249-264.

56. Youchison, D.L., et al., *Thermal performance and flow instabilities in a multi-channel, helium-cooled, porous metal divertor module.* Fusion engineering and design, 2000. **49**: p. 407-415.

57. Fiflis, P., et al., *Wetting properties of liquid lithium on select fusion relevant surfaces.* Fusion Engineering and Design, 2014. **89**(12): p. 2827-2832.

58. Vollmer, M. and K.-P. Möllmann, *Infrared thermal imaging: fundamentals, research and applications*. 2010: John Wiley & Sons.

59. Rosenberg, M., R. Smirnov, and A.Y. Pigarov, *On thermal radiation from fusion related metals.* Fusion Engineering and Design, 2009. **84**(1): p. 38-42.

60. Challis, C., et al., *Current ramp experiments on the scaling of energy confinement.* Nuclear fusion, 1992. **32**(12): p. 2217.

61. Gao, F., J. Chen, and J. Li, *Primary research of heat flux deposition pattern on the surface of HT-7 movable limiter.* Fusion Engineering and Design, 2008. **83**(1): p. 1-5.

62. Ren, J., et al., *First results of flowing liquid lithium limiter in HT-7.* Physica Scripta, 2014. **2014**(T159): p. 014033.

63. Zuo, G., et al., *Comparison of various wall conditionings on the reduction of H content and particle recycling in EAST.* Plasma Physics and Controlled Fusion, 2012. **54**(1): p. 015014.

64. Pearson, J., *On convection cells induced by surface tension.* Journal of fluid mechanics, 1958. **4**(05): p. 489-500.

65. Jaworski, M.A., *Thermoelectric magnetohydrodynamic and thermocapillary driven flows of liquid conductors in magnetic fields.* 2009.

66. Cattadori, G., et al., *Hypervapotron technique in subcooled flow boiling CHF*. Experimental thermal and fluid science, 1993. **7**(3): p. 230-240.

67. Haake, D., et al., *Flow rate limitation in open capillary channel flows.* Annals of the New York Academy of Sciences, 2006. **1077**(1): p. 443-458.

68. Clement, S., et al., *Power deposition in the JET divertor during ELMs.* Journal of nuclear materials, 1999. **266**: p. 285-290.

69. Federici, G., et al., *Effects of ELMs and disruptions on ITER divertor armour materials.* Journal of nuclear materials, 2005. **337**: p. 684-690.

70. Federici, G., A. Loarte, and G. Strohmayer, *Assessment of erosion of the ITER divertor targets during type I ELMs.* Plasma physics and controlled fusion, 2003. **45**(9): p. 1523.

71. Silva, C., et al., *Determination of the particle and energy fluxes in the JET far SOL during ELMs using the reciprocating probe diagnostic.* Journal of nuclear materials, 2005. **337**: p. 722-726.

72. Lasnier, C., et al., *Survey of target plate heat flux in diverted DIII-D tokamak discharges.* Nuclear fusion, 1998. **38**(8): p. 1225.

73. Incropera, F.P., *Introduction to heat transfer*. 2011: John Wiley & Sons.

74. Yu, B., et al., *Thermoelectric property studies on thallium-doped lead telluride prepared by ball milling and hot pressing.* Journal of Applied Physics, 2010. **108**(1): p. 016104-016104-3.

75. Mishra, S., S. Satpathy, and O. Jepsen, *Electronic structure and thermoelectric properties of bismuth telluride and bismuth selenide.* Journal of Physics: Condensed Matter, 1997. **9**(2): p. 461.

Appendix

This appendix includes all the CAD drawings for different versions of LiMIT trenches. If not specified the unit for all labelled numbers is millimeter.

First version LiMIT trenches for SLiDE experiment.

This is the CAD drawing for the first version of LiMIT trenches test on SLiDE project which is a proof of concept design to demonstrate the feasibility of TEMHD driven flow in open channels. See Figure 3.7 and section 3.1 Design LiMIT trenches.

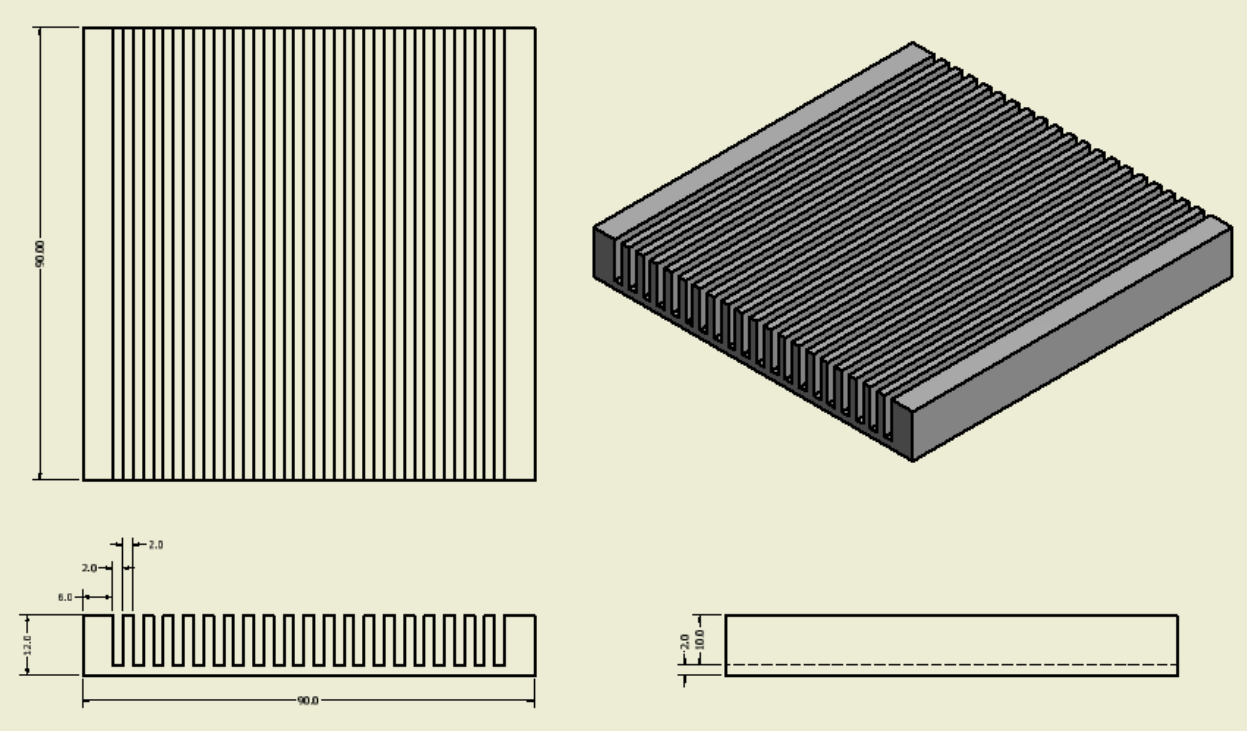

Figure A.1 CAD drawing of trench part

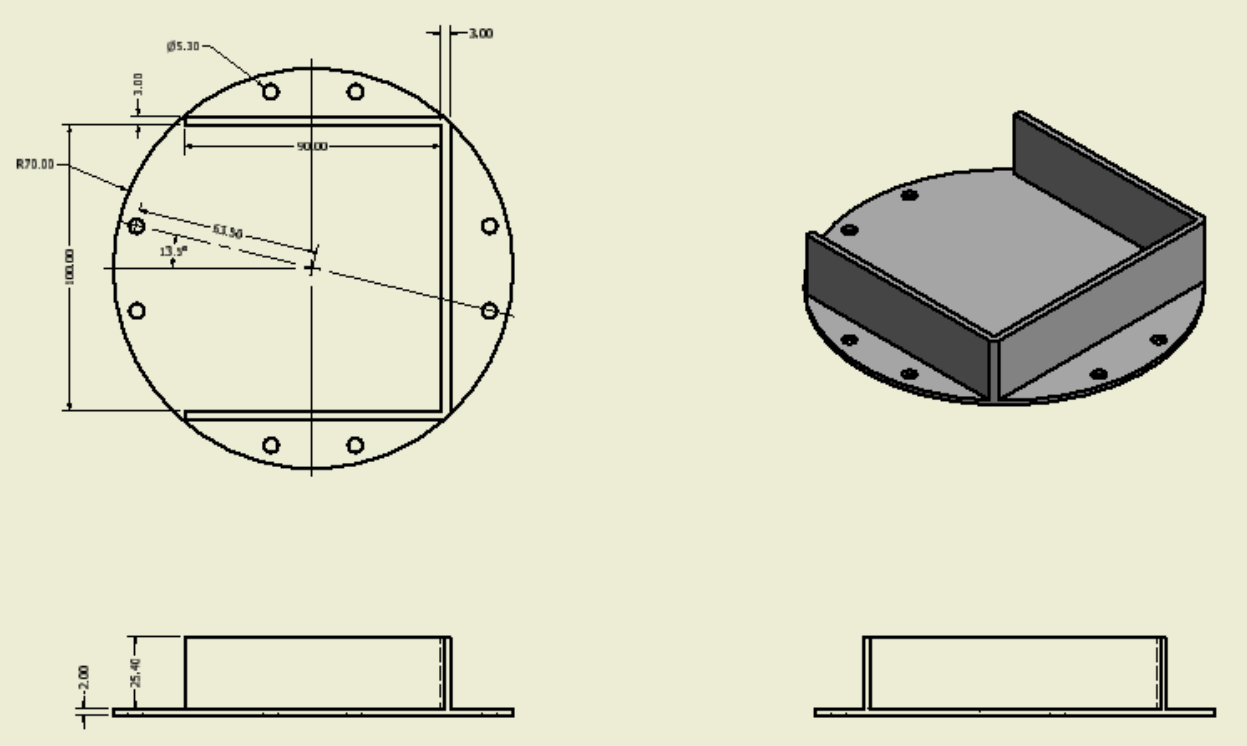

Figure A.2 CAD drawing of the tray

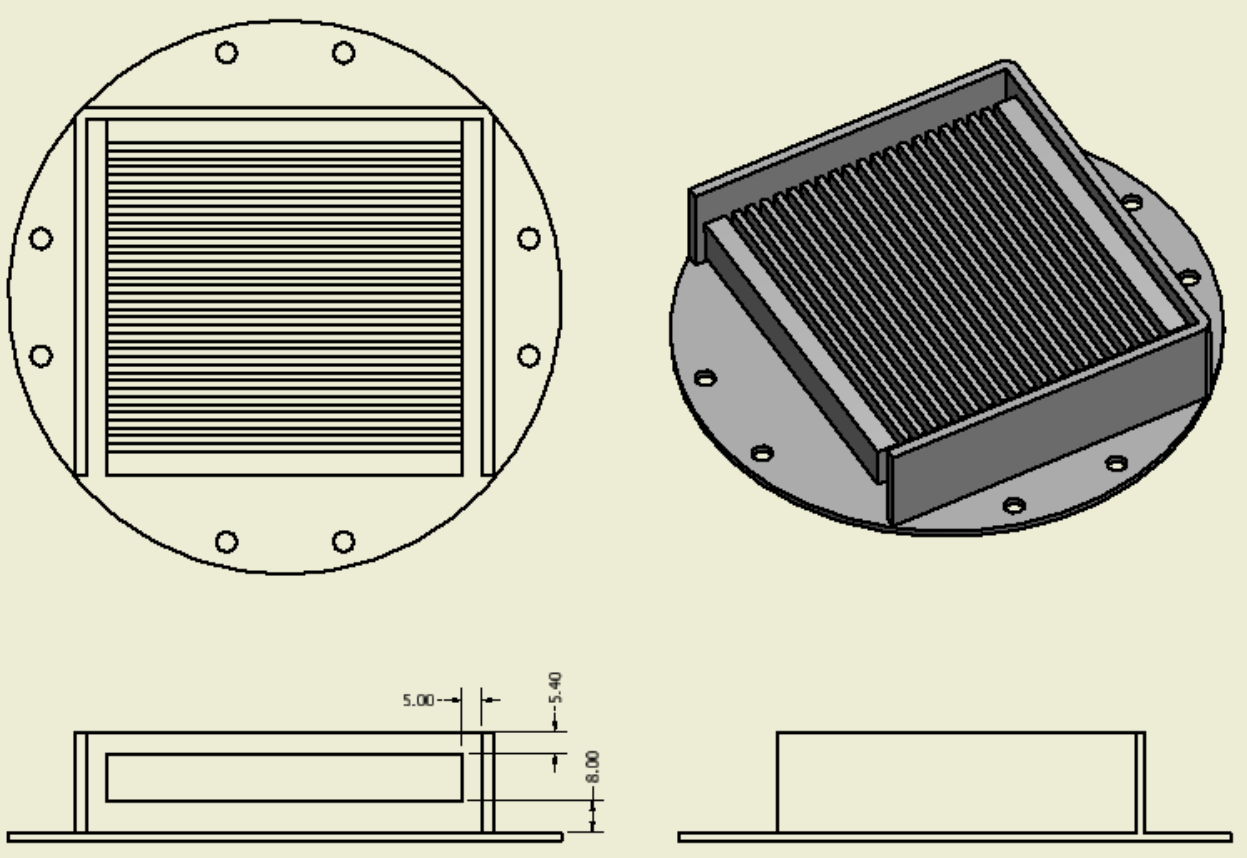

Figure A.3 CAD drawing of the assembled first version LiMIT trenches

Second version LiMIT trenches for SLiDE experiment

This is the second version LiMIT trenches for SLiDE experiment. See Figure 3.9 and section 3.1 Design LiMIT trenches.

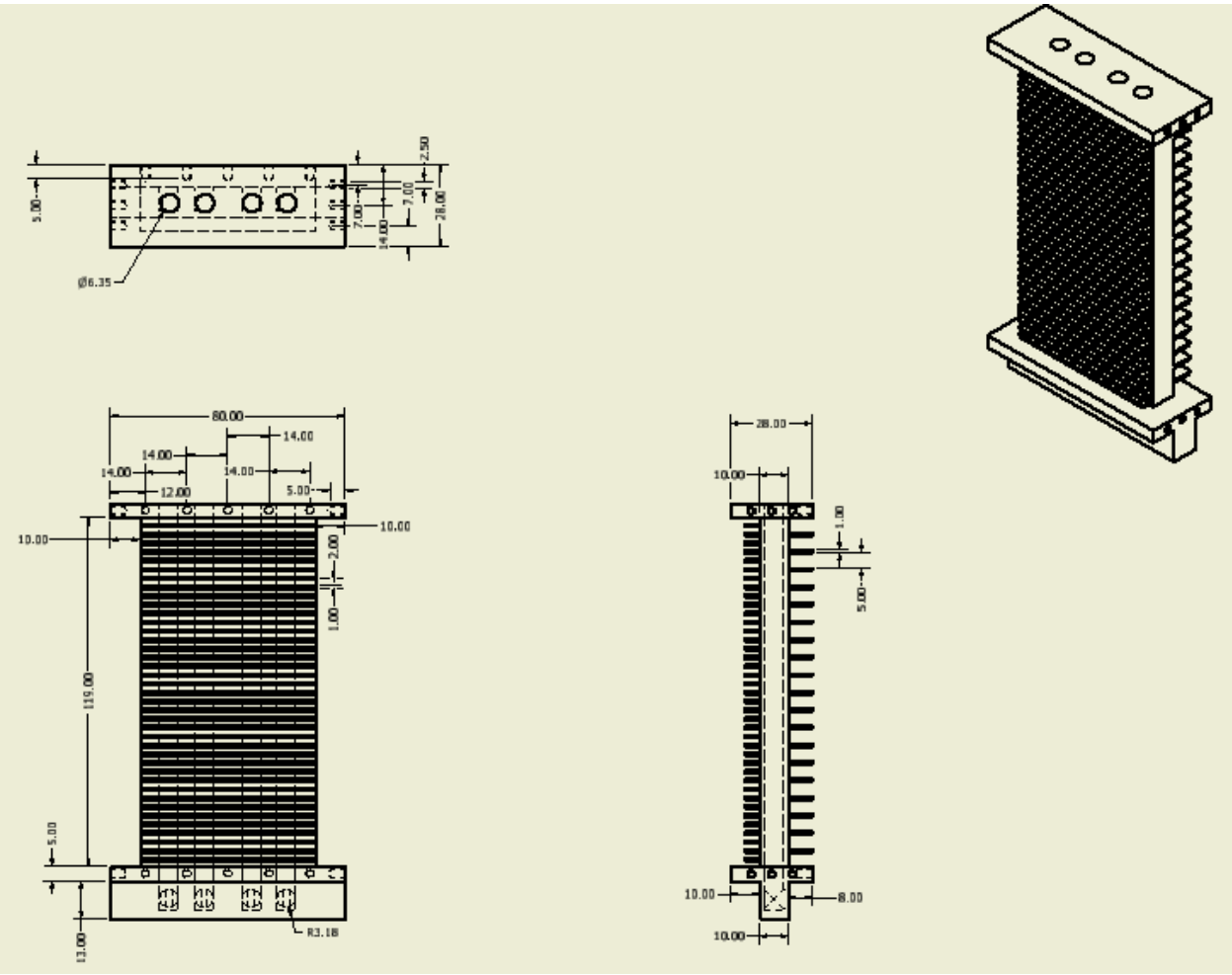

Figure A.4 CAD drawings of the trench part, second version LiMIT trenches

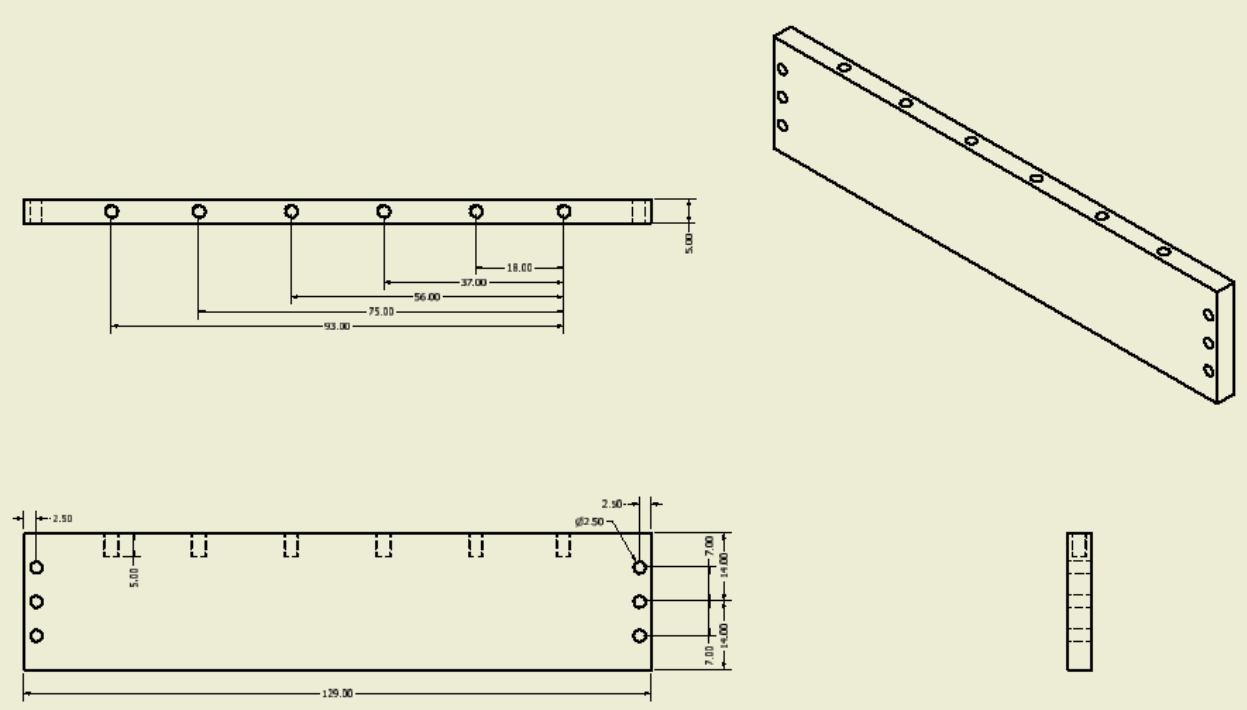

Figure A.5 CAD drawing of the side plate for the second version LiMIT trenches

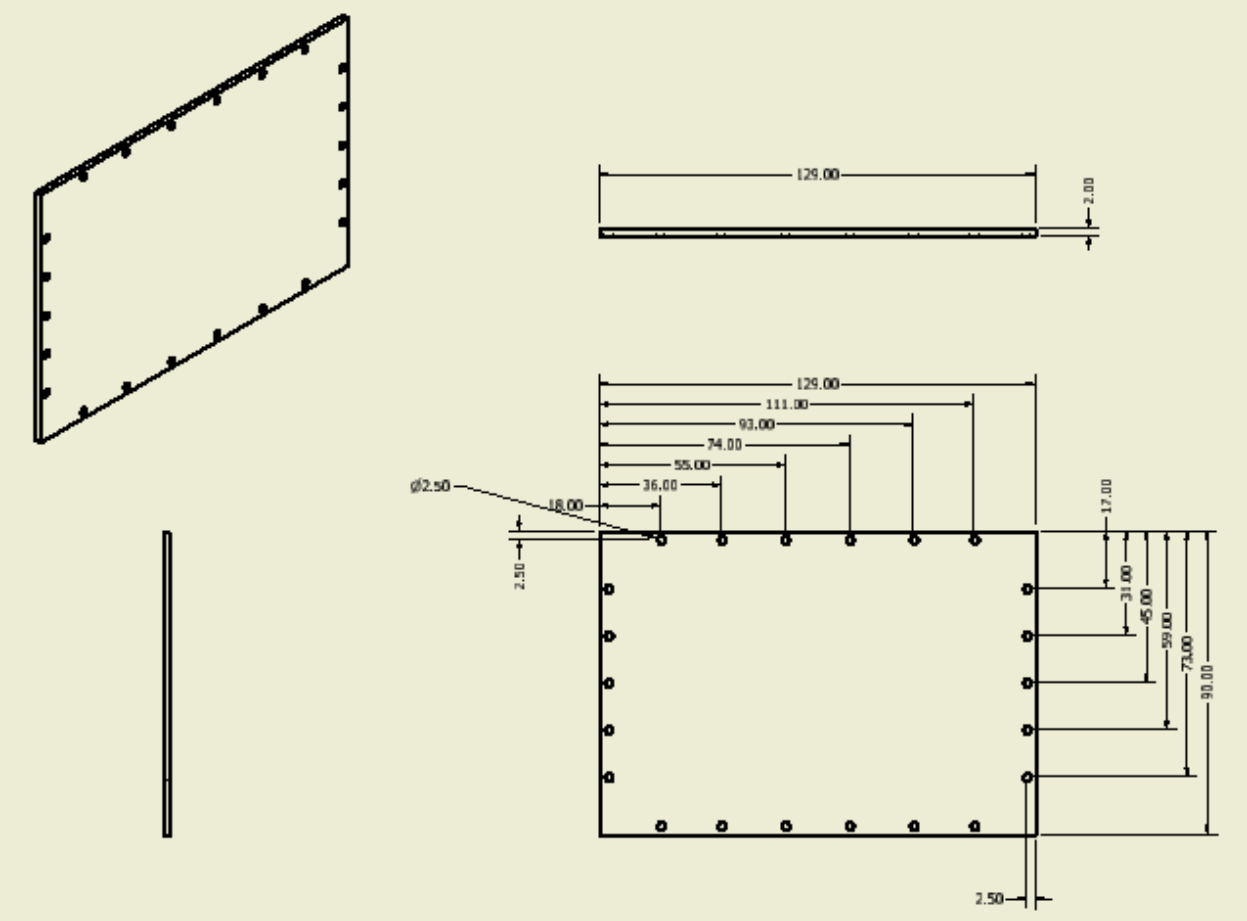

Figure A.6 CAD drawing of the bottom plate for the second version LiMIT trenches

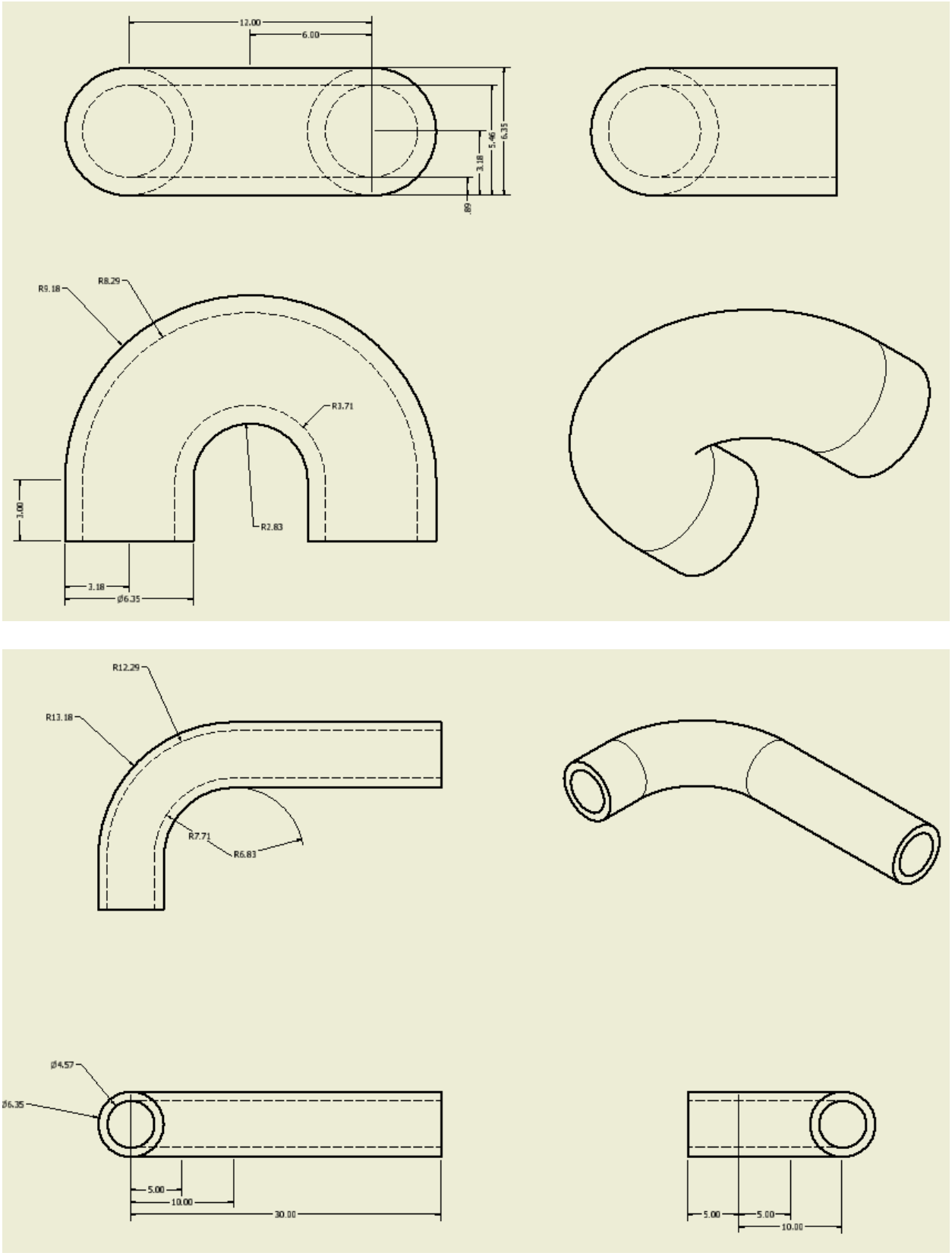

Figure A.7 CAD drawing of the cooling channel elbows for the second version LiMIT trenches

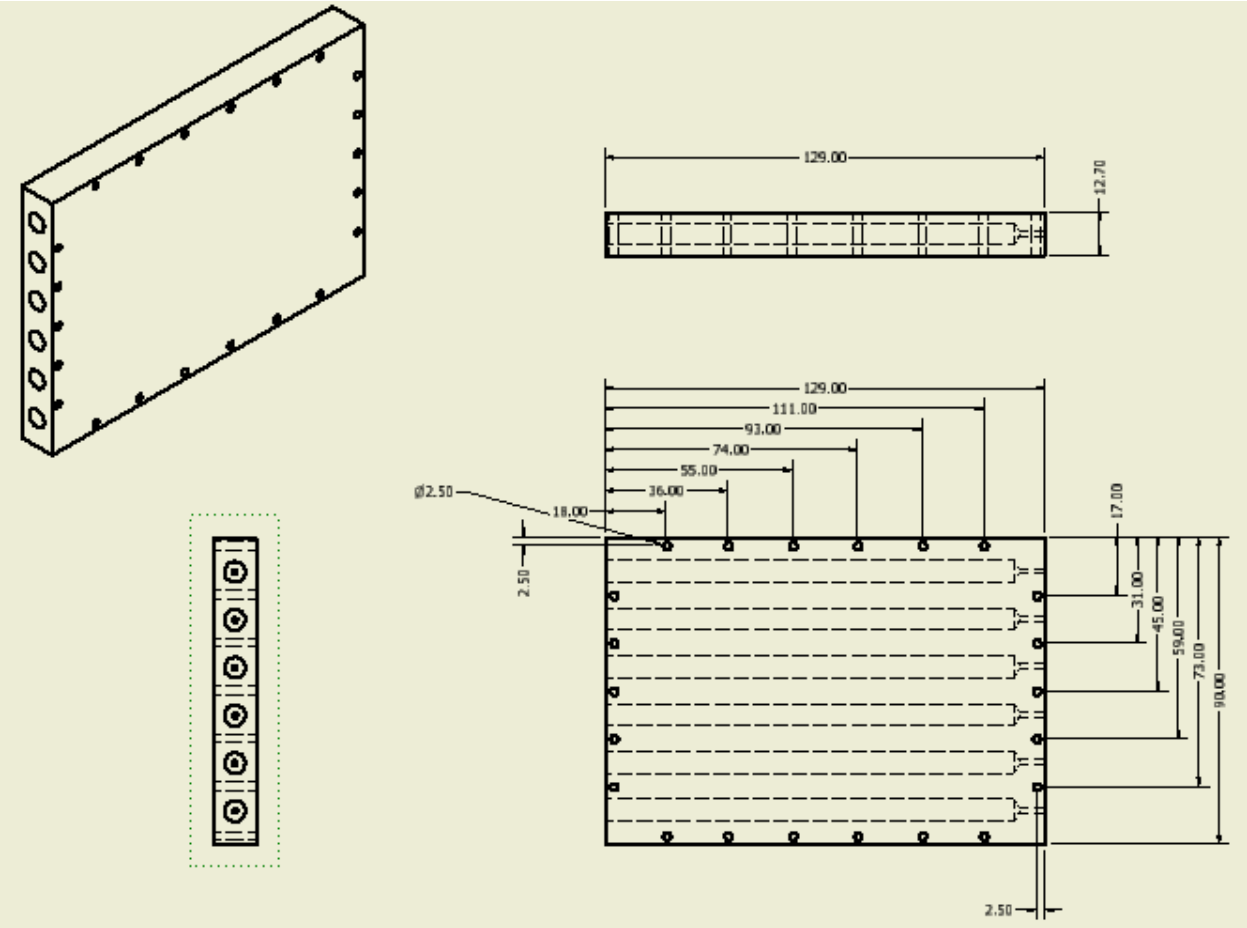

Figure A.8 CAD drawing of the heating plate for the second version LiMIT trenches

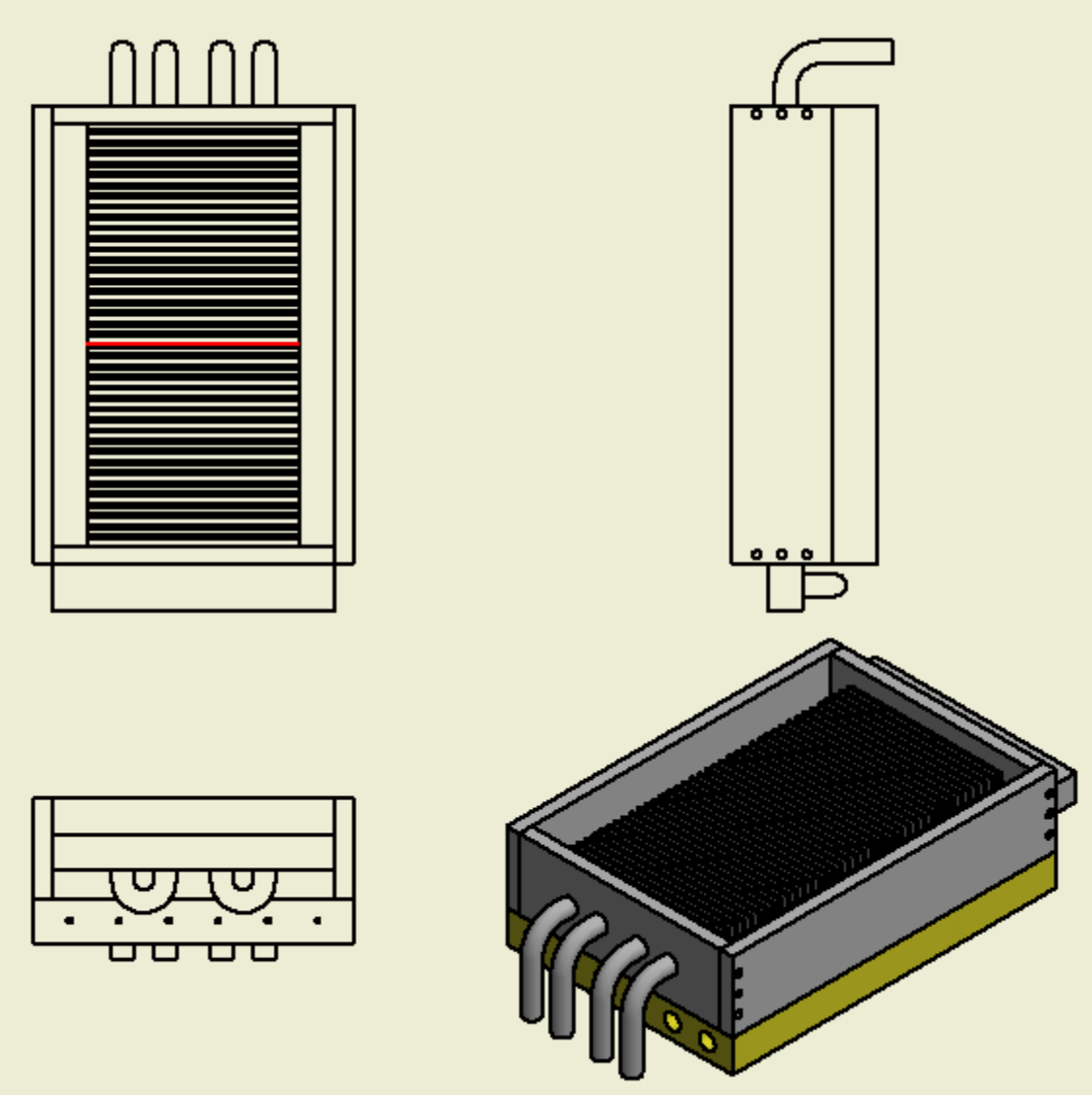

Figure A.9 CAD drawing of the assembled second version LiMIT trenches

LiMIT trenches design for vertical trench test

This is the CAD drawings for the LiMIT trenches design used in the vertical trench test. In this design narrow trenches are used. See section 5.2.1 Design of the LiMIT trenches

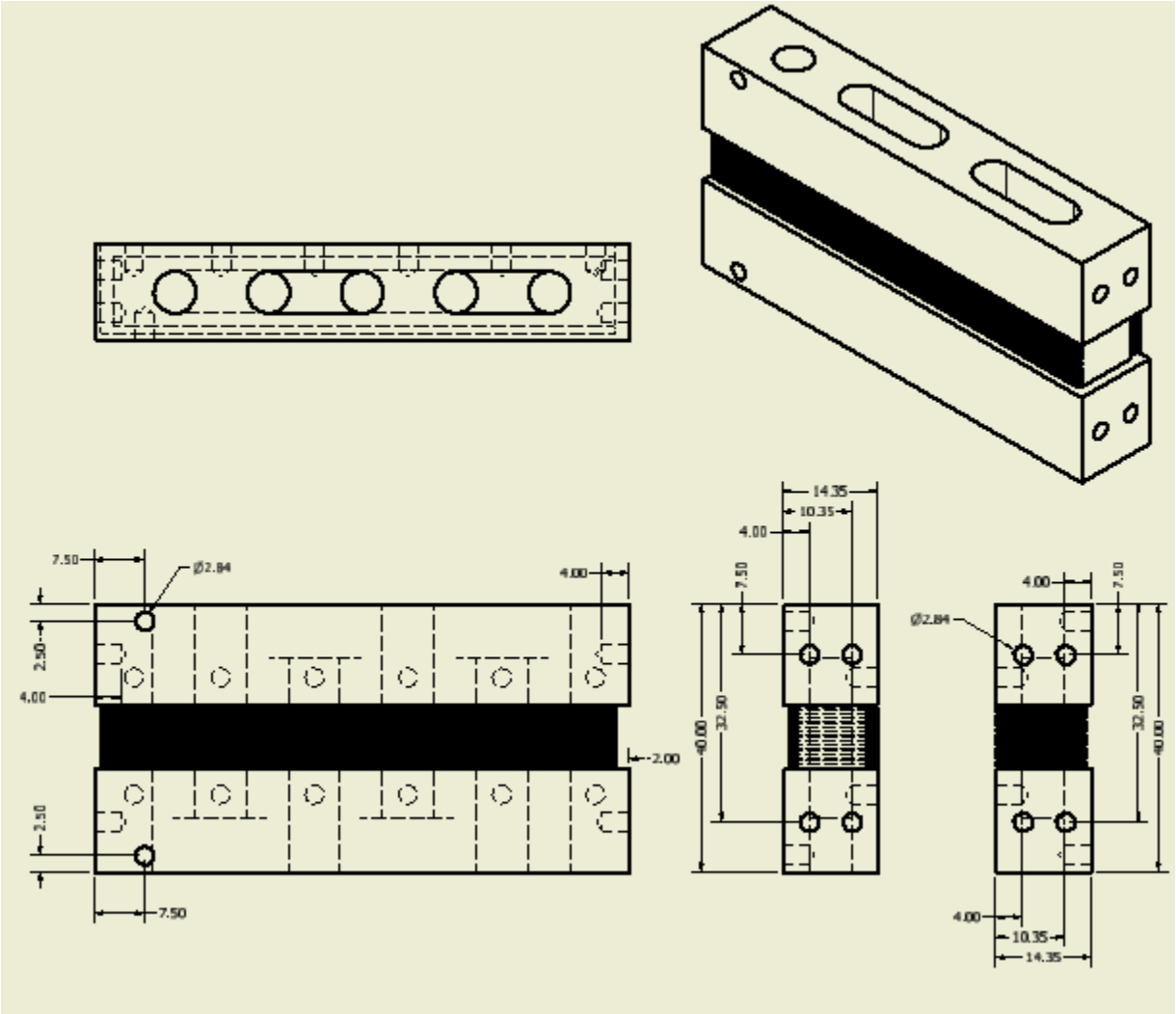

Figure A.10 CAD drawings of the trench part for the vertical trench test

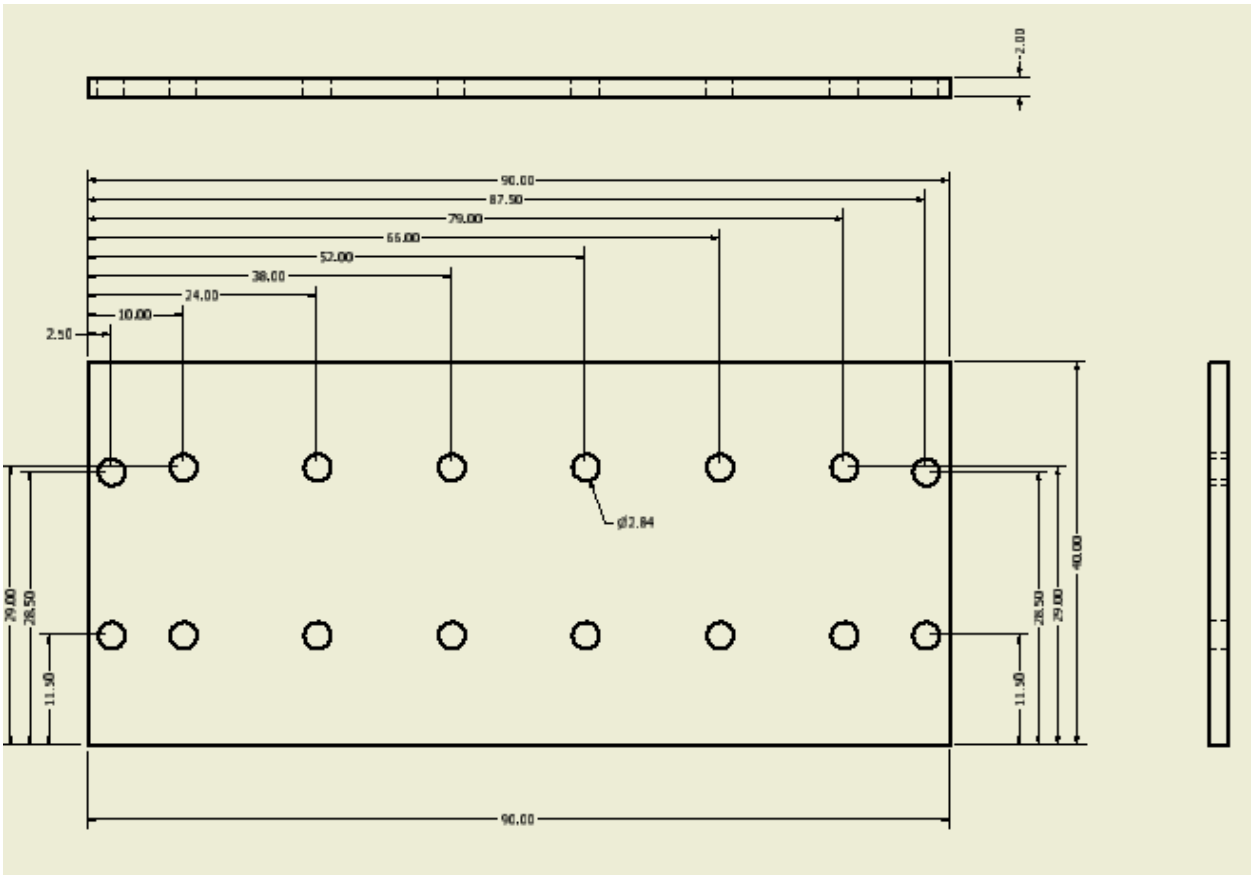

Figure A.11 CAD drawings of the bottom plate for the vertical trench test

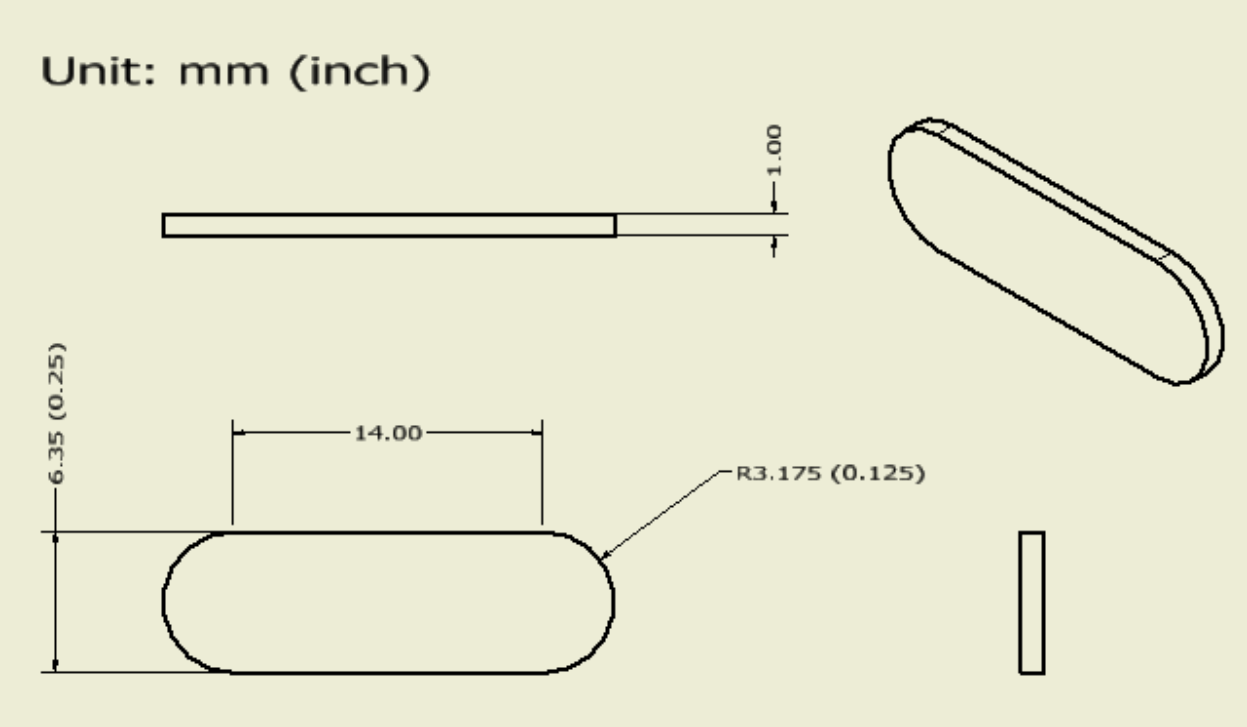

Figure A.12 CAD drawings of cooling channel welding plate for the vertical trench test

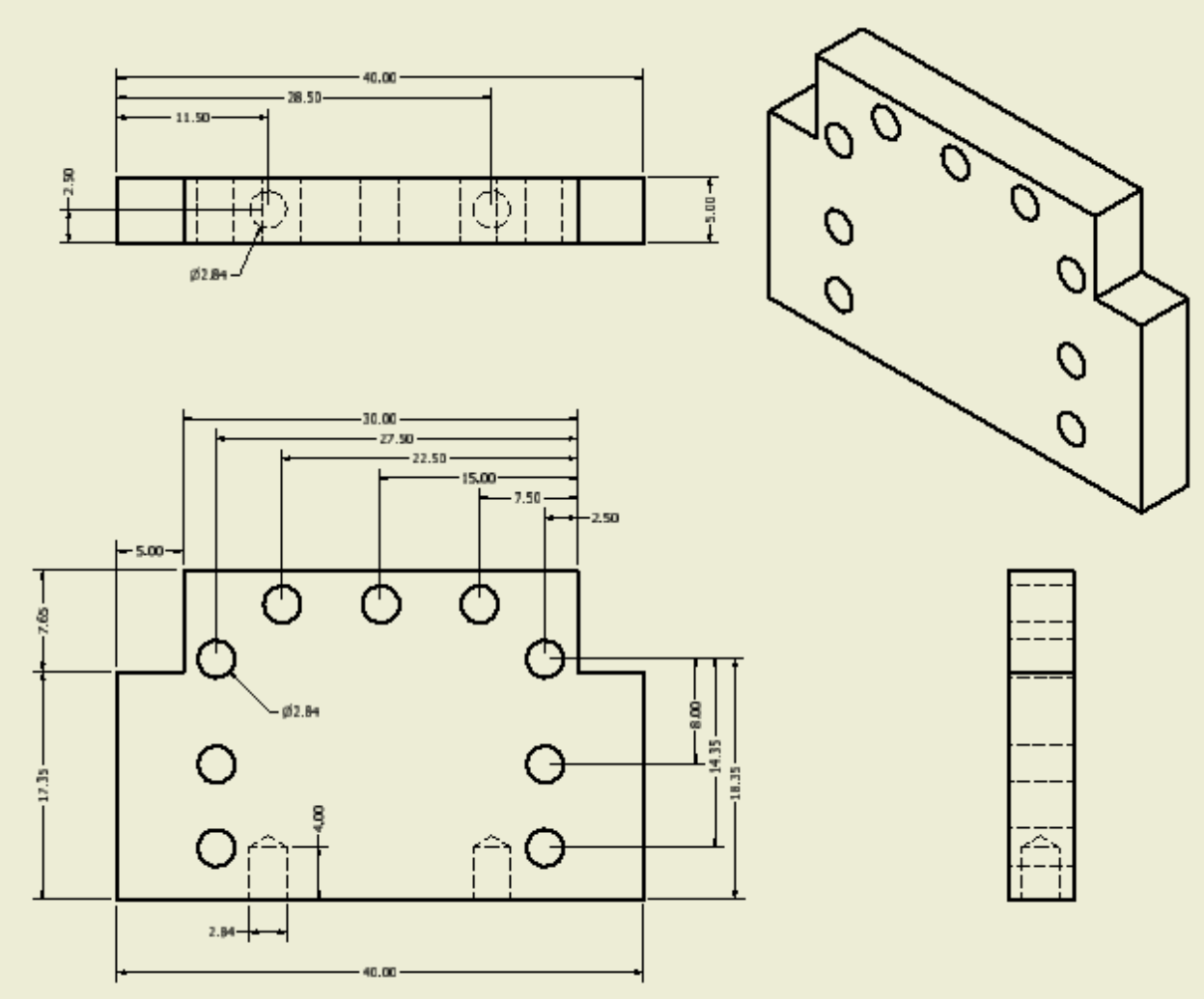

Figure A.13 CAD drawings of the lithium reservoir for the vertical trench test, part one

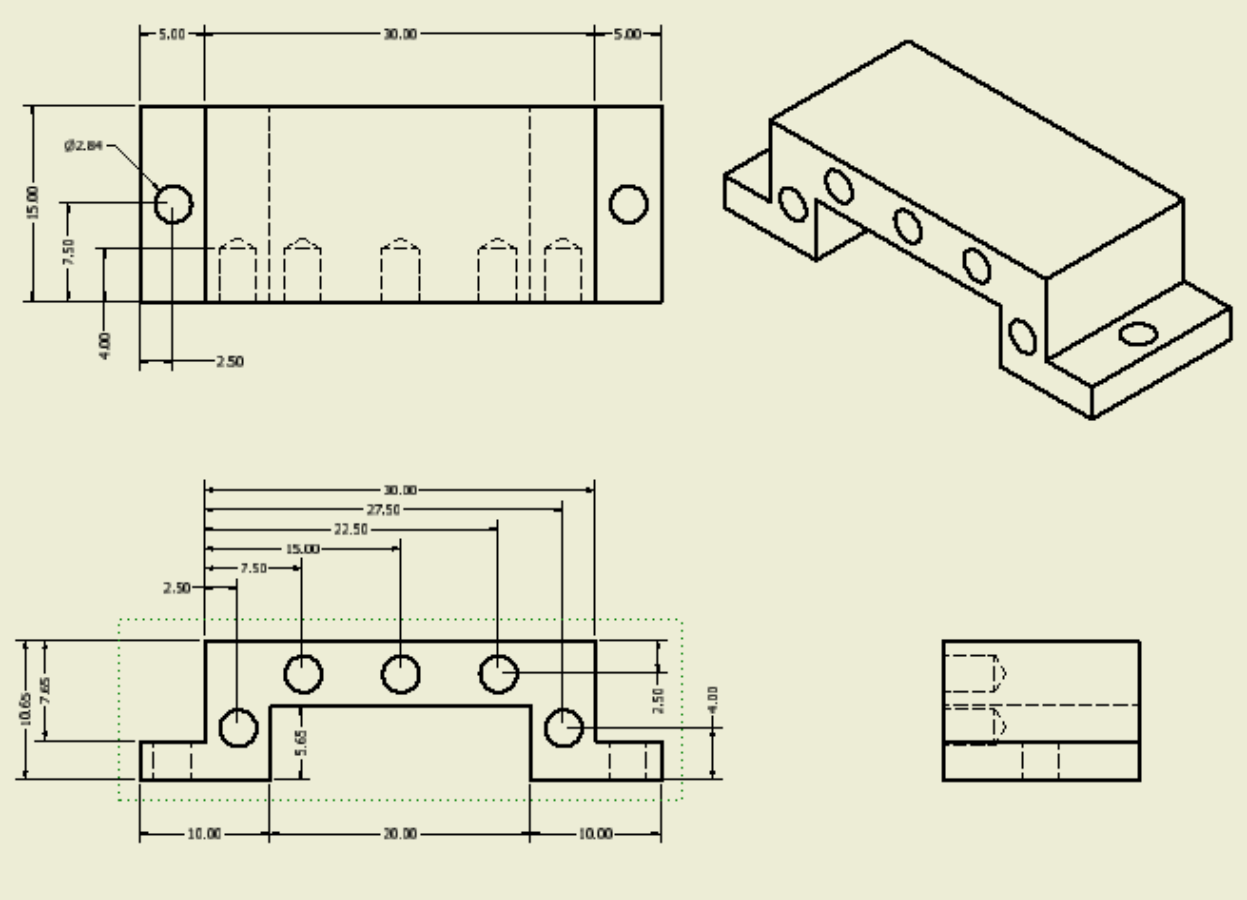

Figure A.14 CAD drawings of the lithium reservoir for the vertical trench test, part two

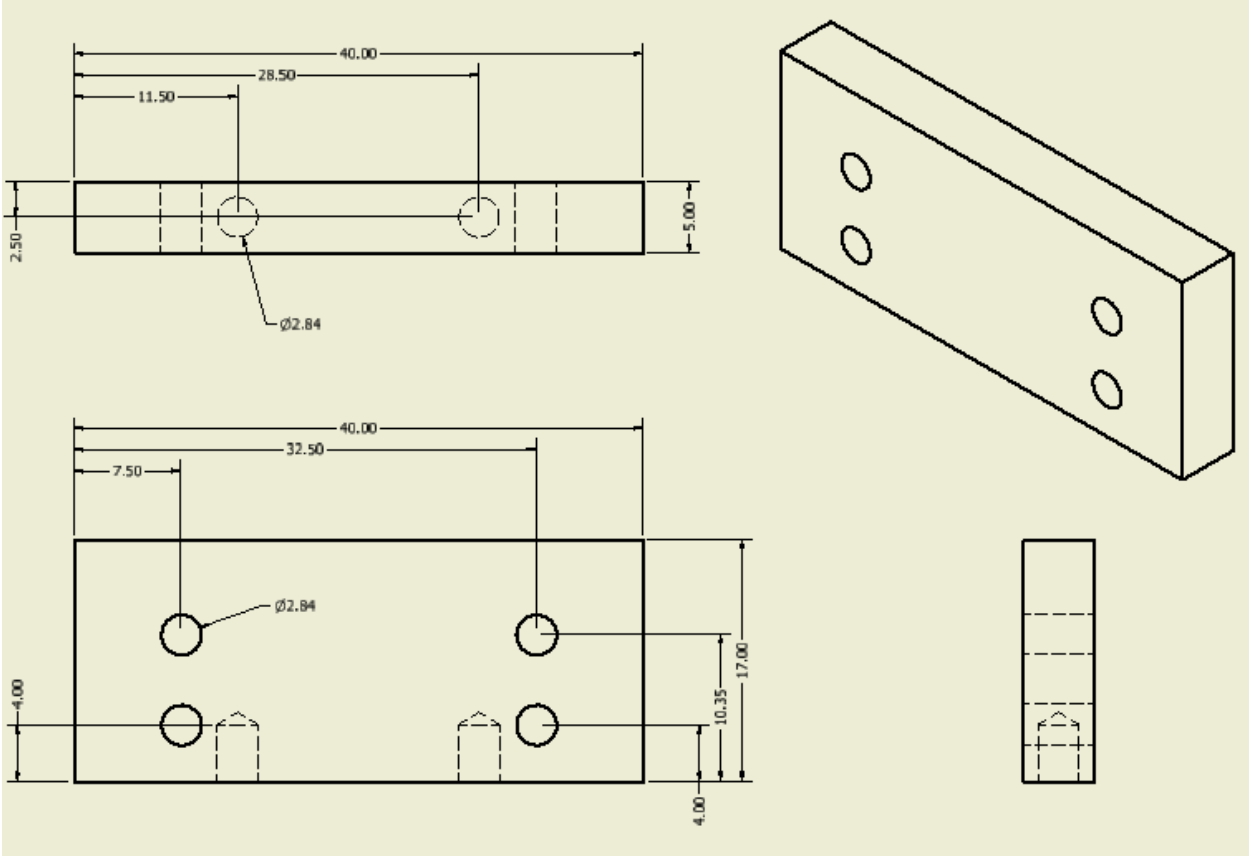

Figure A.15 CAD drawings of the lithium reservoir for the vertical trench test, part three

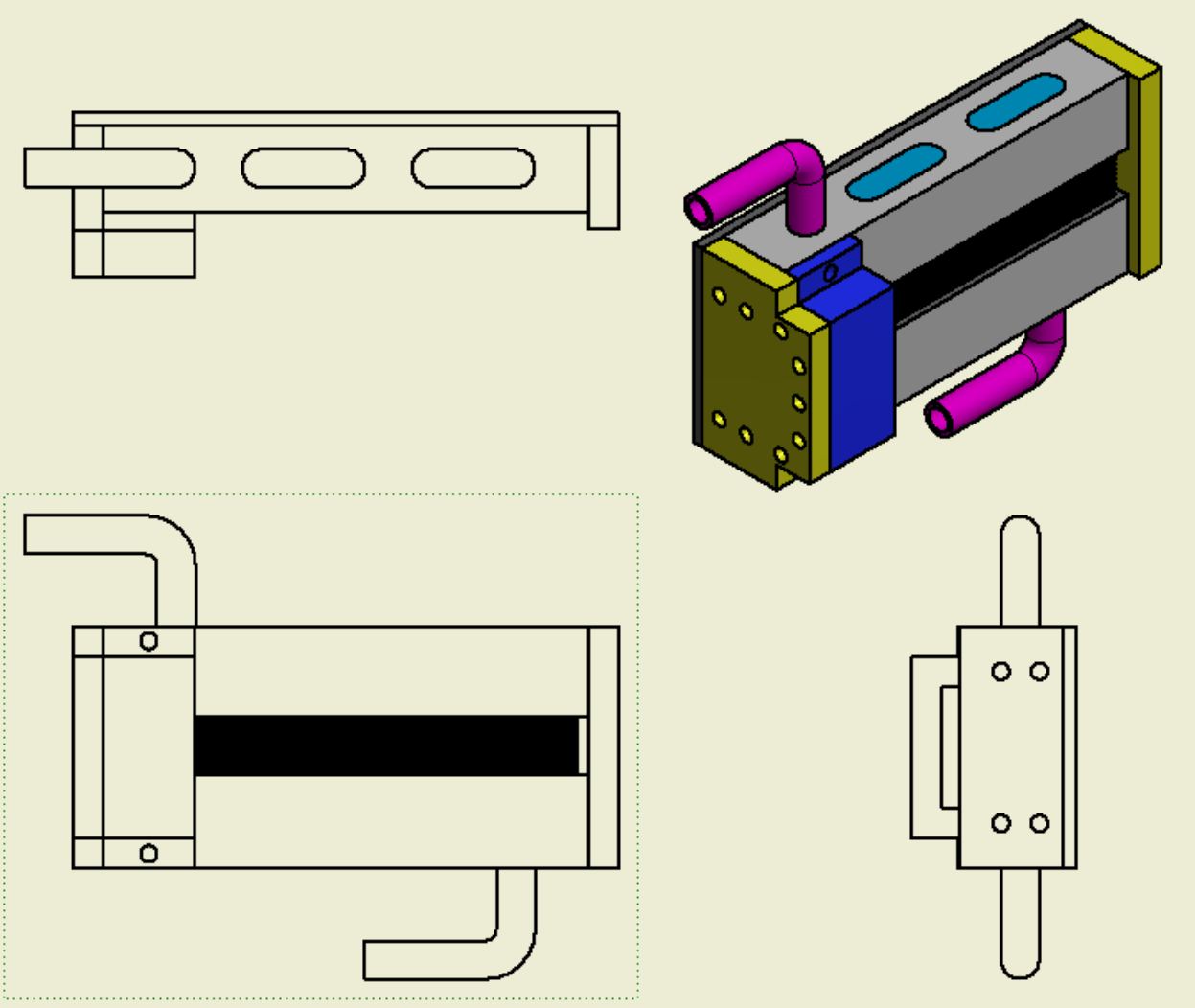

Figure A.16 CAD drawing of the assembled second version LiMIT trenches